Tailoring the synthesis of graphene and other 2D materials towards applications

Vitaliy Babenko

Linacre College

Oxford University

A thesis submitted for the degree of

Doctor of Philosophy in Material Science

Trinity 2016

I confirm that the work presented in this thesis is my own. Where information has been derived from other sources, I confirm that this has been indicated.

Abstract

The field of 2D materials is relatively new, only 11 years have passed since a monolayer of graphene was isolated. Although the number of publications in the field is said to have expanded almost exponentially, many inherently basic problems still need to be solved. How to produce high quality material or enough of it? Which synthesis technique is the most feasible and up-scalable? Are there applications that will be transformed by utilising 2D materials?

This thesis focuses on using Chemical Vapour Deposition (CVD) technique to produce various classes of flat 2D materials and also their three-dimensional architectures. Graphene, hexagonal boron nitride (hBN) and tungsten disulfide (WS_2) are the main examples presented in the study: a conductor, an insulator and a semiconductor respectively. Such materials are elementary "building blocks" in a variety of applications. Many novel advances to CVD synthesis of 2D materials are identified, developed and discussed in this thesis.

Pristine Pt, Pd and Cu substrates were reviewed for graphene growth in a comparable manner together with high-throughput production considerations. Many industrial challenges were identified and addressed, such as improved safety, system automation and consistency of samples on the large scale. Innovative substrate engineering, silicidation, was discovered that allowed the production of millimetre-sized, single crystal, monolayer graphene on the timescales of minutes compared to tens of hours typically needed on pristine substrates. Graphene grown on pristine and silicidated substrates was utilised in the Surface Force Balance (SFB) and Quantum Hall Effect (QHF) measurements to study the fundamental physics of surface interactions and for metrology applications respectively.

In parallel with graphene investigations, the reproducibility and quality of hBN synthesis were improved by undertaking *in situ* studies of the precursor decomposition with temperature and time. Computer-controlled temporal modulation of the precursor temperature was implemented to achieve a consistent flow of volatile B, N species into the CVD system. The resulting material was investigated in lateral hBN-graphene heterostructures and utilised as a dielectric barrier for a CVD-based light-emitting diode (LED). Additionally, a novel volatile precursor, tungsten(VI) oxychloride ($WOCl_4$), and thermodynamically favourable gas-phase chemistry were identified and studied for the synthesis of monolayer, single crystal WS_2 domains. The domain sizes of more than 20 µm are some of the largest reported to date for volatile tungsten precursors.

An up-scalable method for the production of high-quality porous graphene or "graphene foam" from metal powders was developed that is significantly cheaper than the commercially-available alternatives. The foams were tested as a cathode in a prototype Li-oxygen battery and showed promise for a significant improvement in the gravimetric capacity of the battery.

Complimentary characterisation techniques were used to study all of the materials produced, from atomic scale defect characterisation to the large area properties, such as charge carrier mobility. The mechanisms that led to the observed improvements were tentatively identified where possible, for example, by using chemical analysis of the silicidated substrates and hBN precursor decomposition or with thermodynamic calculations for the synthesis of WS_2.

The advances in the CVD syntheses are applicable to a wide variety of families of 2D materials and pave the way for a new level of tailorability and control to achieve high quality materials suitable for many far-reaching applications.

Acknowledgements

I am grateful for all the support from my colleagues and friends, both scientific and personal that helped me through the many ups and downs of my DPhil project. First and foremost, I would like to thank my supervisor and the head of the Nanomaterials by Design Group, Professor Nicole Grobert, whose guidance helped me to stay on track and who provided invaluable support in project direction, planning and infrastructure. I am also grateful for the many conversation held with Dr Antal Koos regarding practical aspects of the CVD system design and the gas line components. He also provided training and maintenance of the equipment that I used when I started. A big thank you also goes to the rest of the "2D-subgroup", especially to Dr Adrian Murdock, who contributed extensively to the characterisation of graphene materials and with useful advice; and also to Dr Jude Britton, Mr Christian van Engers and Dr Arunvinay Prabakaran, whose expertise and assistance allowed a number of important studies to develop. And also to other current and former members of the Nanomaterials by Design group who worked on a variety of other interesting materials and techniques that expanded my understanding of the field, helped me to learn new skills and to organise collaborative studies; Dr Shayan Meysami, Dr Frank Dillon, Dr Rebecca Nicholls, Dr Juan Lozano, Mrs Nataliia Stepina, Ms Fatma Dinc, Ms Madhuri Dutta, Mr Jonathan Quinson and Ms Karwei So.

I wish to thank the master's and summer students who undertook research placements in our group for their contribution in gathering useful data and insight. George Lane, who performed many preliminary hBN synthesis experiments, Remi Tanimoto who assisted with the hBN precursor decomposition measurements, Taylor Uekert and John Hotson who worked on optimising the parameters for the synthesis of graphene foams and Phillip Tucciarone, who performed many initial WS_2 synthesis experiments. I feel that I also learned a lot from the co-supervision and teaching experiences.

I express my gratitude to the many interdisciplinary collaborators from a variety of leading research institutions who collectively helped to acquire and analyse important data for a number of published and developing studies. Dr Lee Johnson, Dr Shanmu Dong and Prof. Peter Bruce from the Materials department at Oxford University; Dr Jack Alexander-Webber, Mr Nathaniel Jian Huang and Prof. Robin Nicholas from the Physics department at Oxford University; Dr Nico Cousens and Prof. Susan Perkin from the Chemistry department at Oxford University; Dr Freddie Withers from the School of Physics and Astronomy at Manchester University; Dr Alison Crossley and Dr Philip Holdway from Oxford Materials Characterisation Service; Dr Jonathan Moffat from Asylum Research.

Oxford University Materials Department is fortunate to have comprehensive support for a variety of equipment, such as electron microscopy, the clean room and the mechanical workshop, which I used frequently. I wish to thank Dr Radka Chakalova for her help with experiments in the clean room, Mr Laurie Walton and Mr John Brumfitt (precision engineering workshop, the Engineering department) for their help in the mechanical workshops. Electron microscopy support staff, Mrs Gabriella Chapman, Mr Greg Cook and Dr Neil Young for their excellent help in training and advice in using electron microscopes.

This DPhil project is supported by the Engineering and Physical Sciences Research Council (EPSRC) doctoral training award.

Finally, I wish to thank my family and friends for keeping me content through many times during my studies.

Contents

List of publications

Published journal articles

1. Vitaliy Babenko, Adrian T. Murdock, Antal A. Koos, Jude Britton, Alison Crossley, Philip Holdway, Jonathan Moffat, Jian Huang, Jack A. Alexander-Webber, Robin J. Nicholas, Nicole Grobert. Rapid epitaxy-free graphene synthesis on silicidated polycrystalline platinum. Nat Commun **6**, 7536 (2015).
2. Jude Britton, Nico E. A. Cousens, Samuel W. Coles, Christian D. van Engers, Vitaliy Babenko, Adrian T. Murdock, Antal A. Koos, Susan Perkin, and Nicole Grobert. A Graphene Surface Force Balance. Langmuir **30** (38), 11485–11492 (2014).

Filed patents

3. **Summary**: This invention relates to the production of two-dimensional nanomaterials by chemical vapour deposition. In particular, the invention relates to processes and substrates for the production of graphene and other two-dimensional nanomaterials by CVD.

   Inventors: Vitaliy Babenko, Nicole Grobert
   Filing date: 31/03/2014.
   Application number: GB1405800.2

4. **Summary**: This invention relates to processes for the production of porous materials comprising two-dimensional nanomaterials, as well as to materials derived therefrom. More particularly, the present invention relates to processes for the production of porous composite materials comprising a two-dimensional nanomaterial and a metal, as well as to porous two-dimensional nanomaterials derived therefrom.

   Inventors: Vitaliy Babenko, Nicole Grobert
   Filing date: 01/08/2014.
   Application number: GB1413701.2

5. **Summary**: This invention relates to a process for producing two-dimensional metal chalcogenide materials by chemical vapour deposition (CVD), and to two-dimensional metal chalcogenide materials which are obtainable by said process.

   Inventors: Vitaliy Babenko, Nicole Grobert
   Filing date: 24/03/2016.
   Application number: GB1605121.1

Manuscripts submitted / in preparation

6. Vitaliy Babenko, *et al*. Temporal control of ammonia borane decomposition for the improved hBN synthesis at atmospheric pressure. *(In preparation)*

7. Vitaliy Babenko, *et al*. Tungsten(VI) oxychloride precursor in the hydrogen- and oxygen-assisted synthesis of tungsten disulfide by CVD. *(In preparation)*
8. Seyyed Shayan Meysami, Frank Dillon, Jonathan Quinson, Laura Miranda Perez, Antal A. Koos, Andrew Searle, Madhuri Dutta, Adrian T. Murdock, Jude Britton, Zabeada Aslam, Vitaliy Babenko, Nicole Grobert. Comprehensive experimental investigation of aerosol-assisted chemical vapour deposition of carbon nanotubes. *(Submitted)*
9. Adrian T. Murdock, Christian van Engers, Jude Britton, Vitaliy Babenko, Seyyed Shayan Meysami, Hugh Bishop, Alison Crossley, Antal A. Koos, Nicole Grobert. Effect of copper foil surface impurities and cleaning treatments on the CVD growth of graphene. *(In preparation)*
10. Christian van Engers, *et al*, Graphene surface force balance measurements. *(In preparation)*

Conference posters and presentations

11. NanoteC conference (2015); Oxford University, Oxford, UK; invited talk and poster presentation. Awarded the best poster prize.
12. 7th Windsor Summer School (2015); Windsor, UK; poster presentation. Received a poster prize.
13. Bio-Nanotechnology Symposium (2014); Toyo University, Bio-Nano Electronics Research Centre, Japan; invited talk and poster presentation.
14. Oxford symposium on quantum materials (2013); Oxford University Physics Department, Oxford, UK; poster presentation.
15. Graphene conference - from research to applications (2012); National Physics Laboratory, Teddington, UK; poster presentation.

List of abbreviations

2D	two-dimensional
3D	three-dimensional
AB	ammonia-borane
APCVD	atmospheric-pressure chemical vapour deposition
ARPES	angle-resolved photoemission spectroscopy
BSE	backscattered electrons
CVD	chemical vapour deposition
e.g.	exempli gratia (for example)
FT	Fourier transform
GO	graphene oxide
hBN	hexagonal boron nitride
HIP	hot isostatic pressing
LED	light emitting diode
LPCVD	low-pressure chemical vapour deposition
MFC	mass flow controller
MIBK	methyl isobutyl ketone
MS	mass spectrometry or mass spectrometer
MSDS	material safety data sheet
Mw	molecular weight
p.p.	partial pressure
PL	photoluminescence
PMMA	poly(methyl methacrylate)
ppb	part per billion
PS	polystyrene
QHE	quantum Hall effect
ref	reference
RMS	root mean square
rxn	reaction
sccm	standard cubic centimetres per minute
SE	secondary electrons
SEM	scanning electron microscope (or microscopy)
SFB	surface force balance
slm	standard litres per minute
SS	stainless steel
TEM	transmission electron microscope (or microscopy)
TMDC	transition metal di-chalcogenide
UV	ultraviolet
vs.	versus

List of tables

List of figures

Chapter 1. Introduction

1.1. From layered materials to 2D-sheets, nanotubes and bucky-balls

Naturally occurring, bulk layered materials have been known for centuries and used in many applications including as refractory materials, high temperature supports, paints, lubricants and batteries. These are materials where planes of atoms are held together by weak inter-plane bonds and strong in-plane bonds, such as van der Walls bonds and covalent bonds respectively and are sometimes referred to as “van der Waals solids”. Figure 1 shows schematic structures of some examples of bulk layered crystals: graphite, hexagonal boron nitride (hBN) and molybdenum disulfide (MoS_2). In graphite and hBN each monolayer consists of a single plane of atoms (Figure 1a, b), whereas in 2H-MoS_2 one monolayer consists of a three planes of atoms: sulfur, molybdenum, sulfur (Figure 1c).

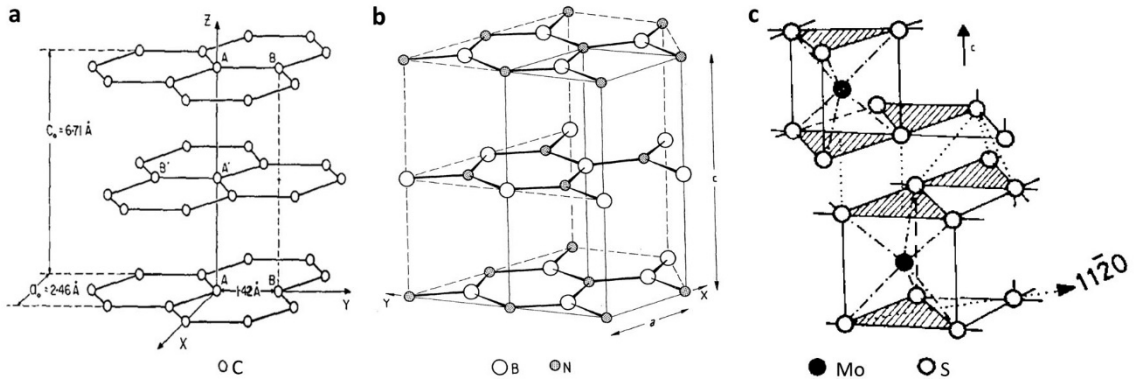

Figure 1. Examples of the bulk crystal structure of some layered materials. a) Graphite. Image credit Soule & Mcclure (1959)[1], b) hBN. Image credit Robertson (1984)[2], c) 2H-MoS_2. Image credit Wilson & Yoffe (1969)[3].

For a long time it was considered that two-dimensional (2D) materials were unstable at any temperature above absolute zero according to theoretical reasoning by Peierls[4] and Landau[5] confirmed by various experimental observations of thin films. The thinner the films were, the lower was their melting temperature. The theory remains correct, but as was understood later, 2D materials are slightly crumpled in the third dimension allowing their existence[6]. Graphene

discovery and first experimental measurements of its electronic properties are attributed to Konstantin Novoselov and Andre Geim, who isolated free-standing atomically thin carbon films in 2004 and studied their properties[7]. They realised that difficulties in characterisation were the main reasons why it took so long to identify this new class of 2D crystals[8] that can exist in free-standing form. The Nobel Prize in Physics in 2010 was awarded to the above authors for their work. It is worth noting that materials that are essentially graphene[9-14], monolayer hBN[15-20], 2D transition metal di-chalcogenides (TMDCs)[21] and even their heterostructures[22] were studied before the work from 2004, as early as 1991, but were modestly called "monolayer graphite", "monolayer hBN", "single molecular layers of MoS_2". Indeed, Novoselov and Geim mention some of these studies in their progress article "The rise of graphene"[23] but emphasise the fact that these materials were not free from the substrate or isolated from dispersions. Nevertheless, the methods used in these articles are actually precedents to modern chemical exfoliation and CVD techniques used for industrial-scale 2D materials syntheses and deserve proper recognition. Until the early nineties, 2D materials were only an idealistic theoretical exercise. In fact, other carbon allotropic forms such as fullerenes (0D) and carbon nanotubes (1D) were experimentally discovered before graphene in 1985[24] and 1991[25] respectively. Figure 2 shows these and other allotropic forms of carbon. While graphene could be considered the building block of these materials, the thin films theory by Peierls[4] and Landau[5] did not forbid their existence due to the 3D organisation of graphene into an overall 0D or 1D structure. It is therefore important to study the basic physical properties of graphene to better understand the above materials.

Graphene has probably the most exotic properties among 2D materials due to the conical electron and hole bands. Its discoverer, Andre Geim, recently commented[26] that while no "killer application" had been found for graphene, the physics studied from it was far more important. Nevertheless, some graphene-enhanced products have already made it to the market, such as a light bulb by Graphene Lighting or a tennis racket by Head BV according to an applications review article "Graphene Beyond the Hype" (ref. 27). Interestingly, the article reveals that

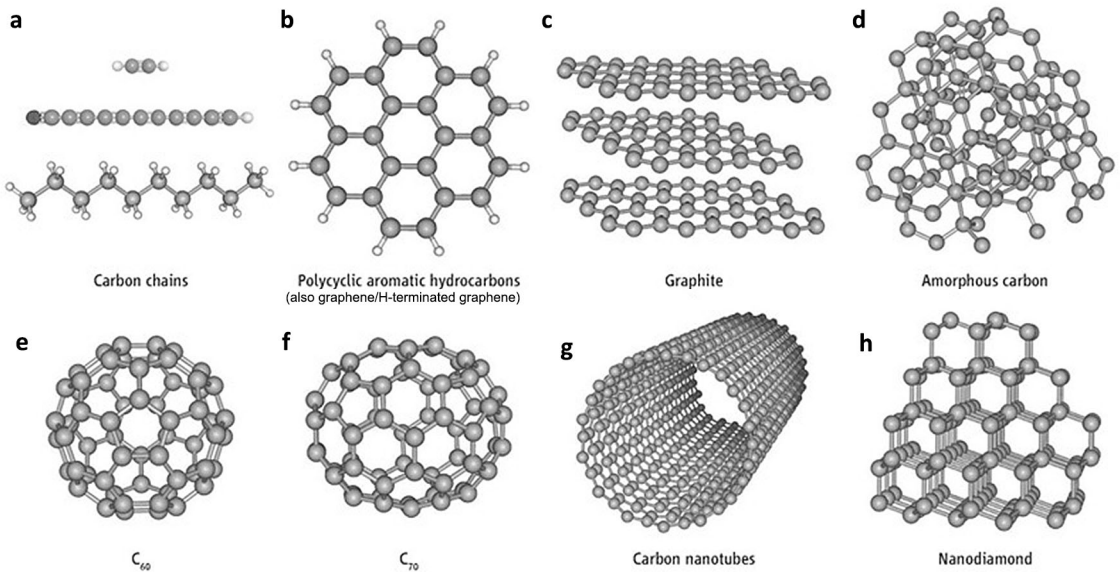

Figure 2. Allotropic forms of carbon: a) carbon chains and polymers (1D), b) graphene and polycyclic aromatic hydrocarbons (2D), c) graphite (3D), d) amorphous carbon (3D), e) C60 fullerene (0D), f) C70 fullerene (0D), g) single-wall carbon nanotubes (1D) or multi-wall carbon nanotubes (1D), h) diamond (3D). (a-h) Image credit Ehrenfreund & Foing (2010)[28].

companies can be currently secretive regarding their graphene-based products, but predicts revolutionary changes in many areas of technology in the future. It goes without saying that it is necessary to be able to reproducibly produce graphene of high quality, that is why understanding and developing better synthesis methods for graphene is of crucial importance. Additionally, this understanding will be applicable to other 2D materials. With such a wide range of 2D materials with different properties it is almost certain that disruptive technological applications will be found with one or combinations of 2D materials in the future.

1.2. "Flatland" families

The word "flatland" refers to materials that are locally 2D, but can be quenched in a quasi-3D configuration[29] (Figure 3a,b). There many types of classifications available for such 2D materials, foremost according to structure or properties. In this chapter I will discuss three representative examples from "families" of 2D materials by electronic properties: a conductor, an insulator and a semiconductor.

1.2.1. Graphene. Structure, properties and potential applications

Graphene is one of the allotropic forms of carbon, where each atom is connected to three others via sp^2 – hybridised electron orbitals in a "honeycomb lattice" as shown in Figure 3c-f. These orbitals form strong σ-bonds that are predominantly responsible for the mechanical properties

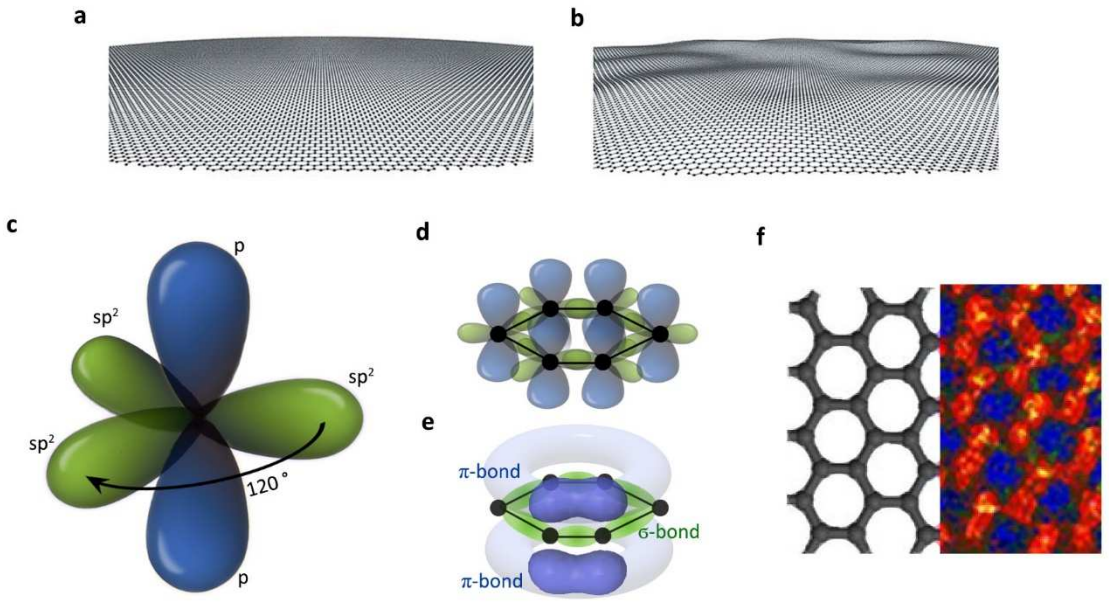

Figure 3. Graphene structure on different scales. a) A large area simulation of a perfectly 2D graphene sheet that in theory cannot exist above absolute zero. Image credit Meyer *et al* (2007)[6]. b) A representative simulation of a slightly corrugated graphene sheet with stabilised structure allowing its existence at high temperatures. Image credit Meyer *et al* (2007)[6]. c) A schematic of the electron orbitals of carbon atoms in graphene showing in-plane sp^2-hybridisation and out-of-plane p-orbitals. d,e) The sp^2-hybridised orbitals form strong σ-bonds between atoms, while p orbitals form π-bonds due to their overlap. f) A model of the graphene lattice overlapped with a false-coloured scanning transmission electron microscope (STEM) image. Image courtesy of Dr Rebecca Nicholls.

of graphene. The out-of-plane p-orbitals also overlap to form π-bonds that give rise to the unique electronic properties. The length of the σ-bonds can be studied with scanning transmission electron microscopy[30] (STEM, Figure 3f) for free-standing graphene or scanning tunnelling microscopy (STM)[31] for graphene on conducting substrates and was confirmed to be similar to that for graphite with a lattice constant of 2.46 Å. Additionally, the "height" of π-bonds or the interaction distance of graphene monolayers with the environment has been studied with atomic force microscopy (AFM)[32], which was measured as approximately 3.6 Å, also very close to the c-lattice constant of graphite (3.4 Å). The unit cell of graphene in real space has two lattice points and belongs to the hexagonal p3m1 symmetry group, as shown in Figure 4a. The reciprocal lattice is thus also hexagonal (Figure 4b). Using this information, Wallace (1947)[33] was able to calculate the electronic band structure of graphene in his work, which became a common teaching exercise in the solid-state physics field. The approach uses the nearest-neighbour tight-binding electron model and outputs the dispersion relation for graphene (equation 1, Figure 4c).

$$E_{\vec{k}} = \pm t\sqrt{1 \pm 4\cos\left(\frac{k_y a}{2}\right)\cos\left(\frac{\sqrt{3}k_x a}{2}\right) + 4\cos^2\left(\frac{k_y a}{2}\right)} \qquad (1)$$

where a=2.46 Å, t is the electron hopping energy term.

This simple electronic properties calculation has been improved to higher and higher accuracy over the years. For example, if it is extended to the next nearest-neighbour or further[34], the

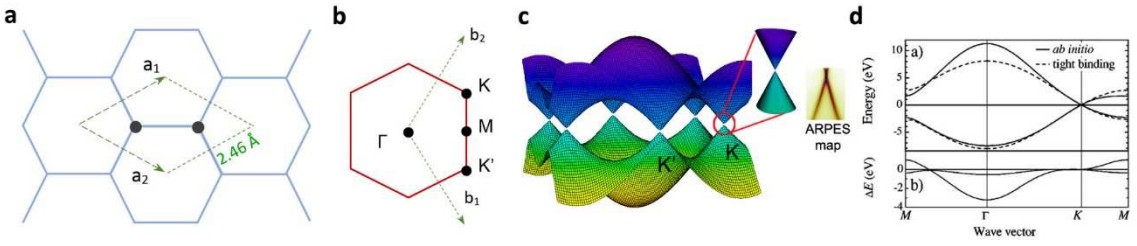

Figure 4. Real and reciprocal lattices of graphene and its band structure. a) Graphene real lattice with one unit cell and lattice vectors drawn. b) Graphene reciprocal lattice, first Brillouin zone. c) A surface plot of the dispersion relation in graphene calculated from equation 1 obtained by Wallace (1947)[33]. Inset: a magnified plot of the K point, showing the two touching cones from valence and conduction bands. ARPES measurement is also shown from ref. 35. d) Band structure of graphene over M, Γ, K, M points showing a comparison between the simple tight-binding model and ab-initio calculations, reproduced from ref. 34.

symmetry of conduction and valence bands is broken (Figure 4d). However, the nature of the dispersion near points K and K' is still remarkably well represented by this simple model, confirmed by matching ab-initio calculations[34] and also experimentally with angle-resolved photoemission spectroscopy (ARPES)[35] shown in Figure 4c (inset). A very interesting consequence of this band structure is the conical dispersion relation with zero band-gap near K and K' points. Graphene's electronic properties depend only on the electrons with states near the K-points (the two non-equivalent points). It turns out that such behaviour occurs in massless Dirac-fermions, which was pointed out by Novoselov and Geim[36] based on previous theoretical work[37]:

"The charge carriers in graphene mimic relativistic particles with zero rest mass and have an effective 'speed of light' $c^* \approx 10^6$ m/s".

A relativistic quantum mechanical treatment is needed to better describe the physics behind graphene. One of the most comprehensive reviews, tilted "the electronic properties of graphene" by Castro Neto *et al* (2009)[38] describes many of the interesting findings that contributed to improving the understainding of graphene and its properties, referencing as many as 450 scientific publications. It is beyond the scope of this thesis to mention all of the phenomena described in the review, but some, such as Quantum Hall effect (QHE) and photon-phonon interactions (Raman spectroscopy) will be mentioned in later chapters.

It is important to define what can be called "graphene", since with every additional layer the band structure of the material changes considerably and after 11 layers the structure carries a 90 % similarity to bulk graphite according to Partoens & Peeters (2006)[39]. Terms "bilayer" and "trilayer" graphene are self-explanatory, while "few-layer" graphene means between 4 to 11 layers of graphene[39]. I will also reserve the word "multilayer graphene" to mean 12-100 layers in this thesis, since thicker structures cannot be distinguished from graphite according to Pumera (2009)[40]. A monolayer of graphene can be considered approximately 2D locally (Figure 3a,b), such that quantum confinement effects give rise to a combination of unusual and

beneficial properties in a single material, some of which are discussed below.

High electron mobility of more than 200 000 $cm^2V^{-1}s^{-1}$ at room temperature was reported by Morozov *et al* (2008)[41], provided the extrinsic sources of scattering had been eliminated (e.g. charged impurities). In such a system, the very large mean free path of charge carriers, on the order of micrometres, meant that they were very insensitive to disorder such as point defects in the lattice. The study established the "benchmark" for graphene, however only small pieces were utilised that were not suitable for any practical application, leaving a big challenge to produce large area graphene with similar properties.

High absorbance of 2.3 % per atomic layer for white light in graphene almost perfectly matched the theoretical prediction[42] defined by the product of two natural constants: the fine structure constant = 1/137 and $\pi \approx 3.14$. Although this value was very high for a single atomic layer, it was still sufficient for applications where flexible transparent conductors were required (<10 % is generally acceptable[43]), provided the sheet resistance of graphene could be substantially lowered (< 100 Ω/□).

Exceptional Young's modulus (monolayer scaled to bulk) of 1 TPa and high intrinsic (ultimate) strength of 130 GPa was experimentally measured[44] in predominantly defect-free monolayer graphene. These values implied that graphene was stronger and stiffer than diamond, yet it could be stretched by up to a quarter of its length. However, it is difficult to produce structural materials based on pure graphene or scale the measured properties to macroscopic applications because currently there is no technology to make a solid 3D structure from a 2D material (e.g. porous graphene structures do not possess the mechanical properties of graphene single crystals). Structural applications, such as 3D printing, lighter, conductive composites, can benefit from these properties, but the production methods would also need to be significantly up-scaled and reduce their cost in order to make graphene-based composites industrially feasible.

Remarkable thermal conductivity exceeding 5000 $Wm^{-1}K^{-1}$ of suspended graphene was reported by Balandin *et al* (2008)[45]. The paper related graphene to carbon nanotubes in terms of heat conduction and reported that the value was larger for graphene than for single-wall carbon nanotubes, but was comparable to their bundles in experimental measurements. Basic heat exchange components for thermal management, present in numerous modern devices or vehicles, can benefit from these properties.

Impermeability to gases was verified by Bunch *et al* (2008)[46] with a sophisticated AFM measurement of graphene-sealed microchambers. Additionally, various functionalised graphene materials have been utilised in proof of concept gas sensors[47] and filters[48]. Nanoporous graphene was also shown as a selective ion membrane for water desalination[49].

Graphene edges and **graphene nanoribbons** have also been a subject to a considerable investigation due to the possibility to open a bandgap[50] for transistor applications.

1.2.2. Hexagonal boron nitride. Structure, properties and potential applications

Bulk hexagonal boron nitride (hBN) is one of the crystal variations of boron nitride, which is analogous to graphite in structure. Accordingly, monolayer hBN resembles graphene in structure[51], but with alternating B and N atoms in the unit cell (Figure 5d). Additionally, the lattice constant is only 1.8 % smaller than in graphene[52]. Nitrogen has higher electronegativity than boron, thus the bonds formed will be significantly distorted (Figure 5a-c) resulting in a very different band structure to that of graphene. Using the nearest neighbour tight-binding approximation Taylor and Coulson (1952)[53] calculated the band structure for hBN showing that it was a wide band-gap insulator. A schematic diagram of this band structures is shown in Figure 5e,f together with an ARPES map[54] near K-point and ab-initio calculations[55].

The band gap of a monolayer hBN is approximately 5 eV[56], typical for an electrically insulating material. Combined with low number of charge impurities and low roughness these properties make hBN an excellent **substrate** for other 2D materials, in comparison to e.g. silica. Indeed, it seems the trend in recent publications[57] points to using hBN in conjunction with graphene and TMDCs to form engineered van der Waals' heterostructures. Interesting observations, such as opening a small bandgap (53 meV) in graphene on hBN have been reported due to a super-lattice formation[58]. Most importantly, an increase of the charge carrier mobility by an order of magnitude compared to the standard SiO_2/Si substrates[59] can be achieved, making hBN a crucial component for future 2D devices.

The band gap energy of 5 eV corresponds to 250 nm wavelength which is in the ultraviolet (UV) region. Studies has been conducted into the possibility of exploiting hBN as a portable **deep UV emitter**[56].

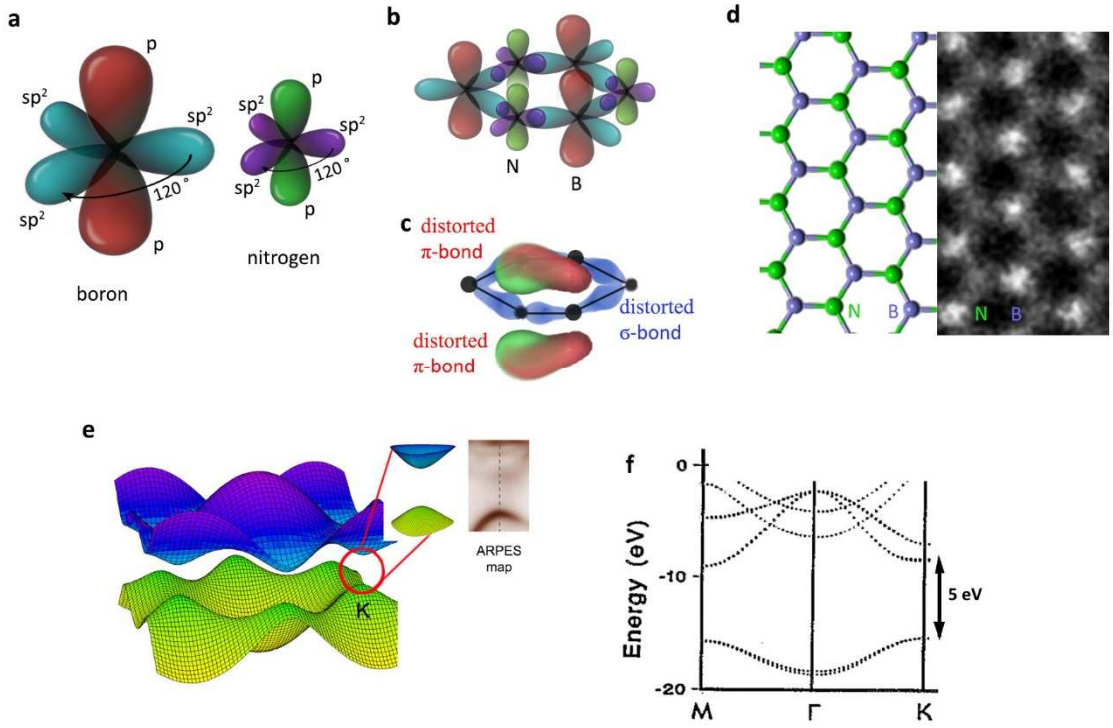

Figure 5. Electron orbitals, lattice structure and band structure of hBN. a) Diagrams of sp^2-hybridised boron and nitrogen. b,c) Electron orbital schematics of an hBN cell with the distorted σ- and π-bonds. d) A diagram of the hBN lattice overlapped with a STEM image from Liu *et al*[51]. e) A surface plot of the band structure from the early nearest-neighbour tight binding model; adapted from Taylor & Coulson (1952)[53]. The inset shows the dispersion around the K-point together with an ARPES measurement by Usachov *et al*[54]. f) Ab initio band structure calculations of hBN by Ma *et al* (1993)[55].

Young's modulus of hBN (monolayer scaled to bulk) is also high and has been reported to be between 0.6 to 1.5 TPa[60], a value that indicates that it is a stiff material if considered in bulk, but its monolayer is still bendable enough to be used where flexible materials are needed. The intrinsic strength is also high, but lower than in graphene with a value of approximately 50 GPa[60], yet it is ten times higher than steel.

Hexagonal boron nitride is sometimes called "white graphene" because of its light optical colouring and **high transparency** that can be considered negligible per monolayer (~0.1 % for visible light[61]). Flexible transparent wearable electronics or devices will benefit from this property.

hBN exhibits **high resistance to oxidation** where it outperforms graphene. While graphene coating can withstand temperatures of up to 200 °C[62] in air, hBN (5 nm film) has been shown to protect metals from oxidation up to 800 °C[51] in air.

Monolayer hBN in particular, exhibits a **good thermal conductivity** of 600 $Wm^{-1}K^{-1}$ for a ceramic insulator, which falls with increasing number of layers[63]. Application where electrical insulators are needed that possess high thermal conductivity can benefit from this material, but many challenges still remain in the synthesis of predominantly monolayer hBN, such as controlling the uniformity of the film and reducing the number of defects such as domain boundaries.

1.2.3. Tungsten disulfide. Structure, properties and potential applications

TMDCs are a large group of compounds with a chemical formula that consists of one atom of a transition metal and two atoms from group 16 elements except oxygen. Many combinations of these elements exist with very different properties: some are insulators (HfS_2), some are semiconductors (MoS_2, WS_2), some are metals (NbS_2, VSe_2) and even superconductors (NbS_2, $NbSe_2$, TaS_2, $TaSe_2$). Not all of the bulk forms of these materials are layered; approximately 40

out of 60 available compounds[3] . A very comprehensive review about the properties of bulk TMDCs was written by Wilson and Yoffe (1969)[3], where they stated that these layered compounds can only be cleaved to 1000 Å. Recently, however, monolayer TMDCs have been produced and became a subject of considerable scientific interest. In particular, semiconducting TMDCs with a technologically useful band gap for transistor and optoelectronic applications. In this thesis tungsten disulfide (WS_2) is studied as an exemplar material from the 2D TMDC group and its properties are described below.

Bulk WS_2 belongs to the $P6_3/mmc$ space group, where the monolayer is not simply a plane of atoms, as in graphene or hBN, but consists of a tungsten atom connected to six sulfur atoms in a double triangular pyramid geometry (Figure 6a,b). Due to the hexagonal symmetry of the layer, visible from the top view (Figure 6a) the band structure of monolayer WS_2 also has hexagonal symmetry (Figure 6c). The band gap of monolayer WS_2 was calculated and measured to be around 1.9-2.1 eV[64,65]. Most importantly, this bandgap changes from direct to indirect when the number of layers increases from monolayer to two or more (Figure 6d,e). Presence of a band gap in WS_2 that is considerably higher than the thermal energy of the surroundings (~26 meV) and good mobility (214 $cm^2V^{-1}s^{-1}$ on hBN[66]) shows promise for **transistor fabrication**.

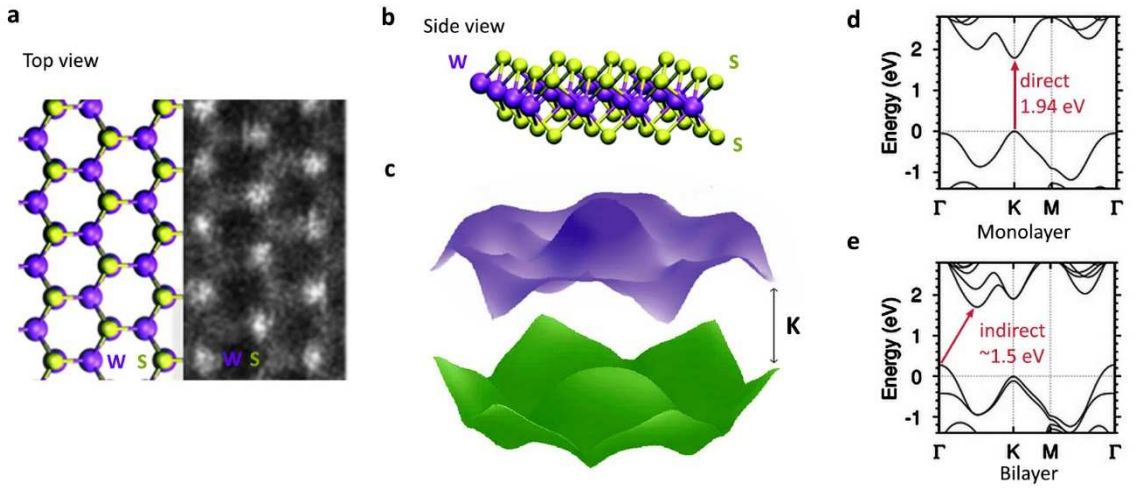

Figure 6. Crystal lattice and band structure of WS_2. a,b) WS_2 structure diagram adapted from Liang & Meunier (2014)[67] with the STEM image from Liu *et al* (2011)[68]. b) A surface plot of the band structure for monolayer MoS_2 from Cao *et al* (2012)[69] that is qualitatively similar to monolayer WS_2. c-e) The band structure of monolayer and bilayer WS_2 by Zeng *et al* (2013)[65] showing that the band gap changes from direct to indirect when the number of layers increases to two or more.

Theoretical calculations made by Liu *et al* (2011)[70] predicted that TMDC-based transistors could outperform Si-based transistors in some parameters (such as the ON-current).

Monolayer WS_2 in particular, has the highest direct band gap from commonly studied TMDC that corresponds to about 600 nm wavelength, known as orange-red colour. Interestingly, this value is close to one of the wavelengths absorbed by chlorophyll (630 – 664 nm), the biomolecule used in photosynthesis. Monolayer WS_2 is a promising candidate as a **photodetector**[71] or **thin-film photovoltaic devices**[72]. Exemplar photodetector structures had very fast photoexcitation response rates with thin-film solar cells showing 5-10 % sunlight absorption with 1 % efficiency at 1 nm thickness. E.g. a 100 nm film could potentially have 10 % overall efficiency.

A conceptually "inverse" optoelectronic process, photoluminescence (PL), has also been studied in TMDCs. The advantage of monolayer WS_2 is its "extraordinary" PL at room temperatures compared to other TMDC monolayers observed by Gutierrez *et al* (2013)[73]. Bandgap tuning in the range of 1.82 – 1.99 eV has also been achieved in $W_xMo_{1-x}S_2$ alloys, where two precursors were utilised for the alloy synthesis[74]. The most promising direction for these materials is in tunable electroluminescent devices such as **light emitting diodes** (**LEDs)**[75] or **lasers**[76]. A prototype laser device has been demonstrated very recently that achieved 6 % quantum yield[76]; a value that is quite low compared to >60 % for modern YAG lasers, but big improvements can be expected in the future.

1.3. Synthesis methods overview

1.3.1. Mechanical exfoliation

Also known as the "sticky-tape method" or "micro-mechanical cleavage", the mechanical exfoliation method is based on sequential splitting of planes of graphite or other van der Waals solids, until a monolayer is obtained. This was the first method to successfully produce monolayer single crystal graphene and simply required contacting a flexible sticky tape with a bulk layered crystal, followed by splitting of the deposits by re-applying the tape. Figure 4 shows a researcher transferring sequentially peeled graphene onto a silicon substrate. Finding large, good quality flakes relies significantly on luck and is time-consuming. The process is therefore expensive and difficult to up-scale. Despite the obvious flaws there are some advantages, such as the quality of graphene produced with mechanical exfoliation is the best currently available and the equipment cost is negligible[23]. These reasons explain why lab-scale applications, where small quantities of the highest quality graphene are needed, predominantly use this method. Attempts have been made to increase the volume of production by employing a liquid exfoliation technique[77-79] or supercritical CO_2 exfoliation[80]. The yield was improved, however, by sacrificing the quality: few-layer graphene was produced in most cases and it was also difficult to separate the better flakes from the lower quality ones.

Development of proof of concept applications has benefited from utilising mechanically

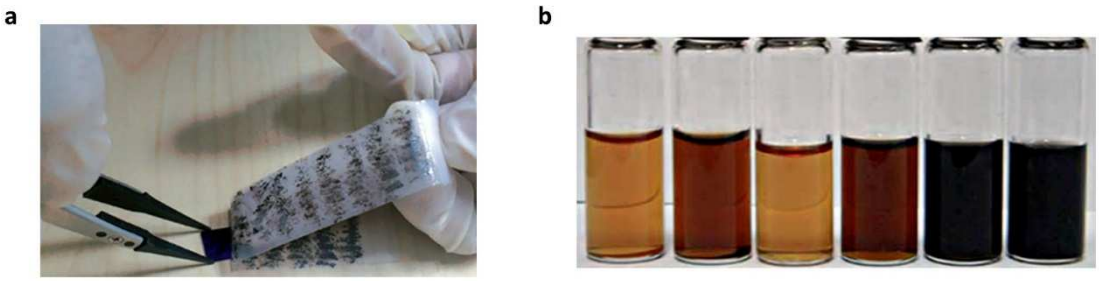

Figure 7. Graphene production with exfoliation methods. a) A transfer process is shown for mechanically exfoliated graphene flakes. Image credit Van Noorden *et al* (2012)[81]. b) Dispersions of different types of graphene are shown that are achieved by chemically exfoliation of graphene oxide (GO), followed by its reduction. Image credit Chen & Yan (2010)[82].

exfoliated graphene, but future technology will require production of large graphene crystals in high volume at low cost that cannot be achieved with the mechanical exfoliation method.

1.3.2. Chemical exfoliation

Chemical exfoliation method relies on separating planes of a layered material by utilising a solvent that forms stronger bonds to atoms of the material than the bond between the planes of the material. In case of graphite, one route is to oxidise the bulk material to form graphite oxide, which forms many sp^3-bonded oxygen-containing moieties in between the layers, such as hydroxyl, carboxylate and epoxy groups. While, sp^2-hybridised sheets are still present in places, the lattice and electronic structure are drastically disrupted, making graphene oxide (GO) a poor conductor. A polar solvent, such as water[83] can be used to exfoliate graphite oxide to form dispersions (Figure 7b) of few-layer GO sheets using an ultrasonic unit. The dispersions are then centrifuged to partially separate the flakes by thickness. In order to restore the conductivity, the flakes are chemically reduced, for example, using hydrogen[84] or hydrazine[85] at elevated temperatures (800 °C). However, the introduced structural defects are difficult to remove completely and after reduction the quality of graphene remains poor: the sp^2 carbon fraction of 80 % or lower is usually recovered[86], while the number of layers is difficult to control. Nevertheless, a number of interesting ideas appeared recently utilising GO. For example, Rozada *et al* (2013)[87] proposed a way to fully repair the defects in reduced GO films by a two-step high temperature annealing method (1500 °C, followed by >2000 °C graphitization step). El-Kady *et al* (2012)[88] used a common LightScribe DVD drive to perform a direct laser reduction of GO, thus directly forming mechanically robust GO films. Commercial products based on chemical exfoliation can be produced in very large quantities. Many new applications with GO films have also been demonstrated and now constitute a large area of research on its own, for example, filtering membranes[89] or reduced GO paper[90].

Many other layered materials can also be exfoliated using the solution-based methods[91], but rely mostly on tweaking the solvent/surfactant/polymer and its bonding strength to the planes of monolayers. Paints, polymer composites, structural materials have been explored for proof of concept applications such as inkjet printing[92], 3D printing[93], aerogels[94] and filtering membranes[95].

1.3.3. Epitaxial growth on silicon carbide and epitaxial segregation on metals

Silicon carbide (SiC) is rare mineral in nature, mostly found in meteorites or upper mantle rock[96]. It has been produced synthetically since 1890, first as a powder and later as large single-crystals[97]. Temperatures of up to 2700 °C are needed for the Lely process[97] to grow SiC wafers of up to 10 cm in diameter. More expensive CVD synthesis processes or polymer decomposition are also used to make the highest purity SiC, which makes the material a relatively expensive substrate for graphene growth. Graphene forms on SiC when Si atoms desorb from the surface at high temperatures (>1100 °C), under various pressures[98]. The main advantages of this approach are the availability of SiC in wafer form, the possibility to pattern SiC directly before growth and that the electronic properties of graphene are not significantly distorted by the underlying silicon layer, allowing high charge carrier mobilities[99]. Nevertheless, there are also various disadvantages, such as roughness of SiC surfaces due to the many small steps (Figure 8a) and thus small graphene domain sizes, difficulties in controlling the number of layers, high cost and high temperatures involved. All of these factors make this method suitable mainly for research or niche applications.

Carbon solubility can be relatively high in some metals and it is therefore possible to purpously saturate the metals with carbon, followed by phase separation of the mixture under high temperature (equlibrium segregation) or during cooling (nonequilibrium segregation). Examples

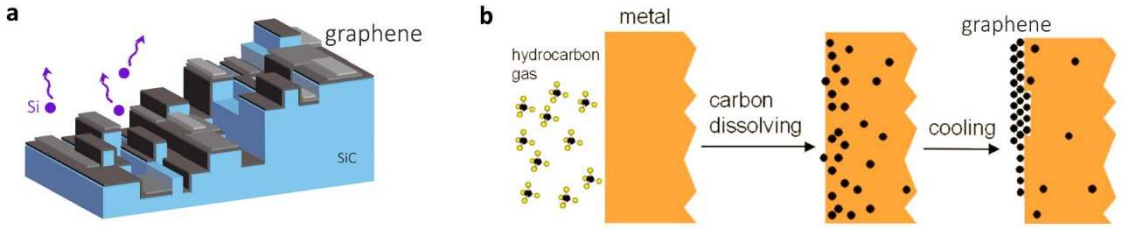

Figure 8. Epitaxial graphene synthesis methods. a) A diagram showing graphene grown on SiC where silicon atoms desorb from the surface, leaving graphene on the surface. Many steps on the substrate degrade graphene quality. Image adapted from Sutter (2009)[98]. b) A process diagram of the epitaxial segregation method from a Ni surface: a hydrocarbon precursor is used to saturate the metal with carbon, followed by cooling to achieve phase separation. Image adapted from Yu *el al* (2008)[100].

of the earliest metals used in this way are nickel[100] and ruthenium[101]. The former being a very abundant element on Earth, while the latter is very rare. Yu *et al* (2008)[100] was able to produce graphene films of varying thickness, from monolayer to few layers, by controlling the cooling rate of carbon-saturated Ni substrates. Follow-on studies[102] showed that by alloying Ni with another metal possessing low C solubility (e.g. Cu), it is possible to improve the uniformity and quality of graphene drammatically, obtaining up to 95 % monolayer coverage on wafer-sized samples. The advantage of this method is its low cost, especially if thin films are used, however, metals also form steps on the surface that can interfere with graphene growth producing varying number of layers[101]. It is also difficult or even impossible to produce large-area single crystals due to the random nature of the segregation process and its preferential occurrence on the grain boundaries of the metal.

1.3.4. Chemical vapour deposition introduction

CVD is a process where a precursor or multiple precursors are introduced into a hot reactor tube where they thermally decompose in gas phase allowing the growth of thin films or 2D materials. The decomposition process can result in simple deposition of the products (such as in pyrolytic BN ceramics) or may require a catalyst, where complicated surface-mediated processes take place. For example, for graphene, the precursor is usually a gaseous carbon precursor (e.g.

methane) mixed with an etching gas (e.g. hydrogen) that are passed over a catalytic transition metal substrate. The basic apparatus for atmospheric pressure CVD (APCVD) is shown in Figure 9a. Various modifications to the system are possible. For example, Li *et al* (2011)[103] used a low-pressure (LPCVD) system to grow large, 0.5 mm dendritic graphene flakes. LPCVD systems require additional components, such as a pump and compression-type connections which increase the cost of the system and some configurations can also be considered more dangerous, because leaks rapidly draw air inside the system. The main benefit of LPCVD systems is the additional control of the background pressure and thus the partial pressure of precursors inside the system. Other types of CVD systems are less common for graphene synthesis, but attempts have been made to utilise them. Plasma-Enhanced CVD (PECVD) was used to grow patches of graphene without a catalyst at low temperature[104-106], however, the quality was compromised due to few-layer graphene formation. Photo-thermal CVD (PTCVD) was used recently to grow good quality graphene films in just 60 seconds[107]. Several cold-wall reactors have also been designed, including commercial ones[108]. In cold-wall CVD systems only the

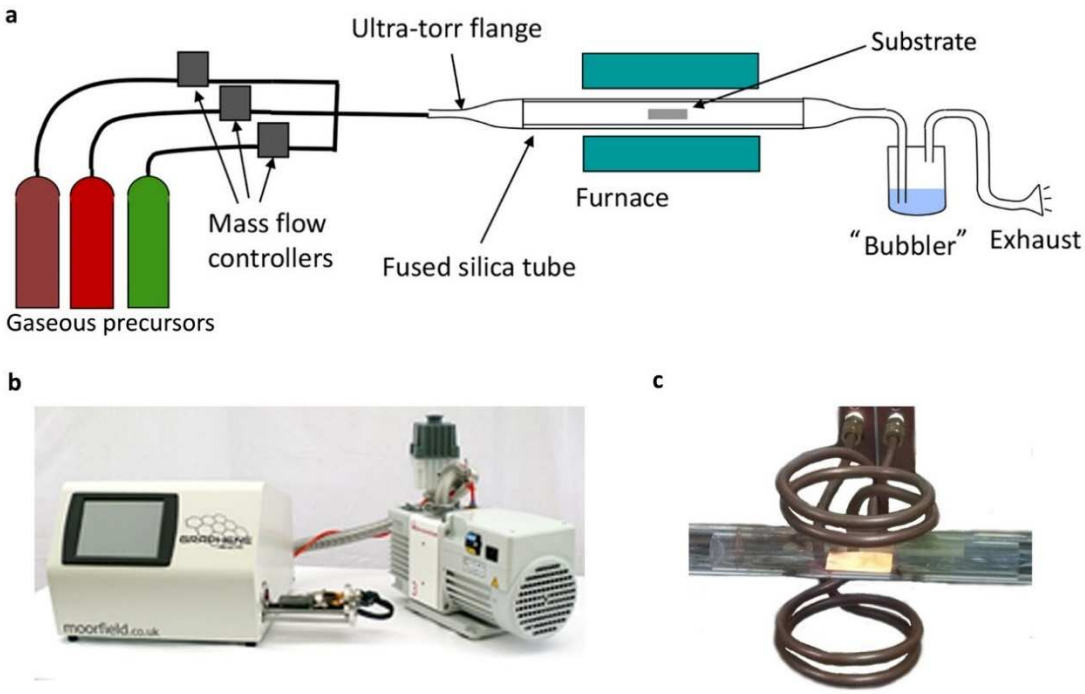

Figure 9. CVD synthesis systems. a) A schematic diagram of an APCVD system. b) A portable commercial graphene synthesis system with a pump and a cold-wall reactor for LPCVD. Image credit ref. 108. c) A variation of a CVD system where the substrate is heated by induction. Image credit Piner *et al* (2013)[109].

substrate or the stage is heated either by resistive heating or induction heating[109], thus saving time and energy.

The approach for precursor introduction in CVD can differ for gaseous, liquid and solid cases. Gaseous precursors (CH_4, H_2) are the most convenient to use by utilising mass flow controllers (MFCs) or rotameters. Liquid precursors have some advantages, such as the lower decomposition temperatures or ease of adding dopants, but usually require a carrier gas or a separate injection system[110-112]. Similarly, solid precursors have also yielded excellent quality graphene flakes of millimetre size[113], but considerable difficulties are typically present in controlling the amount of such precursors going into the reactor and thus reproducibility issues. The next chapter will focus on the specifics of the CVD apparatus and theory of chemical reactions for the 2D materials described in the results chapters.

Chapter 2. Experimental methods

2.1. Apparatus and the procedure for 2D material syntheses

For this thesis I developed and assembled four CVD systems for the synthesis of graphene, up-scaled graphene (chapter 4.3), hBN and WS_2 samples. Different precursors and gas compositions were used for each of the three 2D materials that required appropriate precursor delivery manifolds. The development of these systems took a number of years with the design constantly being refined and upgraded to allow more control and reproducibility. Examples include the assembly of custom stainless steel (SS) gas mixing lines, utilisation of SS compression-type flanges in place of quick-fit glass connections, addition of vacuum pumps and gauges, custom heating elements with dedicated process controllers and others. Comprehensive schematics of the basic components of the final systems are shown in Figure 10. Each apparatus can be considered in three parts:

1. **Precursor delivery manifold**. Gaseous precursors or vaporised solid precursors are directed to the reaction zone from either high pressure gas cylinders or custom-built evaporation chambers respectively.
2. **Precursor decomposition zone.** This part of the system consists of a fused silica tube inserted into a furnace. Precursor decomposition occurs inside the tube at high temperatures. Fused silica is an inert material with a very low thermal expansion coefficient, making it very suitable for use as a reaction tube in CVD for high temperature syntheses up to 1200 °C.
3. **Exhaust**. A “bubbler” device filled with water was used as a basic safety indicator of leaks in the system. Final versions of the developed systems also incorporated vacuum pumps to allow convenient system decontamination from moisture and oxygen by Ar purging.

Specific differences in the methods for each of the 2D material syntheses will be described in more detail in the following sections.

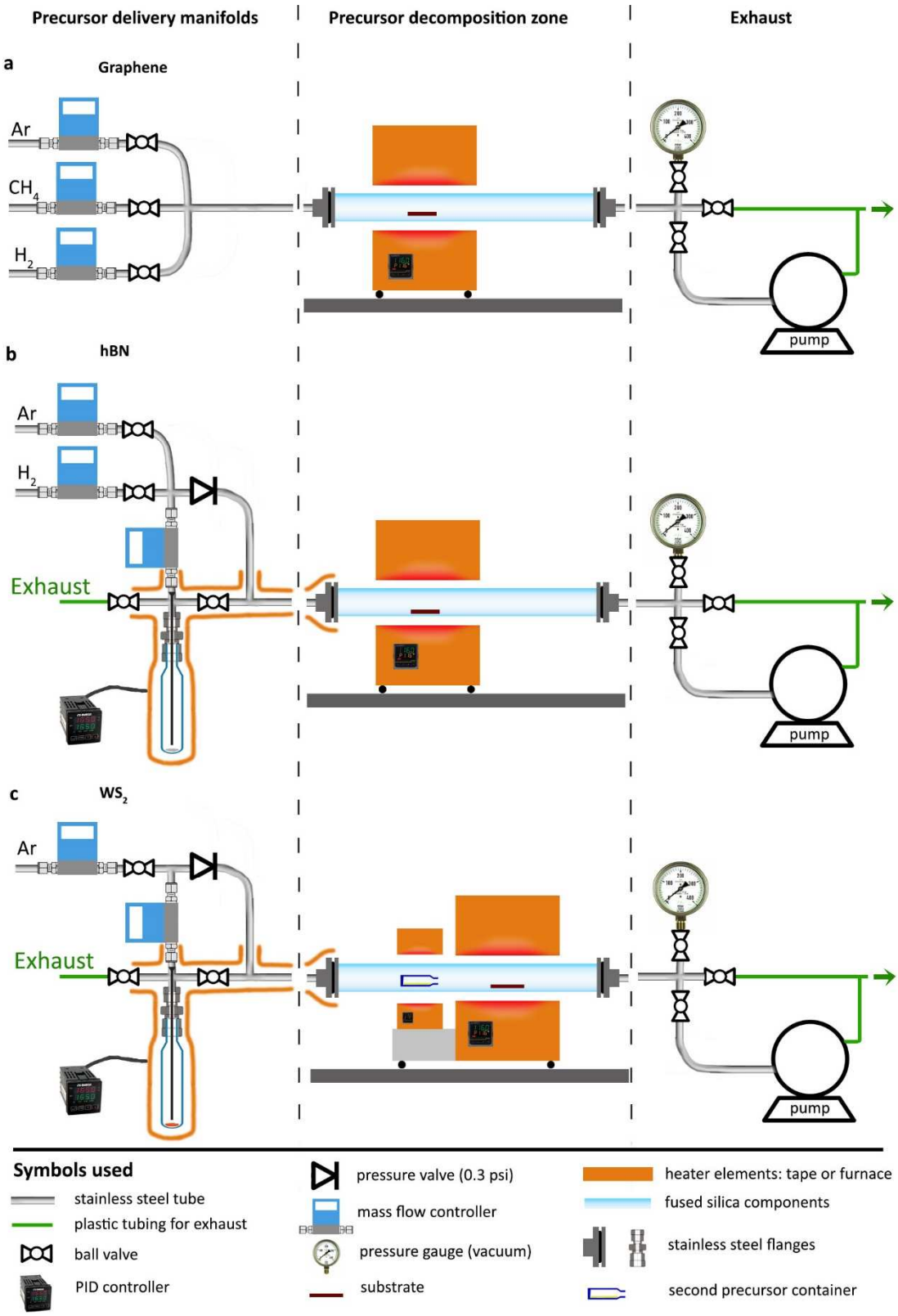

Figure 10. CVD systems with movable furnaces that were designed and assembled for 2D material syntheses. a) A graphene CVD system with gaseous CH_4 and H_2 precursors. b) A hBN CVD system with one solid precursor (ammonia borane), etching (H_2) and purging (Ar) gases. c) A WS_2 CVD system with two solid precursors ($WOCl_4$ and S), a carrier (Ar) gas or a mixtures of gases (Ar/H_2, Ar/O_2).

2.1.1. Graphene synthesis procedure

For graphene synthesis experiments three gases were used; 99.5 % CH_4, 99.995 % H_2 and 99.999 % Ar, where CH_4 and H_2 were the synthesis gases, while Ar was used to purge the system before and after synthesis. The flow of these gases was controlled with MFCs (MKS 1179A) connected to a four channel gas flow and pressure controller (MKS 647C). The chosen maximum flow ranges were 10 standard cubic centimetres per minute (sccm), 1 standard litre per minute (slm) and 5 slm respectively, all with 1 % calibration. An oxygen and water filter (Entegris CE2500KFH) was optionally connected to the manifold after the MFCs to reduce the content of these impurities to less than 1 part per billion (ppb). Compression-type, custom-built flanges were utilised to connect the SS tubing to a 180 cm long fused silica tube (28 mm inner/32 mm outer diameter). The tube was inside the 1.7 kW TSH12/38/500 Elite Thermal Systems Tube furnace, capable of operating at temperatures up to 1200 °C. The furnace was installed on rails, permitting it to be shifted along the silica tube to allow rapid cooling. The end of the tube was connected to a SS manifold allowing switching between atmospheric pressure and low pressure (using the Edwards Vacuum RV12 rotary pump, Figure 10a).

An exemplar procedure for graphene synthesis in this system comprised the following steps:

1) System preparation

i) All of the gas lines were purged to remove any moisture and oxygen adsorbents.

ii) The substrate was loaded into the silica tube, the system was closed and filled with Ar.

iii) (Optional, when the silica tube was stored in air or replaced). The system was pumped down to the base pressure of the pump, and filled with Ar gas three times. The system was then returned to atmospheric pressure.

iv) The furnace was heated to desired temperature (typically 1050 °C).

2) **Annealing stage**: used to condition the substrate

i) The furnace was shifted along the fused silica tube and over the substrate.

ii) H_2 was introduced for prolonged times, usually 30 – 120 mins, at flow rates between 100 to 500 sccm.

3) **Synthesis stage**: used to grow graphene

i) CH_4 flow was added to H_2 flow with typical H_2:CH_4 ratios between 10-100 for Cu substrates and 50-300 for Pt substrates. The synthesis times between 10-90 minutes were explored.

4) **Cooling stage (quenching)**: used to rapidly stop graphene domain growth

i) The furnace was shifted away from the substrate allowing a rapid cooling rate of about 100 °C min^{-1} to quench the state of graphene. This procedure was necessary because of low-quality defective and multilayer deposits forming during prolonged cooling at lower temperatures when cooled in H_2/CH_4 atmosphere. Ar gas was not used for cooling because any small residual oxygen contamination could quickly produce holes in graphene at high temperatures; similarly to cooling in H_2.

ii) After the sample was sufficiently cold (< 100 °C), the tube was purged with Ar and the sample was later removed from the system when it reached room temperature.

2.1.2. Hexagonal boron nitride synthesis procedure

For hBN synthesis two gases were used; 99.995 % H_2 and 99.999 % Ar, controlled in a similar fashion to graphene and utilising an almost identical set-up (Figure 10b). Ar gas was used as a purging gas, while H_2 had a role in the synthesis and as a carrier gas. The only major modification was the addition of a custom vapourisation chamber for the ammonia borane precursor (Sigma-Aldrich, 97 %), consisting of a fused silica vial and a custom-built resistively-heated jacket (appendix 9-D). The jacked was powered by a 100 W DC power supply, while the temperature was measured and controlled with a K-type thermocouple connected to a PID controller (Omega Engineering CN743). The flow of the carrier gas (H_2) through the precursor was controlled with

an additional MFC. In order to give priority of gas flow to this MFC, a 1/3 psi pressure valve was installed, thus the total flow was split into two: a constant flow over the precursor and controlled flow through the pressure valve into the system (Figure 10b). The manifold leading to the tube was heated by a separate heating tape to avoid vapour condensation. It is very advantageous to control the precursor in a separate chamber, in comparison to the "two-stage furnace" apparatus typically used in the literature[60, 114-116], due to a number of reasons:

I) The flow rate in the chamber is independent of the total flow rate, and thus the evaporation rate is independent of the total flow.

II) The main furnace operates at 1050 °C causing infrared heating to the first stage furnace and the precursor inside, which is aimed to be at a much lower temperature, <100 °C.

III) When precursors are evaporated in a "two-stage furnace" apparatus a steady state convective backflow can occur that will lead to ongoing contamination of the system and even blockage, causing safety concerns.

The typical procedure for hBN synthesis in this system comprised the following steps:

1) System preparation

i) All of the gas lines were purged to remove any moisture and oxygen adsorbents.

ii) The substrate and the ammonia borane precursor were loaded into the silica tube and the vaporisation chamber respectively; the system was closed and filled with Ar.

iii) (Optional, when the silica tube was stored in air or replaced) The system was pumped down to the base pressure of the pump, and filled with Ar gas in three purges. The system was then returned to atmospheric pressure.

iv) The furnace and the electrically-heated jacket were set to desired temperature (typically 1050 °C and 90 °C respectively).

2) **Annealing stage**: used to condition the substrate

i) The furnace was shifted along the fused silica tube and positioned over the substrate.

ii) H_2 was introduced for prolonged times, usually 30 – 120 mins, at flow rates between 100 to 500 sccm.

3) **Synthesis stage**: used to grow hBN

i) The hot electrical jacket was placed over the fused silica vial containing the precursor. The H_2 flow rate through the vial was set to 10 sccm, while the total flow was set typically between 300 – 1500 sccm. Synthesis times between 10 – 90 minutes were explored.

ii) Computer control was used to increase the temperature of the jacket in a pre-defined way as to keep the concentration of the precursor vapour constant throughout the experiment (discussed in more detail in section 6.1.3).

4) **Cooling stage (quenching)**: used to rapidly stop hBN domain growth

i) The furnace was shifted away from the substrate allowing a rapid cooling rate of about 100 °C $mins^{-1}$ to quench the state of hBN due to the same reasons as for graphene.

ii) After the sample was sufficiently cold (< 100 °C), the tube was purged with Ar and the sample was later removed from the system when it reached room temperature.

2.1.3. Tungsten disulfide synthesis procedure

Two solid precursors were used for the synthesis of WS_2 with an Ar carrier gas (99.999 %). The first precursor, tungsten (VI) chloride (Sigma-Aldrich, ≥ 99.9 %) or tungsten (VI) oxychloride (Sigma-Aldrich, 98 %) was evaporated in an equivalent manner to ammonia borane, as described in previous section, while the second precursor, sulfur (Sigma-Aldrich, ≥ 99.5 %) was evaporated in a two-stage furnace setup (Figure 10c). Although it would be more beneficial to also control sulfur vapour in a separate chamber, it was not essential, since large quantities of sulfur were evaporated at moderately high temperatures (270 °C) where the two-stage furnace providing sufficient control. Additionally, it was difficult to handle a heating jacket operating in the regime between 200 – 300 °C, needed for sulfur evaporation.

Sulfur management is one of the most important considerations for the WS_2 synthesis system since it is a solid with low molar mass at room temperatures. Substantial volumes of sulfur can deposit inside the system when a relatively modest molar flux is used and can cause blockage of the tubing, pump and its vapour backflow can lead to system contamination. By utilising a vial-like container (Figure 10c) sulfur backflow was completely avoided because conditions leading to an approximately equilibrium vapour pressure were set up inside the container. Additionally, sulfur was captured on the walls of the long silica tube (180 cm) after passing the furnace during synthesis. It was then shifted further and re-deposited in a small region on the end of the tube in bulk by moving the hot furnace. This procedure allowed up to five experiments per day to be performed and hundreds of experiments before the bulk sulfur deposit needed to be removed.

Tungsten contamination management was also established, but was needed less frequently (every 5 experiments or daily). The procedure consisted of introducing 500 sccm of Ar with 0.1 % O_2 through the reaction zone at high temperature (1100 °C). Tungsten deposits on the silica tube turned yellow, indicating the formation of tungsten trioxide, WO_3, which is sufficiently volatile to be removed in vacuum. Medium vacuum (0.2 Torr) was then set up in the system utilising a scroll pump, with a low flow rate of Ar gas (30 sccm). After 1 hour, the yellow deposits on the tube shifted to the cold region after the furnace. The furnace was then slowly shifted further along the tube until all of the tungsten oxide contamination was relocation to the specifically allocated region on the end of the silica tube.

The typical procedure for WS_2 synthesis in this system comprised the following steps:

1) System preparation

i) All of the gas lines were purged to remove moisture and oxygen adsorbents.

ii) The substrates (sapphire or Si/SiO_2 tiles) and sulfur precursor were loaded into the silica tube at specific distances to match the position of the two-stage furnace. The tungsten

precursor was loaded into the evaporation chamber. The system was closed and filled with Ar.

iii) The system was pumped down to the desired pressure (0.5-760 Torr), and filled with Ar.

iv) The two-stage furnace and the electrical jacket were heated to desired temperature (typically 270 °C / 800 °C and 135 °C respectively).

2) **Annealing stage**: used to condition the substrate

i) The larger stage of the two-stage furnace was shifted over the substrate, while the smaller, lower-temperature stage was shifted over the sulfur container.

ii) Sulfur vapour was produced and passed over the substrate for prolonged times (around 30 minutes) to allow the furnace temperatures and the sulfur vapour flow to stabilise, but also to decompose carbonaceous or other contamination on the substrates.

3) **Synthesis stage**: used to grow WS_2

i) The pre-heated electrical jacket was placed over the fused silica vial containing the tungsten precursor. The synthesis times were typically between 10-90 minutes.

4) **Cooling stage (quenching) and sulfur management**: used to rapidly stop WS_2 domain growth and to prepare the system for the next experiment

i) The electrical jacket was removed from the precursor vial.

ii) The two-stage furnace was gradually shifted away from the substrate and along the fused silica tube. This procedure allowed a suitable cooling rate of the substrate, but also to clean sulfur deposits left after synthesis.

iii) The sample was later removed from the system when it reached room temperature.

5) **Tungsten contamination was oxidised and shifted along the tube.**

2.1.4. Practical considerations

The control measures utilised on the CVD systems were assessed, as is often the case that little attention is given to the suitability of controls implemented in some CVD systems, with a large

number of scientific publications utilising primitive precursor controls or failing to mention basic synthesis parameters. CVD systems typically have five main synthesis parameters and numerous secondary parameters or experimental consideration. Table 1 summarises the most important considerations of the CVD systems with the controls that I developed to address these considerations.

System parameter	Measures or controls implemented
Graphene	
Flow rate accuracy	Supplier yearly MFC recalibration; suitable MFC ranges.
Gas purity	Choice of high grade gases (e.g. N5.5 or 99.9995%).
Gas system/line contamination and leaks	High pressure and vacuum leak tests. SS lines and compression-type flanges. O_2 / H_2O filter. Measurement of O_2 and H_2O level with a mass spectrometer (5 ppm and 730 ppm respectively).
Gas mixture controls	Computer controlled automation software with timing precision of less than 1 second.
System cleaning	Reaction tube heated in oxygen, vacuum and with Ar purging.
Furnace temperature	Temperature profile measurement with an external probe.
Sample cooling	Sample quenched at ~ 100 °C min^{-1}. The furnace was placed on moving rails and motorised to achieve consistency in the cooling rate.
Flow geometry over substrate	A flat and inert substrate support was utilised to avoid contact with curved reaction tube, such as quartz, alumina or boron nitride plates.
hBN additional considerations	
Solid precursor vapour control	An electrical jacket with a PID controller was built allowing ± 0.5 °C precision control of the temperature and thus vapour pressure.
Temporal precursor control	A PID controller was connected to a computer allowing temperature control following any function with time.
Vapour condensation prevention	A heating tape with a PID controller was used to heat up the manifolds .
WS_2 additional considerations	
Second solid precursor control	A two stage furnace was used to evaporate the second precusor (sulfur).
Sulfur management	A long silica tube allowed convenient sulfur deposition after the reaction zone and "shifting" with a hot furnace to the storage region on the tube.
Tungsten management	Tungten impurities were oxidised and removed in vacuum at high T.

Table 1. Control measures for the CVD systems used.

2.2. Theory of operation

In this section I will summarise the basic theoretical consideration behind CVD for the synthesis of the materials discussed in this thesis: graphene, hBN and WS_2. I will attempt to explain the anticipated effects of different CVD parameters on the growth of these 2D materials based on simple theory. Most of these parameters will be presented in the results sections without repeated explanations. There are some secondary theoretical considerations that are outside the scope of this thesis, and will only be mentioned for completeness. Some of these are heat transport, convection, flow geometry, transition steps of chemical reaction, multiple-step reactions and radical formation.

First, additional background information is necessary, some of which is loosely based on concepts from "Principles of Chemical Vapor Deposition" by Dobkin (2003)[117] and general Physics concepts.

2.2.1. Chemical reactions: thermodynamics (WS_2 applicable)

CVD is arguably nothing more than an *in situ* chemical reaction and a deposition process. Reactants or "precursors" are converted to products, such as in the generalised equation 2:

$$a \cdot A + b \cdot B \rightleftharpoons c \cdot C + d \cdot D, \quad (2)$$

where A, B, C, D are the chemical species and a, b, c, d are their molar coefficients.

Although in principle the aim is to form stable products, there is always some rate of breakdown of these products back into the reactants.

The thermodynamics of a chemical reaction is concerned with what is the final composition of the gas mixture given enough time. This approach identifies the most stable products (or reactants if the reaction does not proceed) without indicating how long it actually takes to form these products or what intermediate compounds form. The basic concepts are available in most Physics or Chemistry textbooks and will only be mentioned briefly. Considering that CVD

reactions are typically performed at constant temperature (T) and pressure (p), it is useful to use the function of state dependent on these parameters, "Gibbs free energy": *G = G(p, T).*

The change in Gibbs free energy for a reaction (rxn) determines whether the products can form. When the change in Gibbs free energy is negative, the forward reaction is favoured and the reaction equilibrium shifts to the right (i.e. resulting in a higher fraction of products vs. reactants). This notion can be expressed mathematically through the equilibrium constant

$$\therefore\ K_{\mathrm{eq}} = e^{-\frac{\Delta G_0}{RT}} \tag{3}$$

where K_{eq} is the equilibrium constant, ΔG_0 is the standard molar free Gibbs free energy.

From equation 3 it is clear that the forward reaction will only be favourable at standard conditions if $\Delta G_0 < 0$, which is **one of the main considerations when designing a CVD process**. In a closed system, as the reaction progresses, precursors will start to exhaust and eventually the system will reach an equilibrium, such that the negative value of Gibbs free energy will shift to zero, $\Delta G_{\mathrm{rxn}} = 0$ (Figure 11a). CVD systems that I utilised, can be considered as open systems with a continuous supply of precursors. Here, the difference in Gibbs free energy between the gases entering the system and the synthesised material together with the exhaust products is negative. Often different products can form along the reaction tube due to precursor exhaustion with distance or uneven temperature distribution, thus forming a varying spatial distribution of $\Delta G_{\mathrm{rxn}} = \Delta G_{\mathrm{rxn}}(x)$ inside the system.

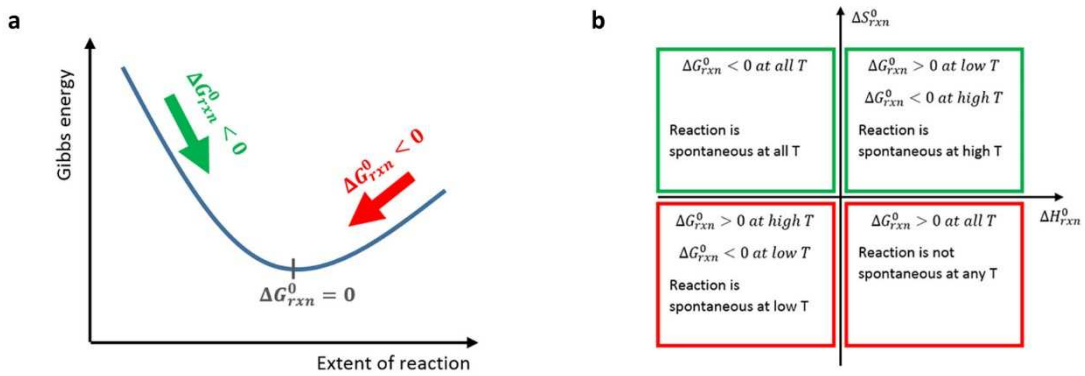

Figure 11. Thermodynamics concepts of chemical reactions. a) Gibbs free energy value changes during an extent of a chemical reaction in a closed system. b) Gibbs free energy dependence on the value of the enthalpy change of formation and the entropy change for a reaction. Positive values of ΔS_{rxn} are the only useful cases for the CVD synthesis of 2D materials.

The value of ΔG_0 for a reaction can be calculated from tables of "the enthalpy of formation at standard conditions" ($\Delta_f H^0$) and "molar entropy at standard conditions" (S^0) of products and reactants:

$$\Delta G^0_{\mathrm{rxn}} = \left(\Delta_f H^0_{\mathrm{products}} - \Delta_f H^0_{\mathrm{reactants}}\right) - T\left(S^0_{\mathrm{products}} - S^0_{\mathrm{reactants}}\right) \quad (4)$$

This expression can be understood from a different perspective: through the interaction of the system with the surroundings via **heat (enthalpy, H)** and **"disorder" (entropy, S)**. Second law of thermodynamics implies that the state of entropy of the universe (signifying the system with the surroundings) can only increase. Also, the entropy change of the surroundings is determined by the heat **given** ("-") to the surroundings at a particular temperature. Therefore,

$$\Delta S_{\mathrm{total}} = \Delta S_{\mathrm{rxn}} + \Delta S_{\mathrm{surroundings}} = \Delta S_{\mathrm{rxn}} - \frac{\Delta H_{\mathrm{rxn}}}{T} > 0 \quad (5)$$

From simple sign considerations of ΔS_{rxn} and ΔH_{rxn} four possible scenarios for the reaction progression can be distinguished (Figure 11b):

I. Reactions where the law is obeyed at all temperatures and which can proceed at any temperature ($\Delta S_{\mathrm{rxn}} > 0$ and $\Delta H_{\mathrm{rxn}} < 0$);

II. Reactions that can only proceed at high temperatures when the contribution from $\Delta H_{\mathrm{rxn}}/T$ is negated by the temperature ($\Delta S_{\mathrm{rxn}} > 0$ and $\Delta H_{\mathrm{rxn}} > 0$, but $\Delta S_{\mathrm{rxn}} > \Delta H_{\mathrm{rxn}}/T$).

III. Reactions that cannot proceed at any temperature ($\Delta S_{\mathrm{rxn}} < 0$ and $\Delta H_{\mathrm{rxn}} > 0$);

IV. Reactions that proceed at low temperatures ($\Delta S_{\mathrm{rxn}} < 0$ and $\Delta H_{\mathrm{rxn}} < 0$, but $\Delta H_{\mathrm{rxn}}/T > \Delta S_{\mathrm{rxn}}$).

As an example, let us consider a commonly used reaction of tungsten (VI) oxide and sulfur for WS_2 synthesis (many other possible products can form, but I chose the most stable ones for simplicity; S_8 sulfur allotrope dominates sulfur vapour[118]):

$$16\ WO_3 + 7\ S_8 \rightleftharpoons 16\ WS_2 + 24\ SO_2 \quad (6)$$

For reaction (6) at 800 °C, from the NIST database[119] and O'Hare *et al* (1984)[120] for 1 mol WO_3:

$$\Delta G^0_{\mathrm{rxn}} = \big((-241) + 3/2 \times (-297) - (-293) - 7/16 \times 0\big) - 1073 \times (0.068 + 3/2 \times 0.248 - 0.286 - 7/16 \times 0.430) = -394 - 1073 \times (-0.034) = -358\ (\mathrm{kJ\ mol^{-1}})$$

This negative value shows that the reaction is spontaneous at 800 °C and the calculation can be extended to show that it is also spontaneous at room temperatures. Importantly, WO_3 is not a volatile precursor and will not produce suitable vapour pressure at 20 °C; high temperatures are required to synthesise WS_2 in this reaction[121]. Nevertheless, the thermodynamics is favourable and high quality WS_2 can be achieved[121]. However, let us compare this reaction with another reported[122] and practically useful precursor combination where WS_2 is synthesised from volatile WCl_6 (again, exemplar stable products were chosen):

$$8\ WCl_6 + 5\ S_8 \rightleftharpoons 8\ WS_2 + 24\ SCl_2 \quad (7)$$

As before, $\Delta G^0_{\mathrm{rxn}} = \big((-241) + 3 \times (-18) - (-494) - 5/8 \times 0\big) - 1073 \times (0.068 + 3 \times 0.282 - 0.419 - 5/8 \times\ 0.430) = 200 - 1073 \times 0.226 = -43\ (\mathrm{kJ\ mol^{-1}})$

Lower in modulus, negative value of ΔG^0 for this reaction at 800 °C (1073 K) indicates that the reaction can proceed at this temperature, but it is not as efficient as the reaction in equation 6. Additionally, the value only becomes negative at 615 °C, indicating that it is the minimum temperature at which the reaction can happen. Equation 7 is one of many possible combinations of products (e.g. WS_3, SCl, Cl_2, S_2Cl_2), and it turns out that the most favourable product for the reaction of WCl_6 and sulfur at 800 °C is another chloride of tungsten[123], WCl_4, which simply passes through the system. These calculations indicate that the reaction of tungsten chlorides

and sulfur is not a good reaction for the CVD synthesis of WS_2 and other precursor combinations should be explored (related experimental results are presented in section 6.2). Interestingly, the quality (size, crystallinity and the number of layers) of WS_2 produced from tungsten chlorides and sulfur is also worse[124] compared to the reaction shown in equation 6, possibly because there is no chemical mechanism that could discriminate between crystalline and defective deposits (evaluated further in section 6.2). In the next section I will briefly discuss what factors affect the rates of forward and reverse reactions.

2.2.2. Chemical reactions: kinetics

Before the products of a chemical reaction can form, the bonds of the reactants need to be partially broken down and re-formed. Similarly, the bonds of the products can also break with some finite probability allowing the reverse reaction to occur with some rate. The energy needed to form the "transition state" is the Gibbs activation energy $\Delta G_{\mathrm{a}}(T)$ that is dependent on the temperature. Another, temperature independent, but related quantity is often used, the "activation energy", E_{a}. The expression for the reaction rate of product formation in its simplest form depends on the specific chemical reaction and the "order of reaction" (m, n). For example, the rate of formation of product C in equation 2 could be as follows:

$$\text{rate of product formation} = \frac{1}{c}\frac{d[C]}{dt} = k_{+}[A]^{m}[B]^{n} \tag{8}$$

where k_+ is the forward reaction constant; m,n are the coefficient of the order of the reaction.

Here, the reaction constant (k_+) can be expressed in terms of the activation energy

$$k_{+} = A_0\, e^{\frac{-E_{\mathrm{a}}}{RT}} \tag{9}$$

Constant "A_0" also depends on the rate of collisions between the molecules and the orientation factor (or the probability of the correct geometrical linking in space). The exponential factor in this treatment can be considered as the Boltzmann distribution of molecules with energies that

can overcome the activation energy. If the activation energy for a certain reaction is too high, then the rate of the reaction will be very slow leading to the formation of kinetically favourable products. On the other hand, if the conditions allow the activation energy to be overcome, then the more thermodynamically stable products will form (Figure 12a). Directing the path of a reaction in the former way is known as "kinetic control", while the latter is "thermodynamic control". For example, it is more energetically favourable for diamond to turn into graphite[117], however, this reaction involves breaking strong diamond bonds that has negligible rate, so this reaction will not occur. While "bond dissociation energies" can serve as an indicator of the activation energy for single-step reactions and are available in tables, real reactions can have a large number of possible mechanisms with different intermediate products and transition states. For this reason many reactions have activation energies much lower than the bond

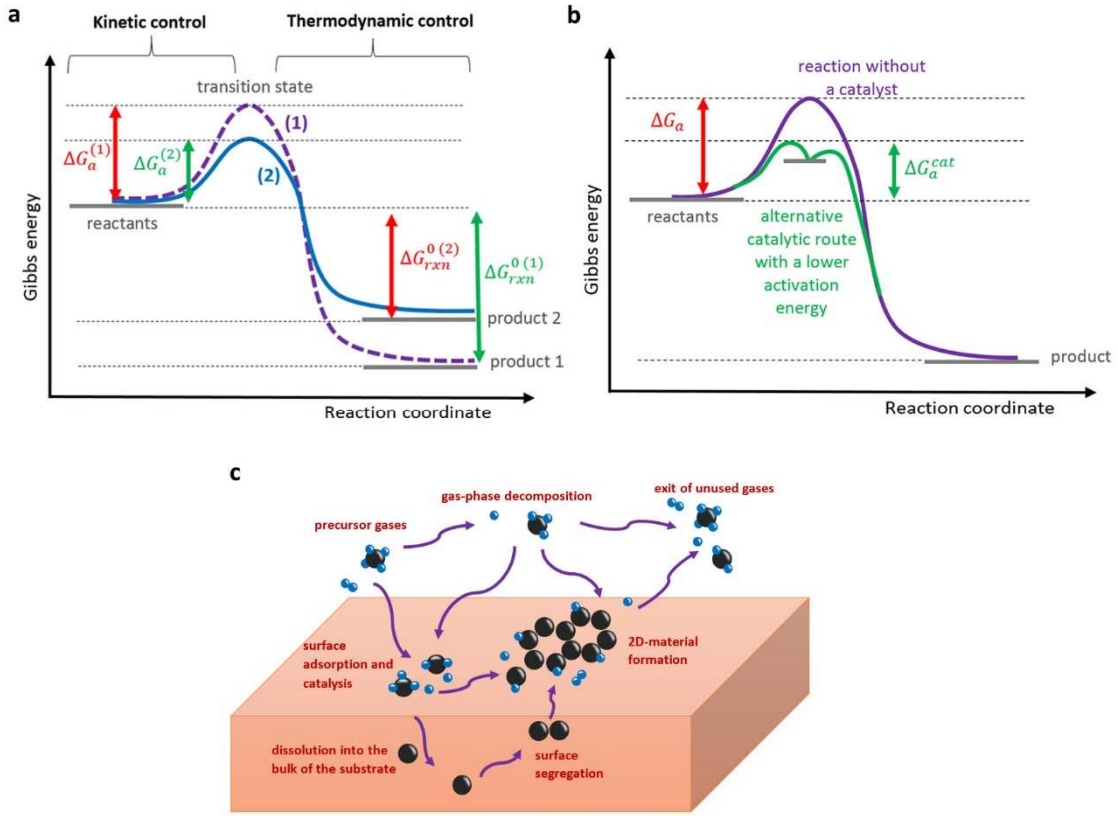

Figure 12. Catalytic substrate influences and processes. a) Kinetic vs. thermodynamic control of the product. The former can be used to discriminate between activation energies for a reaction, while the latter can be used to form the most stable products (assuming sufficient time has passed). b) Catalyst influence on the energetics of a chemical reaction. c) Processes on the surface of transition metals (Cu, Ni) for graphene synthesis are shown as an example. The smaller atom is hydrogen (blue), and the larger atom is carbon (black). Methane (CH_4) and hydrogen (H_2) are used as the reactant gases.

dissociation energies. Unlike the thermodynamics data, very little kinetic data is available for the reactions studied in this thesis for 2D material syntheses. Therefore, no quantitative examples can be given. However, awareness of the kinetics is very important to understand the role of catalytic substrates in CVD reactions that are described in the following section.

2.2.3. Substrate: catalysts and surface processes (graphene, hBN applicable)

The reaction rate of some CVD processes can be significantly improved by utilising a catalyst that will provide an alternative route for the reaction with a lower activation energy (Figure 12b). The rate constant depends on the exponent of the activation energy (equation 9) which leads to a significant increase in the overall reaction rate even with a modest reduction in E_a. Some reactions do not proceed even at high temperature without a catalyst. Graphene and hBN, for example, require a transition metal substrate and do not normally grow (with high quality) on inert or ceramics substrates such as silica or alumina. Generally, there are many pathways that lead to the formation of the desired material from precursor molecules, some with higher and some with lower probability. Figure 12c schematically depicts some of these possibilities for the simple case of methane (CH_4) and hydrogen (H_2) precursors for graphene synthesis. Vlassiouk *et al* (2011)[125] explored the chemical mechanisms for CH_4 and H_2 dissociation and identified their reactions as follows:

$$\mathrm{Cu} + \mathrm{H_2} \rightleftharpoons \mathrm{Cu} + 2\,\mathrm{H_{surface}} \tag{10}$$

$$\mathrm{Cu} + \mathrm{CH_4} \xrightarrow{\text{slow}} \mathrm{Cu} + (\mathrm{CH_3})_{\mathrm{surface}} + \mathrm{H_{surface}} \tag{11}$$

$$\mathrm{Cu} + \mathrm{CH_4} \rightleftharpoons \mathrm{Cu} + (\mathrm{CH_4})_{\mathrm{surface}} \tag{12}$$

$$(\mathrm{CH_4})_{\mathrm{surface}} + \mathrm{H_{surface}} \rightleftharpoons (\mathrm{CH_3})_{\mathrm{surface}} + \mathrm{H_2} \tag{13}$$

$$(\mathrm{CH_3})_{\mathrm{surface}} + \mathrm{graphene} \rightleftharpoons (\mathrm{graphene} + \mathrm{C}) + \mathrm{H_2} \tag{14}$$

$$\mathrm{H_{surface}} + \mathrm{graphene} \rightleftharpoons (\mathrm{graphene} - \mathrm{C}) + (\mathrm{CH_x})_{\mathrm{surface}}\,. \tag{15}$$

From these reactions the author suggested that H_2 could promote activation of physisorbed CH_4 (equations 10, 13), which in turn allowed the formation of dehydrogenated radicals (e.g. CH_2, CH) on the surface and subsequently graphene (equations 11, 12, 14). Weak defective C—C bonds (such as those in 5- or 7- carbon "rings") could be etched by surface-hydrogen (equation 15), which allowed to bias the reaction towards the formation of a perfect graphene lattice. The latter process can be considered the main reason why increasing the hydrogen flow (or partial pressure) usually increases the quality of graphene, but reduces the growth rate. Another consideration is the chemical reduction of native copper oxide by H_2 on the surface to improve the catalytic ability of the substrate. Similar conclusions on Cu, Ni and other metals were drawn by follow-on publications[126-128]. Figure 12c also shows two additional processes: gas-phase decomposition of the precursors, which is expected to have a much lower probability than the catalytic decomposition; and product dissolution and segregation in the catalyst that is important for some metals with high C-solubility (e.g. Ni, Pd).

Hexagonal boron nitride synthesis is expected to follow similar reaction pathways shown in Figure 12c, however, there is a complication due to precursor decomposition which will be discussed in details in section 6.1. From these reasons it can be understood why not all transition metals are suitable as substrates for graphene and hBN syntheses. The following effects need to be considered ("the Sabatier principle"):

i. The strength of the chemical bond between the substrate and the precursor. The former can be divided into two categories: "physisorption", a process where a weak bond (e.g. van der Waals' bond or London force[129]) is formed between the substrate and the precursor; and "chemisorption", a process where a chemical reaction occurs between the substrate and the precursor forming a strong bond (e.g. a covalent or ionic bond).
ii. The solubility of the precursor or its decomposition products in the substrate at elevated temperatures. This consideration is important for the surface segregation processes and

to control of the number of layers in 2D materials. Usually a "balance regime" (ref. 130) can be achieved between surface segregation that results in multilayers and surface-catalytic growth to achieve monolayer-only graphene even in metals with a relatively high carbon solubility. However, the cooling rate becomes very important in such metals due to non-equilibrium carbon segregation.

iii. The catalytic ability of the substrate or by how much the activation energy is lowered on the surface of the metal. This quantity is determined by the intermediate states formed with the catalyst and how stable they, and therefore influences the reaction or growth rates of 2D materials.

iv. A match in the crystallographic lattice of the transition metal and graphene/hBN is needed for epitaxially-dependent synthesis methods (i.e. on solid metals), which can affect the crystallinity of the resulting 2D material.

As an example, I will briefly compare four different metals as substrates for graphene synthesis by CVD: titanium, copper, platinum, nickel. The conclusions are summarised in table 2.

Titanium

Ti is known to form a stable bond with carbon resulting in the formation of titanium carbide (TiC). The bond is often considered "strongly covalent" or "dominantly ionic"[131]. Therefore, surface processes needed for graphene synthesis do not occur on this transition metal, rendering it unsuitable. From a difference perspective, Ti can still be considered a catalyst for CH_4 decomposition but that forms very stable intermediate products (bond dissociation energy ~423 kJ mol^{-1}, ref. 132) with carbon that do not let the reaction proceed in the direction of graphene growth. For comparison, graphene bond dissociation energy is ~400 kJ mol^{-1} (ref. 133), explaining why the stronger C—Ti bond is not likely to reform into the C—C bond of graphene.

Nickel

Ni substrates were some of the first used to show the viability of graphene synthesis with CVD in 2008[134] (the other being rare elements ruthenium and iridium), while having the advantage of being a relatively cheap metal. However, the number of layers was very difficult to control; Reina *et al* (2009)[134] reported polycrystalline graphene grains of 1-20 µm in size and approximately 1-12 layers. The paper suggested that the reason for the large number of layers was the high solubility of C in Ni (0.29 atomic % at 700 °C[135] and even higher at 1050 °C) and that mostly a graphite film was forming, with occasional graphene flakes. Quick cooling (quenching) was required to stop C segregation to the surface and forming additional layers as expected. For comparison, the bond strength between Ni and C is ~ 337 kJ mol^{-1} (ref. 132), which is 20 % lower than the Ti-C bond allowing graphene synthesis to proceed, but with great difficulty in achieving monolayer graphene.

Platinum

Pt has been shown to produce irregularly-shaped graphene domains with a very high growth rate[130, 136, 137] of up to 50 µm min^{-1}, suggesting excellent catalytic ability. This observation can be explained by the value of the Pt-C bond dissociation energy of around 243 kJ mol^{-1} (ref. 138) that is approximately in the middle between the energy values for Cu and Ni. The cooling rate for Pt is a very important synthesis parameter due to relatively high C solubility of about 0.66 atomic % at 700 °C[135], however, a "balance synthesis regime" can easily be achieved[130, 137]. Pt and related catalysts are discussed in more detail in chapters 4 and 5.

	Metal-carbon bond dissociation energy (kJ mol^{-1})	Carbon solubility at 700 °C (atomic %)	Graphene type
Titanium	423	-	No graphene, only titanium carbide
Nickel	337	0.29	Multilayer graphene, fast growth rate
Platinum	243	0.66	Monolayer graphene with rapid cooling, fast growth rate
Copper	195	0.006	Monolayer graphene with slow growth rate

Table 2. A comparison of exemplar transition metal catalysts: Ti, Ni, Pt, Cu. Numerical values were extrapolated from ref. 132, 135, 138-140.

Copper

This transition metal has been used extensively for graphene synthesis and it seems to dominate current research and industry production methods due to its low cost and wide availability. It is known to have a very low C solubility of 0.006 atomic % at 700°C[139]. Also, the Cu–C bond dissociation energy is quite low about 195 kJ mol^{-1} (ref. 140) allowing monolayer graphene synthesis to proceed with ease. However, synthesis times on the order of many hours or even days[141] have been used to achieve large-area graphene. This leads to the conclusion that the catalytic ability of Cu is relatively modest. More experimental details about 2D materials synthesis on Cu are given in sections 4.3, 6.1.5.

2.2.4. Understanding the synthesis parameters

In this section I will discuss the CVD synthesis parameters that are the experimental variables investigated in this thesis and how these parameters can be understood in relation to the theoretical concepts described in previous sections. A number of considerations will be classed as of secondary importance and are outside the scope of this thesis due to the already vast primary parameter space (e.g. flow geometry, precursor evaporation rate dependence on the flow rate, steady-state temperature distribution in the reactor, convection, precursor

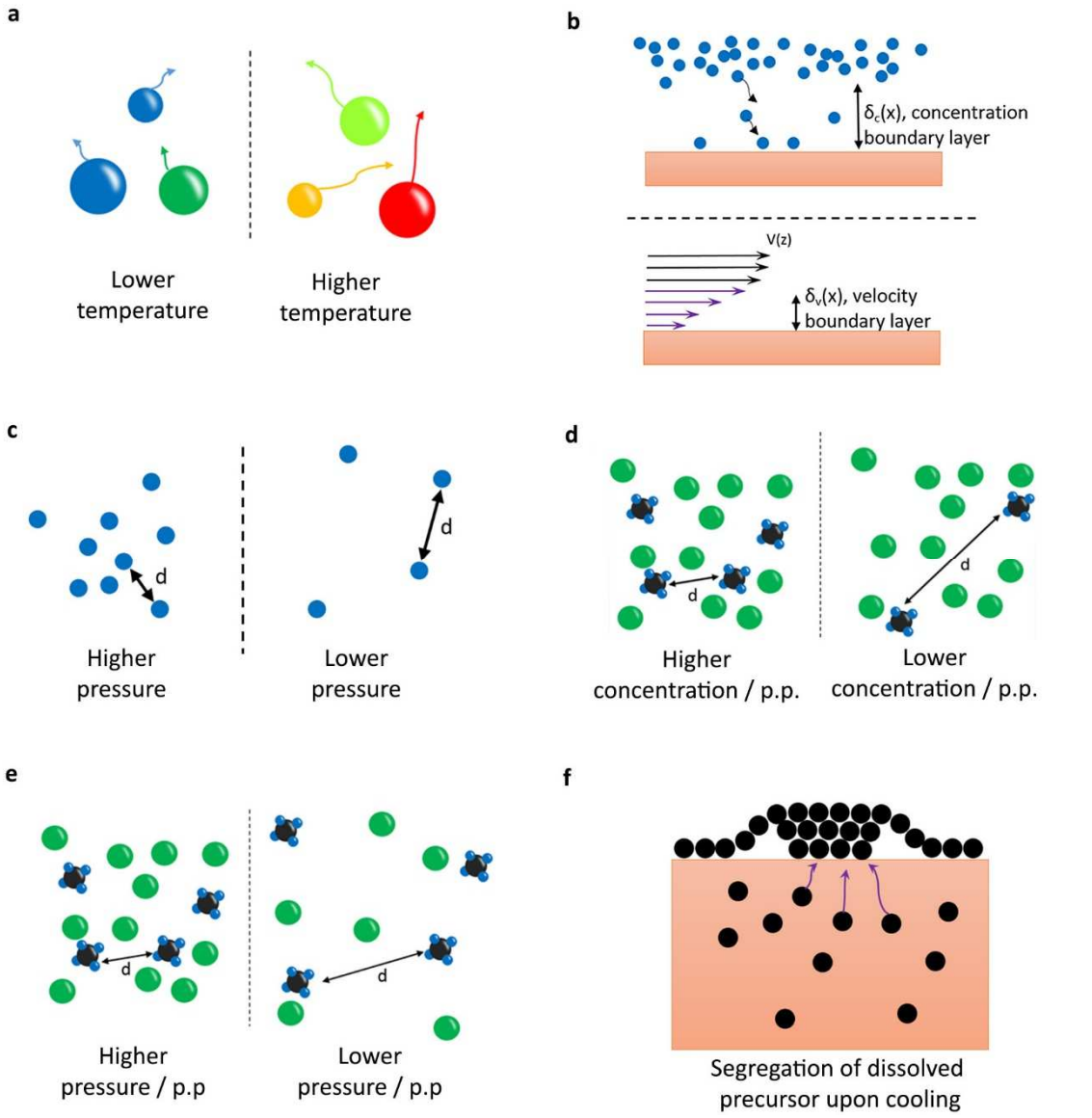

Figure 13. Schematic explanations of the synthesis parameters. a) Temperature: molecules move faster and collide more frequently at higher temperatures speeding up the rate of reactions and changing the thermodynamics of the reaction; b) total flow and the boundary layers: a concentration boundary layer arises due to reactant exhaustion near the surface and a velocity boundary layer arises due to "no-slip" boundary condition; c) total pressure influence on the intermolecular distance, which in turn is related to the probability of a collision between molecules in space. d) partial pressure change due to the decrease in the concentration of the precursor (e.g. methane in argon); e) partial pressure change due to the total pressure change: the average distances between the molecules changes (e.g. methane and argon); f) cooling regime influences the formation of multiple layers due to precursor segregation from the bulk; quenching must be adopted to avoid this.

concentration exhaustion, Thiele modulus, Dahmkohler number and nucleation mechanisms).

Temperature

As was mentioned previously, equations 3 and 4 show that increasing the temperature changes the thermodynamics of a reaction by altering the entropic term ($T\Delta S$) and can allow reactions that are unfavourable at low temperatures to proceed at high temperatures (Figure 11b), such as the reaction between WCl_6 and S (equation 7). Additionally, from equation 9 it is evident that increasing the temperature can also increase the forward reaction rate (depicted schematically in Figure 13a). This parameter is particularly important for graphene growth, where a significant improvement in the growth rate can be achieved with increased temperature[137, 142].

Total flow rate and boundary layers

The concept of the total flow rate can have two different levels of significance depending on the composition of the flow, whether it consists of only the precursor gases with a fixed molar ratio or if it is a carrier gas with a constant absolute precursor flux. Both of these cases will see a change in the boundary layer (explained below) when the total flow is changed. However, the latter case needs to be distinguished because the precursor concentration will be also diluted if the carrier gas flow is increased. This is the same effect as the "partial pressure" change that is discussed later on. The boundary layer can be considered as a combination of different processes, outlined by Carlsson (2010)[143]:

1) The precursor is depleted near the surface due to the product-forming reactions with a concentration gradient being set up between the bulk gas and the surface (Figure 13b), the "concentration boundary layer". This concept is of main importance for CVD, where reactions can be divided into categories:
    a. Diffusion limited (also, "mass" or "transport" limited): the surface reaction proceeds faster than the precursor molecules are replenished near the surface.

b. Surface reaction rate limited: reaction proceeds slowly without significant precursor depletion near the surface, meaning that the boundary layer can be ignored. Consequently, the growth rate in this regime depends on the temperature as in the case for graphene and hBN.

2) The speed of flow near the surface is lower compared to the speed of the bulk gas in the reactor due to the "no-slip boundary condition". From simple fluid dynamics considerations it is possible to estimate the thickness of the "velocity boundary layer" (Figure 13b) for laminar flow as follows[117]:

$$\frac{\delta_{\text{velocity}}(x)}{x} = \frac{1}{\sqrt{Re}} \tag{16}$$

where $\delta_{\text{velocity}}(x)$ is the thickness of the velocity gradient, Re is the Reynolds number

Reynolds number is a quantity that is related to how laminar or turbulent the flow is. The flow is laminar if Re < 2300, transient if 2300 < Re < 4000 and turbulent if Re > 4000. For the flows in the CVD systems that I used for my experiments I can approximately estimate Reynolds numbers using the characteristic geometric system dimensions[117]:

$$Re = \frac{QD}{\nu A} \tag{17}$$

where Q is the volumetric flow rate, D: diameter of the tube, v: kinematic viscosity, A: cross-sectional area.

Substituting in the dimensions and physical quantities[119] gives

$$\text{Re} \approx 500\ \text{cm}^3\ \text{min}^{-1} \times 28\ \text{mm} \ /\ (2.4 \times 10^{-4}\ \text{m}^2\ \text{s}^{-1}) \ /\ (616\ \text{mm}^3) \ = \ 1578$$

This number is in the laminar flow regime. Therefore, $\frac{\delta_{\text{velocity}}(x)}{x} \approx 0.025$. This gradient is very low, meaning that the velocity boundary layer does not change significantly along the reactor and will not be discussed further.

3) There is a thermal boundary layer due to the temperature gradient between the hotter (more thermally conductive) solid surface and bulk gas. It is important to be aware of this concept for precursors with a large molecular mass, but due to a limited number of

controls available to influence this effect it will be considered outside of the scope of this thesis.

The overall conclusions that can be made from all of the above considerations are that

- at very slow total flow rates, the reaction has sufficient time to proceed fully and thermodynamic control has considerable importance;
- at fast total flow rates, the reaction can be in the regime of surface kinetics control or reaction rate limited because there is always an abundance of precursor molecules.

Total pressure

Pressure is related to the force acting per area, however, its effects on the CVD synthesis are better understood in terms of the average distance between molecules from the ideal gas law

$$pV = nRT \tag{18}$$

where p is the pressure, V: volume, n: moles of substance; R: universal gas constant; T: temperature.

The total volume occupied by the gas can be related to the number of molecules and the approximate average intermolecular volume (d^3):

$$V = N \times d^3 \tag{19}$$

where N is the number of molecules in volume V; d: approximate distance between molecules.

$$\therefore\ p \approx \frac{nRT}{N}\ d^{-3} \tag{20}$$

Therefore, the average distance between molecules is inversely proportional to the cubic root of the pressure, which is turn is related to the probability of a collision of molecules in space. Figure 13c schematically shows the difference between higher pressure and lower pressure synthesis regimes (for example, APCVD vs. LPCVD). Changing the total pressure inevitably changes the partial pressure in a mixture of gases (see below), but also it has influences on

- The evaporation rate of solid precursors. Lower pressure results in faster evaporation for the same temperature.
- The boundary layer. Lowering the pressure usually encourages high depletion of precursor molecules and a thicker concentration boundary layer because molecules have to travel longer distances. The flow geometry becomes less important.
- The rates of chemical reactions. These can also change due to a change in the dwell time on the surface (adsorption processes), which is particularly important for nucleation control.
- The thermodynamics: the values of entropy of products and reactants can depend on pressure and thus the value of the change in Gibbs free energy.

Partial pressure (related: concentration, volume flow rate, molar flow rate)

Partial pressure (p.p.) is a concept used in mixtures of gases with the total pressure being the sum of partial pressures of individual gases. For example,

$$\mathrm{P_{tot}} = \mathrm{P_{Ar}} + \mathrm{P_{H_2}} + \mathrm{P_{CH_4}} \tag{21}$$

Also, this can be re-written as

$$\mathrm{P_{CH_4}} = \mathrm{P_{tot}} \times x_{\mathrm{CH_4}} \tag{22}$$

Where, *x* is the mole fraction of any individual gas that can now be calculated from the more useful molar fluxes of the gases in the mixture

$$x_{\mathrm{CH_4}} = \frac{\text{moles of } \mathrm{CH_4}}{\text{total number of moles in the mixture}} \tag{23}$$

Partial pressure affects the thermodynamics of the reaction, for example, the entropy value can be different and therefore the change in Gibbs free energy for a reaction can be different. Additionally, p.p. influences the surface kinetics, e.g. too much precursor can saturate some surface reactions and decrease the rate. It is evident from equation 22 that p.p. can be influenced by the total pressure and the mole fraction, or equivalently the concentration of

gases in the mixture (equation 23). The effect on the distance of the molecules can be understood from schematic diagrams in Figure 13d-e. A thorough investigation into the effects of varying this parameter for different CVD systems is the one of the main aspects of this thesis and will be presented in detail in the results chapters.

Ratio of partial pressures or related quantities

For 2D material syntheses there is usually an etching reaction that is necessary to break weak, non-crystalline bonds (e.g. as in equation 15 for graphene). For this reason, the ratio of the partial pressures of the precursor and etchant gases usually presents a unified single synthesis parameter. It is useful to look for trends in a single synthesis parameter than in two correlated synthesis parameters (e.g. a ratio of H_2:CH_4 flows instead of the absolute value of H_2 flow rate and absolute value of CH_4 flow rate). Sun *et al* (2014)[130] proposed that a "balance regime" is needed between suppressing surface segregation of the precursor from the bulk and surface growth reactions. This can only be achieved with a high etching rate of the defective lattice, for which a high H_2 to CH_4 is needed (e.g. 300[125] at atmospheric pressure).

Time

For 2D material synthesis, provided the thermodynamics and the kinetics are suitable for the material growth, the size and sometimes the thickness of the materials will increase with time. However, depending on the parameters other scenarios can occur:

- no materials produced at any time;
- the growth/etch balance is reached with time and the growth ceases ("self-limited");
- the material is produced too quickly, often resulting in bad quality due to insufficient etching of the defects.

Cooling rate

Slow cooling results in the dissolved precursor segregation from the bulk of the substrate and "growth from below"[130] as shown schematically in Figure 13f. Multiple layers (bilayer, tri-layer etc.) can form very quickly. Cooling rates of hundreds of degrees per minute are typically employed to "quench" the segregation process, which is also used as the standard method in this thesis.

2.3. Summary

Successful CVD synthesis is a delicate balance of many variables, from primary CVD parameters, such as temperature, gas flows and time, to small details such as how the system is heated, cooled, timed and cleaned. Suitable equipment with rigorous controls is a must for reproducible synthesis of 2D materials that are critically sensitive to contamination. I developed advanced CVD systems and procedures for the synthesis of graphene, hBN and WS_2 where I thoroughly assessed the suitability of each part of the apparatus and each step of the procedure.

Exploring the CVD parameter space is by far the most time-consuming task of the 2D material synthesis research. Understanding which physical quantities are the true CVD parameters and which are correlated or non-essential parameters allows to increase the pace and clarity of experimental work. In this chapter, I discussed the theoretical concepts behind the main CVD parameters and substrate effects on the synthesis of graphene, hBN and WS_2 and explained the expected effects that happen when these parameters are changed.

Chapter 3. Characterisation techniques

In this chapter I will briefly describe and discuss the techniques used for characterising the substrates for CVD growth and the resulting 2D materials. Each technique is an active research field of its own, thus, only brief principles of operation can be given. The focus of this chapter will be on the types of information and conclusive evidence that each of the discussed techniques can give regarding 2D materials, substrates or gas composition.

3.1. Transfer of 2D materials

One of the main disadvantages of CVD commercially is the need to transfer the synthesised graphene or hBN from a catalytic metal substrate to an insulator, such as silica, alumina or boron nitride for many applications in order to exploit their electronic properties. Significant effort has been dedicated to finding a breakthrough in the transfer methods, however, a technologically acceptable approach is yet to be found[43]. For some of the characterisation techniques or applications discussed in this thesis, 2D materials also need to be either free-standing (e.g. transmission electron microscopy) or on an insulating substrate (Raman, SFB, QHE, PL). In this section I will discuss a generic

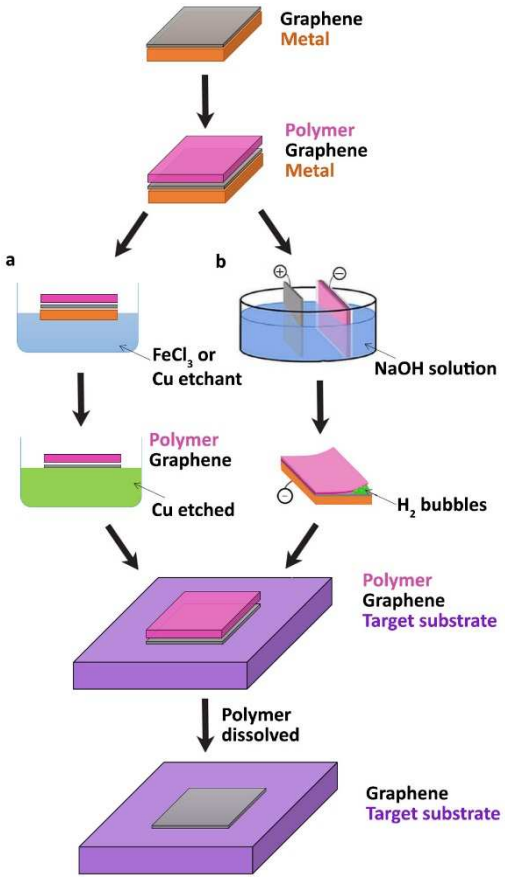

Figure 14. Graphene transfer methods. a) A substrate (Cu) etching transfer technique that requires an intermediate flexible polymer layer that is then placed on a substrate of choice, such as Si/SiO_2. b) An alternative non-destructive transfer method utilising bubble formation in-between the metal and polymer that allows to delaminate the polymer/graphene stack. Adapted from ref. 144.

transfer method that utilises a polymer support for graphene transfer as an example. Without a support, it is very difficult to handle a single or few atomic layer sheet and to distinguish it from water due to its high transparency as was found by Yu e*t al* (2008)[100]. Poly(methyl methacrylate) or PMMA was used in many studies as the polymer support[144-147]. I worked on optimising and refining the many specific details of the transfer procedure throughout the duration of my thesis, with the general steps shown schematically in Figure 14 that consist of the following:

i. A **graphene/metal** stack is spin-coated with a thin polymer layer. For example, PMMA (965 000 Mw, 4 % by weight solution in chlorobenzene) at 3000 RPM and heated to its glass transition temperature, 125 °C, to relax the polymer and let it adhere to graphene.
ii. The **polymer/graphene** stack can be delaminated from the metal substrate in two commonly used ways:
    a. The **metal** (such as Cu) is etched (Figure 14a) in iron (III) chloride or ammonium persulfate, followed by rinsing in deionised water.
    b. The **polymer/graphene/metal** stack is submerged in an electrolyte solution (1M NaOH) connected to the negative (reducing) electrode. Bubbles (H_2) are formed between **polymer/graphene** and the metal, thus delaminating the **polymer/graphene** stack (Figure 14b), which is followed by rinsing in deionised water. This method is particularly important for inert metals that are difficult to etch, such as Pt, but also works for Cu[148].
iii. While the **polymer/graphene** stack is floating in deionised water it is picked up by the target substrate, such as Si/SiO_2 or a transmission electron microscopy (TEM) grid.
iv. The new stack, **polymer/graphene/target substrate,** is dried and heated to relax the polymer and to let graphene adhere to the surface of the target substrate.
v. The stack is then placed in a solvent to dissolve the polymer, typically for at least 6 hours, after which residual solvent is removed with a nitrogen gun allowing the final structure **graphene/target substrate** to be used for applications or further characterisation.

Although it is easier to handle the structure during transfer compared to the support-free methods[100], many impurities, chemical functionalisation and doping occur after the removal of PMMA. Microscopic defects and macroscopic damage (Figure 15) are also difficult to avoid due to the polymer restructuring and trapped water[149]. A number of studies explored small variations to the polymer-assisted transfer method, showing a number of improvements. I attempted to incorporate some of these procedures into the previously discussed procedure; however, while some methods worked, others either did not show improvements or did not work at all. These investigations and the literature on transfer methods are discussed in the remainder of this section.

As a first procedure modification, utilisation of **different polymers** or **different molecular weights** was explored**,** allowing control of the chemical properties, bond strength with graphene and mechanical/elastic properties of the layer. For example, studies have explored polydimethylsiloxane (PDMS)[150], polystyrene (PS) with azide molecules[151], cellulose acetate butyrate (CAB)[149], cellulose nitrate (CN)[149], poly(lactic acid) (PLA)[152], poly(phthalaldehyde) (PPA)[152], poly(bisphenol A carbonate) (PC)[152] as alternatives to PMMA. Each of these investigations showed improvements and attempted to explain the reasons behind them, however, many experimental parameters were different between the studies, making it difficult to compare directly. One common conclusion from the literature is that PMMA is a bad choice of the support polymer. From transfer optimisation experiments I also observed that PMMA never resulted in full-area transfer of a graphene films: too often large chunks of the film were missing as shown in Figure 15a. My experiments with PS (and also with PC) showed much better uniformity, which was suggested and optimised by Christian van Engers based on findings by Song *et al* (2013)[153]. For this reason I replaced PMMA with PS in the optimised transfer procedure. In particular, PS of 280 000 molecular weight in a 4 Wt% in toluene (Sigma-Aldrich, 99.9 %) dramatically reduced the damage during the transfer, resulting in uniform 2D material films with preserved sharp edges after the transfer procedure. Other transfer optimisation

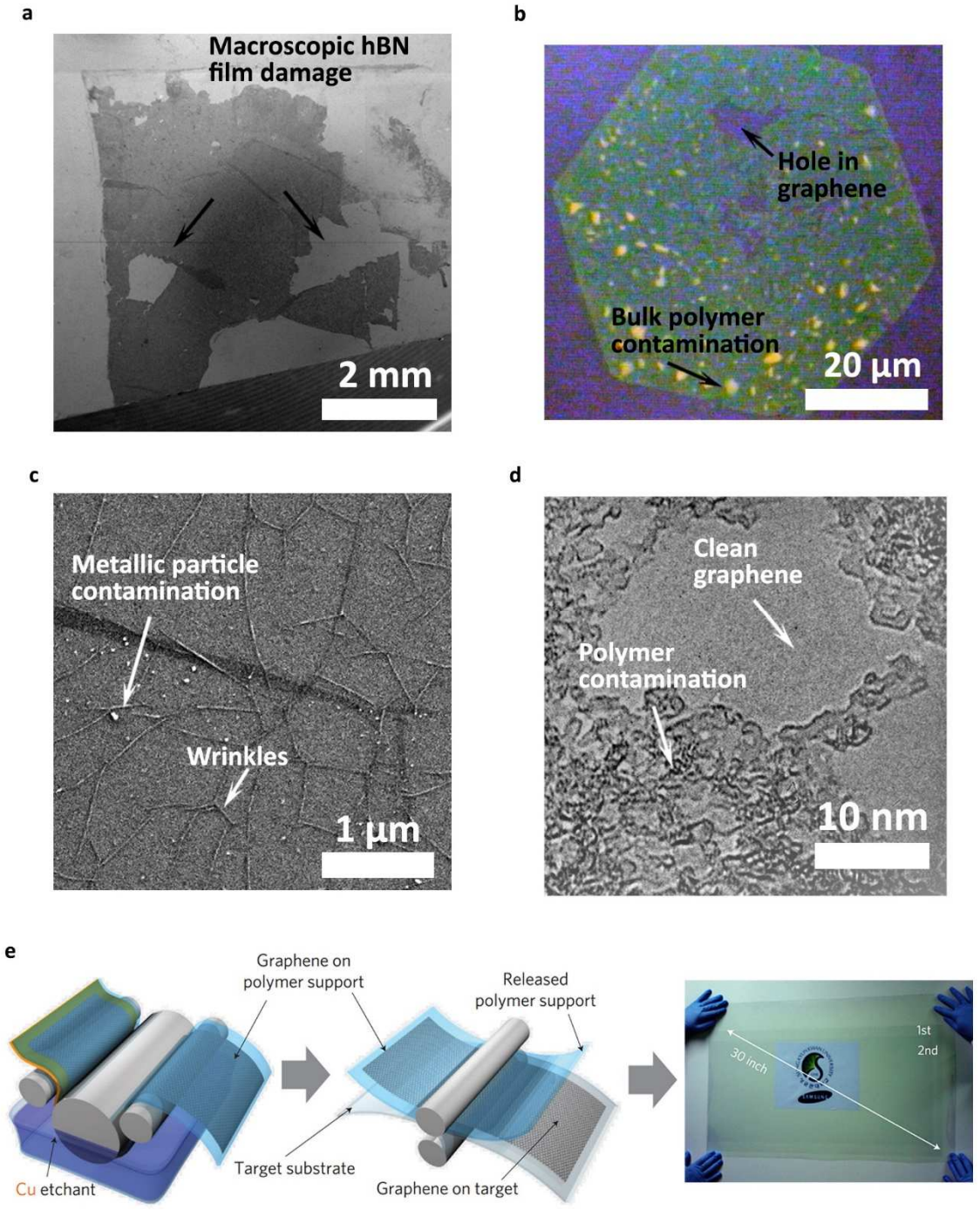

Figure 15. Typical problems of 2D material transfer. a) Macroscopic loss of material during the transfer due to poor adhesion or human errors in handling. Shown is an hBN film on a Si/SiO_2 substrate transferred with PMMA. b) A graphene flake after the transfer with PMMA: microscopic damage (holes) and PMMA residue (white patches) are visible. c) A high magnification scanning electron microscope (SEM) image of a graphene flakes showing a large number of wrinkles due to PMMA restructuring on the surface and small particles from impurities in the chemicals used. d) A high magnification TEM image of graphene, showing thin polymer contamination on the surface after transfer. e) Large-scale roll-to-roll transfer process developed by Bae *et al* (2010)[154] showing a wet transfer technique that allowed the production of 30 inch graphene films.

Solvent	Condition	Effect on transferred graphene
Acetone	50 ˚C, 3 hours	Bulk of PS was removed, but some PS residues remained, even if extended to 24 hours.
Toluene	50 ˚C, 3 hours.	Bulk of PS was removed, but some PS residues remained, even if extended to 24 hours.
Toluene, MIBK	50 ˚C, 3 hours. 50 ˚C, 24 hours.	A considerable improvement was observed in the quality of transferred graphene.
Chloroform	50 ˚C, 3 hours.	Bulk of PS was removed after 3 hours, but graphene Raman spectra showed strong doping after 24 hours, suggesting a harmful side reaction.

Table 3. Influence of different solvents on the quality of transferred graphene with time.

approaches focused on utilising **improved solvents** for the polymers used, such acetic acid for PMMA[155], toluene[153], chloroform[152] or sequential rinsing in multiple solvents, such as acetone followed by formamide[156]. Considerable improvements were reported, but again, the studies were not directly comparable. I therefore performed a systematic investigation into the effects of different solvents on the PS residue: toluene, acetone, methyl isobutyl ketone (MIBK) and chloroform, which are known to be some of the best solvents for PS[157]. Table 3 summarises the effects of these solvents on graphene quality. The final choice for the PS dissolution procedure was as follows: toluene was used to remove the bulk of PS (such as shown in Figure 15b), followed by MIBK, which seemed to better remove persistent residues of PS as was found using Raman spectroscopy (section 3.4.1.). The polymer peak decreased, the characteristic graphene peaks ratio improved from 0.7 to 1.2 on one sample, indicating less contamination on the surface; additionally, graphene peak positions shifted from p-doped to pristine graphene by simply adding the MIBK step, indicating an improvement in the electronic properties.

An extension of the generic procedure shown in Figure 14 can be **annealing** the graphene on the target substrate stack at different conditions after the transfer in order to remove stubborn contamination, relax graphene and remove weakly adsorbed chemicals. For example, a high magnification image from a transmission electron microscope (TEM) of a graphene domain is shown in Figure 15d with amorphous hydrocarbon contamination clearly visible. Various

annealing methods have been reported to treat such contaminations: medium vacuum (10^{-3} torr)[158], high vacuum (10^{-5} torr)[159], ultra-high vacuum (7.5×10^{-10} torr)[160], hydrogen[161] and oxygen/air[161]. Vacuum annealing facilitated desorption of PMMA and solvent molecules from the surface, while H_2 or O_2 chemically etched PMMA. H_2 is also known to be a weak etchant of graphene[125], while O_2 is known to be a very strong etchant[125]. For instance, Lin *et al* (2012)[161] observed cleaner, but damaged graphene after annealing in O_2. Clearly, it was not possible to avoid graphene damage with heat treatments in O_2, therefore, I did not investigate this method. Additionally, my experiments of annealing in medium vacuum (10^{-2} torr) showed macroscopic damage to the graphene film, most likely due to trapped water in between the graphene film and the substrate that formed vapour and teared through graphene upon heating. Again, it did not seem possible to steer away from damage to graphene with vacuum annealing and therefore it was also ruled out. However, in my experiments, hydrogen annealing at 200 °C for 3 hours, on the contrary, did not cause any damage to transferred graphene samples and showed a substantial decrease in the chemical doping found by Raman spectroscopy (section 3.4.1): the characteristic graphene peaks shifted from p-doped to pristine.

Some other studies looked at more elaborate modifications to the transfer procedure. Li *et al* (2009)[145] claimed that secondary drop casting of the PMMA solution on the dry, transferred layer and curing it afterwards allowed crack-free transfer. Possibly due to mechanical relaxation of graphene and PMMA leading to better contact with the substrate. I also investigated this approach, but found that practically most of such transfer experiments failed because the second PMMA droplet tended to spread all over the substrate and in between graphene and the substrate. This process not only delaminated graphene from the substrate, but also introduced damage and addition contamination in between graphene and the target substrate. Jeong *et al* (2012)[162] devised a double polymer coating method that consisted of coating graphene/metal with a low Mw PMMA, followed by curing the layer in UV in order to change its structure, followed by coating by another layer of high Mw PMMA. UV exposure was expected to decrease

the adhesion strength to graphene and facilitate better polymer–residue removal. I found that practically, this approach was cumbersome while not giving the structural integrity achieved with polystyrene.

Bae *et al* (2010)[154] was able to significantly up-scale the size of transferred samples using a roll-to-roll process, achieving large 30-inch films for transparent electronics applications. Unfortunately, only very small-area characterisation methods were shown, such as ~ 2 μm quantum Hall device and point Raman spectra, raising questions regarding the uniformity of the transfer. Nevertheless, these findings show promise for graphene transfer as a standard industrial fabrication technique in the future, but further large-scale optimisation and characterisation are needed.

Unlike graphene and hBN, WS_2 can grow on insulating substrates[124], making transfer considerations not as important technological issue for this material. Nevertheless, this material also has to be transferred for characterisation purposes or for heterostructure applications. Methods for WS_2 are typically very similar to those for graphene and therefore transfer procedure improvements optimised for one material will be beneficial for whole families of 2D materials. Although a transfer-free way of synthesising 2D materials would always be superior, more research needs to be conducted in both of these directions.

3.2. Visual characterisation techniques

3.2.1. Optical microscopy

Geometrical optics has been known to scientists for many centuries, with the first compound optical microscope invented as early as 1595[163] that consisted of just two lenses in a tube. The resolution of such a microscope was diffraction-limited reaching approximately 0.5 µm. A modest improvement was achieved by utilising a confocal microscope geometry in 1951[164] that reached resolutions of approximately 0.2 µm (Figure 16a) . Such microscopes are used routinely nowadays for a wide variety of applications. Indeed, Andre Geim and Konstantin Novoselov were able to discover monolayer graphene flakes only after transferring them to a Si/SiO_2 substrate where interference due to the 300 nm SiO_2 layer boosted graphene visibility considerably[8].

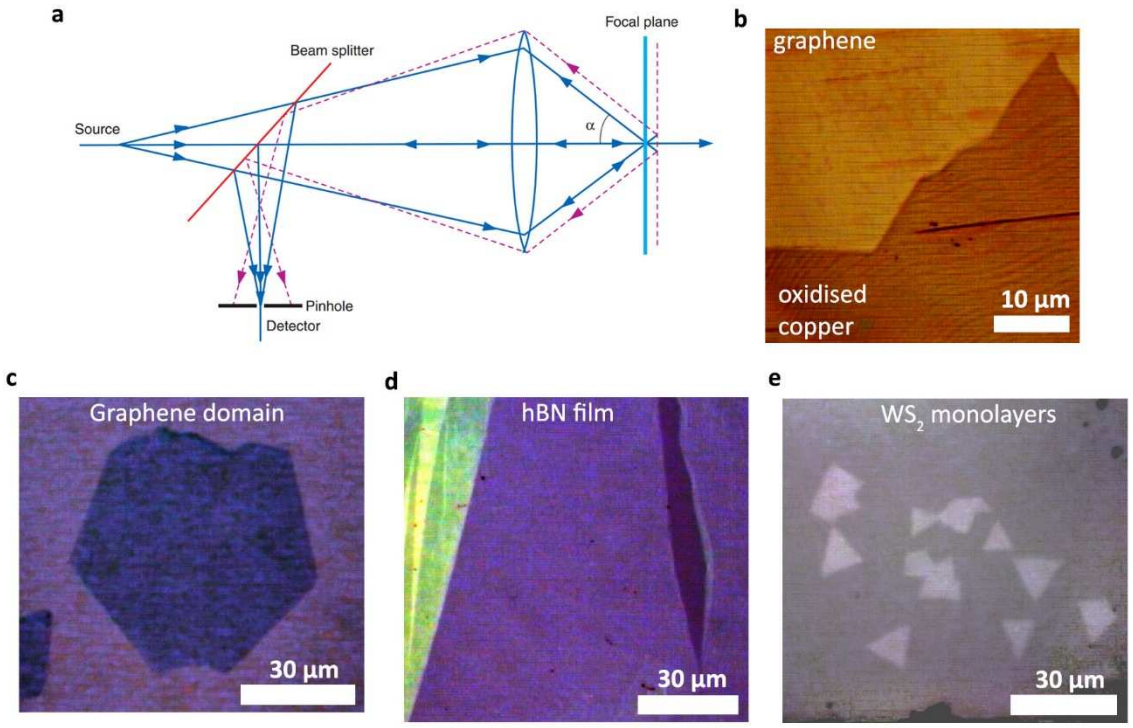

Figure 16. Optical microscopy for 2D material characterisation. a) A ray diagram of a confocal microscope. Image ref. 164. b) An optical image of graphene directly on Cu. The contrast is generated by oxidising uncovered Cu surface (darker). c) A graphene flake transferred to a Si/SiO_2 substrate. Hexagonal shape was partially preserved after the transfer with the top edge slightly folding on itself. d) An hBN film with a folded region, and a hole, showing the variation in contrast between the substrate, the film and the thicker film. e) Monolayer WS_2 flakes can be just distinguished from the sapphire background with increased contrast. Only presence of the 2D materials and their shape can be obtained with optical microscopy; typically it has to be combined with other complimentary techniques, such as Raman spectroscopy.

Owning to the fact that graphene absorbance is only 2.3 %, interpreting the images can be difficult. Optical images also give no conclusive evidence and only an indication of the number of layers in the sample and therefore are often combined with other techniques, such as Raman spectroscopy or AFM. Modern microscopes, however, utilise sensitive digital cameras that can distinguish features such as cracks or contamination in graphene. For example, I used a JY Horiba LabRAM ARAMIS confocal microscope to check the presence of graphene on my samples and evaluate the success of graphene transfers. Interestingly, graphene is not visible on metallic substrates due to their high reflectance, unless a "trick" is used, where the metal is oxidised around the 2D material giving some contrast difference (Figure 16b). Optical microscopy is particularly important for graphene transferred to insulating or flexible polymer substrates that cannot be placed in an electron microscope. Figure 16c shows a sample with a graphene domain transferred to a Si/SiO_2 substrate (1 mm/300 nm respectively) with a purple tint. As was mentioned in section 1.2.2, the light absorbance for hBN is much lower than for graphene, only around 0.1 %, making optical microscopy practically unsuitable for characterising monolayer hBN. It should be noted that multilayer films of hBN are more technologically favourable because of the improved electrical insulation in heterostructures. Such thin films can be studied with optical microscopy because the absorbance multiplies with increasing number of layers. As an example, a multilayer film of hBN is shown in Figure 16d with a hole and a folded region exhibiting different contrast. Similar reasoning can be applied to WS_2 materials, there is a minute contrast between monolayer triangles of WS_2 and the sapphire substrate and additionally a distinguishable contrast between monolayer and few layers of WS_2 (Figure 16e). However, for high resolution characterisation other techniques need to be employed.

3.2.2. Scanning electron microscopy

SEM can be considered as the most convenient technique for routine sample characterisation needed during the synthesis optimisation. Samples of graphene and hBN are grown on metallic

substrates in CVD due to the need for a catalytic surface. These conductive substrates are very suitable for the electron beam interaction processes to occur which are then picked up by various detectors. In the case when the substrate is not very conductive (such as Si/SiO_2 or sapphire), modern microscopes with a high signal-to-noise ratio and low voltage detectors can still obtain useful images of the samples. SEM does not require cumbersome sample preparation and is not destructive. Unlike optical microscopy, where the resolution is limited by diffraction, the wavelength of an electron beam is very small (10^{-10}-10^{-12} m) making technological challenges rather than fundamental ones more important. Spherical, chromatic aberrations and astigmatism occur due to the limitations in electromagnetic lens construction, spread of energies in the electron beam and the geometry of electromagnetic lenses respectively. Modern microscopes developed tools to successfully counter these problems and achieve resolution of 0.8 nm (Carl Zeiss Merlin, at 15 kV[165]), which is about 250 times better than optical microscopy. The range of magnifications also spans nearly six orders of magnitude.

A SEM focuses the electron beam created in the gun into a surface probe on the sample using a series of lenses as shown schematically in Figure 17a. Condenser lenses control the beam spot size, while the objective lens focuses the probe on the sample depending on the distance. The size and depth of penetration of the probe (interaction volume) into the sample determine the resolution and depend on the imaging conditions, such as the acceleration voltage and electron beam current. Various physical processes happen in the volume of interaction (Figure 17b) leading to the emission of

- **Secondary electrons (SE)**. These are produced when the primary beam electrons lose some of their energy during interactions with the **electron cloud** of atoms in the sample. Electrons from the cloud can become ionized and escape from the surface to the SE-detector. SE generated deeper in the surface of interaction are likely to be re-absorbed, therefore the emitted SE give surface-sensitive information, such as topography.

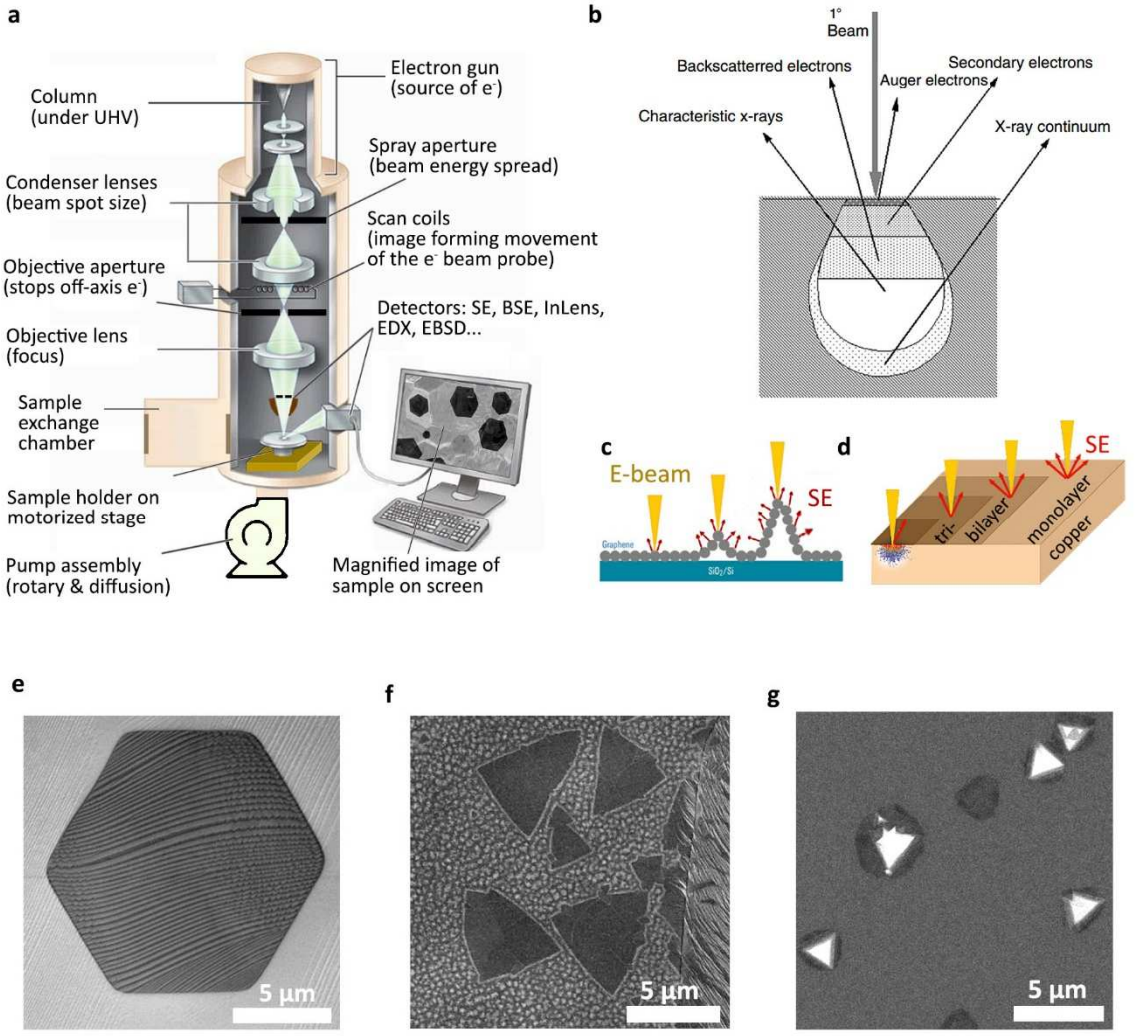

Figure 17. Electron microscopy principles of operation and exemplar images. a) A ray diagram and a schematic of a basic electron microscope, adapted from Mescher (2013)[166]. b) Processes occurring when the electron beam interacts with the sample. Some processes penetrate deeper in the bulk, while others are more surface sensitive. Image ref. 167. c-d) Mechanisms of contrast formation of graphene on insulating and metallic surfaces respectively. The former causes only a small change in contrast due to SE from graphene surface, while the latter produces good contrast due to the attenuation of SE emitted from the metal by graphene. Image ref. 168. e) A monolayer graphene flake on Pt showing uniform, darker contrast with the background due to SE attenuation. Image credit: Dr Adrian Murdock. f) Monolayer hBN flakes on Ni surface that look darker than the background (white speckles are non-crystalline deposits). g) WS_2 flakes on sapphire showing both dark (monolayer) and light (multilayer) contrast. The latter is due to the Z-contrast from heavy tungsten atoms overtaking SE attenuation from monolayer.

- **Backscattered electrons (BSE)**: electrons that elastically recoil due to interaction with the **nuclei** of atoms from the sample. These have high energy and carry information about the atomic composition of the sample. For example, high-Z metals such as Pt will be brighter than for example, silicon-containing regions in a BSE-detector.

- **Characteristic X-rays.** These high energy photons are produced after the electron beam ejects electrons from the inner shells of the sample atoms (K-shell, L-shell), followed by filling of the vacancy by furthermost electrons that lose energy in the process. The energy spectrum is characteristic for different chemical elements and is discussed in more detail in section 3.3.1.
- **Auger electrons.** The process is somewhat similar to the X-ray process, but instead of X-ray formation, the energy from the electron in the outer shells falling into an inner shell is transferred to another electron that is ejected (called Auger electron). These electrons also carry compositional information, but are much more surface-sensitive than X-rays.
- **Cathodoluminescene (only for luminescent materials).** In semiconductors, beam electrons can transfer energy to electrons in the sample thus promoting them from the valence band to the conduction band, leaving a hole in the valence band. Soon after, the electron and the hole can recombine to emit a photon, typically in the visible range.

When imaging 2D materials it is necessary to understand how the contrast is formed and why is it even possible to see atomically thin materials. Xie & Spallas (2012)[168] explored possible contrast mechanisms of graphene on different substrates. They showed that on insulating substrates, such as Si/SiO_2 or sapphire, wrinkles in the material or its edges are lighter because of the increased surface for SE emission (Figure 17c). However, on metals, a fundamentally different contrast mechanism is in place. 2D materials look darker because they stop a fraction of SE escaping from the surface. Consequently, bilayers, trilayers and so on have darker and darker contrast respectively (Figure 17d, 18a). I found that in practice these simple consideration do not always work, for example, on insulating substrates, the material can start charging, leading to different contrast every time. Even metallic substrates (e.g. Cu) can oxidise over time, leading to atomic-z contrast underneath graphene. Thin uniform films need additional attention, since if the sample is covered with a uniform layer of a 2D material, it is not possible to tell directly if the surface is covered or empty. Secondary features have to be employed as

supplementary ways of characterising the material produced. Let us consider graphene as an example. The material grows on hot, thermally expanded metal that, when cooled down, shrinks significantly. Graphene, on the other hand, does not shirk considerably when cooled, with studies suggesting that has a negative thermal expansion coefficient below 400 K[169]. This is why most of the CVD-grown graphene films on solid metals have wrinkles. Additionally, synthesis on liquid Cu or similar methods can cause cracks formation in graphene due to macroscopic restructuring of Cu surface[148]. These features are considered degrading to the properties of graphene[170], though without them it would be very difficult to use SEM for routine characterisation. Figure 18a shows an image of a graphene sample that seems to be individual flakes of graphene, however, on closer inspection there are dark lines that span the field of view, graphene wrinkles, that are characteristic of an underlying layer of monolayer graphene. The hexagons in Figure 18a are therefore bilayers, with one region of stacked multilayers (darkest).

From experimental observations I found that it is much more difficult to image hBN than graphene in a standard SE-mode. Currently, there is no scientific literature with exact studies of hBN contrast mechanisms in SEM and it is likely that hBN is simply more permeable for

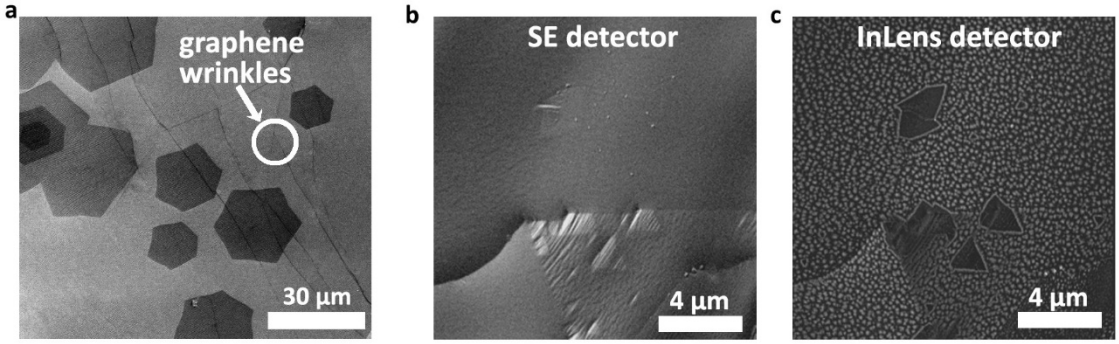

Figure 18. SEM imaging of features in 2D materials. a) Full coverage graphene film with visible hexagonal multilayers and graphene wrinkles that allow to infer that there is a monolayer film of graphene throughout the field of view. b-c) A comparison of the secondary electron (SE) detector and the more sensitive in-lens detector for hBN flakes. The former produces small topography contrast due to the roughness of hBN flakes. In-Lens detector produces stronger contrast because it of the higher signal-to-noise ratio for SE electrons.

SE than graphene. One explanation could be the fact that hBN flakes were found to be very rough and under some conditions modern topography-sensitive SE detectors allowed me to distinguish triangular shapes that had clear difference in roughness from the background, as shown in Figure 18b. Unfortunately, this approach is limited because different grain orientations of the underlying metal also have very different roughness and can make hBN almost completely invisible. I utilised a modern SEM with an in-lens detector, Carl Zeiss Merlin SEM, that allowed more efficient collection of SE electrons to obtain better surface-sensitivity and contrast. The detector in this geometry is located vertically above the electron probe on the surface, collecting electrons that were scattered by 180°. The contrast improvement is likely due to the electronic structure variations[171] between insulating hBN flakes and conducting metal around it. hBN flakes were routinely visible with this detector after correct imaging parameters were identified, as shown in Figure 18c.

3.2.3. Transmission electron microscopy

Permitting the electron beam to go through the sample allows higher resolution imaging of the sample due to the reduced interaction volume. A diagram of a TEM microscope is shown in Figure 19a. There are a number of variations of TEM microscopes in the way they function: high resolutions transmission electron microscopes (HRTEM), aberration corrected transmission electron microscopes (AC-TEM) and scanning transmission electron microscopes (STEM). The latter focuses the beam into a probe and scans the sample to generate an image. Exemplar achievable resolutions[172] of the above microscopes are 0.2 nm (JEOL JEM-2100F), 0.12 nm (JEOL JEM-2200MCO) and 0.08 nm (JEOL JEM-ARM200F) respectively. The reason for smaller interaction volume is related to the very small thickness of the samples. The main difficulty of this technique is the sample preparation necessary to achieve such thin structures without contamination or damage. The atomic thickness of 2D materials is very advantageous for TEM

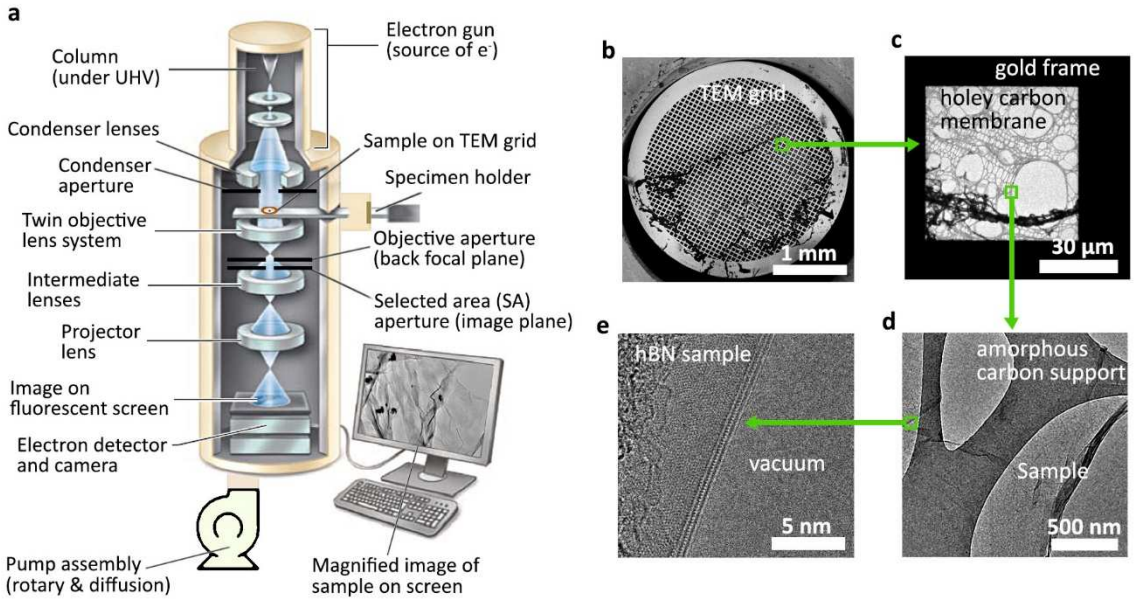

Figure 19. TEM microscopy concepts. a) A diagram of a transmission electron microscope with labelled main components, adapted from Mescher (2013)[166]. b) A low magnification SEM micrograph of a TEM grid showing its structure. c) A TEM micrograph of a cell of a TEM grid, showing opaque Cu grid and partially-transparent carbon support membrane. d) HRTEM image of a region where the sample is suspended over the carbon membrane. Amorphous carbon membrane is thicker and thus is darker than the sample. e) AC-TEM image showing lattice resolution of an hBN sample. The number of layers can be counted directly from the image. Image taken by Dr Jude Britton.

imaging, but on the other hand, these materials are very fragile, demanding elaborate transfer methods (described in section 3.2.1). Gold TEM grids (Figure 19b) are utilised that are resistant to the substrate etchant during the transfer. Additionally, the grids need to have an amorphous carbon membrane (e.g. “holey carbon”, “lacey carbon” or Quantifoil®) to locally support 2D materials (Figure 19c-d). While some structural characterisation, such as the number of layers in a 2D material (Figure 19e), can be deduced from visual images in TEM, it is usually combined with other techniques to obtain quantitative information. Interestingly, in annular dark-field STEM imaging mode, not only atomic resolution imaging can be achieved, but also the brightness (intensity) of atoms is related to the Z-number. This allows to study the lattice of the material and identify foreign atoms. The technique produced hundreds of publications ranging from O, N, B, H dopants in graphene to mixed TMDC characterisations.

3.3. Chemical analysis techniques

3.3.1. Energy-dispersive X-ray spectroscopy for substrate analysis

Energy-dispersive X-ray spectroscopy (EDX) is the analysis of X-rays emitted by the sample during its interaction with the electron beam in order to identify the X-ray "fingerprint" of the elements in the sample. Inner-shell electrons are ejected from the sample by the beam, followed by filling of the vacancy by the electrons in the higher energy shells. The energy released corresponds to characteristic wavelengths that depend on the energy difference between the shells (Figure 20a). For example, the wavelength for an electron undergoing a transition from L-shell to K-shell is abbreviated as K_α, M-shell to K-shell as K_β, M-shell to L-shell as L_α and so on. Additionally, as electrons from the beam approach atoms they decelerate due to the repulsion from the electron cloud. This results in the emission of background radiation or "Bremsstrahlung". An EDX spectrum of an exemplar contamination particle on Pt foil is shown in Figure 20b indicating that the particle may contain Ca and Si or their oxides. EDX detectors are often present on both SEM and TEM microscopes making it a convenient and quick complimentary characterisation technique. It must be noted that since X-rays are produced from the whole volume of interaction in SEM, the resolution and surface sensitivity are poor, on the order of hundreds of nm.

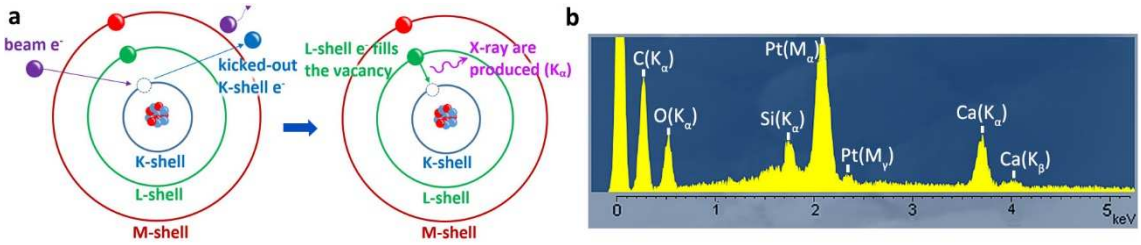

Figure 20. EDX concepts. a) A diagram of X-ray generation when an electron beam interacts with the inner shell electrons in the sample. Electrons from upper shells emit X-rays and fill the vacancy. b) An exemplar EDX spectrum of a contaminant particle typically found on Pt foils.

3.3.2. X-ray photoelectron spectroscopy for substrate analysis

Unlike EDX, X-ray photoelectron spectroscopy (XPS) is a technique that allows the identification of elemental species and their local bonding environment (chemical state) in the top surface of a sample. Typically the probe spans large areas of the sample (around 0.1 mm) due to the limitations in focusing X-rays. Sensitivity of tens of atomic layers or few nm can be achieved. The technique utilises an X-ray source[173] (e.g. Al K_α) to produce high energy photons that interact with atoms in the sample, ejecting electrons from different electron shells as shown schematically in Figure 21a. The (kinetic) energies of the ejected electrons are measured with an electron energy analyser and the spectrum is generated on a computer screen (Figure 21b). The binding energy is calculated from the conservation of energy principle:

$$E_{\mathrm{e}^-,\mathrm{binding}} = E_{\mathrm{photon}} - (E_{\mathrm{e}^-,\mathrm{kinetic}} + \phi), \quad (24)$$

where ϕ is the work function of the material .

Elements on the periodic table have characteristic peaks corresponding to their electron configuration (1s, 2s, 2p, 3s…) as shown in the spectrum of a Pt foils in Figure 21c. Using the areas under the peaks and relative sensitivity factors (RSF) of the elements it is possible to estimate the atomic composition of the surface. Additionally, the peaks can be scanned in higher resolution and deconvoluted according to the local bonding environment by referring to literature or databases, such as NIST X-ray Photoelectron Spectroscopy Database[174]. For example, a high resolution XPS scan of Pt 4f peak is shown in Figure 21d. The doublet Pt $4f_{7/2}$ and Pt $4f_{5/2}$ is visible (each singlet carries identical information). Individual peaks are manually deconvoluted based on the expected elements in the system and from database references, for example, Pt[174] $4f_{7/2}$ at 71.2 eV and Pt/Si[174] $4f_{7/2}$ at 72.5 eV can be identified in the spectrum. 2D materials experience the immediate environment of the top surface of the substrate, which, conveniently, is what is detected in XPS. Catalytic ability of the substrate, nucleation density and doping of 2D materials depend on the presence of contamination on the surface. For example, studies[141, 175] have shown that on Cu, oxygen impurity from the top surface is of particular

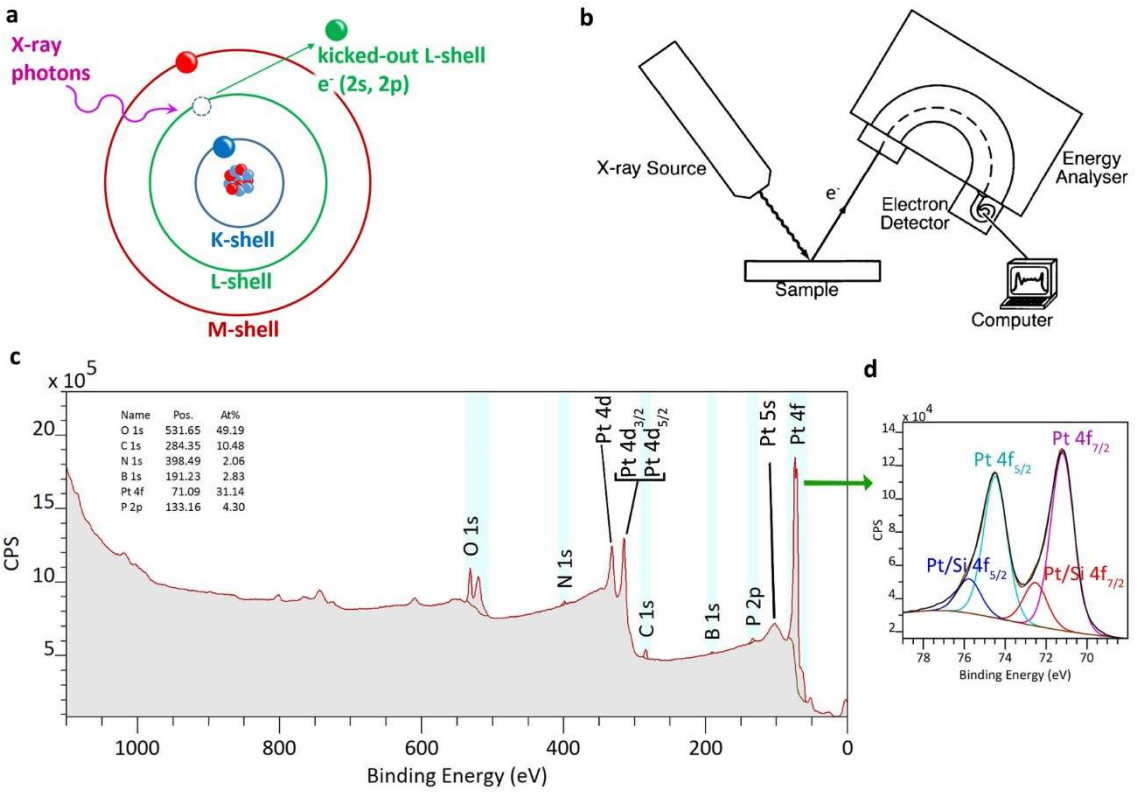

Figure 21. X-ray photoelectron spectroscopy. a) A schematic diagram of the processes involved in generating XPS signal. b) The apparatus diagram from O'Connor *et al* (2003)[173]. c) Exemplar XPS spectrum of the surface of Pt foil, showing large quantities of carbon and oxygen contamination. d) A high resolution scan of Pt 4f peak, showing 5/2 and 7/2 spin splitting, which have been deconvoluted into the pure Pt energy peak and Pt reacted with Si peak identified from the NIST XPS Database[174].

importance to control the number of nucleation sites and thus the size of graphene crystals.

3.3.3. Mass spectrometry for gas and precursor vapour analysis

While precursors for some 2D materials are commonly used and are widely available, there are many novel precursor combinations that are not well-understood and need to be developed. For example, methane gas, the gas used for household cooking is the most commonly used precursor for graphene synthesis. Other materials studied in this thesis, hBN and WS_2 consist of two elements, opening up many choices of precursors. Mass spectrometry (MS) allows the identification of molecular masses of species comprising a gas mixture and gives an indication of the partial pressure of these species. Various designs of the apparatus exist.

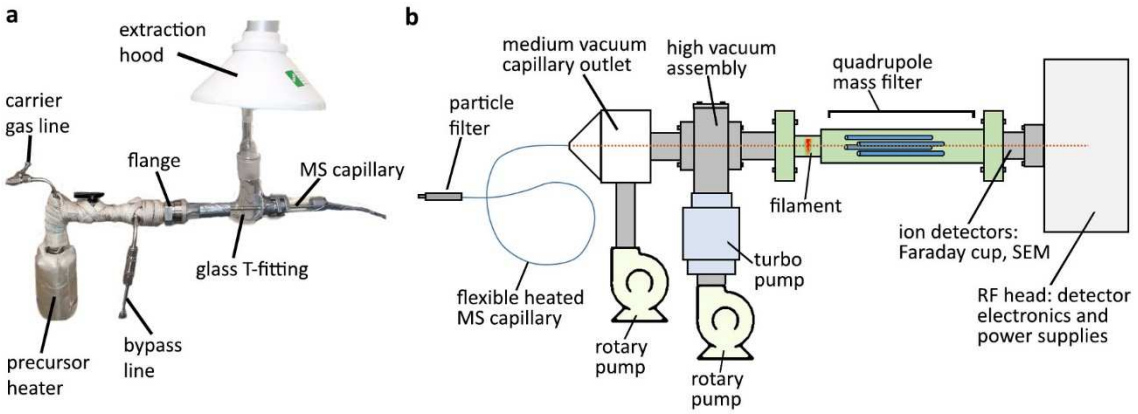

Figure 22. MS apparatus. a) A picture of the SS precursor delivery manifold (section 2.1) that was adapted for the MS measurement. The MS capillary passes through a glass T-fitting allowing the gas mixture to flow around it and into the extraction hood. b) A schematic diagram of the Hiden Analytical HPR-20 QIC quadrupole MS based on component diagrams from the manual.

I used a quadrupole mass filter spectrometer, Hiden Analytical HPR-20 QIC EGA, connected to the inlet of the MS capillary as shown in Figure 22a. Additionally, main components of the MS are shown in Figure 22b. This design offers fast scan rate, high sensitivity while still being compact. A particularly useful feature is the presence of a flexible heated silica capillary that allows a **pressure gradient** to be set up from the inlet to the outlet of the capillary such that gases can be measured at atmospheric pressure. Gas molecules are ionised by the filament and enter a quadrupole mass filter that consists of four parallel rods. Here, radio-frequency oscillating voltages[176] are applied between opposite rods such that only specific ion mass trajectories can be stable. The counts of ions from the detector are then displayed as a spectrum. Specific utilisation of the technique will be discussed in section 4.3.2 for the gas line impurity measurements and in section 6.1.2 for *in situ* hBN precursor analysis.

3.4. Structural characterisation techniques

3.4.1. Raman spectroscopy

Raman spectroscopy is an important, non-destructive technique to study the quality of 2D materials. While Raman spectroscopy can be utilised to study materials from first principle simulations of spectra, in this thesis it is used by comparing the measured data to reference spectra from published studies. Peak intensities, positions, widths and intensity ratios of two peaks carry useful characterisation information. Below I will discuss the general principle behind Raman spectroscopy, followed by the specific peak information for graphene, hBN and WS_2 that will be used in the results chapters.

In the most basic description, Raman spectroscopy is the inelastic scattering of optical photons from the sample with loss of energy to lattice vibrations of the sample. Normal modes that are symmetric by inversion can be Raman active and occur as disturbances (phonons) in the lattice that depend on the lattice symmetry, the mass of atoms in the lattice, the interactions between atoms and local environment (temperature, pressure, mechanical stress etc). Scattered photons with energies different to the reference light ("Raman shift") are recorded and are shown on the screen as characteristic peaks of the material. In graphene and graphite there is a strong electron-phonon interaction[177] that significantly complicates this simple picture, indeed, good understanding of this process was only developed in 2000 with a proposed "double-scattering" mechanism[178].

Graphene Raman spectrum

Ferrari & Basko (2013)[179] wrote a comprehensive review of Raman processes in graphene, where they clarified the notation for graphene peaks, touched on the history of Raman for graphite and discussed the theory. While the theoretical treatments are beyond the scope of this thesis, I will adopt their suggested notation and pictorially explain the origin of Raman peaks. Double,

triple and higher "resonant Raman scattering" occurs because there is no electronic band gap in graphene (Figure 4f) and incoming photons always excite electrons to an **available** electron state, which then can decay to a vibrational level ("Stokes scattering", the most probable inelastic process). The intensity of Raman peaks is therefore very high for an atomically-thin material.

Characteristic peaks of different allotropic forms of carbon are shown in Figure 23a for excitation wavelength of 532 nm. The "**G-peak**" occurs in all carbon structures and in pristine monolayer graphene at 1584 cm^{-1} (ref. 180). The mechanism involves a (single) resonant process where the incident photon creates an electron (e^-) and hole (h^+) pair and promotes the e^- to an excited state without changing its crystal momentum (Figure 23e). This process is followed by the e^- relaxation to a vibrational energy state with the release of a phonon (Γ-point, E_{2g} mode, Figure 23c) and annihilation of the e^- and a h^+ to create a Raman photon (Figure 23e) such that

$$E_{\text{incident photon}} = E_{\text{Raman photon}} + E_{\text{phonon}}. \quad (25)$$

The "**2D-peak**" is generated in a double resonance process, where e^- crystal momentum can change from K to K' point in the electron band structure (Figure 4f), allowing two "opposite" phonons from the K-point (A_1') of the dispersion relation to be created (Figure 23c, f). Lee *et al* (2012)[180] measured the position of this peak to be at 2691 cm^{-1} for pristine monolayer graphene.

The next important peak (at 1350 cm^{-1}) for graphene is the "**D-peak**" often called the "defect peak" since it only appears where multiple defects are present in graphene lattice that give rise to elastic e^- scattering. Similar to the 2D-peak there is an intravalley change in e^- momentum followed by the release of phonon(s), a Raman photon and elastic e^- scattering (7 processes are possible, one of which is shown in Figure 23d). Other less intense peaks will not be discussed, but mentioned for completeness C at ~30 cm^{-1}, D' at ~1620 cm^{-1}, D+D'' at ~2470cm^{-1}, D+D' at

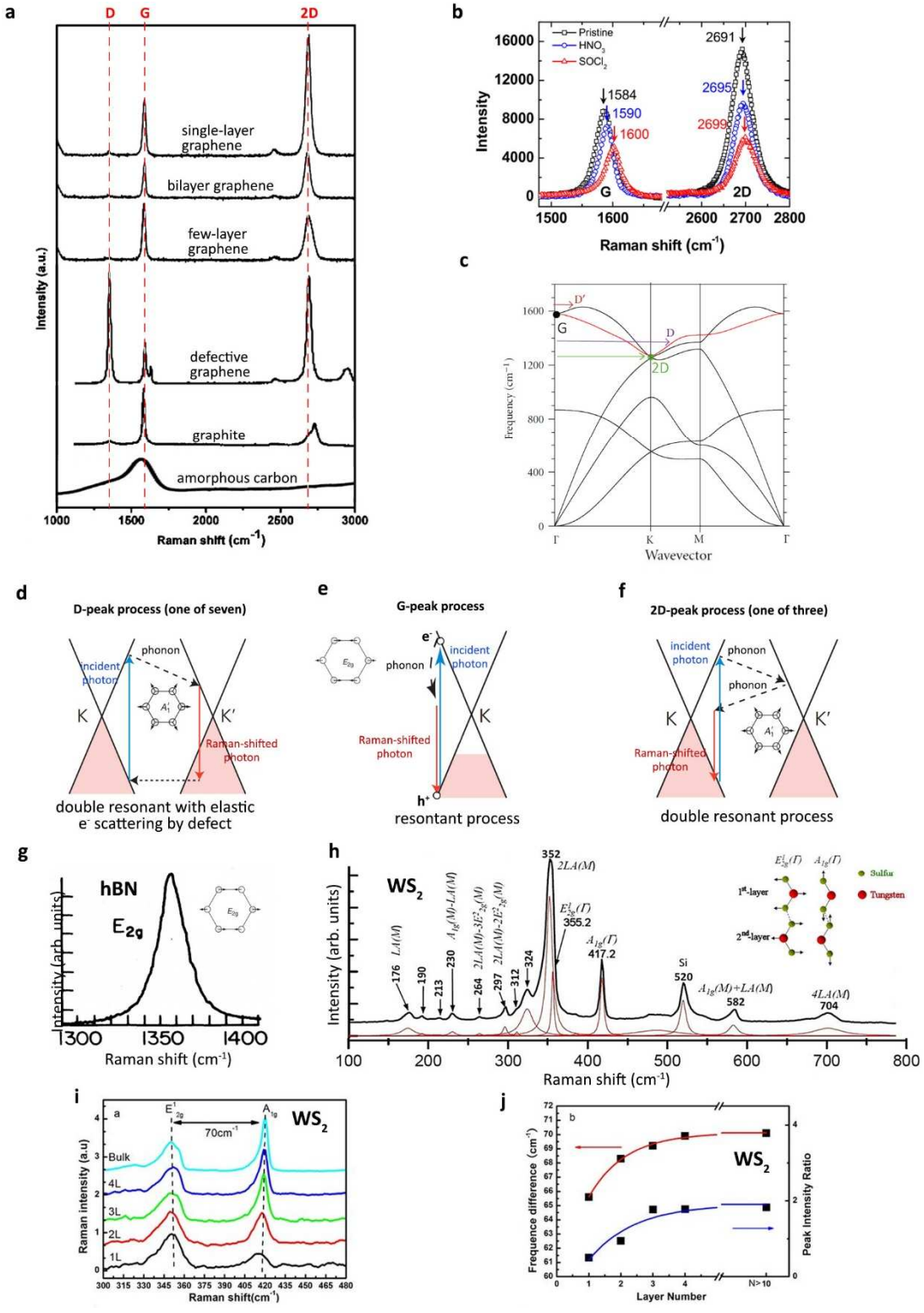

Figure 23. Raman spectroscopy of 2D materials. a) Raman spectra of allotropic forms of carbon, adapted from ref. 181-183. b) Blue shift of graphene peaks due to p-doping. Image from ref. 180. Opposite effect is expected for n-doping. c) Graphene phonon dispersion with labelled phonons corresponding to characteristic Raman peaks from ref. 184. d-f) Schematic representations of electronic and vibrational transitions for D, G, and 2D-peaks respectively. Images adapted from ref. 179. g) Raman spectrum for bulk hBN from ref. 185. Thinner hBN has lower intensity. h) Raman spectrum for WS_2 with a 514.5 nm laser with deconvoluted peaks in red. Peaks labelled as E^1_{2g}, 2LA(M) and A_{1g} are of particular importance for characterisation. Ref. 186. i-j) Wavenumber separation and intensity ratio of A_{1g} and E^1_{2g} peaks for WS_2 characterisation. Ref. 65.

~2940cm^{-1}, 2D' at ~3250 cm^{-1}; naming employed from Ferrari & Basko (2013)[179] and values are from Raman measurements of my samples with a 532 nm laser. In bilayer or multilayer graphene two or more Dirac cones are present in the electron band structure that allow new transitions of slightly different wavenumber to appear. Consequently, the 2D-peak consists of a convolution of peaks which increase the full width at half maximum (FWHM) of the 2D-peak and reduce its intensity. The ratio of intensities of 2D to G peaks is therefore indicative of the number of layers[187]. Monolayer graphene typically exhibits a ratio of > 2, bilayer = 1, and tri or more layers < 1. However, care needs to be taken, since if graphene stacking is turbostratic the layers can be considered non-interacting and the spectra will add up[181]. Nevertheless, bilayers are usually small and this case can be ruled out from optical contrast.

Positions of the peaks in graphene, especially the G-peak, are strongly dependent on the doping level[180]. Doping shifts Fermi level of the electronic band structure. If Fermi level is shifted down (p-doped) then the energy of the generated phonon decreases and thus the detected Raman-shifted photon energy increases (equation 25). For example, as shown in Figure 23e by the region shaded in red. The G-peak position therefore shifts to higher values of the wavenumber (cm^{-1}) as shown in Figure 23b. And vice versa for n-doping, where the position of the G-peak shifts to lower values of wavenumber (cm^{-1}). Such shifts in the position of the peaks have been used to study B-doped graphene, N-doped graphene, acid functionalisation, PMMA and water residue[180]. The latter is particularly useful to study the suitability of transfer techniques, as described in section 3.1.

Additionally, measured values of the peaks and their intensities strongly depends on physical conditions such as temperature, pressure, humidity, substrate as summarised by Jorio *et al* (2012)[184]. For this reason, in this thesis, all measurements were performed under consistent conditions with laser wavelength of 532 nm, at atmospheric pressure and room temperature on substrates with a 300nm SiO_2 layer on Si (unless specified otherwise).

Hexagonal boron nitride Raman spectrum

Since the band gap of hBN is very wide (Figure 5f), the Raman processes are not resonant like in graphene, unless UV light is used. Theoretically it becomes much easier to understand, since only one phonon near Γ-point is generated as shown in Figure 23g with wavenumber position of 1367 cm^{-1} (ref. 185). However, practically this conclusion means that the intensity of the hBN peak becomes very low with decreasing number of layers, making it time consuming to acquire spectra. Interestingly, this peak often overlaps with the D-peak in graphene making it difficult to characterise graphene-hBN heterostructures.

WS_2 Raman spectrum

WS_2 is a semiconductor and depending on the laser photon energy either resonant or non-resonant processes can become prominent. For this material the characteristic features of the Raman spectrum are the ratio of intensities and also the wavenumber difference between the two prominent peaks. For monolayer WS_2 with the 532 nm laser excitation wavelength, I measured the E^1_{2g} peak at 356 cm^{-1} and the A_{1g} at 420 cm^{-1}. The difference in the peaks' wavenumbers was therefore 64, while the ratio of intensities of A_{1g} to E^1_{2g} was 0.3. In comparison, for bulk WS_2 the 2LA(M) peak became dominant at 352 cm^{-1}, while the A_{1g} peaks shifted slightly to 417.5 cm^{-1}. Therefore, the difference in wavenumber and the ratio of intensities for bulk WS_2 was 67 cm^{-1} and 1.1 respectively, in good agreement with literature[65] as shown in Figure 23i,j. Interestingly, studies[186] with a 514.5 nm laser have shown that the 2LA(M) peak intensity becomes very high due to a double resonance process and many secondary peaks become noticeable (Figure 23h). It is therefore important to compare Raman spectra only with the same excitation wavelength.

While monolayer and multilayer WS_2 deposits can be easily distinguished with Raman spectroscopy, identifying the exact number of layers is more challenging due to small relative

changes in the wavenumber difference and the ratio of peak intensities. TEM, AFM and PL measurements can be used as supplementary characterisation techniques.

3.4.2. X-Ray diffraction, electron backscatter diffraction and selected area electron diffraction

Diffraction techniques in principle come from Bragg's law (equation 26) where constructive interference of the incident beam occurs from families of lattice planes of the material in study.

$$2d \sin\theta = n\lambda, \tag{26}$$

where d is the distance between lattice planes; θ is the scattering angle; n is a positive integer; λ is the wavelength of the incident wave.

X-Ray diffraction (XRD) and electron backscatter diffraction (EBSD) were used for substrate structure analysis while selected area electron diffraction (SAED) was used for 2D material analysis. The general principle of diffraction from Bragg's law is shown in Figure 24a. XRD, EBSD and SAED can be considered as various geometrical configurations of diffraction with different sources (X-rays or electrons). While EBSD and SAED are add-on in SEM/TEM, XRD is performed on a single purpose apparatus, a diffractometer.

XRD spectra recorded for samples in this thesis were compared to peaks in databases or literature. Provided the chemical elements composing the samples are know it is usually possible to identify the stoichiometry and crystallographic lattice of the sample.

EBSD is used in the geometry where a focused electron probe scans the sample and a series of specific diffractions patterns (known as Kikuchi lines) are recorded. Instrument software was then used to automatically analyse the lines and extract a map of crystallographic orientations from the scanned points on the sample. For this technique the crystallographic lattice and spacing need to be known prior to analysis. By correlating the surface crystallographic orientation with 2D materials morphology it is possible to study the influence of epitaxy on the

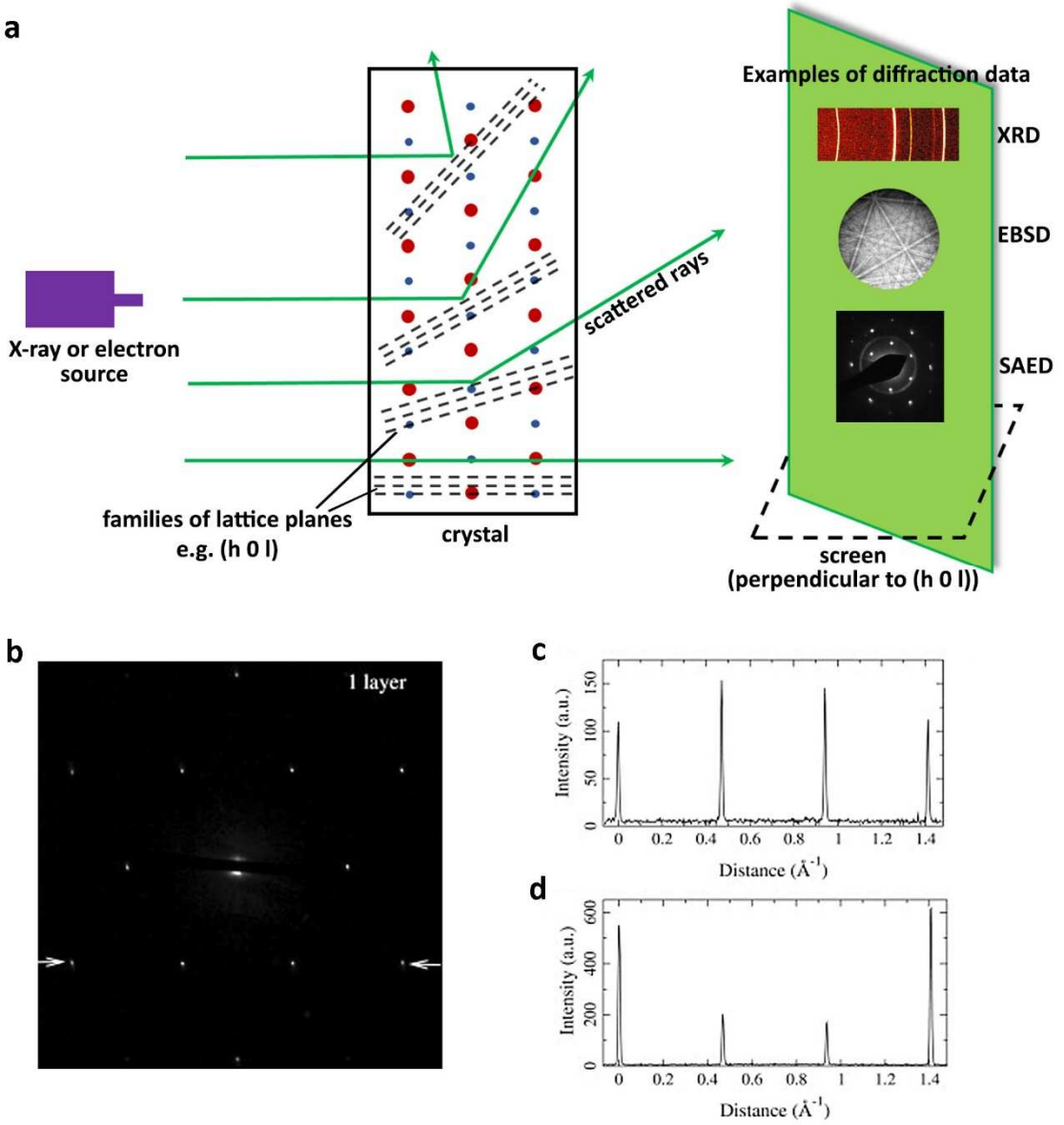

Figure 24. Diffraction concepts. a) An X-ray or electron beam scatters from the crystal forming a diffraction pattern on the screen (in SAED additional lenses are utilised after the beam has passed the sample). Examples of XRD, EBSD and SAED patterns are shown (XRD image ref. 188). Further data analysis is typically employed for EBSD and SAED. b-d) An example of a SAED pattern of monolayer graphene. Arrows indicate a line of the intensity profile. Intensity profiles shown in (c), (d) are characteristic for monolayer and bilayer graphene respectively. Images adapted from Meyer *et al* (2007)[189].

growth. This technique is used in sections 6.1.4 and 6.1.5.

SAED shows the crystal lattice symmetry of 2D materials and can also be used to identify the number of layers in graphene by either counting the number of rotated rings in the pattern for turbostratically-stacked graphene or by analysing a line intensity profile across four points of the

pattern[189]. Figure 24b shows an example of a SAED for monolayer graphene. If an intensity profile is taken across two inner and two outer points (as indicated by the arrows in Figure 24b) it is possible to distinguish monolayer graphene and AB-stacked bilayer (or thicker) graphene. Figures 24c,d shows characteristic intensity profiles for monolayer and AB-stacked bilayer graphene respectively, identified by Meyer *et al* (2007)[189].

3.5. Summary

In order to characterise the properties of 2D materials and elucidate their synthesis mechanisms a wide variety of visual, chemical and structural techniques need to be utilised. Foremost, I discussed and improved the cumbersome polymer-assisted transfer method for 2D materials. Notably, many seemingly small details could make the difference between success and failure. While there is scope for improvement of the procedure further, a reproducible and effective transfer method was developed.

I also reviewed the operation principle of a number of characterisation techniques and the types of conclusive information that can be obtained from each of these techniques for 2D materials, substrates or precursors.

Chapter 4. Graphene synthesis on pristine metals

The CVD synthesis of graphene has recently been investigated on different transition metals[190], for example, Ni, Cu, Ru, Rh, Ir, Pt, Au. Many of which succeeded in producing material of good quality. The quality can be defined in a number of ways, depending on the final application, but usually the main priorities are to reduce the number of defects, control the number of layers and to increase the size of single crystal graphene domains. In the plethora of publications on graphene synthesis with APCVD[190] there is a substantial variation in the type of graphene produced with seemingly similar CVD parameters. It is unclear, what advantages and disadvantages different substrates possess if compared in a systematic manner, whether there are unknown types of contamination in CVD systems that influence graphene growth and finally, if gas impurities need to be measured and specified between CVD systems to allow a direct comparison.

In this chapter I re-investigate the synthesis parameters on pristine metals, Pt, Pd and Cu in a comparable manner to elucidate the reasons for the variation between CVD studies and rigorously re-assess the control methods available in current CVD systems. I also attempt to up-scale the production of graphene samples in order to understand the problems that arise in this CVD system implementation and in the surface processes on the substrate. Graphene is characterised with a number of complimentary techniques. Additionally, the resulting graphene is transferred via a novel ultra-flat method and is utilised for measurements in the surface force balance (SFB) apparatus, a technique that is very sensitive to contamination and thus can be used to assess the quality of the transferred graphene.

4.1. Graphene on platinum

Pt is a noble transition metal that has been known historically for its high catalytic ability in chemistry and as an expensive, precious metal for jewellery. Promising results were reported by

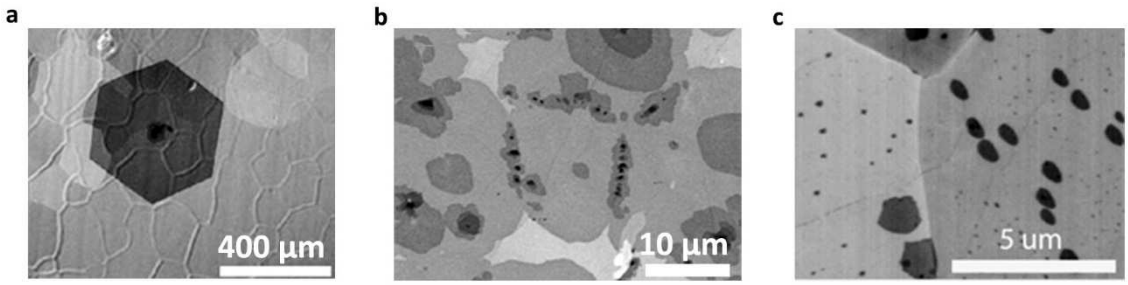

Figure 25. Literature reports for graphene synthesis on pristine Pt. a) Large hexagonal graphene flakes synthesised by Gao *et al* (2012)[144]. b-c) Images of graphene flakes synthesised by Sun *et al* (2014)[130] and Ping & Fuhrer (2014)[136] respectively. Striking differences in flake morphology are seen compared to Gao *et al* (2012)[144].

Gao *et al*[144] in 2012 when mm-sized graphene crystal were obtained on seemingly pristine Pt foils (Figure 25a). Additionally, the study introduced a novel "bubbling" transfer method for graphene (section 3.1). However, Sun *et al* (2014)[130] and Ping & Fuhrer (2014)[136] also explored graphene synthesis on pristine Pt, but did not achieve quality comparable to Gao *et al*, despite utilising similar methods (Figure 25b,c). Such variation in results required further investigation, because the publications with lower quality graphene have often been overlooked. I re-assess the synthesis of graphene on pristine Pt to find out the correct graphene type and optimise the CVD parameters to achieve larger size, more uniform graphene domains.

4.1.1. Synthesis parameter trends

Prior to the synthesis, the substrates were prepared as follows: pristine Pt foil (Goodfellow, 99.95 % purity, 25 µm thickness) was cut into small pieces (10 mm x 5 mm), cleaned in acetone and deionised water and loaded into the CVD system on a BN support plate, followed by the standard annealing and synthesis procedure described in section 2.1.1. Five synthesis parameters were systematically investigated: methane flow rate, hydrogen flow rate, total flow rate, furnace temperature and synthesis time. It was quickly found that the total flow rate was not a significant parameter in the range allowed by the MFC. Additionally, from theoretical considerations (section 2.2.3) and experimental observations the CH_4 and H_2 flows were clearly

correlated in their effects on graphene morphology. In particular, decreasing CH_4 flow had the same effect as increasing H_2 flow. Thus, for clarity, a derived parameter, the ratio of H_2:CH_4 flow rates, was introduced instead. This parameter, furnace temperature and time define the conditions to predictably tailor the type of graphene produced in the CVD system. Trends observed from varying each of these parameters are described below.

H_2:CH_4 ratio of flow rates

In my experiments I could differentiate a number of graphene growth scenarios on pristine Pt in the large parameter space available depending on the H_2 to CH_4 ratio. While keeping all other parameters constant, at high ratios (e.g. 175, 1040 °C) no graphene could be observed even after prolonged synthesis times (> 2 hours); at medium ratios (e.g. 125) small, completely monolayer graphene flakes were forming with very slow growth rates; at low ratios (e.g. 100) large multilayer graphene flakes were forming with fast growth rates and finally at very low ratios (e.g. 50) a graphene film fully covered the substrate with fast growth rates. This trend is shown in Figure 26a (first column) with representative SEM images of the achieved flakes. Care needs to be taken to distinguish graphene domains from Pt grains in the background as discussed in section 3.2.2.

Synthesis time

Provided that the H_2 to CH_4 allowed any graphene deposits to form, I observed that longer synthesis time resulted in larger flakes until a film was created. First, small graphene islands were forming and growing in size with time. Often, flakes of multilayer graphene appeared and were also growing with time (likely underneath the first layer of graphene[130]). Eventually the graphene domains joined into a continuous film, typically with patches of multilayers. Figure 26b (middle column) shows four images of graphene islands evolving with time. Although self-

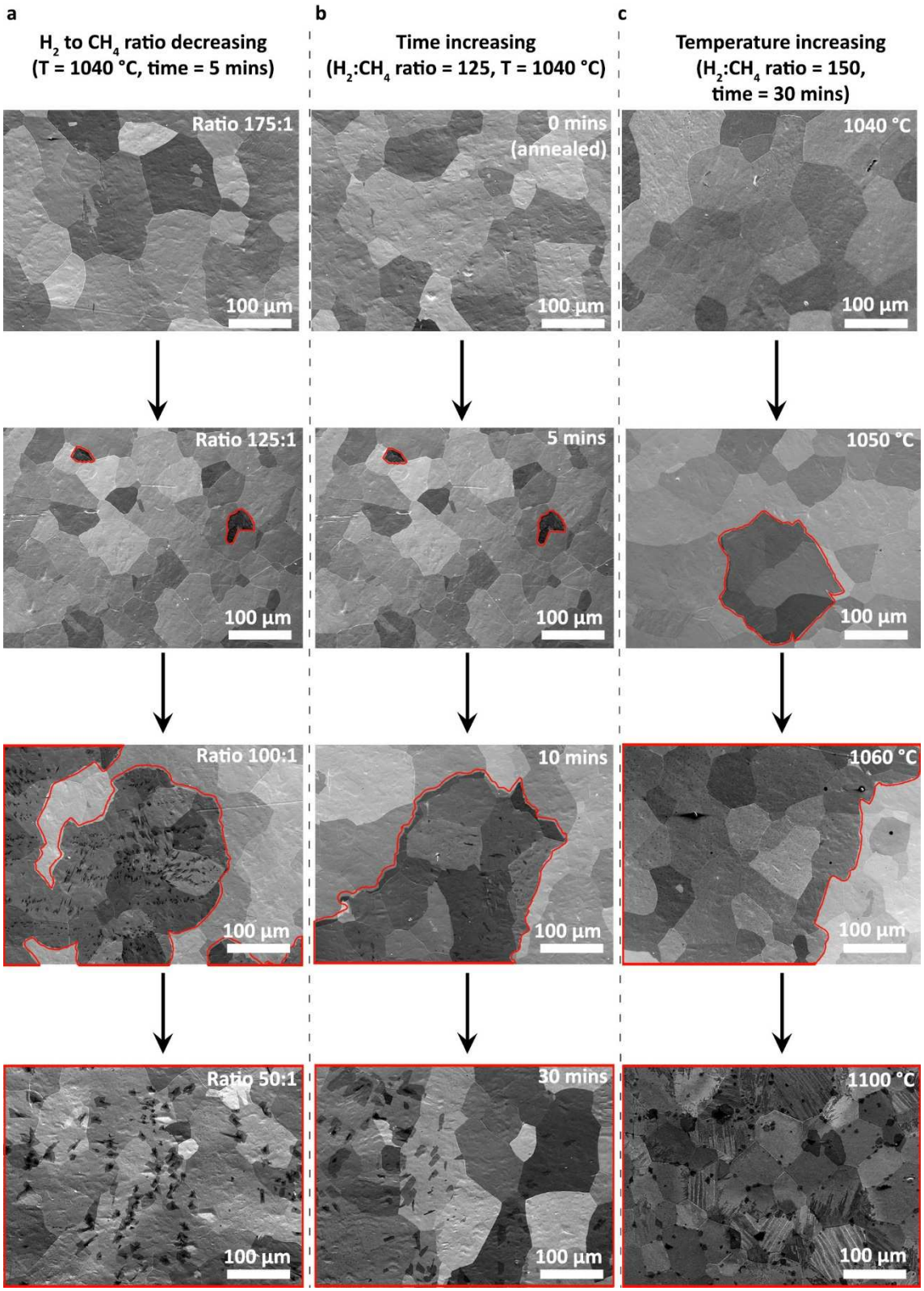

Figure 26. Main CVD parameter trends for graphene growth on pristine Pt. Graphene flakes are outlined in red to help in distinguishing them from Pt grains in the background. a) Graphene growth rate and the number of layers decrease with increasing H_2:CH_4 ratio. Increased etching of carbonaceous deposits improves the quality but sacrifices the growth rate. b) Longer experiments generate more graphene deposits, provided there is enough carbon to sustain the growth. c) Higher temperature facilitates faster growth rates due to the kinetically controlled synthesis regime.

limited graphene growth was an additional possibility (where the size of graphene flakes reached a maximum), I did not observe this in my experiments on Pt. Most likely because the regimes that I explored always had sufficient carbon for continuous synthesis.

Synthesis temperature

From theoretical reasoning outlined in sections 2.2.2 – 2.2.4 it is expected that increasing the temperature increases the rate of product formation. Indeed, this is what I observed for graphene growth on Pt as can be inferred from Figure 26c. The growth rate increased from approximately 5 μm min^{-1} at 1040 °C to 40 μm min^{-1} at 1150 °C as summarised in Figure 27a, however, in order to maintain the synthesis of monolayer graphene, the H_2:CH_4 ratio was increased for these experiments such as in Figure 27b. The increasing trend in the growth rate with temperature and time can be considered as a confirmation of the kinetic or surface reaction rate limited regime (sections 2.2.3, 2.2.4). Such dependence on the temperature has also been reported on Cu[142], albeit with much lower growth rate values.

Another useful quality indicator, the nucleation point separation or the maximum possible average size of graphene flakes, also increased with increasing temperature. Although the increase was not as fast as the growth rate (Figure 27b), it was still appreciable. E.g. when the temperature was increased from 1040 °C to 1150 °C the nucleation point separation quadrupled from 300 μm to 1200 μm. The likely explanation for this observation is the difference in the CVD parameters needed to initiate a nucleation site and to continue graphene growth from the edge of a flake. Therefore, increasing the temperature simultaneously with increasing the H_2:CH_4 ratio overall increased the growth rate of graphene domains. However, it is likely that the temperature increase did not stimulate the rate of nucleation site formation while increased H_2:CH_4 ratio reduced it, overall leading to the observed dependence.

Simultaneous parameters optimisation

It must be noted that for graphene quality optimisation it was very useful to stop the synthesis before the flakes coalesced together. This approach allowed to see the shape of the flakes easily, which is related to crystallinity[144]; also, the flake size distribution, related to growth rate and the nucleation point separation, related to the maximum achievable flake size. The aim of the parameter optimisation was to achieve large area completely monolayer graphene domains.

Additionally, the synthesis parameters have limits defined by the components of the system. For example, the flow ranges and thus the gas ratios had limits specified by the MFCs: 50-1000 sccm for H_2, 50-1000 for Ar and 0.5-10 sccm for CH_4. Temperature limits were between 700 °C and 1150 °C; the former set by the kinetic energies needed to overcome activation energies for graphene growth, while the latter was due to fused silica tube softening above 1200 °C. Time was not specifically limited, but the shortest time was not less than 5 minutes to minimise human errors in running experiments, while the longest time was set to 2 hours due to the consumable costs considerations. By fixing the time at around 30 minutes it was possible to systematically find the H_2:CH_4 ratios for different temperatures that resulted in individual graphene flakes as summarised in Figure 27c. It was evident that the H_2 to CH_4 ratio had to be simultaneously increased to slow down the growth rate and prevent full coverage with increasing temperature. Therefore, increasing the temperature was used as a way to increase the growth rate, while higher H_2:CH_4 ratio was used to reduce the number of layers to one.

For clarity, two temperature regimes can be considered: the lower temperature regime (1050 °C) and the higher temperature regime (1150 °C). For the former, after the parameter optimisation, the H_2:CH_4 ratio of 140 allowed monolayer graphene to be synthesised with a growth rate of 12 μm min^{-1} and the latter required a higher ratio of 170 to achieve predominately monolayer graphene with growth rate of 50 μm min^{-1}. These values are significantly faster than the achievable growth rate on Cu (~1 μm min^{-1}). Interestingly, only irregular shaped monolayer

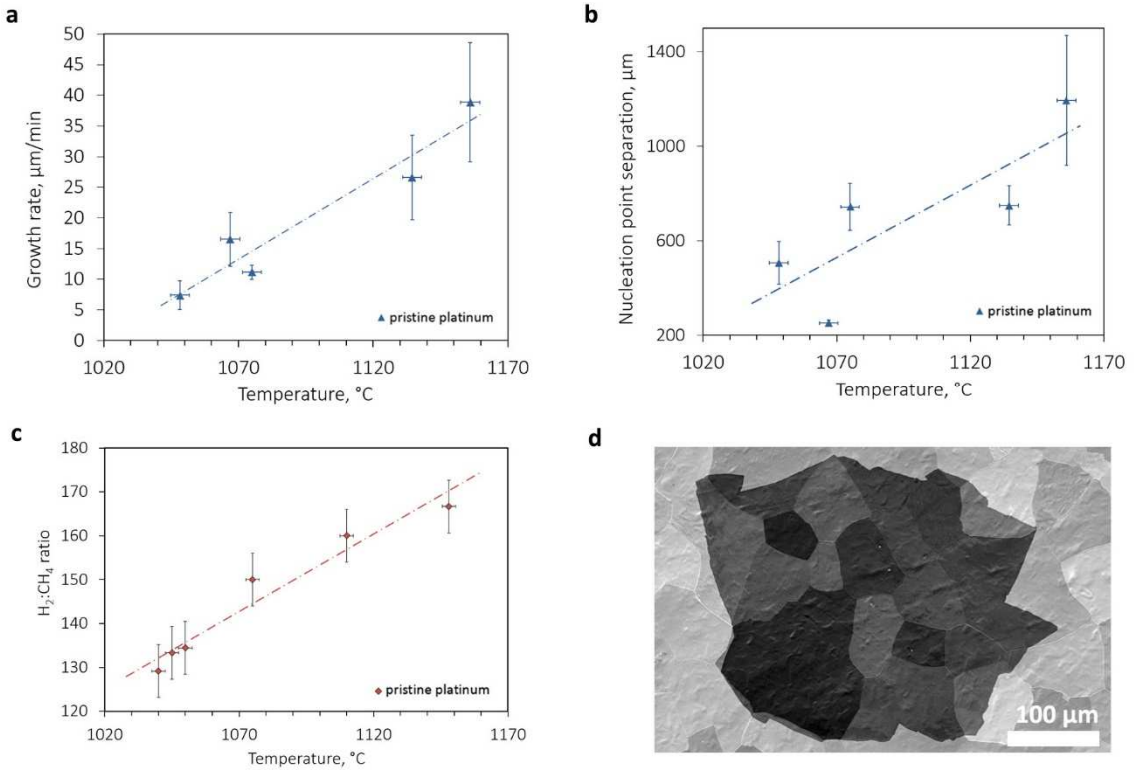

Figure 27. Statistical measurements of experimental data for graphene grown on pristine Pt foils. a) Graphene growth rate and nucleation point separation as functions of temperature. c) Synthesis parameter choice for the growth of uncoalesced, predominantly monolayer graphene flakes on pristine Pt. d) A SEM micrograph of a completely monolayer graphene flake achieved after parameter optimisation (1050 °C), this image is representative of many other experiments on pristine Pt.

graphene was observed in all the experiments on pristine Pt as shown in Figure 27d, very much in line with graphene type reported by the later publications on Pt[130,136]. Hexagonal graphene domains were not observed on pristine Pt, contrary to the study by Gao *et al* (2012)[144]. Although there is yet no theoretical reason why no hexagonal domains were observed, it is well know that Pt has a large lattice constant that leads to a lattice mismatch between graphene and Pt and thus to incommensurate growth. For example, on Cu(111) the lattice constant mismatch with graphene is 3.6 %, whereas on Pt(111) it is significantly higher at 12.5 %, suggesting why graphene is distorted not only when crossing from one Pt grain to another, but also on individual Pt grains.

During the parameter optimisation investigation I made some unexpected experimental observations: the Pt foil seemed to bond to the silica tube, and at high temperatures there was

more growth around the edges of the Pt foil where the foil was in contact with silica. For this reason a BN or alumina support was used in the experiments on pristine Pt to avoid contact with silica. Additionally, I concluded that there was a possibility of a chemical reaction between the two compounds. I investigated this interpretation in more detail in chapter 5 and found that *in situ* formation of platinum silicide in the CVD system facilitated the growth of hexagonal graphene domains, but led to irreproducibility if it was not controlled.

4.1.2. Nucleation point analysis

Both homogeneous and heterogeneous graphene domain nucleation often occurred on pristine Pt. Here, homogeneous nucleation is a process where graphene nucleates on flat Pt grains (Figure 28a), while heterogeneous nucleation occurs at preferential sites (Figure 28b,c). Understanding what influences the nucleation could allow more control and a way to increase the nucleation point separation, leading to larger graphene flakes. Two possible effects that could influence nucleation mechanisms are 1) topography, where the local flow is disturbed by contamination particles or grain boundaries (Figure 28b, c); 2) local chemical composition of the substrate that influenced the kinetics of surface reactions. I attempted to quantify the influence of topography by counting how many graphene flakes nucleated on particles and grain boundaries and how many on clean Pt grains. The data is presented in Table 4. If nucleation occurred completely randomly and grain boundaries were not influencing the number of nucleation sites then the contribution from grain boundaries should be less than 2 % by considering the relative approximate areas of Pt grains to grain boundaries (~6000 μm^2 and ~100 μm^2 respectively). On average, homogeneous nucleation on Pt grain and heterogeneous nucleation (the sum of nucleation sites on grain boundaries and particles) were approximately the same (55 % vs. 45 %). This observation leads to the conclusion that decreasing the number of grain boundaries, contamination particles and roughness could significantly improve the size

of graphene domains. It must be noted that Pt has a high melting point which makes it difficult to enlarge Pt grains by annealing. Additionally, because it is a noble metal it is not possible to electrochemically polish in readily available reagents in order to reduce the roughness. Other methods for smoothing the surface must be sought, for example silicidation, described in chapter 5.

In order to probe the influences of local chemical composition around contamination particles, EDX scans were performed on such nucleation sites. Chemical elements composing the particles were widely distributed on the periodic table, with Pt, Al, Si, Ca, Na, K, Lu and Fe appearing. This broad distribution of elements resulted in similar graphene morphology at each site, indicating that the topography, rather than the chemical environment, is the more likely cause of nucleation. Tailoring Pt cleaning methods to reduce these known types of contamination could help to increase the size of graphene domains. For example, the "RCA cleaning" methods could be used to chemically and mechanically (via bubbles) remove particulate contamination and consist of two steps: the SC-1 step, where the samples are sonicated in a solution of H_2O:NH_4OH:H_2O_2 = 15:1:1 at 60 °C for 30 minutes;

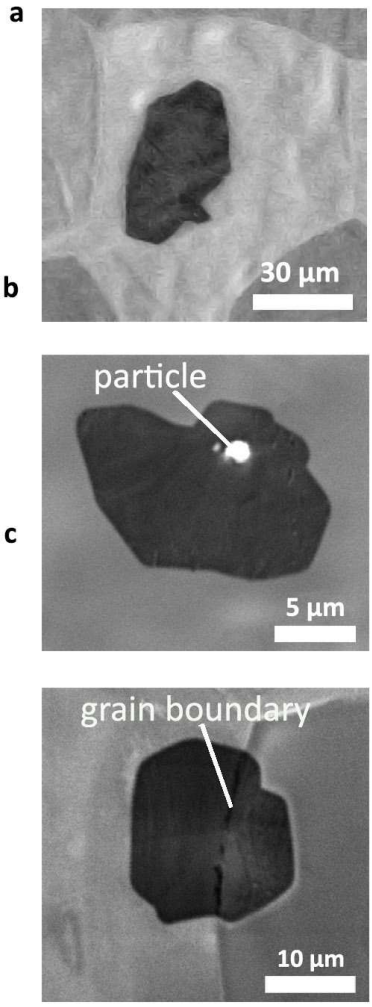

Figure 28. Graphene nucleation. a) Homogeneous nucleation. b-c) Heterogeneous nucleation on a contamination particle and Pt grain boundary respectively.

#	Substrate	Total number of flakes	Flakes nucleated on Pt grains	Flakes nucleated on grain boundaries	Flakes nucleated on contamination particles
1	Pristine Pt	43	22 (51 %)	7 (16 %)	14 (33 %)
2	Pristine Pt	13	9 (69 %)	1 (8 %)	3 (23 %)
3	Pristine Pt	11	5 (45 %)	4 (36 %)	2 (18 %)
	Average %		**55(±13) %**	**20(±14) %**	**25(±8) %**

Table 4. Nucleation point statistics for graphene flakes on pristine Pt.

followed by the SC-2 step, where the solution is changed to H_2O:HCl:H_2O_2 = 15:1:1 with the same conditions.

4.1.3. Graphene characterisation

A number of techniques were used to extensively assess the properties of graphene synthesised on Pt, such as size, shape, crystallinity and number of layers. Raman spectroscopy of graphene domains transferred to Si/SiO_2 substrates confirmed defect-free monolayer coverage: the ratio of 2D to G peaks was around 3 and the D-peak was nearly indistinguishable from the background (Figure 29a). While the transfer typically introduced hydrocarbon contamination, analysis of clean regions with high resolution, aberration-corrected TEM showed monolayer graphene lattice with hexagonal symmetry (Figure 29b-c). Studies[144] have shown previously that presence

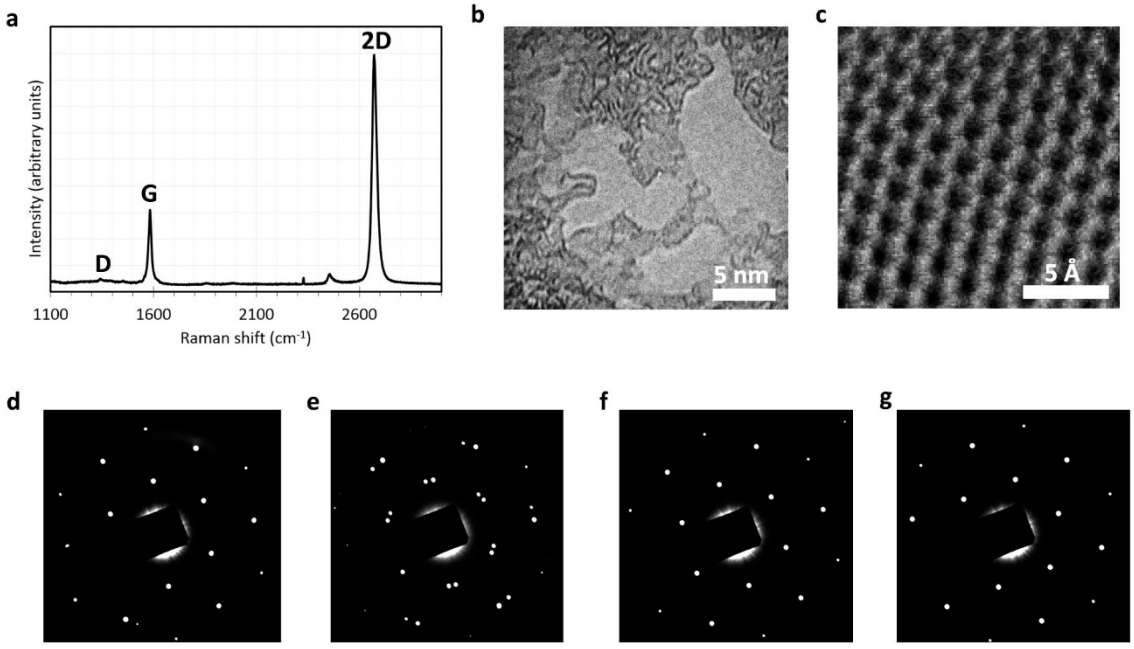

Figure 29. Graphene characterisation on pristine Pt, after parameter optimisation. a) A Raman spectrum of graphene transferred to a Si/SiO_2 substrate, indicating monolayer, low-defect graphene. b) A TEM image of graphene after the transfer to a TEM grid. Hydrocarbon contamination is observable, but clean regions exist. c) A lattice-resolved AC-TEM image of a clean region of graphene showing hexagonal symmetry. Image taken by Dr Jude Britton. d-g) SAED patterns of a representative, irregularly-shaped graphene flake synthesised on pristine Pt. Rotations of the lattice indicate polycrystals of graphene; the image with two hexagonal patterns confirms a grain boundary between the crystals in the field of view.

of reflex angles in graphene flakes indicated grain boundaries, but in order to undoubtedly verify this I recorded SAED patterns across large areas of graphene flakes synthesised on pristine Pt. Figure 29d-g show these patterns that confirm the presence of domain boundaries (Figure 29e) and rotated domains. In summary, monolayer, low-defect **polycrystalline** graphene was synthesised on pristine Pt with substantially high growth rates.

4.2. Graphene on palladium

Pd belongs to the platinum group of noble metals, and it is expected to possess similar properties in terms of catalytic activity for graphene synthesis. The biggest advantage compared to Pt is its price, which is approximately half of Pt. Two studies[191,192] explored Pd as a substrate for graphene synthesis at the same time as my investigation, with parameters and features of graphene in good agreement with my results. Most beneficially, Pd foils from Alfa Aesar (99.9 %, 25 µm) seemed very clean from particle contamination, allowing nucleation point separation to be extremely low with flake sizes of up to 4 mm at elevated temperatures, as shown in Figure 30a. CVD parameters follow similar trends to Pt, thus high temperature regime was adopted to achieve the fastest growth rate. For example, at 1150 °C with a 330 H_2:CH_4 ratio after 40 minutes, domains of 2 mm in size were achieved with growth rate of approximately 50 µm min^{-1}, very

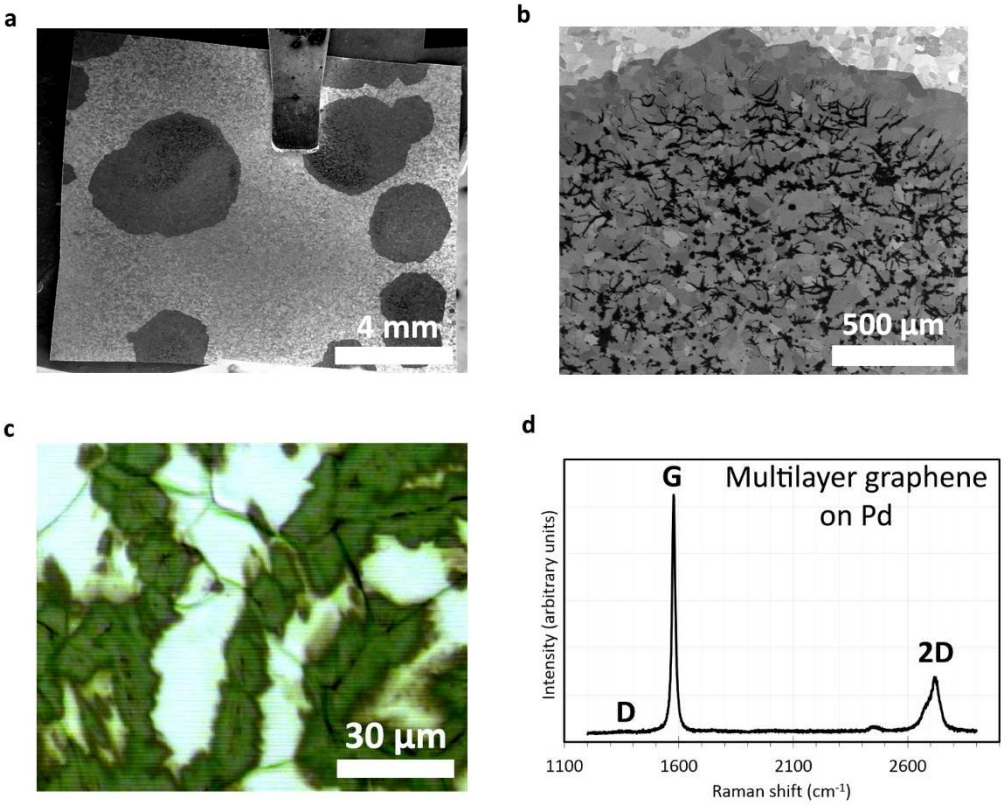

Figure 30. Graphene synthesis on Pd. a) A low magnification SEM microgram of Pd foil showing very large polycrystalline flakes. b) Sudden appearance of a thick multilayer network for syntheses with un-optimised parameters. c) An optical image of graphene multilayers directly on Pd indicating thick deposits. d) Raman spectrum of graphene multilayers on Pd, showing resemblance to graphite.

close to that of Pt. The flakes were circular on the large scale, indicating induced polycrystallinity when crossing multiple Pd grains (thousands) and their boundaries. This observation is not surprising, since Pd and Pt lattice constants are very similar and the lattice mismatch between graphene and Pd(111) is also around 12 %.

One considerable difference between Pd and Pt was the very fast growth of graphite-like multilayers on Pd, confirmed by Raman spectroscopy (Figure 30c, d). The 2D to G peak ratio was very low, and the 2D peak had the characteristic skewed shape typical for graphite. These multilayers grew as a network, rather than by increasing in lateral dimensions (observed on Pt). The reason for this type of growth is likely the slightly higher C solubility in Pd compared to Pt (e.g. 0.66 atomic % vs. 0.71 atomic % at 700 °C[135]). With parameter optimisation, similar to that discussed on Pt (increasing H_2:CH_4 ratio and time), the reaction can be tailored for almost 100 % monolayer graphene. To summarise, Pd can be used as a cheaper alternative for graphene growth on Pt that achieves large, monolayer, but **polycrystalline** flakes.

4.3. High-throughput graphene production on copper

Graphene synthesis on polycrystalline Cu has been studied by dozens of studies, and while good crystallinity can be easily achieved, the domains are usually small, around 20-30 μm[193], unless additional procedures are utilised. In particular, electropolishing[194], re-solidification[195], Cu surface oxidation[141] and parameter variation with time[113] have been shown recently to achieve mm-sized hexagonal domains of graphene. Nevertheless, monolayer, single crystals can only grow at very slow rates on Cu of around 1 μm min^{-1} due to the lower catalytic ability of Cu if compared to Pt or Pd. While consumable costs are significantly higher for running the CVD systems for prolonged times, Cu substrate is considerably cheaper than Pt (by around 15 times for purified metal foils). Cu is therefore a potential candidate substrate for graphene synthesis on the industrial scale.

For the purpose of industrial production, additional considerations need to be taken into account, for example, operational safety. While small lab-scale CVD reactors can be filled with explosive H_2 gas, it is a different matter if a large volume, up-scaled vessel is used. It is of such importance that, for example, an early study by Yan *et al* (2012)[194] was followed by a targeted correction[196] with "safety measures for using hydrogen at 2 atm in a glass CVD apparatus". Literature is currently divided between procedures that use pure H_2, CH_4 gases for graphene synthesis and those using Ar mixtures of these gases. Yet, where mixtures are used, often these are still classed as flammable according to Material Safety Data Sheets (MSDS).

Additionally, effects of moisture and oxygen impurity have been debated in the literature, but few attempted to measure them. Provided these effects are influential, in order for CVD systems to be comparable, the concentration of impurities need to measured and stated in the specifications of the system. The design of an up-scaled CVD system and the synthesis procedures also need to achieve constant impurity concentrations between experiments.

Human error and labour costs are other two important factors for industrial production of 2D materials. If an operator is needed for every step in the synthesis process this could result in irreproducibility and high cost. To address all of these issues I designed, assembled and tested a larger CVD system together with a high purity, inert gas mixing manifold aimed towards high-throughput synthesis of graphene samples. I automated the system to minimise operator involvement and optimised the synthesis parameters for Cu substrates in order to grow large-area monolayer graphene films. The main considerations of this work will be discussed in the remainder of this chapter.

4.3.1. Non-flammable up-scaled system design and automation

A large furnace (Carbolite CTF12/65/550) and a 6 cm fused silica tube (Robson Scientific, 180cm length) were used as the basis for the larger CVD system. The furnace was mobilised on a custom-built rail platform (parts from MG Automation Ltd); and the fused silica tube was supported by SS compression-type flanges welded to the rail platform as shown in Figure 31. The purposely built gas line utilised Swagelok compression fittings throughout and high purity manifolds (rated for gases up to 99.9999 % purity), but had the same structure as schematically shown in Figure 10a. The values of flows on the MFC (Brooks 4850) were set from the computer.

The 6 cm fused silica tube allowed larger samples of different geometry to be produced depending on the target specification: four 2" standard size wafers, or a 5 cm x 20 cm strip supported on an alumina plate or 15 cm x 20 cm Cu rolls. Compared to typical research samples (1 cm x 3 cm) this corresponds to 28x, 30x and 100x increase in graphene area.

The major difference of this system was the utilisation of MSDS non-flammable and non-explosive gas mixtures. For H_2 in Ar this corresponds to <2.93 %, while for CH_4 in Ar the value is <9.1 %. However, Vlassiouk *et al* (2013)[197] reported that only 30-100 ppm CH_4 concentration was needed for non-flammable systems. Therefore, two gas mixtures of 2.5 % H_2 in Ar and 250 ppm

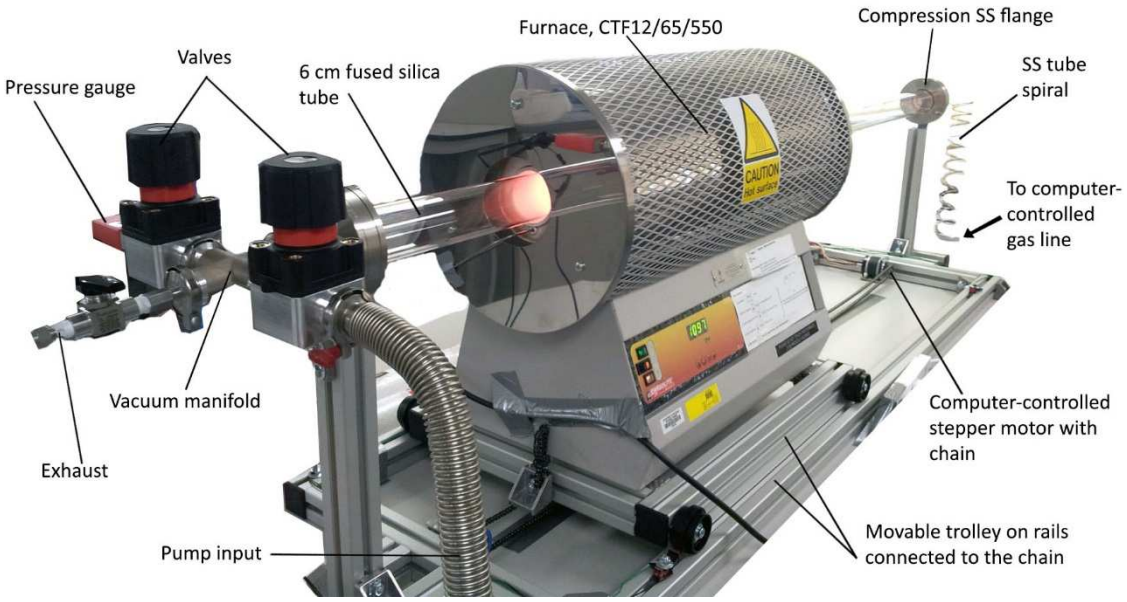

Figure 31. Up-scaled and automated CVD system with main components labelled.

CH_4 in Ar were chosen, giving the H_2:CH_4 ratio of 100 for 1 to 1 flow. The choice of gases meant that even if the system was opened during a synthesis experiment it would not cause a safety hazard. The gas mixture controller (Brooks 0254) was connected to a computer running Matlab via an RS-232 port. Additionally, the furnace was moved by a stepper motor that was also connected to the computer via a StepperBee+ board that consisted of a microcontroller with a stepper motor drive. Computer automation allowed the construction of custom recipes for graphene synthesis where the operator only needed to place the sample into the CVD system and switch on the furnace. Parameters such as experimental timing and sample cooling rates were much more precisely controlled, eliminating human errors. More information about the automation devices and software is given in appendix 9-A.

4.3.2. Gas line impurity analysis

It is commonly known that oxygen and moisture rapidly react with carbonaceous deposits at high temperature, for example, in char[198] the relative etching rates of O_2:H_2O:CO_2:H_2 are 20000:250:10:1 (adapted from the activation energy values). Such striking influence means that

if O_2 impurity in the system (2.5 % Ar/H_2 mixture) is ~1 ppm, it could still be profoundly influencing graphene synthesis (evaluated later in the text), supported by studies[199] where minute oxygen impurities damaged graphene during cooling. When defining specifications of a CVD system for 2D material synthesis it is necessary to know the level of O_2 and H_2O impurities. I utilised mass spectrometry (section 3.3.3) to measure O_2 and H_2O level in the non-flammable CVD system, where the MS probe was inserted deep inside the silica reaction tube from the rear end and the insertion point was loosely sealed to allow overpressure inside the tube. Three gases were measured, Ar (99.999 %), Ar (99.999 %) balanced with 2.5% H_2 (99.995 %) and Ar (99.999 %) balanced with 250 ppm CH_4 (99.995 %). An industrial O_2 and H_2O filter (Entegris CE2500KFH), capable of achieving < 1 ppb impurity level, was used to calibrate the background reading in the MS. The procedure for obtaining the ppm values of impurities relied on the mole fraction of Ar-38 and Ar-36 isotopes, which are known to appear in concentration of 633 ppm and 3365 ppm respectively[200] in Ar gas. Therefore, the counts of O_2 (m/z=16) and H_2O (m/z=32) from the MS measurement were divided by the counts of Ar-38 (m/z=36) and Ar-36 (m/z=38), followed by multiplying by their respective ppm concentrations.

In the measurement, the gases were routed through and around the filter while levels of O_2 and H_2O were recorded. Two sources of impurities were identified: 1) a constant source of impurity in the gas cylinder, 2) a slowly decaying source of impurities from adsorbed O_2 and H_2O inside the system. The former could be measured by comparing the change in impurity level between filtered and unfiltered gases (an assumption was made that filtered impurity was negligible). While, the latter could be quantified by estimating the initial background level and its rate of decay. The background of the O_2 and H_2O measurement started at 4 ppm and 720 ppm respectively and slowly decreased with time at 0.5 ppm $hour^{-1}$ and 15 ppm $hour^{-1}$ respectively. The decaying profiles were normalised (linearly) to keep the background constant and the resulting measurements are shown in Figure 32 (e.g. the difference in O_2 level between filtered and unfiltered Ar gas is ~0.5 ppm). Results from all the measurements are presented in Table 5.

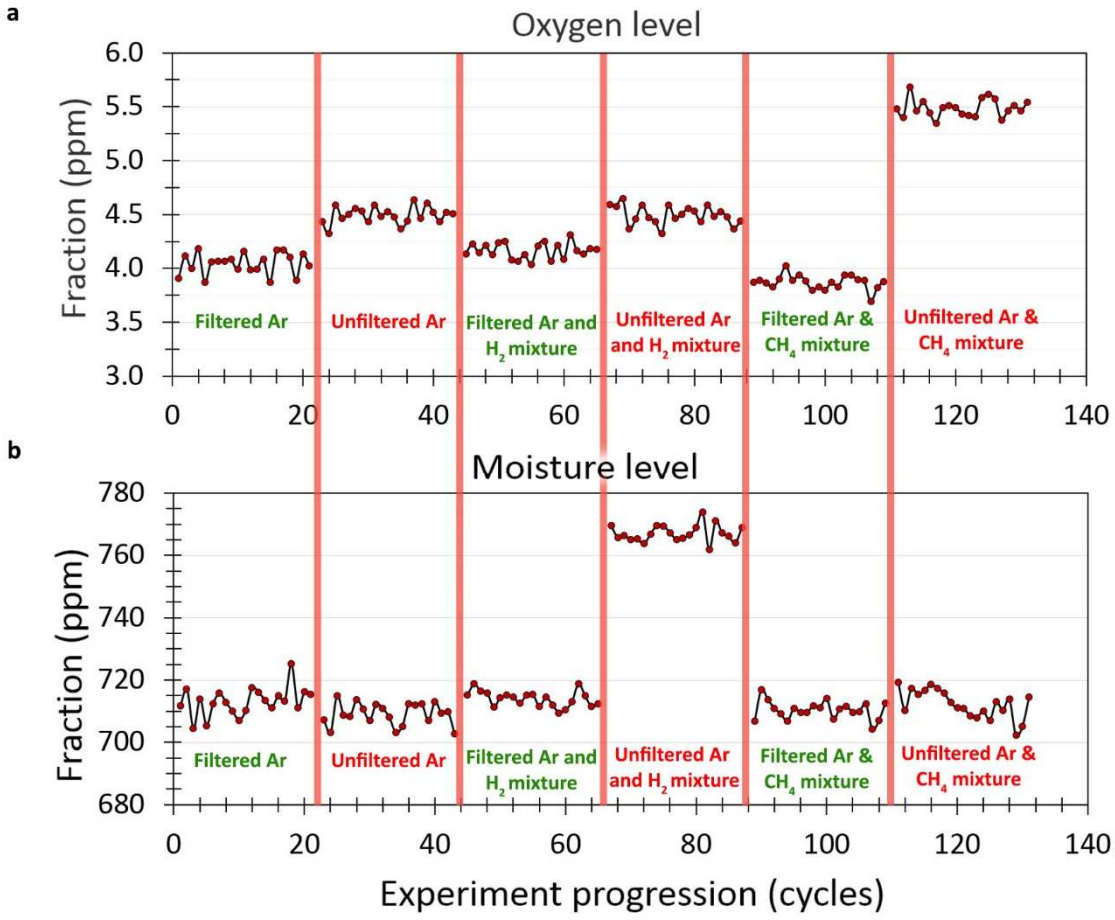

Figure 32. Impurity measurement in the fused silica tube of the large, non-flammable CVD system with MS. Both measurements had approximately linearly decreasing baseline with time due to impurity desorption which was normalised to a constant as explained in the main text. a) The oxygen level measurement depending on the gas mixture and filtering. b) The moisture level depending on the gas mixture and filtering. Ppm values were calibrated from the known Ar isotope abundances.

Gas	O_2 in gas (ppm)	O_2 background (ppm)	O_2 background decay rate (ppm hour^{-1})	H_2O in gas (ppm)	H_2O background (ppm)	H_2O background decay rate (ppm hour^{-1})
Ar	0.5	4	0.5	<10	720	15
Ar/CH_4	1.5			<10		
Ar/H_2	0.5			50		

Table 5. Measured approximate oxygen and water impurity in gas mixtures.

Water level in Ar and Ar/CH_4 gases was difficult to measure due to a very high background (~720 ppm), and it was assumed to be less than the noise level (<10 ppm). Surprisingly, water level in the Ar/H_2 gas mixture was higher at 50 ppm.

Although O_2 was fastest etching impurity, presence of H_2 inside the CVD system at high temperatures meant that O_2 was converted to H_2O and that the 20000:1 carbon etching rate was not realised, also supported by recent studies[201]. The more crucial influence on CVD synthesis came from water. For example, if the relative etching rate of H_2O to H_2 is around 250:1, only 100 ppm of H_2O is needed to have influences comparable to H_2. This may be one of the reasons why systems utilising non-flammable mixtures of gases have very different H_2 to CH_4 gas flow ratios.

To summarise, the recorded measurements show that methods are needed to keep the system free from atmospheric contaminants, which are the highest contributors to the O_2 and H_2O readings. As a consequence I kept the system under high vacuum (3 mTorr) in between experiments and used suitable purging procedures as described in section 2.1.1. The values can be used for definitive comparison to other CVD system in future studies and are important to set industrial apparatus standards.

4.3.3. Procedure and synthesis parameter optimisation for large area, monolayer, uniforms graphene films

Procedure considerations

While the synthesis parameter trends on Cu matched well with other pristine metals that I investigated (sections 4.1, 4.2), the absolute values of the H_2:CH_4 ratio were considerably different to those used in the CVD system with pure H_2 and CH_4 gases. At 1050 °C with pure H_2, CH_4 gases, the ratio was around 80, while for the system with 250 ppm CH_4 and 2.5 % H_2 mixtures

in Ar it was 2300. In addition to the previously mentioned up-scaling consideration, a study by Vlassiouk *et al* (2013)[197] identified a number of additional factors that could affect an industrially-sized CVD system, in particular, the following:

- avoiding low pressure that causes Cu evaporation and safety concerns; cleaning procedure to remove surface contaminants on the substrate;
- polishing methods to smoothen the surface;
- varying H_2:CH_4 composition with time during synthesis to avoid non-uniform growth along the sample due to precursor exhaustion along the length of the sample;
- sample cooling;
- crystallographic orientations of Cu foils.

I compared my up-scaled system and procedure to the one reported by Vlassiouk *et al* (2013)[197] in Table 6. The system dimensions were very different, however, the flow speed (a derived parameter calculated from the flow rate in $cm^3\,min^{-1}$ divided by the inner area of the fused silica tube in cm^3), annealing time and synthesis times were very close, allowing better evaluation. The difference in the H_2:CH_4 ratio can be explained by the difference in the synthesis temperature: at lower temperatures the H_2:CH_4 ratio has to be lowered to increase the growth rate of graphene deposits. Because the furnace utilised by Vlassiouk *et al* (2013)[197] was not movable, the substrate had to be cooled for prolonged periods of time (12 hours) under inert atmosphere until the system could be opened to avoid oxidation of the material. Additionally, in the study the sample was loaded in a "rolled" geometry (Figure 33a) with length of 90 cm and 15 cm in diameter which required rigid, thicker and thus more expensive Cu foil (125 µm). These two factors considerably increased the material production cost, which partially negated the cost savings due to the large scale of production. For comparison, I utilised an alumina plate holder (Figure 33b) to easily load thinner Cu foils (25 µm) and a movable furnace to quench the sample. Such system allowed fast production of medium-sized batches of graphene on Cu

Parameter	Vlassiouk *et al* (2013)[197]	My study
Cleaning	Acetone/IPA, $FeCl_3$/HCl, H_2O	Acetone/acetic acid/H_2O
Polishing	Electropolishing, H_3PO_4 (85 % in H_2O)	Electropolishing, H_2O:ethanol:H_3PO_4, 100 mL : 100 mL : 500 mL
Temperature	1000 °C	1050 °C
Flow speed	27 cm/min	21 cm/min
Annealing time	1 hour	1 hour
Total synthesis	3 hours	3.67 hours
H_2:CH_4 ratio steps with time	833/45 mins, 500/45 mins, 357/45 mins, 250/45 mins 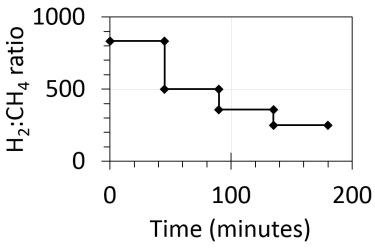	2500/30mins, 2416/30mins, 2359/20mins, 2304/20mins, 2252/20mins, 2203/20mins, 2174/30 mins, 2083/20 mins, 2000/20 mins 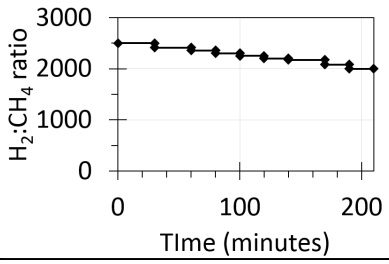
Cooling rate	1.4 °C/min	100 °C/min
Cooling time	720 mins	5 mins
Total time	16 hours	5 hours
Approximate consumables per cm^2 of graphene	£0.05	£0.08
System cost and maintenance	High	Low

Table 6. A comparison of the industrial CVD system by Vlassiouk *et al* (2013)[197] and my CVD system, with exemplar synthesis parameters.

that was still costs effective. Additionally, the overall cost of the CVD system was lower. In future work it would be beneficial to combine the very large scale synthesis with the fast turnaround modifications that I developed to allow even higher savings in consumables, energy and time.

Cleaning and polishing

During the procedure optimisation, I utilised standard cleaning methods for Cu foil: sonication in acetone to de-grease the surface, followed by sonication in acetic acid to remove surface oxides and particulate impurities. Acetic acid is an organic acid and cannot introduce unwanted

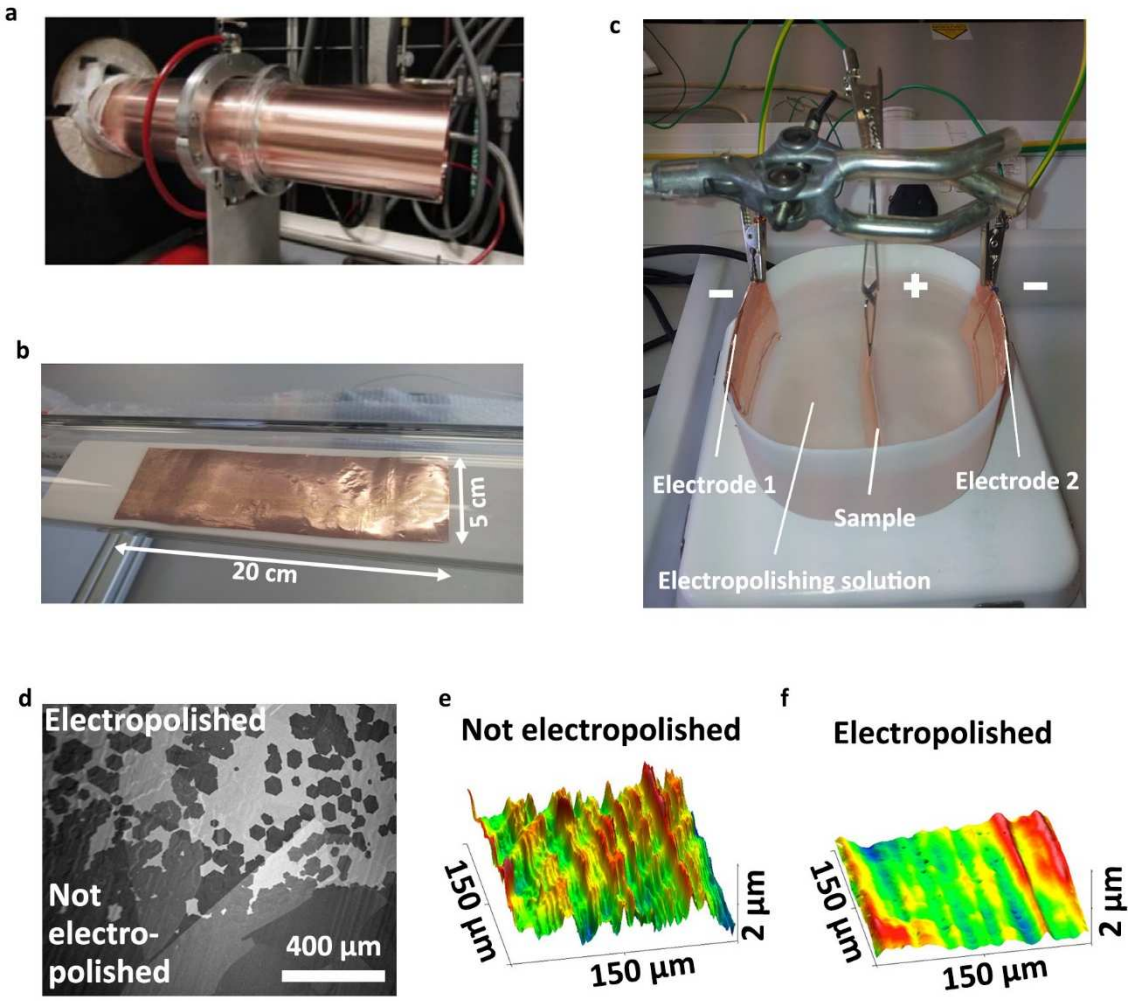

Figure 33. Sample processing considerations in the up-scaled CVD system for graphene synthesis. a) Rolled Cu sample loading by Vlassiouk *et al* (2013)[197] that allows to increase the substrate area, but is difficult to use with thinner Cu foils. b) Flat substrate loading on an alumina plate support in my CVD system that is more convenient to handle. c) A three electrode electropolishing apparatus (the sample of Cu foil is in the middle). d) Difference in graphene coverage on electropolished and not electropolished regions; the latter exhibits a much higher nucleation density due to roughness. e-f) Optical profile measurement of not electropolished and electropolished Cu surfaces. While rolling lines are visible on both samples, the electropolished surface is much smoother locally. RMS roughness is 200 nm and 50 nm respectively.

inorganic contamination on the surface (for comparison $FeCl_3$ or HCl can leave significant chlorine contamination of up to 3 % on Cu surface[197]). While important, cleaning methods did not seem to influence graphene growth significantly, apart from reducing the number of contamination particles; likely because the follow-on annealing in H_2 at high temperatures had the same effect as cleaning. On the other hand, surface polishing had a profound effect on graphene coverage on Cu foils as shown in Figure 33d. Microscopic roughness caused very high

nucleation density on not electropolished Cu regions. In order to decrease the nucleation density and therefore to increase graphene domain sizes constituting the film electropolishing was necessary. A simple apparatus, shown in Figure 33c, was utilised consisting of two negative electrodes to improve the uniformity of electropolishing. Two electropolishing solutions were investigated:

1) A low molarity H_3PO_4 solution consisting of deionised water, ethanol, H_3PO_4, isopropyl alcohol and urea in the following combination: 200 mL, 100 mL, 100 mL, 20 mL and 2 g respectively as outlined by Zhang *et al* (2012)[202].
2) A high molarity H_3PO_4 solution consisting of H_3PO_4, deionised water and ethanol in the following combination: 500 mL, 100 mL, 100 mL respectively; adapted from Vlassiouk *et al* (2012)[197].

Both solutions smoothed the surface compared to that without electropolishing, however, solution 1 often resulted in optically noticeable residue and was not acceptably uniform. Solution 2, on the other hand, could be fully removed with deionised water and gave good uniformity. It was found that the solution (2) could also be re-used for a number of experiments (up to 20). Current density was set high at around 0.05 A cm^{-2} for 5 minutes, which was necessary to reduce the high "rolling lines" on the Cu foil (Alfa Aesar, annealed, uncoated, 99.8 % purity) that had been introduced during the foil manufacturing process. Optical profilometry was used to assess the roughness of not electropolished and electropolished Cu foils (Figure 33e,f). Not electropolished foils exhibited RMS roughness of around 200 nm, while for electropolished foils the value was much lower at around 50 nm. This processing was adopted to achieve low graphene nucleation density and therefore produce films with large graphene single crystal domains sizes of around 100 μm.

Synthesis parameter optimisation

During synthesis parameter optimisation I looked at the influence of the H_2:CH_4 ratio for a set temperature (1050 °C), which was chosen not too close to the melting point of Cu, 1085 °C, but also, not too low to improve the growth rate. At 1050 °C the H_2:CH_4 ratio of 1540 resulted in full coverage with about 25 % of the surface being bilayer graphene flakes (Figure 34a). A ratio of 1700 resulted in 16 % bilayer coverage. Increasing the ratio further to 2090 resulted in only 5 % bilayer coverage and finally, a ratio of 2300 resulted in < 0.1 % bilayer coverage. With the latter ratio, prolonged synthesis times of more than 3 hours still only partially covered the substrate as shown in Figure 34b; individual hexagonal domains were present. Most likely a self-limited regime was reached, where the catalytic Cu surface area was reduced so much by the graphene coverage that the growth rate became far too low. This process is shown schematically in Figure 34d. To counter the reduction in the available catalytic area, the ratio of H_2 to CH_4 needed to decrease with time to stimulate graphene growth rate, while preventing the formation of multilayers. I found that continuous decrease in the ratio by 20 % over 3 hours was sufficient to achieve predominantly monolayer, full coverage graphene film (Figure 34c, table 6).

An additional consideration for decreasing the H_2 to CH_4 ratio with time, fundamentally different to the reduction in the catalytic Cu surface area, is precursor exhaustion with distance for extended substrates. This effect is depicted in Figure 34e and played a major role in the study by Vlassiouk *et al* (2013)[197] for the 90 cm long samples, where the ratio had to be non-linearly decreased by 330 % over the period of 3 hours (table 6). Without this adjustment completely different graphene types could form across the substrate: from multilayer graphene near the inlet to small individual domains near the outlet. In my experiments, there was no noticeable non-uniformity along the sample, which meant that for substrates with dimensions of < 20 cm were not in the regime where this effect was important. Raman spectra, separated by large distances (4 cm) were recorded directly on Cu to confirm that there was little variation across

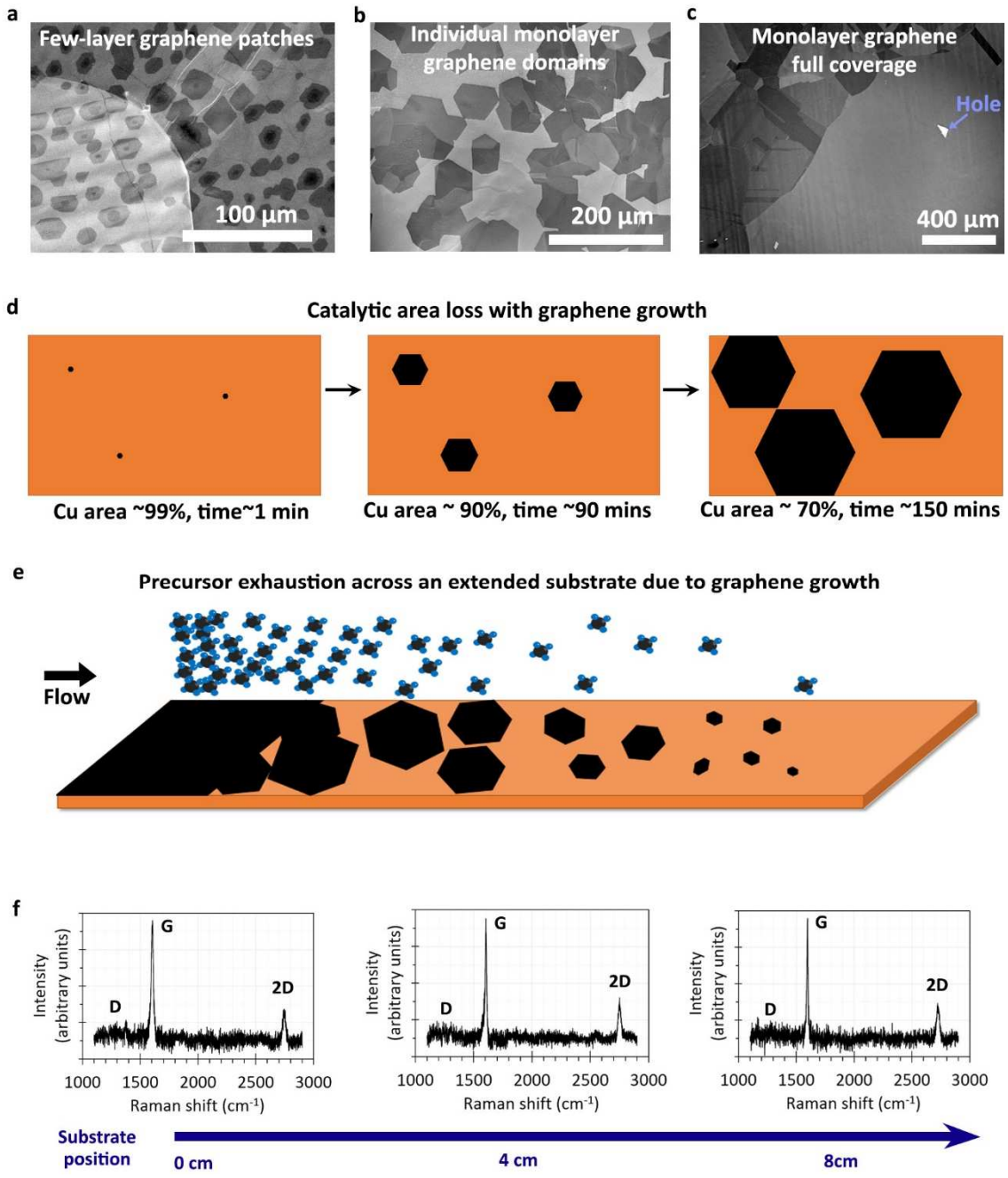

Figure 34. Synthesis parameter optimisation. a) A SEM micrograph of full coverage graphene with many bilayer and multilayer regions on Cu when the synthesis parameters were not balanced for monolayer graphene growth. b) Individual graphene flakes before coalescing. Domain sizes of 100 µm were commonly achieved on electropolished, large size samples. c) 99 % coverage, predominantly monolayer film consisting of large graphene domains was achieved after the synthesis parameter optimisation, as shown, which was the target material. d) A diagram showing how the catalytic Cu surface area can decrease with time as graphene domains increase in size, resulting in self-limited growth and incomplete coverage. e) A diagram of non-uniform graphene coverage due to precursor exhaustion over an extended substrate. f) Raman spectra of a large graphene sample recorded directly on Cu substrate showing consistent film quality across 8 cm distance. The D-peak is indistinguishable from noise, indicating low defect density. Raman background from Cu substrate was subtracted. (Please note, directly on Cu with a 532 nm laser wavelength, the ratio of the 2D to G peaks cannot be used for determining the number of layers[203]; monolayer graphene was confirmed by Raman spectroscopy after being transferred to a Si/SiO_2 substrate).

the foil in graphene coverage on the larger scale (Figure 34f). The 2D and G peaks had consistent intensity, while the D peaks was below noise level, indicating uniform, defect-free graphene. It must be noted that in order to extract useful information from Raman spectra directly on Cu, such as the ratio of 2D to G peaks, the excitation laser wavelength needs to be in the UV region[203], which was not available. However, after the transfer to a SiO_2/Si substrate, the obtained Raman spectrum was similar to that shown in Figure 29a, with 2D to G peaks ratio of 2.

In conclusion, an up-scaled CVD system and procedure were developed for the large-area synthesis of monolayer graphene with complete reproducibility and fast samples turnaround.

4.3.4. Ultra-flat graphene transfer for the Surface Force Balance measurements

Ultra-flat transfer method

In order to understand a number of important fundamental properties of graphene and other 2D materials, such as the surface energy, strength of interaction between the layers or heterostructures and influences of the surrounding medium on these values, it is necessary to be able to prepare large area surfaces of clean, smooth graphene and other 2D materials. Towards this purpose an "ultra-flat" transfer method has been developed and optimised recently in my group[204], where I assisted with SEM characterisation and synthesised single layer graphene films, as described in previous chapter, for transfer optimisation and measurements. The transfer is a specialised modification of the procedure described in section 3.1, shown schematically in Figure 35a (for the target substrate of specially prepared quartz lenses). The key difference is the intermediate step of templating the graphene/PMMA stack on top of freshly cleaved mica, an atomically flat, defect and contamination-free substrate. Additionally, the side of graphene in contact with PMMA is placed on the target substrate after PMMA has been dissolved, effectively turning the stack upside-down. Finally, the mica template is removed from

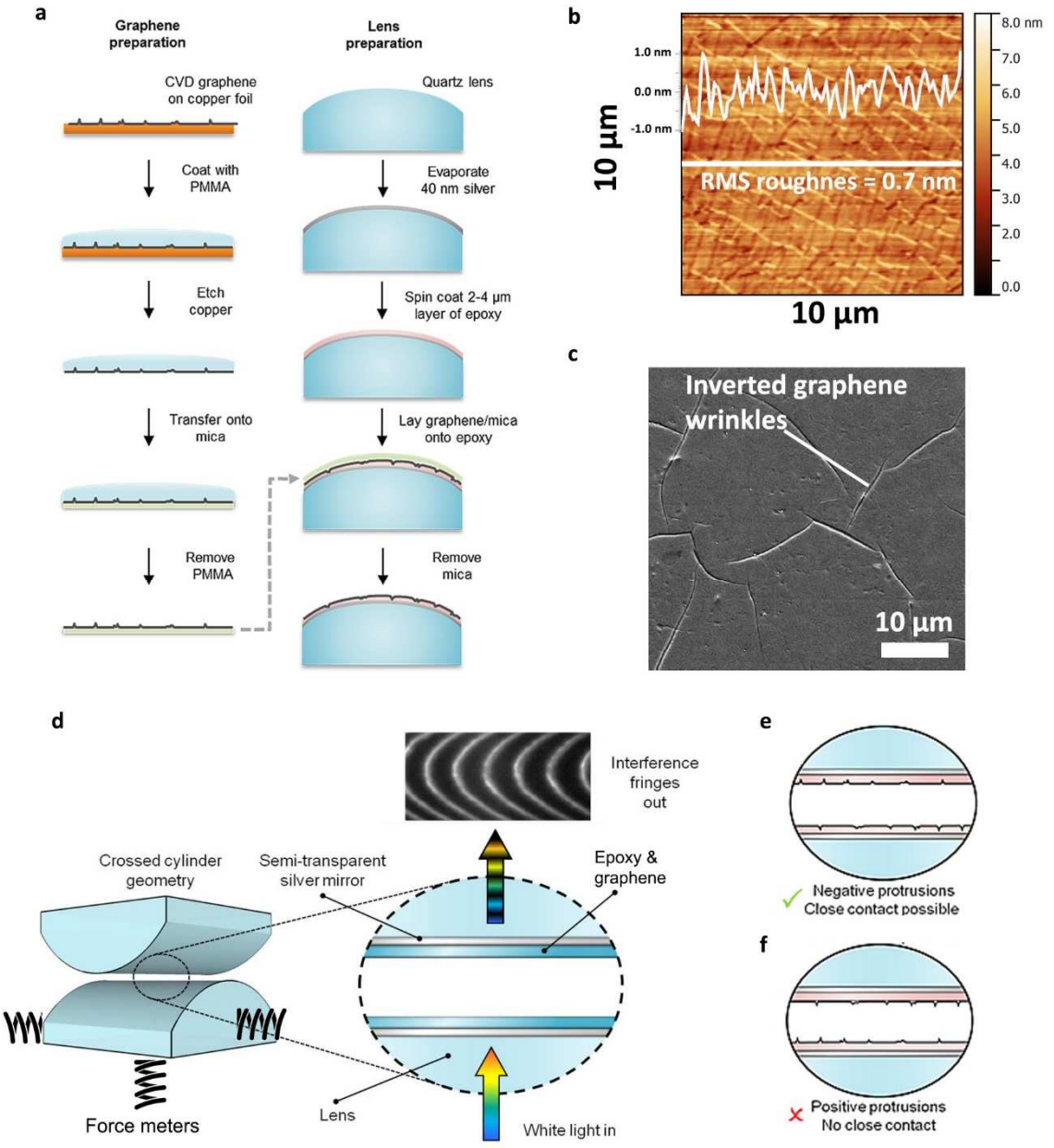

Figure 35. Ultra-flat graphene transfer and the SFB apparatus. a) Procedure steps for the transfer to quartz lenses utilised in the surface force balance apparatus. Diagram credit ref. 204. b) An AFM scan of 10 µm x 10 µm of single layer graphene transferred to an epoxy-coated quartz lens using the ultra-flat technique, exhibiting very low surface roughness of < 0.7 nm. Data recorded by Christian van Engers. c) A SEM micrograph of graphene transferred to a glass slide with the ultra-flat technique showing inverted wrinkles. d) A schematic diagram of the graphene surface force balance apparatus, showing main components, including lens' geometry and materials transferred onto the lens' surface. An example of fringes produced by the apparatus from white light is shown. Diagram adapted from ref. 204. e-f) Schematics of graphene surface transferred with the ultra-flat methods and normal method respectively. The latter is not suitable for the surface force balance measurements due to positive protrusions that get in the way of moving the surfaces closer together.

graphene resulting in very low roughness. An AFM scan of single layer graphene directly on the SFB lens is shown in Figure 35b, with an RMS roughness of 0.7 nm (of the shown linear profile). The resulting surface is very clean because it was only exposed to a highly soluble salt solution (ammonium persulfate) that was effectively removed with deionised water, followed by contact with freshly cleaved mica surface. Because of flattening of wrinkles on top of mica the surface only has negative protrusions (Figure 35c) which do not significantly affect average surface interaction measurements over large areas.

The Graphene Surface Force Balance

SFB is a technique where the normal and lateral forces between two surfaces are measured as a function of the separation between the surfaces. White light interferometry between two silver-coated lenses is used to measure the distances, with resolution down to 0.1 nm. The geometry of the lenses is semi-cylindrical as shown in Figure 35d, allowing a small contact spot with geometry related to two parallel plates. The measurement is therefore an area average over the contact spot. For the **graphene** surface force balance the material is transferred using the ultra-flat transfer technique to cover the surface of the lenses. This technique is particularly suited for this apparatus because it does not produce positive protrusions which would get in the way of achieving very small distances between the surfaces (Figure 35e,f). Measurements using the apparatus, performed by Christian van Engers, successfully utilised large area monolayer graphene films and showed that the cleanliness of the transfer, the low roughness and the quality of the films was suitable to measure the surface energy between two graphene sheets. The surface energy of monolayer graphene in air was 255 ± 4 mJ m^{-2}, while the value in an aqueous solution of sodium cholate was 57 ± 12 mJ m^{-2}. This insight, for example, allows to understand what happens to graphene when it is dried from a solution: layers are prone to re-stack together. This preliminary result is important for the graphene foam investigation discussed in chapter 7, where it was difficult to dry porous graphene foam materials without a

significant collapse in the structure. Additionally, the graphene SFB opens up many exciting possibilities for novel surface electrochemistry measurements between two conductive sheets where the solution can be confined in a very small volume, which is useful to understand processes such as lubrication or electrochemical energy storage[204].

4.4. Summary

In this study I mapped the CVD parameter space on pristine Pt and optimised the synthesis towards large area monolayer graphene synthesis, which was thoroughly characterised. A related investigation was conducted on Pd. It was found that graphene domain shape on these substrates is irregular, unlike reported by previous studies, however, very high growth rates can be achieved, up to 50 μm min^{-1}, due to excellent catalytic ability of the substrates. Additionally, it was observed that the contact of Pt and Pd foils with the silica tube resulted in bonding and influenced graphene morphology, leading to irreproducibility (explored in more detail in chapter 5). This example shows that the components of CVD systems are not as inert as they are perceived and can be a source of unknown contamination.

Graphene synthesis on Cu showed hexagonal monolayer graphene domains, but only with very low growth rates of around 1 μm min^{-1}. Nevertheless, due to the low costs of this substrate it was useful to study for higher-throughput graphene synthesis. Improved control methods were developed for the larger CVD system, including automation. Measurements of O_2 and H_2O impurities with MS in the gases and adsorbed to the connection determined that these cannot be ignored, but must be monitored and stated to allow a better comparison between CVD studies. The synthesis was substantially up-scaled using inert gas mixtures where methods were developed to address a number of important issues with the large-size sample fabrication: temporal variation of the precursor composition, polishing of the substrate and loading of the sample. The resulting material was utilised to develop an ultra-flat transfer method for measurements of fundamental interactions between surfaces in the graphene surface force balance or to investigate novel surface electrochemistry in future work.

Chapter 5. Silicidation, a novel substrate engineering technique*

In chapter 4 I established that large-area synthesis of high quality, single crystal, monolayer graphene by CVD is possible on solid Cu, but requires polishing or substrate grain enlargement followed by a lengthy growth period due to the low catalytic ability of Cu. With unmodified commercially available polycrystalline Cu the achievable flake size is limited to only tens of micrometres[205]. It is also very difficult to attain uniformity in the size and shape of graphene flakes within a sample on solid substrates due to the presence of grains and grain boundaries. I also found that pristine Pt and Pd substrates could not form single crystal graphene domains contrary to the previous study by Gao *et al* (2012)[144], most likely due to the very large lattice mismatch; but exhibited fast growth rates. Generally, when a solid substrate is used with APCVD, graphene growth is strongly influenced by the crystallographic lattice of the substrate, its defects, roughness and grain boundaries and has been explored by a number of studies[206-209]. Consequently, graphene films grown on solid polycrystalline metals often consist of small, irregular sized domains with many high-angle domain boundaries, which degrade the quality of graphene[210]. Domain boundaries between graphene crystals form linear defects comprising alternating 5- and 7- carbon rings which can scatter electrons and phonons leading to worsened properties. Therefore, good crystallinity is an important quality factor for CVD-grown graphene, as it offers superior electronic and tensile properties, chemical resistivity and impermeability[210]. Millimetre-sized single-crystal graphene flakes have been recently synthesised on solid Cu[113]. The syntheses times lasted tens of hours and significant quantities of source materials were required. Finding ways to dramatically improve the growth rate, while retaining good crystallinity is very important for commercial production of graphene and other 2D materials.

An alternative approach, investigated by other studies[193], has shown that CVD on liquid Cu generates aligned and undistorted hexagonal graphene flakes of regular size distribution of 20-30 μm with a growth rate of about 1 μm min^{-1}. When these flakes coalesce they often have good

* A patent related to this work was filed on 01/08/2014. Application number GB1413701.2.

crystallinity and low-angle grain boundaries. However, there is little control of the nucleation and the size of such flakes. The method is also difficult to up-scale due to the liquidity or droplet formation and cannot be applied to Pt and Pd due to the very high melting temperature.

In this chapter I demonstrate a novel and up-scalable substrate processing method to achieve super-fast growth rate of graphene and significantly improve its crystallinity by using widely available, solid polycrystalline metallic substrates in conjunction with a thin, liquid surface layer. The layer is formed by coating Pt and Pd polycrystalline metal foils with a silicon-containing film, which forms a wetting liquid silicide surface *in situ* for graphene growth over the entire substrate surface when heated. This process significantly reduces the influence of the defects, roughness and the crystallographic orientations of the substrate on the quality of graphene. Substrates covered with the film exhibit increased growth rates of up to 120 μm min^{-1} at elevated temperatures, one of the fastest reported to date. While metal alloys[211-214] and dielectric substrates[215] have been shown in CVD, such a metal – silicon eutectic system is utilised for the first time as a substrate for graphene synthesis in CVD.

5.1. Graphene on silicidated platinum

In this section, I keep the structure similar to section 4.1 to allow a better comparison between the studies on pristine and silicidated Pt. First I will describe how the substrate is prepared and the synthesis parameter trends, followed by the nucleation point analysis and graphene characterisation. Additionally, in the final parts of the section, the silicidated substrate is characterisation to reveal a possible mechanism and the synthesised graphene is tested in the QHE measurements.

5.1.1. Substrate preparation and large area graphene synthesis

To prepare the silicidated substrates for graphene synthesis, pristine Pt was used as-received from the manufacturer followed by cleaning in acetone and deionised water. A silicon-containing film was then deposited on Pt foil. Various compounds can be utilised Si, SiN, SiO and SiO_2 because Pt has high affinity for Si at high temperatures[216]. This was also hinted by two preliminary experimental observations: where Pt foil edge was in contact with the fused silica tube of the CVD system or in the vicinity of large SiO_2 particles (Figure 36a,b) the coverage was higher. Additionally, in these regions, the hexagonality of the graphene domains improved significantly compared to pristine Pt. However, these methods were not controllable resulting in excessive reaction with Pt that damaged the foil. I therefore explored more suitable ways for the SiO_2 deposition. The most convenient deposition routes were

1) thermal evaporation of pure SiO_2 powder (Testbourne, 99.999 %),
2) CVD with a tetraethyl orthosilicate (TEOS, Sigma-Aldrich, 98 %) precursor,
3) gel deposition from a TEOS solution ("sol-gel" process),
4) spin coating of a viscous TEOS/polymer solution.

Figure 36c-f show the morphology of films obtained via these methods. It must be noted that because of complete chemical reaction between Pt and SiO_2 the quality of the SiO_2 film did not

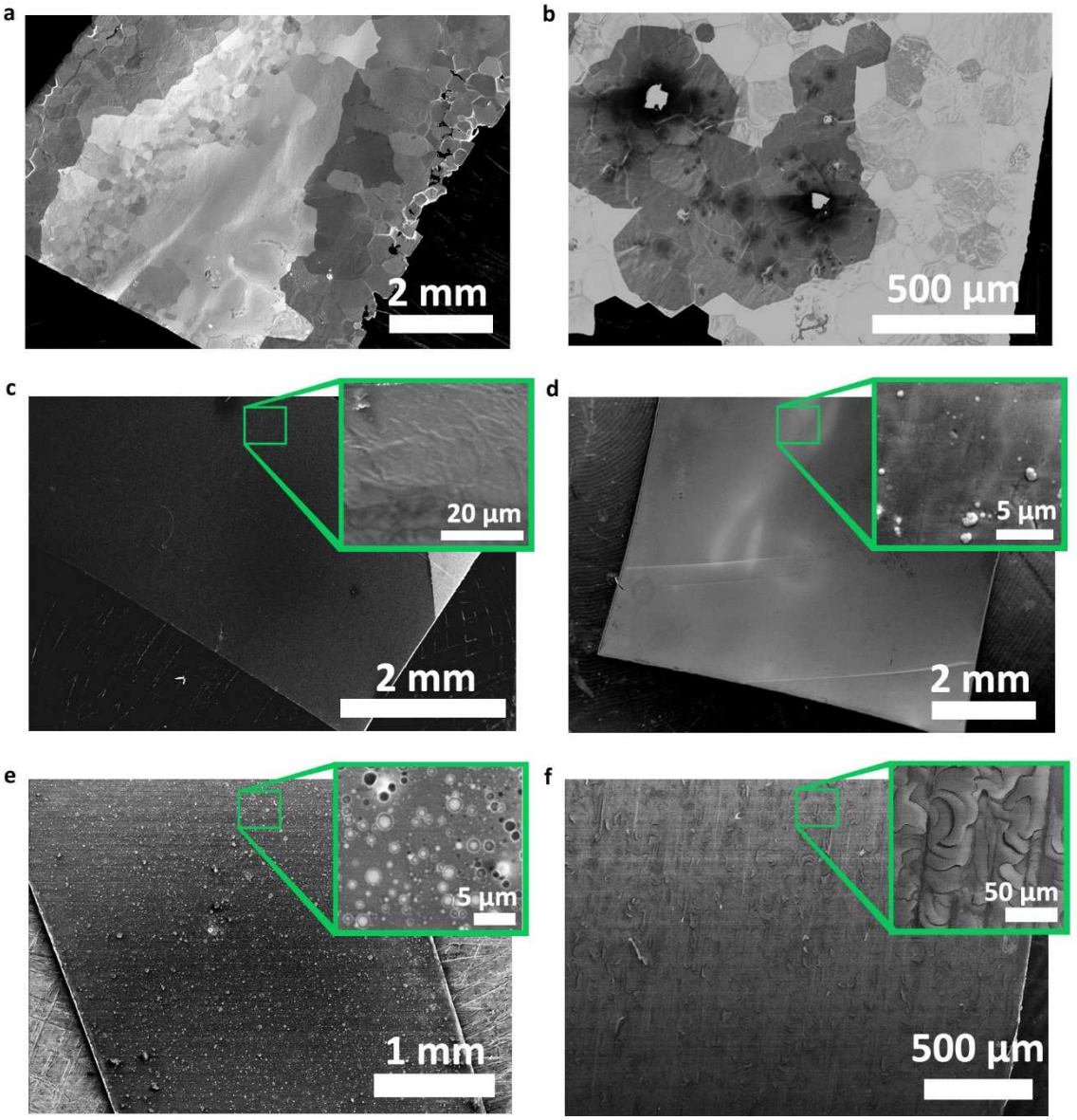

Figure 36. Silica deposition methods. a) Observation of Pt foil after contact with the fused silica tube inside the CVD system. The grains are significantly restructured, while graphene growth is strongly influenced. b) First controlled addition of SiO_2 particles showed significant influence on graphene growth in their vicinity. The growth rate and hexagonality improved. c-f) Thermal evaporation, TEOS CVD deposition, colloidal TEOS sol-gel deposition and TEOS/PMMA sol-gel spin coating methods respectively for controlled addition of uniform SiO_2 films to Pt foils. Insets show magnified morphology.

improve the effectiveness of the resulting silicidated substrate. In fact, it turned out to be the opposite. The very large difference in the thermal expansion coefficients between silica and Pt could result in the accumulation of significant thermal stress in the Pt/SiO_2 stack during annealing and subsequent curling of the foil that was detrimental to graphene films. Thermal evaporation produced very uniform SiO_2 films, however the needed film thickness (~1 µm)

meant the deposition took excessive time and energy, especially considering that the high quality of the film was not essential. The SiO_2 film deposited on pristine Pt with a CVD-based process proved fast, cheap and controllable. For example, a SiO_2 film of about 1 µm thickness could be grown with CVD by passing Ar gas (350 sccm) through a TEOS precursor in a "bubbler" that was carried to a furnace with Pt substrates heated to 700 °C for 30 minutes. TEOS sol-gel process was fast and inexpensive, but the control of the total amount of silica on the surface proved difficult due to the colloid formation of SiO_2 spheres (inset of Figure 36e). Finally, spin-coating a viscous TEOS/polymer solution resulted in interesting film morphology (Figure 36f), but the polymer solution contained a number of impurities that were left on the surface and increased the nucleation density of graphene. To summarise, the investigated silica deposition methods showed similar trends in graphene growth after the optimisation of the procedure, but CVD of TEOS was clean, fast, cheap, controllable and could be performed in a single CVD system prior to synthesis and was therefore chosen as the main deposition route.

To synthesise graphene, the Pt/SiO_2 stack was subjected to a CVD procedure that consisted of an annealing stage, a synthesis stage and a cooling stage at atmospheric pressure. The Pt/SiO_2 stack was placed on a boron nitride holder inside a fused silica tube (28 mm inner diameter) at sufficient distance from the walls of the tube. Boron nitride was used due to its stability in a reducing atmosphere and not-wetting by the silicide. The tube was then purged with Ar (99.999 % purity) and shifted into a pre-heated furnace, followed by annealing in H_2 (99.995 %, 200 sccm) to allow Pt silicide formation and to stabilise the temperature of the furnace. Upon annealing the SiO_2 layer disappeared resulting in the formation of silicidated Pt. The useful annealing time to form silicidated Pt strongly depended on the temperature and the silica thickness. For example, at 1070 °C with a 1 µm thick silica layer, 30 minutes annealing time was suitable. For comparison, at 1050 °C with a 1 µm silica film after 30 minutes, 10 % of the SiO_2 film still remained. In the experiments where reusing silicidated Pt was tested, the annealing time was shortened to 5 minutes to simply re-heat the solidified silicide.

To synthesise graphene, a mixture of CH_4 (99.5 %) and H_2 (99.995 %) was introduced. The gas ratio and the duration of the synthesis also depended greatly on the temperature and the silica layer thickness. The former trend is summarized in Figure 37a. For example, for a 1 µm thick silica layer at 1070 °C the flow rates were set to 4 sccm CH_4 and 600 sccm H_2 for 20 minutes, resulting in approximately 0.5 mm sized graphene flakes. Directly after this step, the furnace was shifted from the substrates to quench graphene growth and later purged with Ar.

Similarly to pristine metals, a compromise had to be made between the length of an experiment versus the size and quality of graphene domains because the ratio of H_2 to CH_4 needed to be kept high[125] in order to bias the CVD reaction towards single crystal, monolayer graphene growth. For example, at a temperature of 1070 °C with a H_2:CH_4 ratio of 200:1, no growth could be observed after 30 minutes on silicidated Pt. A ratio of 160:1 at the same conditions resulted

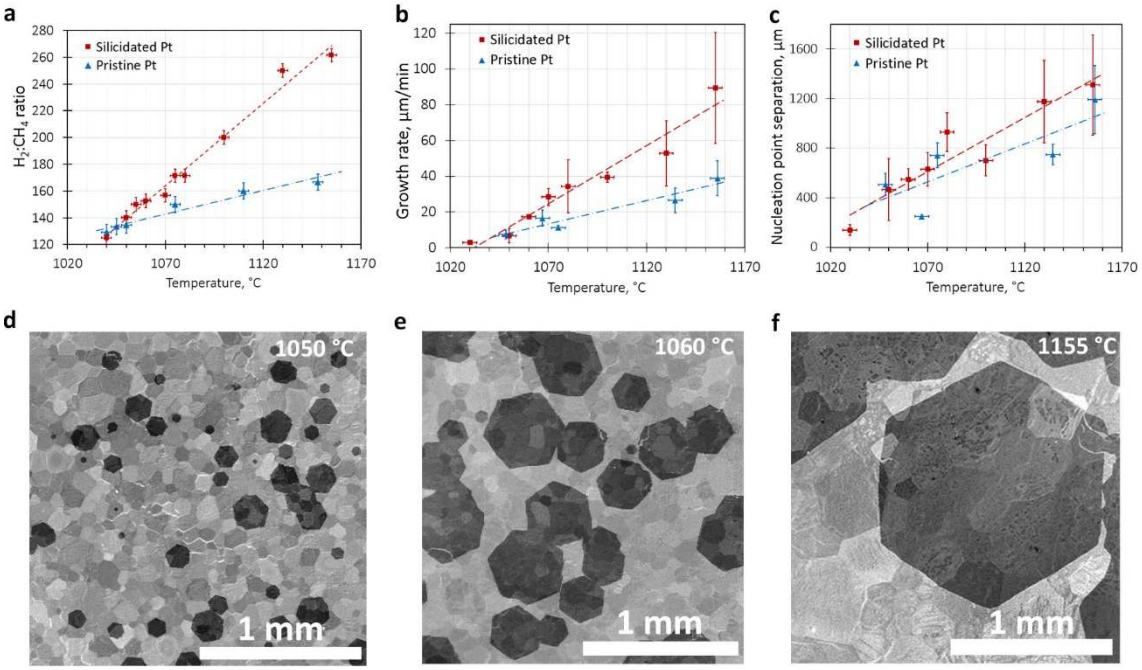

Figure 37. Graphene synthesis on silicidated Pt exhibiting single crystal, hexagonal graphene domains. a) The difference in the synthesis parameters for un-coalesced graphene flakes on silicidated and pristine Pt. Pristine Pt resulted in irregular-sized flakes, while silicidated Pt resulted in hexagonal flakes. Total flow was kept at around 500 sccm, and synthesis time of 30 minutes was used. b-c) The growth rate and the nucleation point separation as functions of temperature. These two parameters determine the overall size of graphene flakes. Values for irregularly-shaped graphene grown on pristine Pt are shown for comparison. d-f) SEM micrographs of graphene domains at different temperatures on the mm-scale showing a significant improvement in the domain size.

in the slow formation of high quality monolayer graphene, while rapid formation of multilayer graphene occurred at a H_2:CH_4 ratio of 100:1.

The ratio of H_2 to CH_4 on silicidated Pt compared to pristine Pt had to be increased by as much as 50 % (1150 °C) to reduce the carbon deposition and achieve flakes of comparable size to those on pristine Pt. The comparison of the synthesis parameters on pristine and silicidated Pt is presented in Figure 37a. This trend meant that the quality of graphene flakes improved on silicidated Pt without sacrificing the short experimental time. The difference in the kinetics for graphene nucleation and growth on pristine and silicidated Pt could be tentatively proposed as the cause for the observed difference. Studies show that the bond strength of Si-C (~318 kJ per mol[217]) is higher than of Pt-C (~225 kJ per mol[218]), but still lower than the graphene bond (≳400 kJ per mol[133]) presenting a "stickier" silicide surface. This suggests that the associated dwell time of carbon atoms on the silicidated surface could be prolonged, leading to the observed increase in the growth rate. The dependence of the growth rate as a function of temperature for silicidated and pristine Pt substrates is shown in Figure 37b, showing a significant difference between the two substrates. The maximum achievable growth rate value of 120 μm min^{-1} is one of the highest reported to date.

Similar to previous studies[142] on Cu, where the nucleation density of the domains decreased with higher temperatures, the nucleation density also decreased on Pt. The nucleation point separation (S), related to the nucleation density as $\pi^{-1}(S/2)^{-2}$, is shown in Figure 37c. The difference in this quantity between pristine Pt and silicidated Pt is not as significant as the difference in the growth rate, yet it is still noticeable. The domain sizes of hexagonal or irregularly-shaped graphene grown on Cu, pristine Pt and silicidated Pt are comparatively related as follows

$$\text{Cu (1050 °C)} < \text{Pt (1050 °C)} < \text{Pt (1150 °C)} < \text{silicidated Pt (1150 °C)}. \quad (27)$$

Figure 37d-f depict the improvement in the overall size of the flakes on the mm-scale that can

be obtained with higher temperature on silicidated Pt. While graphene on pristine Pt showed similar trends, only smaller, polycrystalline flakes of irregular shape were observed throughout the CVD parameter space. Interestingly, the high melting point of Pt allowed me to probe temperatures above 1100 °C for the first time for graphene synthesis with CVD, at which single crystal graphene flakes of up to 1.8 mm were obtained in 15 minutes on silicidated Pt. For comparison, the window of useful H_2 to CH_4 ratios on Cu is usually such that synthesis would need to be conducted for 17 hours[141] in order to grow a graphene crystal of the same size.

5.1.2. Nucleation point analysis

Complimentary to the analysis of nucleation sites on pristine Pt (section 4.1.2) the same analysis was performed for silicidated Pt. Nucleation sites on grain boundaries, particles and silicidated Pt domains were counted and are summarised in table 7. This table can be directly compared to Table 4 for pristine Pt. Again, if nucleation occurred completely randomly and grain boundaries were not influencing the number of nucleation sites then the contribution from grain boundaries should be less than 10 % by considering the relative approximate areas of Pt grains to grain boundaries (~10000 μm^2 and ~700 μm^2 respectively). On silicidated Pt the grain boundaries seem to be enlarged. Nevertheless, the results suggest that the influence of silicidated grain boundaries on the number of nucleation points is considerably reduced compared to pristine platinum. The most significant difference, however, is the low nucleation number on contaminant particles (1 % vs. 25 %) and therefore high homogeneous nucleation (84 % vs. 55 %), while the fraction of nucleation sites on grain boundaries remained very similar (16 % vs. 20 %). A possible explanation for this is the liquid nature of the silicide that facilitates the dissolution of contamination particles in the surface to form ternary and higher eutectic compounds. For example, alumina (Al_2O_3) can react with Pt silicide to form a liquid Pt aluminide and silicide alloy[216]. Reduction in contamination particles leads to lower nucleation density and

#	Substrate	Total number of flakes	Flakes nucleated on Pt grains	Flakes nucleated on grain boundaries	Flakes nucleated on contamination particles
1	Silicidated Pt	44	36 (82 %)	7 (16 %)	1 (2 %)
2	Silicidated Pt	22	18 (82 %)	4 (18 %)	0 (0 %)
3	Silicidated Pt	30	26 (87 %)	4 (13 %)	0 (0 %)
	Average %		**84(±3) %**	**16(±3) %**	**1(±1) %**

Table 7. Nucleation point analysis on silicidated Pt.

can explain the trend observed in Figure 37c: there is a small, but noticeable difference. This difference is likely not because of a change in the surface chemistry or synthesis reactions, but due to fewer nucleation sites from contaminants.

5.1.3. Graphene characterisation

Graphene characterisation techniques similar to those for pristine Pt (section 4.1.2) were employed for graphene on silicidated Pt, allowing a direct comparison. Size, shape, crystallinity, number of layers and electronics properties were assessed. It was established in section 4.1.2 and elsewhere[144] that the irregularly-sized graphene flakes on pristine Pt had numerous domain boundaries along reflex angles and the edge morphology varied from one Pt grain to another. On the other hand, the hexagonal graphene flakes of millimetre size grown on silicidated Pt were observed to cross sometimes hundreds of the Pt grains and their boundaries without any effect. Interestingly, bilayers and multilayers also had hexagonal shape on silicidated Pt, while they had irregular shape on pristine Pt. In the study by Gao *et al* (2012)[144] Pt was reused hundreds of times inside a fused silica tube that uncontrollably accumulated silicide impurity. Silicides are conductive and are not easily distinguishable in a SEM without additional chemical analysis (shown later in the chapter), explaining why the presence of silicides has not been noticed and their striking influence on graphene growth in CVD has not been studied or reported before. The possibility to reuse Pt in combination with short experimental times can reduce costs and ensure the development of high quality graphene syntheses commercially. I confirmed that the

silicidated Pt substrates were also inert in the electrolyte solution (NaOH) that was used for a non-destructive “bubbling” graphene transfer[144] and thus could be reused using transfer methods outlined in section 3.1.

Monolayer graphene was also easily achieved silicidated Pt, most likely due to the proposed "balance regime" (ref. 130) between surface catalysis and segregation. Graphene was transferred to Si/SiO_2 substrates for Raman measurements. Figure 38a shows a typical Raman spectrum of transferred graphene; the D-peak was almost indistinguishable from the background indicating low defect concentration. The ratio of 2D to G peaks exceeded two over large areas, as expected for good quality monolayer graphene[187].

Large area graphene was also transferred to plain TEM grids (Au, Agar) without amorphous carbon support as outlined in section 3.1. TEM images and SAED patterns were recorded with a JEOL JEM-2010 microscope at 80 kV. A line profile of the SAED pattern (Figure 38b) provided additional supporting evidence for monolayer graphene[189]. The hexagonal shape of the flakes suggested good crystallinity, but in order to confirm this SAED patterns were recorded at points across large areas of a graphene flake on a TEM grid and showed very small rotation of the lattice. Additionally, lattice-resolution AFM scans of 6 nm x 6 nm were recorded on as-grown graphene on silicidated Pt (Figure 38c). AFM measurements were performed by Dr Jonathan Moffat using a Cypher AFM (Asylum Research). The scan was done in contact mode by looking at the lateral motion due to changes in friction as the probe scanned over the surface. To eliminate the effects of the direction of probe movement and also any topographic effects the trace scan was subtracted from retrace for the lattice-resolved image in real space. 2D fast Fourier transforms (FT) were taken of the AFM scans, the absolute values of which were then calculated and plotted on log scale; the contrast of the final images was adjusted to reduce the background (Figure 38d-e). The roughness of the substrate after solidification was limiting the resolution of AFM images, but small area scans were sufficiently flat and thus suitable for the FT

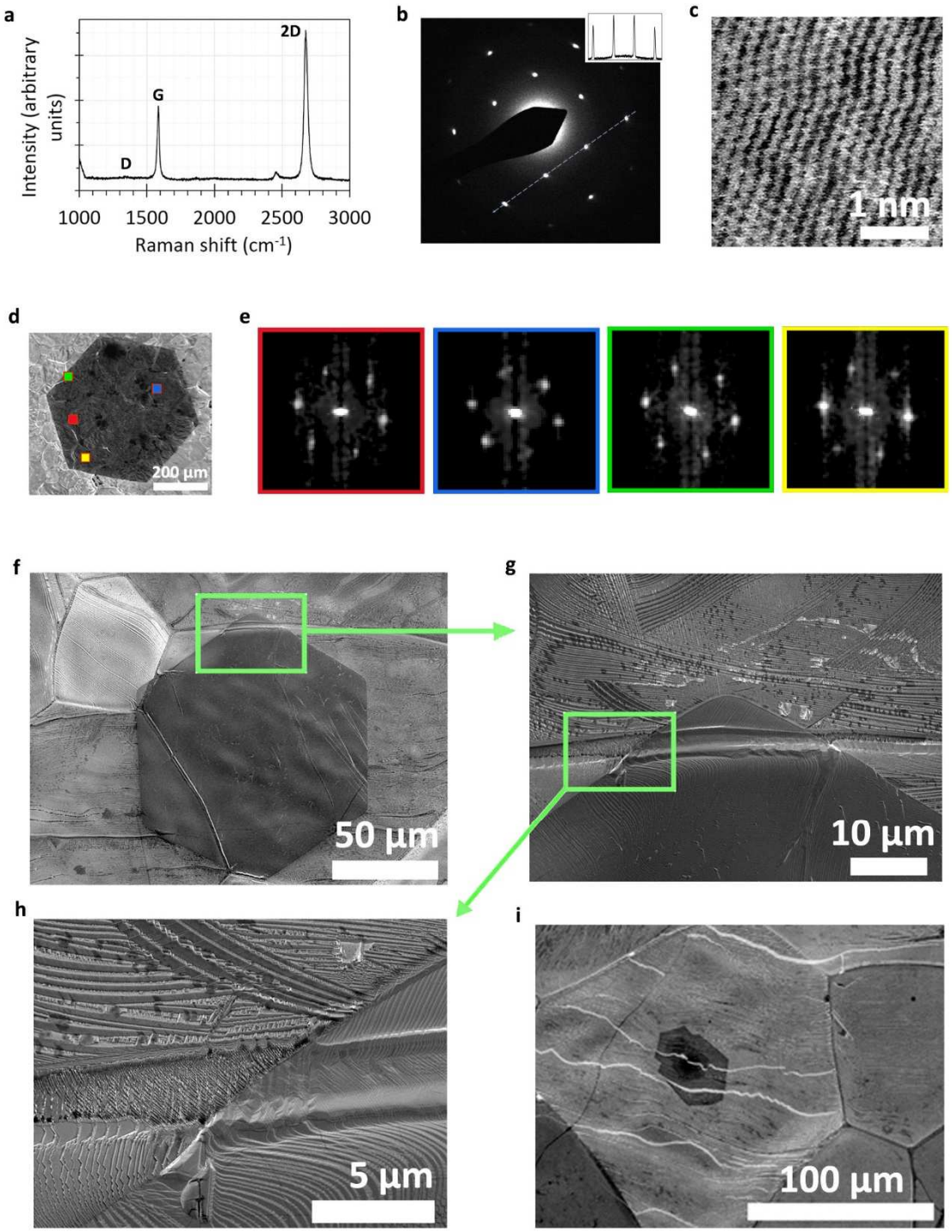

Figure 38. Graphene characterisation on silicidated Pt. a) A representative Raman spectrum of graphene transferred to Si/SiO2 substrates from silicidated Pt. b) SAED of the synthesised graphene with a line profile (inset) indicating monolayer graphene. c) A lattice-resolved AFM scan of graphene directly on silicidated Pt. Data recorded by Dr Jonathan Moffat, Asylum Research. d-e) Crystallinity analysis of graphene showing a SEM image of a hexagonal flake with marked areas of where lattice-resolved AFM scans were recorded. 2D fast Fourier transforms (FT) were taken of the AFM scans; very small rotation of the FT patterns indicates good crystallinity over hundreds of micrometres. f-g) A small graphene flake extended over five silicidated grains. No change to the hexagonal shape is observed, confirming reduced dependence on the crystallographic orientation of the substrate and its grain boundaries. h) A high magnification micrograph of a graphene edge (right) crossing a grain boundary, showing high roughness of the re-crystallized silicide and a clear influence of graphene presence on the topography. i) Occasional, anisotropic crack formation in graphene was observed, perhaps due to strain induced by the silicide re-crystallisation or phase change. Such cracks have been reported previously on a liquid Cu substrate[148].

analysis. These methods provided ways to measure the rotation of the lattice over distances of hundreds of micrometres. The measured values showed no significant changes in the rotation of the lattice and confirmed that the synthesised graphene was indeed a single crystal. The roughness of quenched silicidated surface was higher than for pristine Pt (Figure 38f-h), while mostly large areas of good quality graphene were forming, occasionally cracks appeared on particular Pt grains (Figure 38i). Most likely some specific crystallographic orientations of Pt templated the formation of tall striations in the silicide layer upon cooling that caused anisotropic cracks. Similar cracks have been reported by Fan *et al* (2014)[148] for graphene grown on liquid Cu, caused by massive liquid Cu restructuring during cooling. The study also showed an effective solution to the problem by slowly cooling the substrate in the synthesis atmosphere to facilitate slower Cu restructuring and healing of any cracks in graphene. To avoid the formation of such cracks on silicidated substrates the thickness of the liquid layer needs to be kept low.

It is known that silicon can incorporate into graphene lattice, a behaviour observed by Lee *et al* (2012)[219] on a cluster of Si atoms in graphene and further confirmed by Wang *et al* (2015)[220], who synthesised Si-doped graphene from two precursors. It is a possibility that some silicon atoms can be introduced into graphene from silicidated substrates, however, Wang *et al* (2015)[220] also observed a very high "defect" D-peak for Si-doped graphene, which I did not observe. This suggests that if there is silicon doping it is very low. The QHE measurements presented in section 5.1.6 also confirm very low doping either from silicon or, more likely, from impurities added in the processing stages (transfer).

5.1.4. Silicidated substrate characterisation and silicidation mechanism

It is commonly known that Pt is a noble metal that is very inert; hot aqua regia and a handful of other reagents can successfully etch it. Silicon dioxide (SiO_2), fused silica or quartz are also described as inert due to the strong Si—O bond, which can be broken by hydrofluoric acid or

some strong bases. However, when these compounds are in contact in a reducing H_2 atmosphere at elevated temperatures SiO_2 can be reduced to Si, catalysed by Pt, and react with Pt to form various phases of eutectic Pt silicides as reported by numerous studies[221-224]. The two simplified reactions are as follows

$$SiO_2 + 2 \cdot H_2 \rightarrow Si + 2 \cdot H_2O \quad (28)$$

$$x \cdot Si + y \cdot Pt \rightarrow Pt_ySi_x \quad (29)$$

If pure silicon is deposited onto Pt, then the reaction proceeds much quicker and starts at lower temperatures. Other films, such as SiO, SiN also react in a similar fashion.

Characterisation of the annealed and cooled substrate prior to graphene synthesis was performed. The cooling was rapid (quenched) to obtain the closest possible condition to that during the synthesis. The first noteworthy difference between the pristine and silicidated substrates was thickness of the boundaries between the grains (Figure 39a-b): the latter had much thicker grain boundaries. From phase diagram of the Pt-Si system (appendix 9-B) it can be hypothesised that an alloy of Pt and Si with a low melting temperature was forming. However, further characterisation was necessary to understand whether the alloy was still present on the surface and actively influenced the synthesis or if it completely evaporated simply leading to Pt surface restructuring.

EDX

Figure 39c,d shows a SEM image of a grain boundary of the substrate and its corresponding EDX (section 3.3.1) spectral map of the Si peak. The grain boundary and the small topographic defect had higher silicon content compared to the surroundings. The silicon peak was very prominent (Figure 39e) in such valleys, but was typically much lower, though often detectable on the Pt grains. The presence of a variety of “frosted” features and striations in SEM also supported the formation of a thin silicide layer. Cross-sectional EDX maps were recorded on Pt foils with a

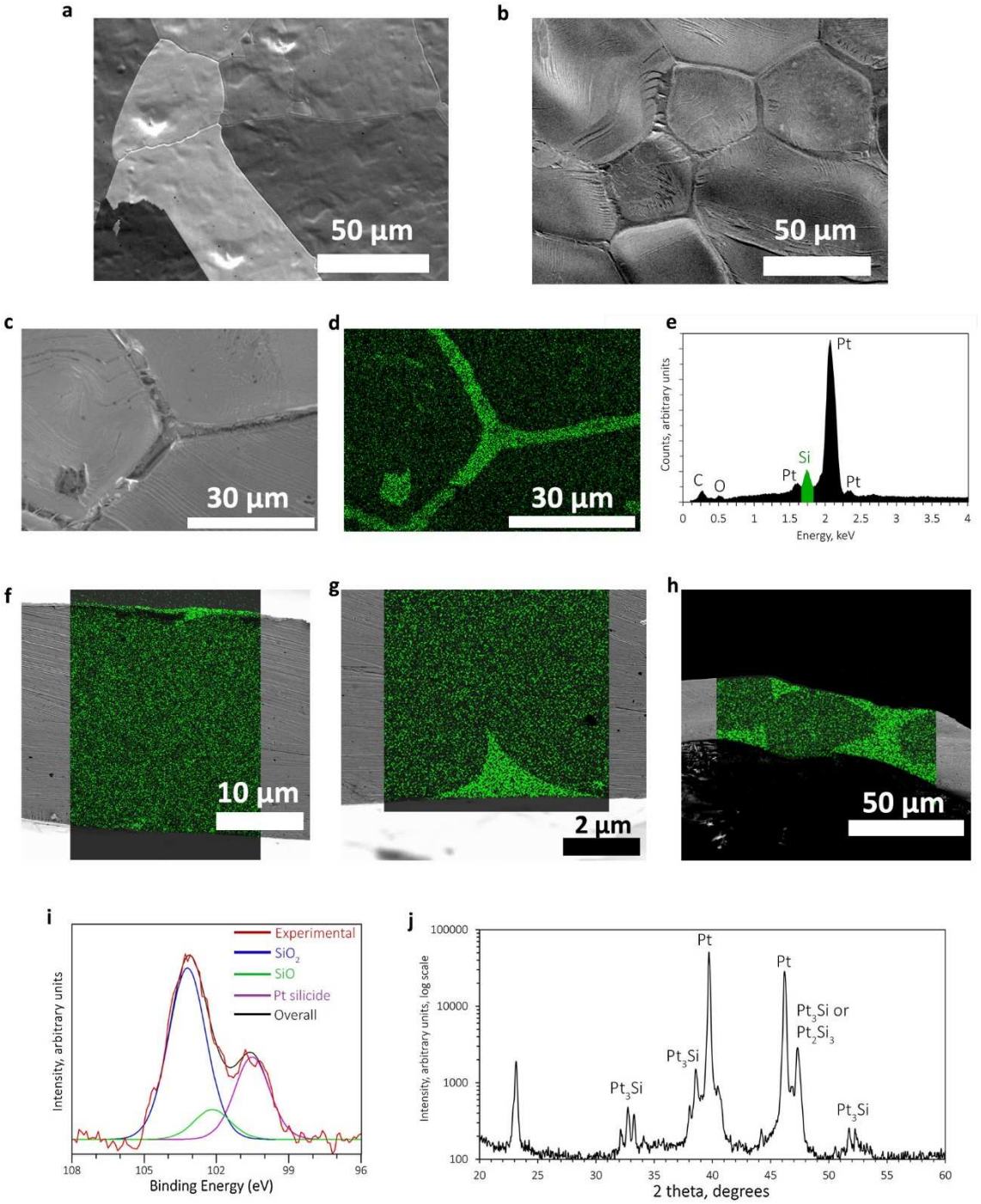

Figure 39. Characterisation of the Pt/SiO_2 substrate after annealing in hydrogen. a) Pristine Pt from the manufacturer after annealing. b) Appearance of silicidated Pt in a SEM after cooling: striations, frosted features and thicker grain boundaries are noticeable, indicating liquid origins. From these features the presence of platinum silicide can often be deduced without additional chemical analysis. c) A SEM image of the annealed and cooled silicidated substrate with a filled Pt grain boundary. d) An EDX map of the Si peak, showing the valleys filled with a silicon-rich compound (green). The darker regions correspond to Pt grains with a much smaller Si peak. e) An EDX spectrum of the Si-rich area from the grain boundary. f-h) Crossectional EDX maps of the Si peak overlapped with SEM micrographs of the silicidated Pt samples. Low, medium and high silica thicknesses result in undetectable, medium and high silicide-phase presence. The silicon-containing regions and pristine Pt grains are completely indistinguishable in SEM mode. Restructuring and degradation of the foil can be observed for the samples with excess silica. i) XPS spectrum with fitted peaks, showing a matching silicide peak and silicon oxide peaks. j) XRD spectrum of the substrate (on log scale), confirming the phase as Pt_3Si (monoclinic when solid).

varying thickness of the silica layer in order to better understand the Pt/SiO_2 reaction and the chemical composition in the bulk. After the sample was annealed and quenched, regions with a thin silica layer (≲500 nm) did not show a detectable silicon peak in the EDX maps (Figure 39f). Regions with a higher initial silica thickness (>500 nm) showed a high silicon signal (Figure 39g) around the grain boundaries, suggesting that the reaction proceeded faster in those areas while progressing slowly into the bulk of the grains. Finally, excess silica (≳3000 nm) resulted in the restructuring and degradation of the foil due to the formation of a two-phase composite (Figure 39h), where the shrunken Pt grains were held together by the Si-containing compound.

XPS

XPS analysis (section 3.3.2) revealed that Pt silicide covered the entire substrate due to a large peak at around 100.5 eV[225] (Figure 39j) corresponding to the metal-silicon bond. Additional SiO/SiO_2 peaks[226] were also observed at 103.1 eV and most likely formed when the silicide was exposed to air. The XPS measurements were performed by Dr Alison Crossley at base pressure of 5 x 10^{-10} torr on a VG nine channel CLAM4 electron energy analyzer with a 250 W Al X-ray excitation. I used CasaXPS software to analyse and present the final data.

XRD

Complimentary XRD measurements (section 3.4.2) were recorded to confirm the chemical composition found with XPS, but also to identify the phase of the solidified silicide. Bruker D5000 diffractometer was used by Dr Philip Holdway to record the measurement. For this, a thick SiO_2 (~3 μm) film was deposited on Pt to get the material in excess, resulting in the formation of the Pt_3Si phase that matched well with the literature[227] (Figure 39j), but possibly other phases were present under different synthesis conditions.

Silicidation mechanism

Based on experimental observations of the SiO_2 film before and after annealing a simple mechanism of the liquid silicide formation is proposed that explains why the morphologies of graphene were so different on pristine and silicidated Pt. Most Pt silicide phases have reduced (eutectic) melting points[228], especially in the form of a thin film. For example, the identified monoclinic Pt_3Si phase melts at around 830 °C[228]. Figure 40 shows a diagram of a possible silicide formation mechanism and the corresponding SEM images of the Pt/SiO_2 stack. The deposited silica layer is not conductive and appears dark under the electron beam. Upon heating, a spontaneous reaction occurs at a variety of points in the film that start to spread in a circular manner. The circular holes in the silica film are filled with a thin layer of a conductive liquid, which when cooled appear similar to the pristine Pt but with a "frosted" surface (Figure 38f-h, Figure 39b). The silicide evaporates from the surface, diffuses into the bulk and locally smoothes any topographical defects, such as Pt grain boundaries, as inferred from the cross-sectional EDX maps in Figure 39g-i. It should be noted that the annealing time becomes an important parameter. Graphene synthesis can be started shortly after the SiO_2 thin film completely reacts with Pt and the surface has a uniform chemical composition. Possibly there are chemical influences on the reaction mechanism by the silicidated Pt surface in addition to simple mechanical (liquid) effects. For example, the silicide route could produce a form of silicon carbide as an intermediate state with a lower activation energy.

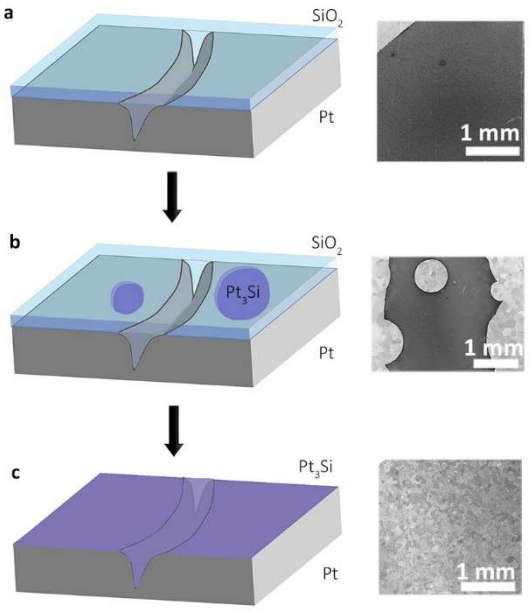

Figure 40. Stages of the silicide formation. a) The substrate is coated with a SiO_2 film. b) Upon annealing a spontaneous reaction occurs resulting in circular holes in the film. c) A thin liquid silicide layer covers the substrate and fills in any valleys or Pt grain boundaries.

5.1.5. Graphene crystallinity control

The ability to control the crystallinity allows to tailor the material towards high-end applications. A systematic investigation into the effect of the thickness of the deposited silica layer on the hexagonality of graphene flakes was conducted. The thickness of the SiO_2 films was measured with a Nanometrics Nanospec AFT interferometer on co-deposited Si tiles. I used a simple analysis technique to distinguish between different levels of hexagonality of the synthesised samples. MATLAB was used to find a threshold value of SEM micrographs, which were then converted into binary images (Figure 41a-d). The ratio of the perimeter (P) squared to area (A) was calculated for each geometric shape. This unit-less number is usually indicative of specific geometric shapes. For example, for a circle it is $4\pi \approx 12.57$ (the lowest possible value), for an octagon it is ≈ 13, for a hexagon √192 ≈ 13.86, for a pentagon ≈ 15, for a square it is 16 etc. Concave polygons have higher P^2/A values. If the calculated ratio (P^2/A) for a shape is X, then I defined the hexagonality as

$$\text{hexagonality} \approx 1 - \frac{|X - \sqrt{192}|}{\sqrt{192}} \tag{30}$$

or as a percentage, multiplied by 100 %.

This quantity indicates that a shape with a value close to 100 % is close to a perfect hexagon. The standard deviation of the % hexagonality for a sample indicates how non-uniform the shape distribution is. It is understood that rounded convex or concave polygons can introduce an uncertainty in the measurement, since, for example, a rounded square can have the ratio of the perimeter squared to area similar to a hexagon. However, in the data, either hexagonal shapes (silicidated Pt) or concave polygons (pristine Pt) were present, thus, for a large number of graphene domains the approach characterises the samples sufficiently. Specific details about the processing steps are given in appendix 9-C. The overall trend is presented in Figure 41e and matches well with the expectation: the more silica is added, the thicker the liquid silicide layer is and thus the flakes grow more independently from the underlying solid substrate. The value

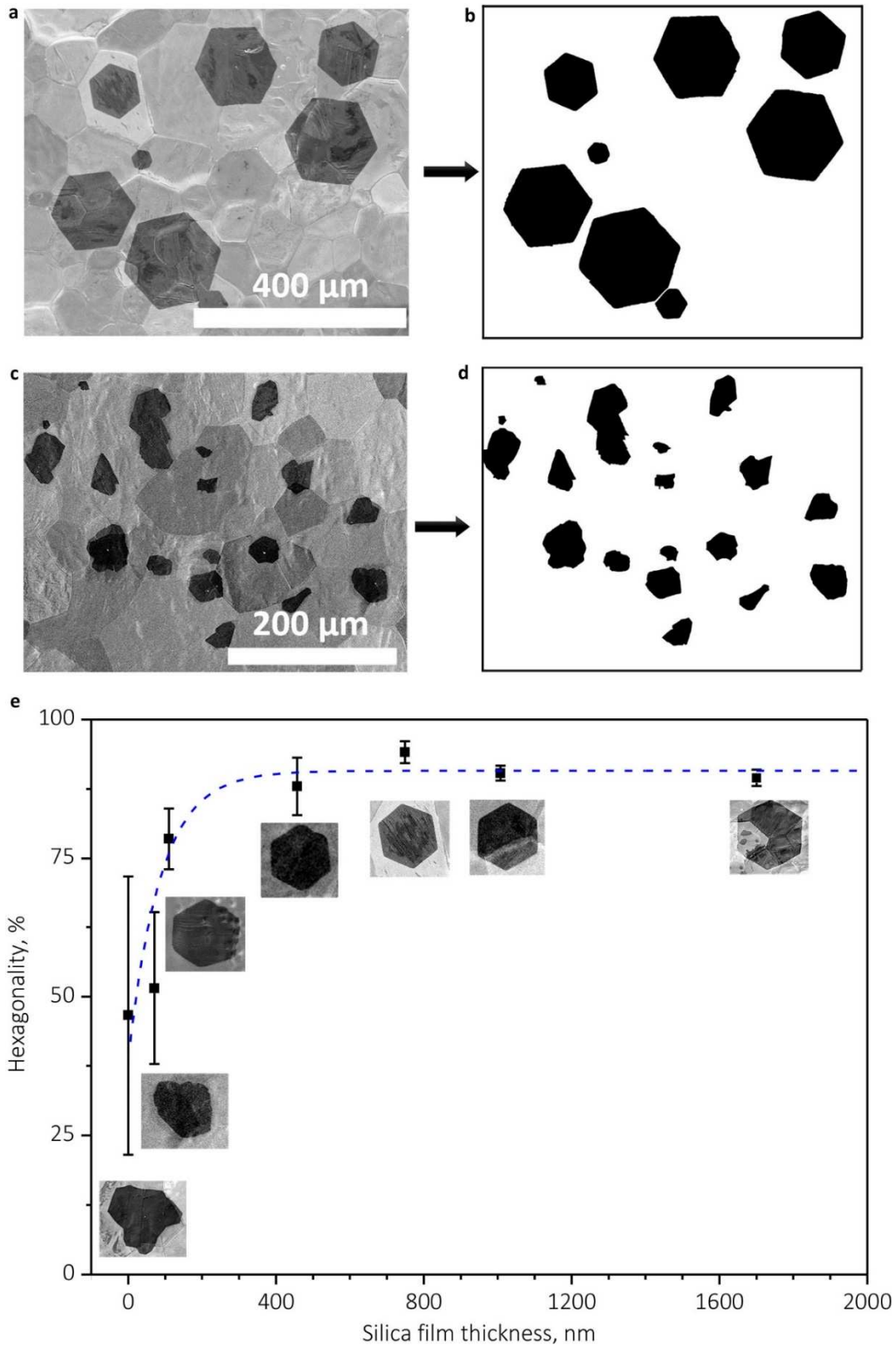

Figure 41. Influence of the silica layer thickness on the hexagonality and thus the crystallinity of the CVD graphene. a,b) A sample with a high hexagonality and uniformity of graphene domains on silicidated Pt. A SEM micrograph is shown with a processed binary image of the resulting shape distribution. c,d) A sample with low hexagonality and shape uniformity on pristine Pt. e) With increased silica layer thickness the crystallinity and the shape uniformity increases. Error bars represent the distribution of shapes on the sample. The dashed line is a guide to the eye.

of hexagonality saturated at 800 nm thick silica layer reaching 91 % similarity to a perfect hexagon. Another important quality indicator, the uniformity of the shapes, also decreased significantly from about 50 % fluctuation at 0 nm to less than 5 % at 800 nm, as shown by the error bars. Usable silica layer thicknesses were limited by the thickness of the Pt foil. If there was too much silica (> 2 µm) the 25 µm Pt foil could start to degrade (Figure 39i) or curl during the synthesis due to thermal stress caused because of the differences in the thermal expansion coefficients of Pt and silica. For these reasons the optimum deposited silica values were between 500 - 800 nm.

5.1.6. Quantum Hall effect measurements towards metrology applications

Recently, graphene has been shown to be an exceptional candidate for quantum Hall metrology[229] showing promise in redefining the quantum resistance standard; additionally exhibiting the highest breakdown current density of any material[230]. To assess the electronic properties of CVD graphene grown on silicidated Pt an 8-leg, 15 µm × 130 µm Hall-bar device was fabricated from graphene transferred onto SiO_2/Si substrates as shown in Figure 42a. The device was fabricated and measured by Dr Jack Alexander-Webber and Mr Nathaniel Jian Huang using the methods outlined below. E-beam lithography followed by oxygen plasma etching were utilised to shape the features of the device. A two-step ohmic contacting method[231] was used with thermally evaporated Cr/Au outer contacts and Au-only inner contacts. The final devices were coated in ma-N 2405 photoresist as a dielectric layer and a corona discharge technique[232] was employed to control the charge carrier density. Electrical measurements were carried out at 1.4 K in an Oxford Instruments 21 T superconducting magnet, where magnetic fields B were applied perpendicular to the sample surface. A small AC current with peak amplitude of 40 nA was applied in the longitudinal direction (I_{xx}). The longitudinal voltage V_{xx} and the Hall voltage V_{xy} were simultaneously measured using the standard lock-in technique. The longitudinal

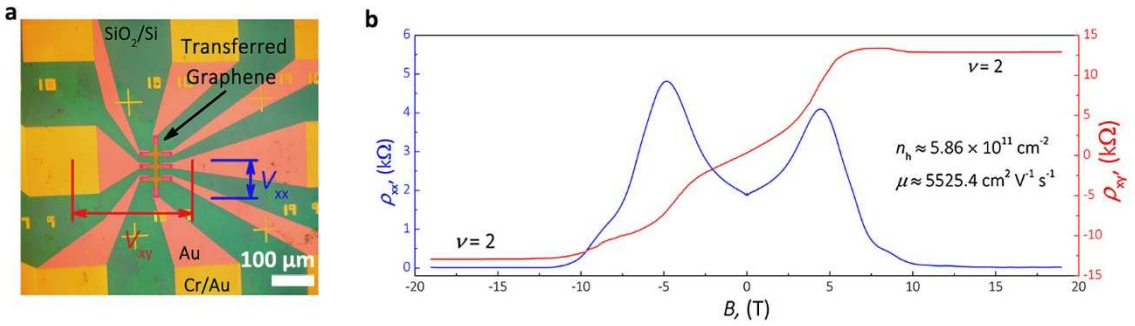

Figure 42. Graphene in QHE measurements. a) The optical image of the device, where small contrast can be observed between the transferred graphene (light blue) and the SiO_2/Si substrate (dark blue), and also between the Cr/Au (yellow) and Au-only (pink) contacts. On top of the Hall bar is the ma-N 2405 resist (brown). V_{xx} and V_{xy} are also labelled. b) The longitudinal resistivity (ρ_{xx}) and the Hall resistivity (ρ_{xy}) as functions of magnetic field. The carrier density and mobility shown were determined from the low-field Hall coefficient and the longitudinal resistance at 0 T. Also shown are the well-defined $\nu = 2$ quantum Hall states with quantised ρ_{xy} and vanishing ρ_{xx} at $|B| > 12$ T. Device fabrication and measurements were performed by Dr Jack Alexander-Webber and Mr Nathaniel Jian Huang.

resistivity ρ_{xx} and the Hall resistivity ρ_{xy} (Figure 42b) were determined as $(W/L)\cdot V_{xx}/I_{xx}$ and V_{xy}/I_{xx},respectively, where L and W are the length and the width of the device. The carrier density n and mobility μ of the device were determined from the low-field Hall measurements with

$$n = \left(e \cdot \partial \rho_{xy}/\partial B\right)^{-1} \text{ and} \tag{31}$$

$$\mu = (en\rho_{xx})^{-1}. \tag{32}$$

Small p-type doping was observed from the measurement, which is also commonly seen in transferred graphene on SiO_2/Si substrates and considered to be due to the adsorption of water molecules between the interfaces[233,234] or possibly due to some silicon incorporation into graphene lattice. Figure 42b shows the ρ_{xx} and ρ_{xy} as functions of magnetic field from -19 T to +19 T for a typical device. A high hole mobility of 5525 $cm^2V^{-1}s^{-1}$ was observed at a hole density of 5.86×10^{11} cm^{-2}. In the sample, at $|B| > 12$ T, well defined $\nu = 2$ quantum Hall states was clearly observed with

$$\rho_{xy} = h/2e^2 \tag{33}$$

and $\rho_{xx} = 0$, consistent with its carrier density

$$\left|B_{(\nu=2)}\right| = \frac{nh}{2e}. \quad (34)$$

These observations confirm the high quality of graphene synthesised on silicidated Pt with good crystallinity, very low defects and impurities, and that large-area graphene grown using this method may be useful for quantum resistance metrology. The carrier mobilities obtained from the magnetotransport measurements are among the highest of reported values for CVD graphene[235] on SiO_2/Si substrates and are comparable to those in epitaxial graphene grown on SiC[229]. For comparison, commonly reported[235, 236] CVD graphene mobilities are between 2000-4000 $cm^2V^{-1}s^{-1}$ However, exfoliated graphene transferred to Si/SiO_2 with an "all-dry" methods showed mobility values of 15000 $cm^2V^{-1}s^{-1}$ recently[237]. Using more sophisticated transfer methods or substrates with less charged impurities, such as *h*-BN[237,238], further improvement of the carrier mobility is expected.

5.2. Graphene on silicidated palladium

Pd was also explored as a substrate for silicidation due to similar reasons discussed in section 4.2, mainly the lower cost. It was found that the metal was easily silicidated with methods developed for Pt, such as thermal evaporation of SiO_2, but unlike for Pt, much thinner SiO_2 layer was needed. For example, a 50 nm silica film already resulted in perfectly hexagonal graphene domains, possibly because lower Si atomic fraction was needed to form the first eutectic Pd-Si compound[239] (15 % vs. 22 %[228]) or lower Si diffusion into the bulk of Pd. A Si peak was observed in grain boundaries on silicidated Pd with EDX (Figure 43a), suggesting a similar mechanism to silicidated Pt. Additionally, the synthesis parameter trends were very alike: longer syntheses times resulted in larger domains, higher temperature facilitated faster growth rates and higher H_2:CH_4 improved the flake quality, but decreased the growth rate. One major difference between the two substrates for graphene growth was the increase in graphitic multilayer formation after silicidation as shown in Figure 43b and inset, which were discussed and characterised in section 4.2. The growth of 100 % monolayer graphene (Figure 43c) could only be achieved with a very high H_2:CH_4 ratio of around 400 that resulted in reduced growth rate of around 30 µm min^{-1} (1150 °C). While this value is ~10 times faster than on Cu, it is 4 times slower than on silicidated Pt at the same temperature. Unless methods can be found to supress multilayer formation without affecting the growth rate, graphene synthesis on silicidated Pd can be considered an intermediate improvement over Cu at lower cost compared to silicidated Pt.

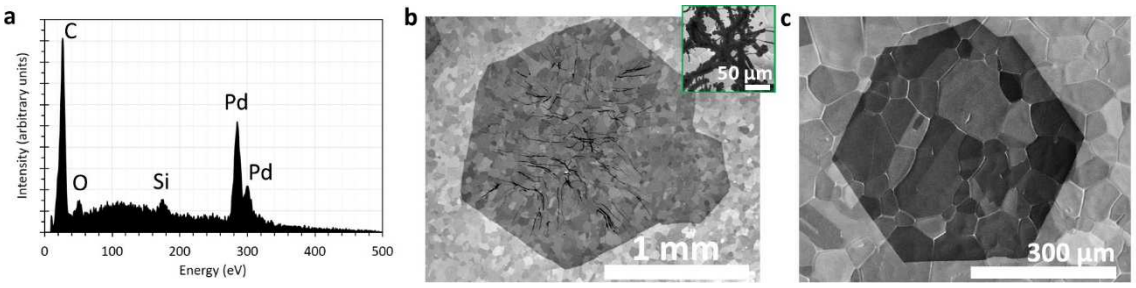

Figure 43. Graphene on silicidated Pd. a) EDX spectrum of the boundary between grains indicating high silicon content. b) A large graphene flake grown with a low H_2:CH_4 ratio, resulting in a network of graphitic multilayers. c) A monolayer graphene flake grown with a high H_2:CH_4 ratio, but at a reduced growth rate.

5.3. Copper and nickel, difficult to silicidate substrates

Metal silicides[240] are a well-known component in silicon-integrated circuits and other electronic devices. Many of these compounds are well studied, but usually for temperatures lower than typical CVD temperature used for graphene growth. From the results obtained from Pt and Pd I explored the possibility of two other cheap metals used for graphene growth: Ni and Cu. Silica was deposited on Ni using TEOS CVD and annealed for 2 hours at 1100 °C. Most of the film was still present on Ni after annealing, with large regions delaminating from the surface (Figure 44a). Interestingly there were regions, where the film reacted with Ni to form Ni silicide as shown in Figure 44b and in the EDX spectra in Figure 44c, d. The oxygen peak decreased significantly, while the Ni peak became the most prominent. Although there is scope for further investigation, for example, by employing higher temperatures or longer annealing time, I concluded that this

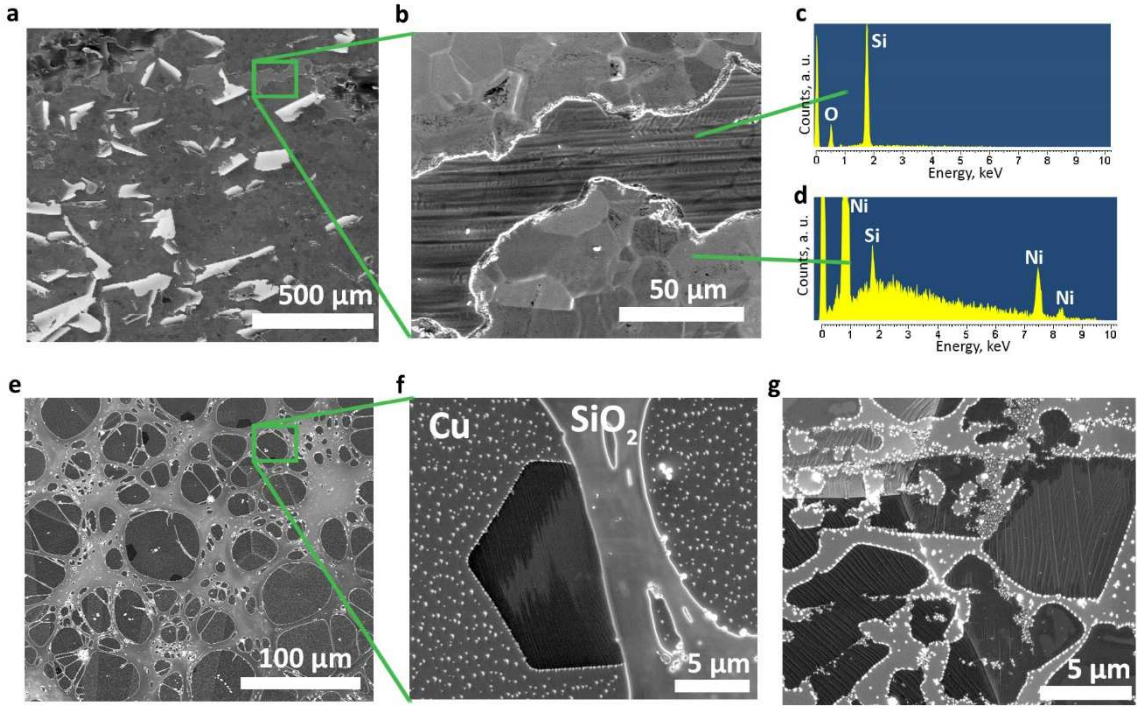

Figure 44. Silicidation of Ni and Cu. a) A SEM micrograph of a silica film deposited on Ni after annealing at 1100 °C for two hours. Large areas of the films delaminated and have not reacted. b) A micrograph of an area where the silica film partially reacted with Ni, showing silicidated regions (top and bottom of the image) and the original film (middle). c-d) EDX spectra of the regions where the silica has not reacted and reacted to form nickel silicide respectively. e-f) Cu foil with a thermally evaporated Si film after annealing in a CVD system. SiO_2 remnants from the film were left completely unreacted. Small SiO_2 islands were present everywhere. This indicates that Cu only does not react with SiO_2 even in a reducing H_2 atmosphere. g) Graphene flakes on silicidated Cu were typically distorted and separated by SiO_2 contaminants.

approach was not suitable for graphene synthesis due to high processing cost and time.

Cu foils were also investigated for silicidation. But did not react with SiO_2, however, some reaction was observed with a thermally evaporated Si film from Si powder. While large portion of the Si film disappeared, a network of SiO_2 was left of the surface unreacted (Figure 44e,f). The causes for the formation of SiO_2 could be from small oxygen impurity inside the thermal evaporator or due to exposure of the film to air when moving from one system to another. Graphene flakes were prevented from growing by the SiO_2 network and in the regions where there was no continuous network, there were still small particles of SiO_2. These particles degraded the quality of graphene (Figure 44g). For these reasons I also concluded that Cu was not a suitable substrate for silicidation

5.4. Summary

In this chapter I developed and optimised a novel, low-cost substrate processing procedure to achieve rapid, efficient synthesis of millimetre-sized single crystal graphene. Silicidation of polycrystalline foils can be used as a replacement for expensive single-crystal substrates or as an alternative to polishing and grain enlargement. Large topographic defects, such as grain boundaries, are locally smoothed and the lattice of the grains is screened by a liquid surface, making silicidated polycrystalline foils superior to single crystal substrates due to epitaxy-free synthesis. This ensures that graphene grows in its undistorted hexagonal shape. Silicidated polycrystalline Pt also exhibits low graphene domain nucleation density of down to 0.3 mm^{-2} and enhanced growth rates of up to 120 µm min^{-1} at elevated temperatures, allowing millimetre-sized flakes to grow easily in minutes. This value is more than two orders of magnitude higher than on Cu with standard synthesis methods.

The silicide film formation on the substrates is an important parameter for graphene growth and has beneficial effects if controlled. However, it is likely that some results in the literature were influenced by these silicides from contamination but were overlooked. The beneficial effects can make silicidation feasible commercially, especially if the procedure is extended to other metals. There is significant potential for future developments of the method, such as a liquid surface for low temperature graphene synthesis or extension of the methods to ternary or higher eutectic alloys. *In situ* liquid layer formation is generally applicable and paves the way for a whole new field of eutectic substrates for the growth of superior quality 2D materials.

Interestingly, studies[241] show that it is possible to oxidise intercalated silicides to achieve transfer-free graphene on an insulating surface, suggesting another potential benefit of the synthesis directly on metal silicides to be explored in future work.

Chapter 6. Synthesis of non-graphene 2D materials towards heterostructure-enabled applications

After graphene's discovery many other 2D materials were quickly identified. Currently, their properties and suitability for applications have been preliminary determined, however, the synthesis methods are still in their infancy. The reason for this is the shorter elapsed time for advancement of the methods, but fundamentally, two or more elements comprise these materials. The choice of precursors and their combinations is therefore much larger than for graphene and need more time to study.

Initial experiments that were performed using methods from the literature resulted in preliminary hBN and WS_2 materials but with no reproducibility; moreover, without any possibility to tailor the material. For my investigation into these non-graphene 2D materials, I re-built and upgraded two purposely-designed CVD systems with improved precursor controls and methods (as discussed in section 2.1) that were developed over a number of years. Specifically, I focused on studying and controlling the precursors for these materials. *In situ* measurements of hBN precursor decomposition distinguish this study from others, where the search of the synthesis parameters was performed at random. Additionally, novel chemistry for WS_2 synthesis, based on optimised thermodynamics, was developed and allowed an insight into the mechanisms of crystalline WS_2 formation. As a result, reproducibly synthesised high quality hBN and WS_2 materials were achieved, but most importantly, advanced understanding of the precursors, the chemical reactions involved in the synthesis and improved control methods will be of outmost significance to achieve better 2D materials in future work.

6.1. Hexagonal boron nitride synthesis at atmospheric pressure

Few-layer, polycrystalline hBN films are typically sufficient for applications where they are used as a substrate. However, synthesis of larger hBN crystallites comprising the film and control of the number of layers can be beneficial in a number of ways. For example, it has been shown that highly crystalline hBN flakes serve as a better template for graphene[58] due to the low lattice mismatch. Similarly, epitaxial growth of monolayer WS_2 on small, mechanically exfoliated hBN crystals showed good alignment of WS_2 flakes that lead to low-angle grain boundaries and better electronic properties[124]. Methods need to be developed to control the growth of hBN, and more importantly to improve the uniformity, reproducibility and dielectric properties of hBN films.

6.1.1. Broad CVD parameter investigation on nickel

A number of preliminary synthesis experiments were performed with the apparatus described in section 2.1, but with simple heating of the precursor to constant temperature with an oil bath. Four variables were investigated: the mass and temperature of ammonia borane powder, H_2 gas flow rate and the synthesis time to broadly map the parameter space. Higher temperature, lower H_2 flow rate and longer synthesis time resulted in more hBN deposition, similar to graphene and in line with theoretical explanations from sections 2.2.3-2.2.4. Examples of the

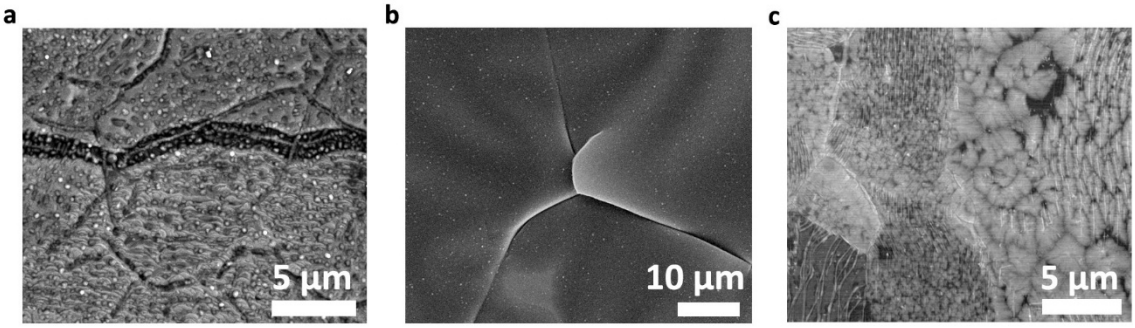

Figure 45. Preliminary hBN synthesis experiments. a) A thick film covered with 3D particles was formed when H_2 flow was very low (20 sccm). b) A thick BN film formed when more hydrogen was added (200 sccm). c) A thin hBN film, covered with multilayer BN flakes was formed when H_2 gas flow was increased even further (300 sccm). The mass of the precursor and the synthesis time were kept at 100 mg and 30 mins respectively.

structures obtained are shown in Figure 45. The highest deposition resulted in 3D structure formation such as particles (Figure 45a). Reducing the deposition by increasing the H_2 gas flow rate resulted in a very thick film (Figure 45b) that cracked upon cooling, likely due to the difference in thermal expansion coefficients between Ni and BN. Increasing H_2 flow even more resulted in a few-layer hBN film with additional multilayers islands (white flakes, Figure 45c). Further increase in H_2 level resulted in irreproducibility: occasionally forming thin hBN films or often no deposits were formed. A number of reasons were identified, the most influential ones were insufficient precursor controls in the early system and lack of understanding of time-dependent precursor chemistry as discussed in the following chapter.

6.1.2. Ammonia borane precursor decomposition analysis

The synthesis of high quality hBN by CVD has been plagued with challenges, some are similar to those of graphene where the right CVD parameters have to be found. But a more inherent difficulty arises from the choice of the precursor or precursors where both nitrogen and boron must be present. A variety of precursors have been used in the literature: diborane/ammonia[242], b-tricholoroborazine[243], decaborane/ammonia[244], borazine($B_3N_3H_6$)[245-252] and others. Most are toxic, spontaneously igniting, corrosive, unstable or difficult to store, presenting obvious safety concerns. For this reason, ammonia borane (H_3BNH_3) precursor (also known as borazane), classed as a "**not hazardous substance or mixture**", has been gaining popularity as the precursor of choice for hBN synthesis[60, 114-116, 253-256]. Ammonia borane decomposition has been previously studied due to its potential for hydrogen storage applications[257-259]. Unfortunately, the studies did not focus on practically useful heating regimes for CVD synthesis at atmospheric pressure. Figure 46a shows the commonly reported reaction stages for hydrogen release, depending on the temperature. Understanding the hBN synthesis chemistry is challenging because ammonia borane is not the final precursor for hBN synthesis at atmospheric pressure, but rather a

precursor for volatile species that are picked up by the carrier gas and are introduced into the CVD system. It has been shown that the precursor can be completely decomposed below its melting point (~112 °C)[260] through the release of B-, N- species. Additionally, if the lower temperature regimes are adopted, there is a long induction period before ammonia borane produces volatile compounds containing B and N[258]. In most recent studies[258] the proposed explanation for the induction period is the slow phase change of ammonia borane to its less stable ionic isomer "diammoniate of diborane", $[H_2B(NH_3)_2]^+[BH_4]^-$ at low temperatures (< 80 °C). The heating rate can also lead to different decomposition routes and therefore irreproducibility[260]. Consequently, the reported reactions vary from one report to another[257-263] and are not well established in the lower temperature regime, but can be inferred to approximately follow the equations below.

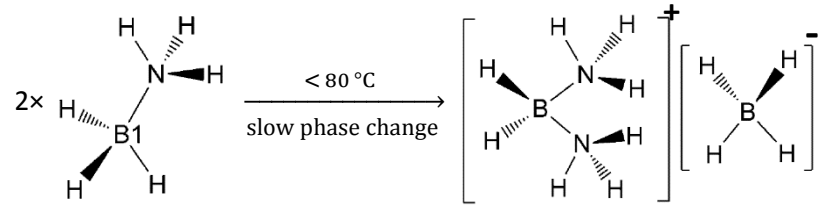

ammonia borane — diammoniate of diborane (35)

$$3\ [H_2B(NH_3)_2]^+[BH_4]^- \xrightarrow{>80\ ^\circ C} 2\cdot B_3N_3H_6 + 12\ H_2 \quad \text{(36)}$$

borazine (g)

$$3\ H_3BNH_3 \xrightarrow{>100\ ^\circ C} B_3N_3H_6 + 6\cdot H_2 \quad \text{(37)}$$

$$H_3BNH_3\ (\text{or}\ [H_2B(NH_3)_2]^+[BH_4]^-) \xrightarrow{70-120\ ^\circ C} NH_2BH_2 + 2\ H_2 \quad \text{(38)}$$

monomeric aminoborane (g)

$$n\cdot H_3BNH_3\ (\text{or}\ [H_2B(NH_3)_2]^+[BH_4]^-) \xrightarrow{70-120\ ^\circ C} (NH_2BH_2)_n + H_2 \quad \text{(39)}$$

polyaminoborane (solid)

$$n\cdot H_3BNH_3\ (\text{or}\ [H_2B(NH_3)_2]^+[BH_4]^-) \xrightarrow{120-180\ ^\circ C} (NHBH)_n + 2\ H_2 \quad \text{(40)}$$

polyiminoborane (s)

$$n \cdot H_3BNH_3 \text{ (or } [H_2B(NH_3)_2]^+[BH_4]^-) \xrightarrow{400-900\ ^\circ C} (BN)_n + 3\ H_2 \quad (41)$$

Equations 36-38 show the formation of volatile decomposition products: borazine and monomeric aminoborane, while equations 35, 39-41 show the formation of solid products. Solid decomposition products can be either polymers or BN. Reaction in equation 39, however, can be ignored in atmospheric pressure CVD because of the lower vapour pressure of ammonia borane compared to the other volatile species. Therefore, possible precursors for BN synthesis could be borazine, aminoborane[259] or other B-, N- species[260] which has also been reported as decomposition products of ammonia borane: diborane (B_2H_6), ammonia (NH_3), triborane (B_3H_7) etc. Equation 42 shows the route for hBN synthesis, and also explains why excess hydrogen can etch hBN deposits: due to the reverse reaction forming aminoborohydrates or other volatile species.

$$B_xN_yH_z \xleftrightarrow{>400\ ^\circ C} (BN)_3 + 3\ H_2 \quad (42)$$

In this investigation mass spectrometry (section 3.3.3) was used as a convenient tool for *in situ* monitoring the relative quantity of borazine with time when produced from ammonia borane, before it enters the CVD reactor tube. I found that the temporal profile of borazine, an indicative fragment of ammonia borane decomposition, is wholly unsuitable for growing high quality hBN domains. Unlike mass flow controllers that can be used to deliver methane for graphene synthesis, simply heating a solid or liquid precursors may not deliver the required control to achieve consistency in the 2D material growth. With ammonia borane the situation is further exacerbated by the stochastic decomposition and polymerisation reaction[258] that causes foaming. The size of monolayer single crystal hBN flakes produced from ammonia borane seems to have stagnated in recent publications, reaching sizes up to 6 µm at atmospheric pressure[116] and 20 µm for low pressure[256] synthesis. The consistent reproducibility of the synthesis of high

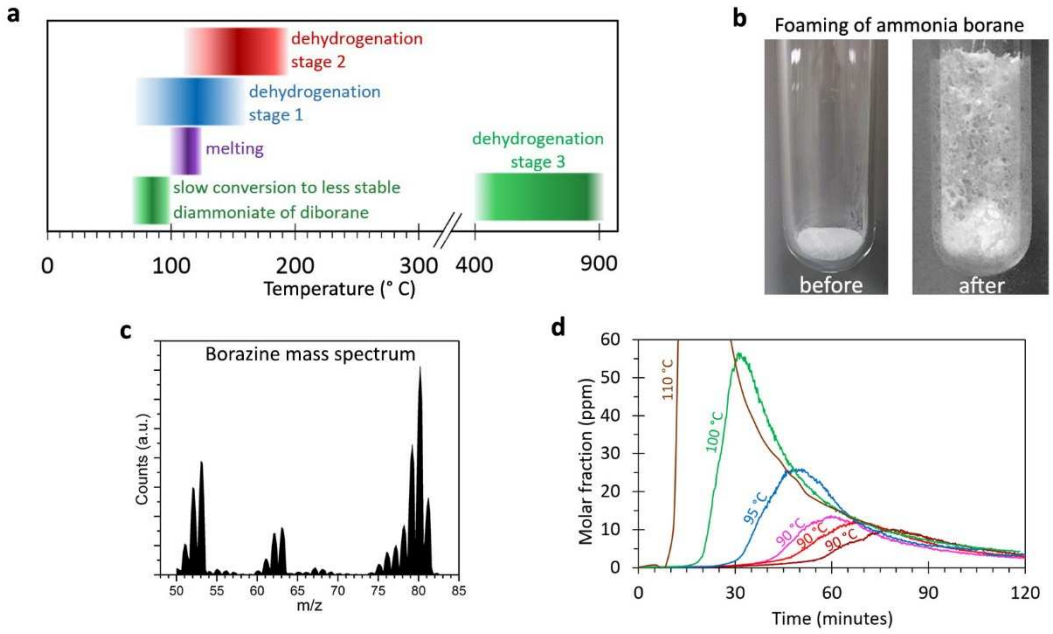

Figure 46. Ammonia borane precursor complex decomposition. a) Commonly reported decomposition reactions of ammonia borane. Colour intensity represents approximate reaction rate. Adapted from refs. 257-263. b) Optical picture of the precursor powder before and after heating. c) Mass spectrum of borazine released by ammonia borane showing the characteristic peaks in the 50-80 m/z range. d) Time evolution of the mole fraction of borazine at different temperatures. An incubation period is followed by a sigmoidal increase, a peak and a decaying profile. Profiles corresponding to temperatures of 90 °C, 95 °C, 100 °C and 110 °C are measured showing that the varying borazine concentration is wholly inadequate for reproducible hBN synthesis. Additionally, the useful borazine mole fraction level of < 5 ppm requires an incubation period of > 90 minutes, while still rapidly decaying. Repeated measurements performed at the same conditions (90 °C) do not produce the same temporal profile.

quality hBN is rarely discussed. It is likely that this is due to the lack of knowledge of the temporal evolution of this solid precursor that undergoes foaming and is difficult to control.

It was observed that the decomposition of ammonia borane was very sensitive to the temperature and even small variation (± 1 °C) from experiment to experiment could lead to irreproducibility. A dedicated CVD system with a custom precursor evaporation chamber was assembled as discussed in section 2.1. The temperature of the precursor could be controlled to < 0.5 °C accuracy and changes in the set temperature could be typically reached within seconds by using a 100 W heating coil (appendix 9-D) at heating rate of about 15 °C/min. For the MS measurements, the probe was inserted into the fused silica reactor tube, where the substrate would be placed during a CVD experiment. The measurements were done with a H_2 carrier gas to achieve the closest possible dynamic equilibrium for ammonia borane decomposition to that

of a CVD experiment. The effect of foaming upon heating the precursor that starts stochastically and follows the "nucleation and growth" polymerization process[258] is shown in Figure 46b. To approximately understand the temporal profile of B-, N- species released from ammonia borane, the borazine fragments is recorded with time, since it does not overlap with strong MS background. Borazine has three characteristic peaks at m/z of 53, 63 and 80 with additional fragments and isotopes clustered around the peaks (Figure 46c). A total of 500 sccm (100 sccm in the evaporation chamber and 400 sccm in the bypass line) of H_2 was flowing through the system during the measurement for which the m/z =2 and m/z =80 were recorded with time. Taking a ratio of the intensities of the peaks allowed to cancel out the fluctuations in the total pressure of the MS and to estimate the mole fraction of the borazine fragment with the assumption that the concentration of borazine was much smaller than of H_2. The total mole fraction (in ppm) of borazine could be estimated by multiplying the fraction of the m/z=80 fragment by the relative integral of all borazine fragments, which was approximately 4, however, the absolute value can have a high systematic error due to the unknown relative sensitivity factor of the apparatus. The total mole fraction of the borazine is plotted in Figure 46d for four different temperatures: 110 °C, 100 °C, 95 °C and 90 °C. Each profile had four common stages: an incubation time, a sigmoidal increase in the concentration of the products (as predicted by the "nucleation and growth" mechanism), a peak in the concentration, which was followed by an approximately exponential decay. Most notably, experiments with exactly the same conditions did not result in the same borazine curves as shown in Figure 46d, where three repeated measurement at 90 °C are plotted. The incubation time was different due to random polymerisation; the peak height was also often different by as much as 100 % due to different packing of the ammonia borane powder granules, and therefore the **decay** profile did not follow the same shape due to varying levels of the reactant exhaustion between different experiments. For these reasons controlling the initial stages of borazine release is of crucial importance for the overall consistency of the synthesis.

6.1.3. Temporal precursor control and calibration

In order to control the mole fraction of B-,N- species during the synthesis, I investigated a number of methods to achieve a constant temporal borazine profile. Initially, computer-controlled variation of the gas flow was attempted that followed the borazine profile. From MS measurements a very constant borazine mole fraction with time was achieved, however, the total flow rate had to be varied from 50 sccm to 3000 sccm during an experiment, which could influence the boundary layers and the surface reactions considerably. For this reason, other control measures needed to be utilised. In particular, four aims were identified

i. Stochastic nature of polymerisation had to be suppressed.
ii. Long induction time needed to be shortened.
iii. The peak in the borazine mole fraction needed to be appear at the same time between experiments, so that the decay curve would be consistent between experiments.
iv. The decaying region needed to be countered to level out the borazine mole fraction.

It was discovered that point (i) could be addressed by mixing ammonia borane powder with a filler, such as BN powder in a 1 to 10 weight ratio respectively to separate ammonia borane granules. This allowed to form a granule size distribution, where each granule could start the polymerisation reaction at random, however, on average the borazine release profile became very reproducible between measurements. Figure 47 schematically summarises the mechanism behind controlling the polymerisation process. Most importantly, the time when the borazine peak appeared became consistent. Another important benefit of this method was that changing the mass of the precursor mix allowed to shift the borazine concentration profile up or down. The increase was linear (e.g. doubling the mass doubled the borazine mole fraction) because simply more separated polymerisation sites (Figure 47c-d) were added that did not interfere with each other.

Points (ii)-(iv) were addressed by designing an appropriate heating profile. A 5 minute long,

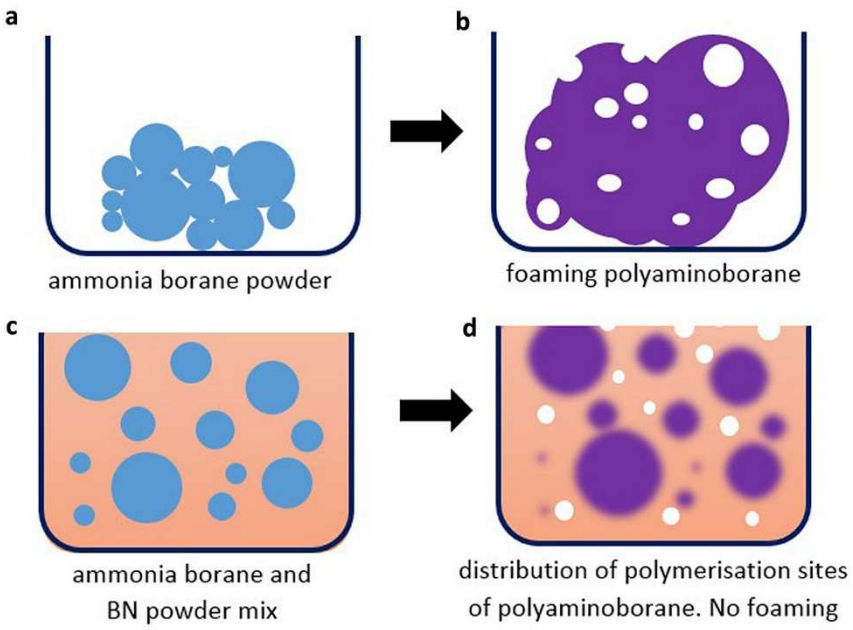

Figure 47. Schematic representation of polymerisation of ammonia borane. a-b) Pristine ammonia borane powder starts to polymerise randomly, producing a large block of foaming polyaminoborane with H_2 and B-, N- containing gases (white holes). c-d) Ammonia borane powder mixed with BN powder produces a size distribution of ammonia borane granules that have a well-defined average reaction time.

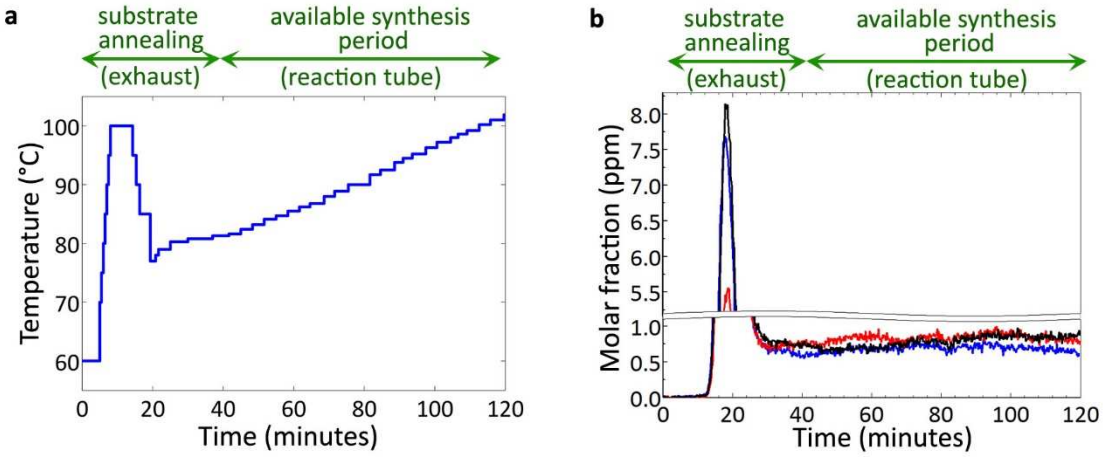

Figure 48. Calibration of borazine release with mass spectrometry. a) The optimised temperature profile for heating ammonia borane and BN powder mix. A 60 °C, 5 minute long stabilisation stage from room temperature is followed by a short peak (100 °C) to reduce the induction time, which is followed by a temperature ramping stage to counter precursor exhaustion with time. b) Three repeated measurements of the response in the borazine mole fraction with time that is achieved when heating ammonia borane according to the optimised temperature profile. Available synthesis time is around 1.5 hours with a constant borazine mole fraction. The initial spike in borazine concentration is released through a bypass exhaust line while the substrate is simultaneously annealed in H_2.

60 °C initial heating stage was added to reduce the impact of heating the container from varying room temperatures to the first temperature profile value. Additionally, an early spike in precursor temperature was needed to reduce the incubation time (points ii, iii), which was followed by a slowly increasing non-linear temperature ramping stage to counter precursor exhaustion (point iv). An example of the heating profile and the response in the release of borazine is shown in Figure 48a,b. Optimising such temperature profiles was difficult due to the very long delay in the measurement after changes in temperature. Once the profile was calibrated it was used for the synthesis experiments without further MS monitoring.

6.1.4. Hexagonal boron nitride synthesis and characterisation on nickel

The mechanism for hBN growth is expected to be analogous to graphene, as discussed in sections 2.2.3-2.2.4, in particular, H_2 gas is necessary to etch less stable defects and sp^3 deposits (equation 42). Therefore, if borazine profile is calibrated to produce a constant partial pressure between different experiments, controlling the flow of H_2 and the synthesis time is sufficient to control the type of material produced. Using the new control in the temperature profile it was possible to systematically and reproducibly study hBN synthesis on Ni foils. Thick triangular deposits, thin triangular deposits (monolayer to few-layer) of hBN were obtained (Figure 49a-d). However, hBN growth morphology was significantly different on different Ni grains. It was not possible to obtain a large-area uniform film. On each Ni foil some grains produced separated thin triangles, while others produced “wavy” patterns fully covered with hBN film as shown in Figure 49c. Additionally, multiple white speckles were observed on the samples (Figure 49d). These deposits are likely to be a results of a multiple B-, N- precursors entering the CVD system during ammonia borane decomposition (such as monomeric aminoborane or its oligomers) and have been observed elsewhere[264]. While these speckles did not seem to influence the growth of hBN triangles or interfere in how the triangles coalesced, methods need to be developed in

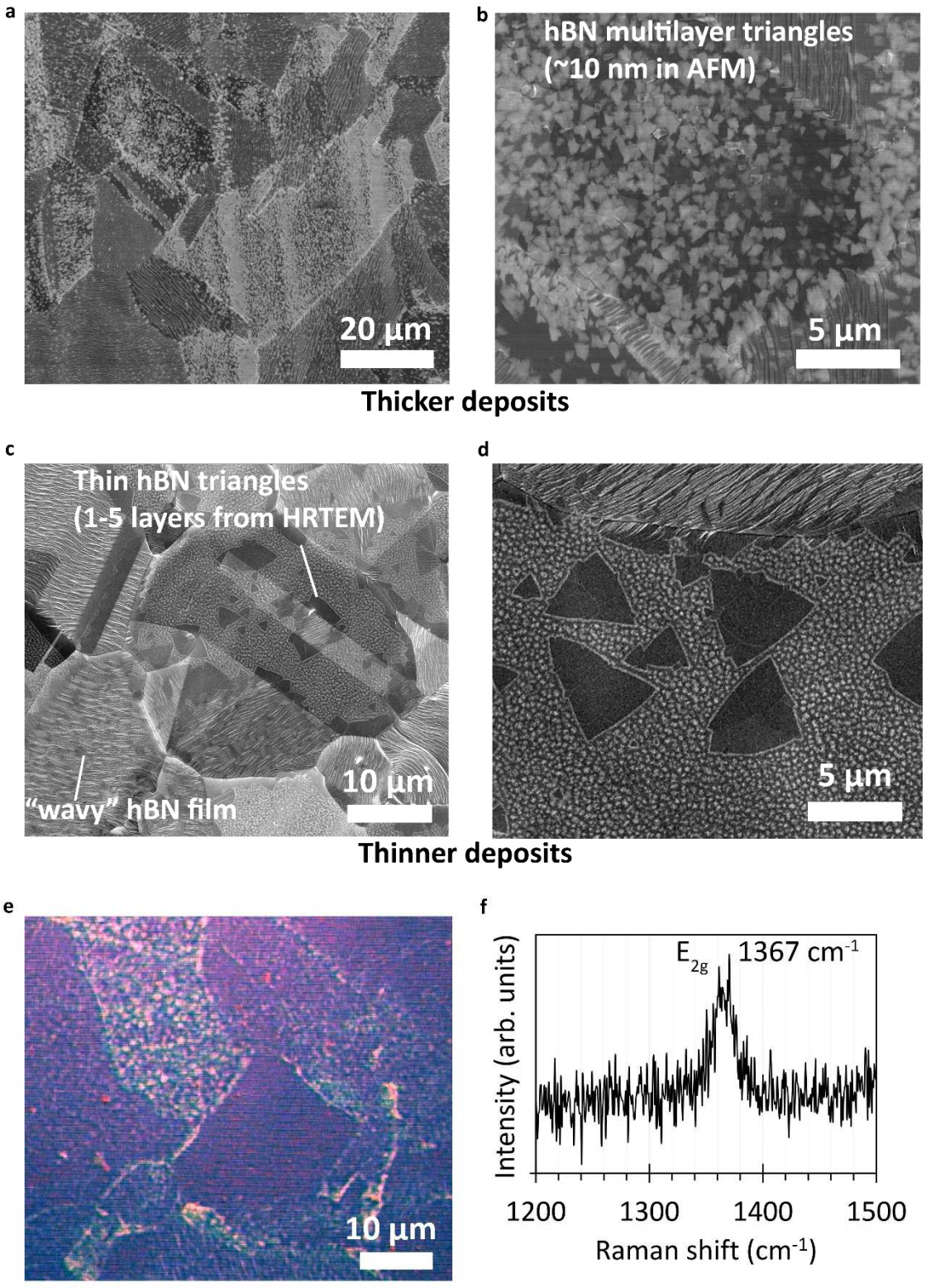

Figure 49. hBN synthesis on Ni foils. a-b) SEM micrographs of thicker hBN deposits showing white multilayer hBN domains. Deposition thickness and morphology greatly depends on the crystallographic orientation of Ni grains. c-d) Thinner depots (monolayer to few-layer): individual dark triangles and "wavy" deposits constituting a thin full coverage film. Additionally, white speckles are observed on the foil that are likely due to a secondary B, N precursor (aminoborane) entering the reaction tube. e) An optical image of the transferred hBN film with visible outlines of Ni grains due to non-uniform deposition on each grain. f) A Raman spectrum of the film with a characteristic hBN peak at around 1367 cm^{-1}.

future work to address the formation of these secondary deposits. For example, low pressure synthesis could suppress precursor decomposition or utilising a Pt substrate that would catalyse decomposition of aminoborane (proposed based on observations by Lu *et al* (2015)[264]).

Optical microscopy combined with Raman spectroscopy was used to confirm presence of the hexagonal phase of BN. As was mentioned in sections 3.2.1, 3.2.2 and 3.4.1 characterising hBN is much more difficult than graphene due to low contrast optically and in a SEM; additionally, diminishing peak intensity in Raman spectroscopy leads to difficulties in characterising thinner samples. Figure 49e shows an optical image of a thicker hBN deposited transferred from Ni to a Si/SiO_2 substrate. Outlines of Ni grains can be seen because of different thickness of the deposits and different morphology on individual grains. A characteristic Raman peak (Figure 49f) at 1367 cm^{-1} was recorded for these deposits confirming the presence of the hBN phase.

Foremost, methods need to be found to reduce the dependence of the growth on the underlying substrate or alternatively single crystal substrates could be utilised to achieve uniform deposition. Specific grain dependence on hBN flakes was investigated further with EBSD in the following chapter.

Dependence of hBN growth on Ni grain orientations

EBSD studies were performed to identify Ni grains which result in triangular hBN domains and also those that result in full coverage or empty regions. I used Matlab with the MTEX toolbox[265] to visually compare EBSD maps with SEM images (Figure 50a,b) in order to gather statistics on how Ni grain orientations influenced the morphology of hBN flakes. Grains close to Ni (111) orientation (Figure 50c) resulted in the highest hBN flake deposition with “wavy” morphology, confirmed by Raman spectra measurements. The topography of the grains is most likely a result of Ni surface steps and therefore anisotropic roughness of these grains. Increased deposition is a result of the increased nucleation density because of the roughness (similar to graphene and

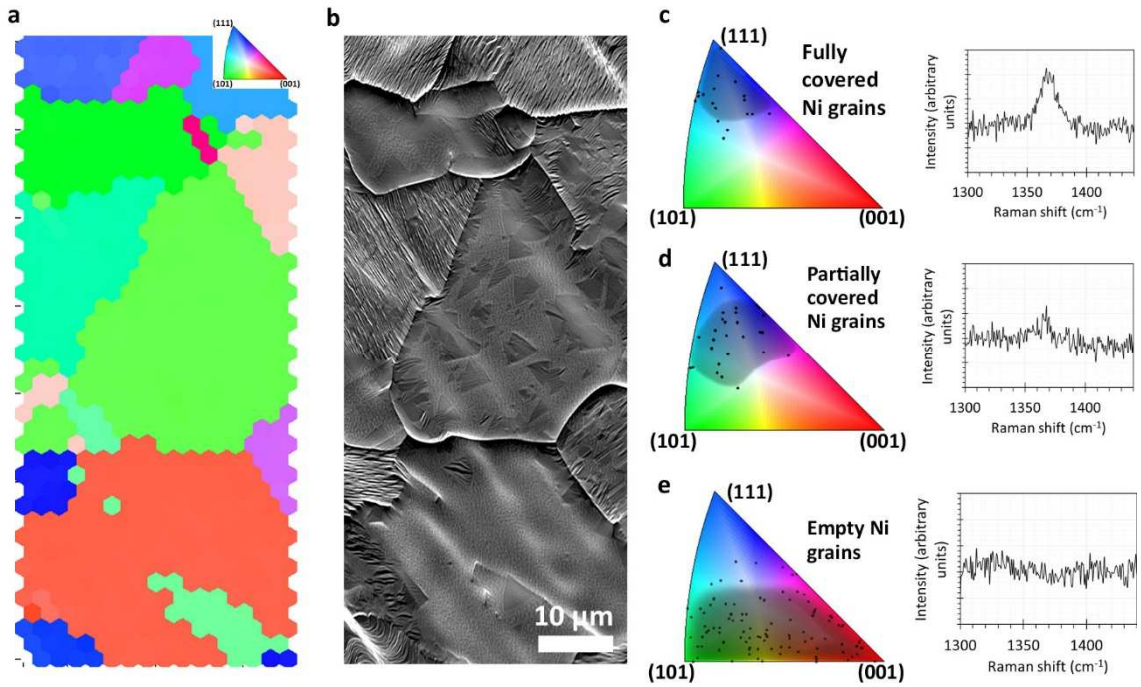

Figure 50. Dependence of hBN coverage on the Ni grain orientations. a) An EBSD map of an exemplar Ni substrate, coloured following an inverse pole figure. b) A corresponding SEM image showing fully covered ("wavy"), partially covered and empty Ni grains. c-e) Inverse pole figures showing the statistical sample of orientations for each of the three cases: fully covered grains, partially covered and empty Ni grains respectively. Shaded area is a guide to the eye of the average trend. The colour coding for the inverse pole figures is for lattice planes in the normal direction to the sample. Adjacent are the corresponding representative Raman spectra of fully covered, partially covered and empty grains recorded directly on Ni to confirm the observed correlation.

is seen again in the following section on not electropolished Cu). Grains further from Ni(111), near the middle of the inverse pole figure (Figure 50d) that were not as rough and had partial coverage with triangular hBN domains. And finally, grains close to the (101) and (001) orientations (Figure 50e) had less deposits and were either empty or with small hBN domains. Only a small sample of orientations (texture) of Ni grains were available on the utilised Ni foils and most importantly, almost no perfect (111), (101) or (001) grains were sampled, which means that the statistical analysis (Figure 50c-e) is only indicative.

From this investigation it is possible to cautiously suggest that Ni substrates, whether polycrystalline or widely available single crystals are unsuitable for uniform, large area hBN synthesis. Ni(111) grain orientation resulted in very rough hBN deposits, while Ni(101) and Ni(001) resulted in low deposition. Uncommon grain orientations showed good quality material

deposition, but are unsuitable for industrial production. Other substrates or methods need to be explored.

6.1.5. Hexagonal boron nitride synthesis and characterisation on copper

Cu was explored as an alternative substrate to Ni. Much more uniform films could be grown on Cu that could be suitable for applications. Although some dependence in hBN domains' morphology on the crystallographic orientation was found (discussed later in this chapter), crucially, the thickness remained consistent. Effects of electropolishing on the nucleation density of hBN domains were explored. Similar to graphene, the nucleation density reduced significantly after electropolishing (same methods as described in section 4.3.3). Consequently, films with larger hBN crystallites could be achieved. Figure 51a shows the difference between electropolished and not electropolished regions.

Additionally, a bimodal domain size distribution was observed (Figure 51b) for hBN synthesises on Cu with the ammonia borane precursor, similar to hBN deposition observed on Ni substrates and previous studies on Cu[264]. It is expected that multiple volatile precursors can enter the CVD

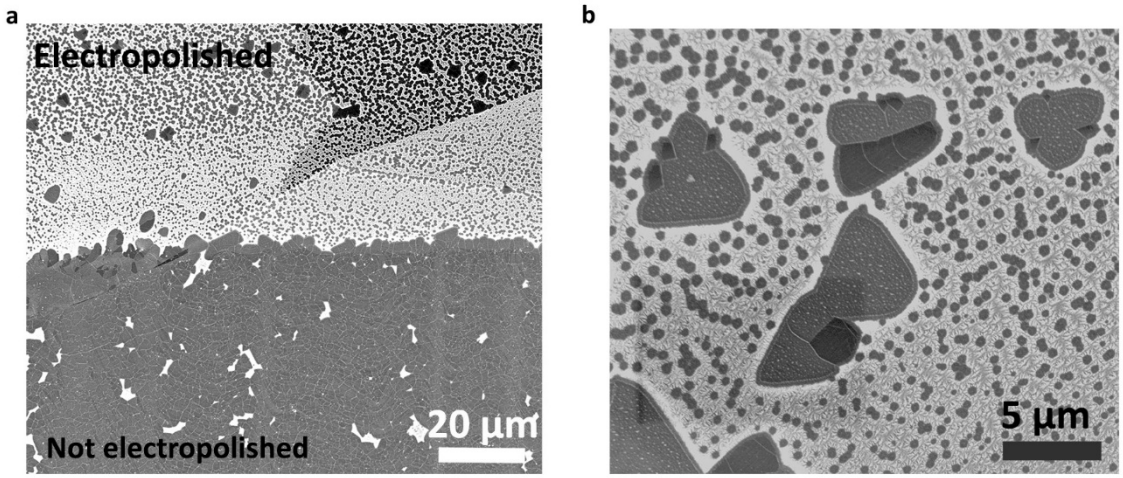

Figure 51. hBN growth on Cu. a) Effect of electropolishing on the nucleation density. Much more deposition is observed on rough, not electropolished Cu. b) A commonly observed bimodal distribution of shapes on Cu substrate: large geometric shapes and small circular, "fuzzy" deposits. Most likely these form due to multiple BN precursors entering the reaction tube. The former is expected to be crystalline, while the latter is amorphous[264].

system resulting in two different morphologies of the deposits. Geometrically-shaped domains are expected to be more crystalline, while the circular, "fuzzy" deposits are expected to be more defective. An alternative reason for the formation of the circular deposits could be growth during the cooling stage of the CVD process, where the conditions are not balanced for crystalline deposits. Geometric shapes were surrounded with a boundary of the "fuzzy" deposits, of the same thickness as the radius of the small circles (Figure 51b).

A systematic synthesis parameter investigation was performed to explore the effects of CVD variables on the type of material produced. The borazine mole fraction (in ppm) and the synthesis time can be regarded as the characteristic synthesis parameters, although it does not quantify the absolute flow of B-, N- species, only relative. The former was determined with MS when heated with a temperature profile as described previously for a mixture of ammonia borane and BN powder (1:10) with a total mass of 110 mg under 500 sccm H_2 gas flow. The values were then scaled for different H_2 flow rates. The furnace temperature was set to 1040 °C.

Table 8 summarises the typical experimental parameters for hBN synthesis on Cu. Corresponding SEM images of the experiments A-F are shown in Figure 52a-f. It is evident that increasing the mole fraction of borazine or increasing the synthesis time leads to more deposition. Initially, small triangles formed surrounded by amorphous deposits. The two types of deposits could be distinguished from topography (Figure 52b, inset) because hBN triangles had corrugated morphology; likely due to Cu substrate contraction during cooling of the CVD system. Crystalline deposits increased in size with time, while amorphous deposits did not

Experiment	$B_3N_3H_6$ (ppm)	Time (mins)	Electropolishing	Synthesis temperature
A	0.5	5	✓	1040 °C
B	0.8	5	✓	1040 °C
C	0.8	60	✓	1040 °C
D	0.8	60	✗	1040 °C
E	1.2	15	✓	1040 °C
F	25	10	✓	1040 °C

Table 8. Synthesis parameters for hBN growth on Cu (representative examples are given and only relative ppm level comparison should be used).

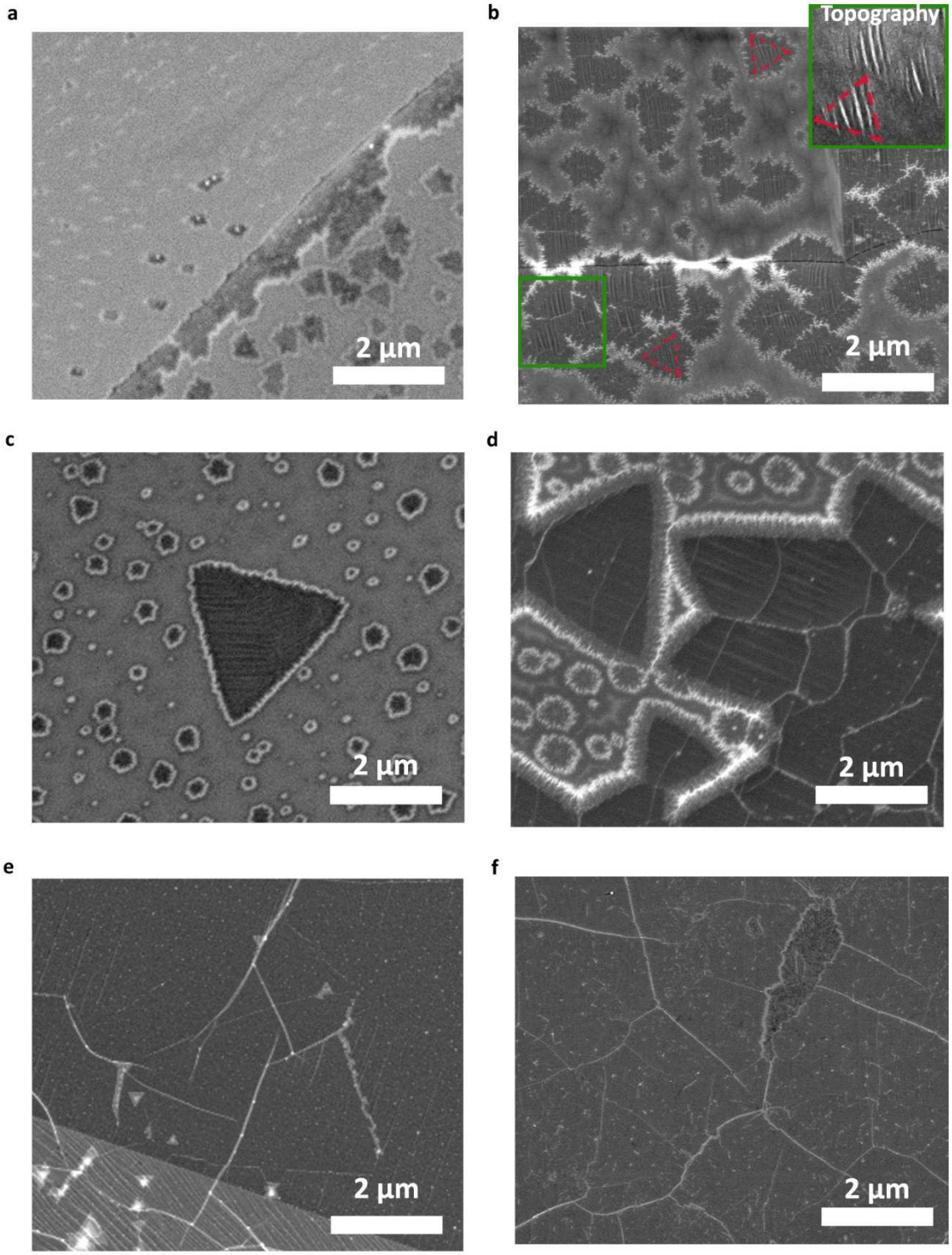

Figure 52. Synthesis parameter investigation of hBN on electropolished Cu complimentary to table 8. a-f) SEM images of experiments A-F (table 8). Higher borazine mole fraction and longer synthesis time result in more deposition. A bimodal domain size distribution is also observed, however, crystalline hBN triangles displace circular, amorphous deposits as they grown, eventually coalescing into a polycrystalline film. hBN multilayers appear as white triangles.

change, which made it possible to distinguish larger triangular shapes (Figure 52c). When triangular deposits were close to each other they were not influences by amorphous deposits and seamlessly coalesced as shown in Figure 52d. In thinner hBN films (Figure 52e), occasional thicker multilayer deposits could also be distinguished in SEM and appeared as small white triangles or lines. Finally, if the borazine mole fraction was set very high, thick multilayer hBN films could be grown at high rates (Figure 52f) with thicknesses from 5-50 nm (measured by optical profilometry).

hBN characterisation

hBN domains were characterised optically, with Raman spectroscopy and TEM in addition to SEM micrographs. The polymer-assisted transfer method described in section 3.1 was used to transfer hBN to TEM grids and to Si/SiO_2 tiles. Sufficiently large area of pristine hBN were

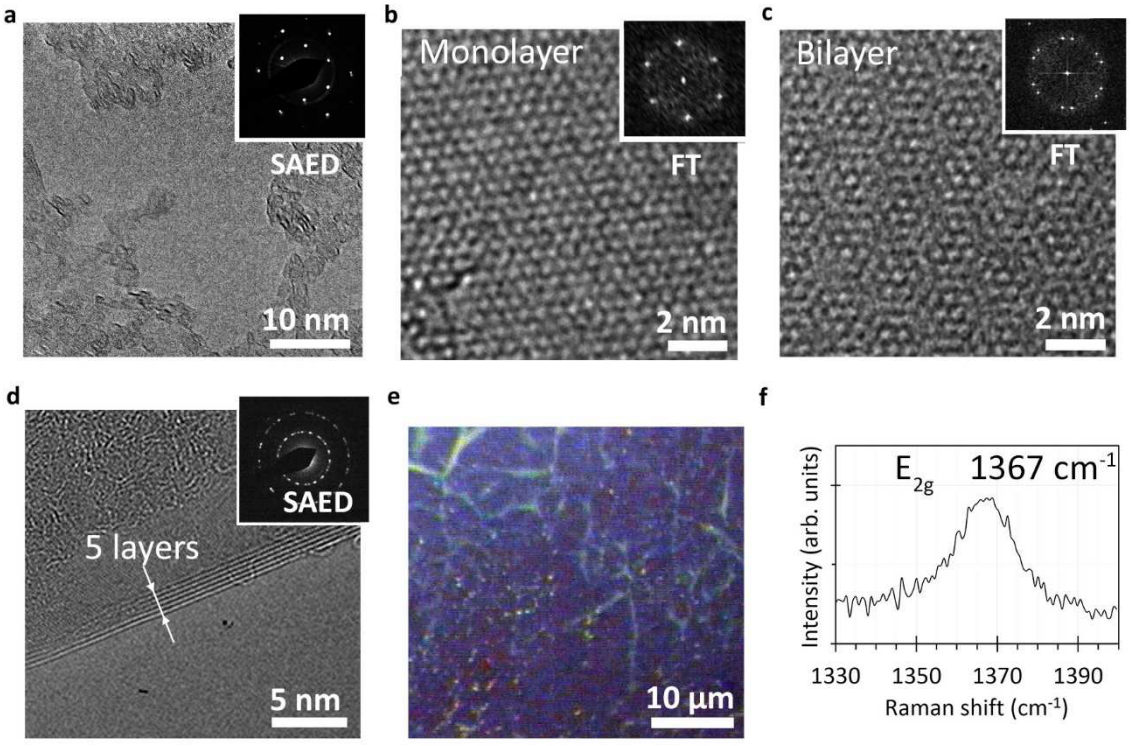

Figure 53. Characterisation of hBN films grown on Cu. a) A low magnification TEM image showing large area transferred hBN film. Inset: a SAED pattern indicating predominantly monolayer hBN. b-c) Bright field AC-TEM lattice-resolved images of monolayer and bilayer hBN regions on the same sample. The latter shows a characteristic Moire pattern. Insets: Fourier transforms of the regions are shown. Images taken by Dr Judy Britton. d) An AC-TEM image of a thicker region on sample, consisting of with 3-5 hBN layers. Image taken by Dr Judy Britton. e) Optical image of the thicker hBN film transferred to a Si/SiO_2 substrate. f) A characteristic hBN Raman peak at 1367 cm^{-1} was observed from the transferred film.

obtained for TEM characterisation (Figure 53a). AC-TEM images of the thinner hBN film were recorded by Dr Jude Britton. This sample correspond to experiment E in table 8 and to the SEM micrograph in Figure 52e. Regions of monolayer, bilayer and up to 5 layers were identified on the sample as shown in Figure 53a-d.

Thicker films were transferred to Si/SiO_2 substrates with the polymer-assisted method (Figure 53e). Raman spectra exhibited a characteristic hBN peak at around 1367 cm^{-1} (Figure 53e). Optical profilometry was used to measure the thickness of the thicker films and by controlling the H_2 flow it was possible to synthesise uniform hBN with thickness between few nm to 50 nm.

Dependence of hBN growth on Cu grain orientations

Similarly to the methods for Ni, the correlation between hBN domain morphology and Cu grain orientation was investigated with EBSD. The thickness and nucleation density of hBN domains were not significantly influenced, however, flake growth rate and shape had subtle dependence on grain orientations. The most likely reason is the lower roughness of Cu grain on the pristine foil, which is further reduced with electropolishing. Orientations near (111) resulted in slightly smaller domains with circular or with a truncated tringle shape (Figure 54a). Cu grains near (101) and (001) produced triangular flakes, typically with one distorted vertex or obtuse triangles respectively. These findings are different to other reports[266] in the literature, where nearly equilateral triangular domains were produced on all grains. However, the difference in the synthesis methods (low pressure vs. atmospheric pressure) or different textures of Cu foils could be possible explanations. The foils that I utilised (Alfa Aesar, annealed, uncoated, 99.8 % purity) did not have the common lattice planes, but rather complicated directions, for example, (1 1 12) and not (001). Other studies[266] investigated near perfect (111), (001) and (101) grains.

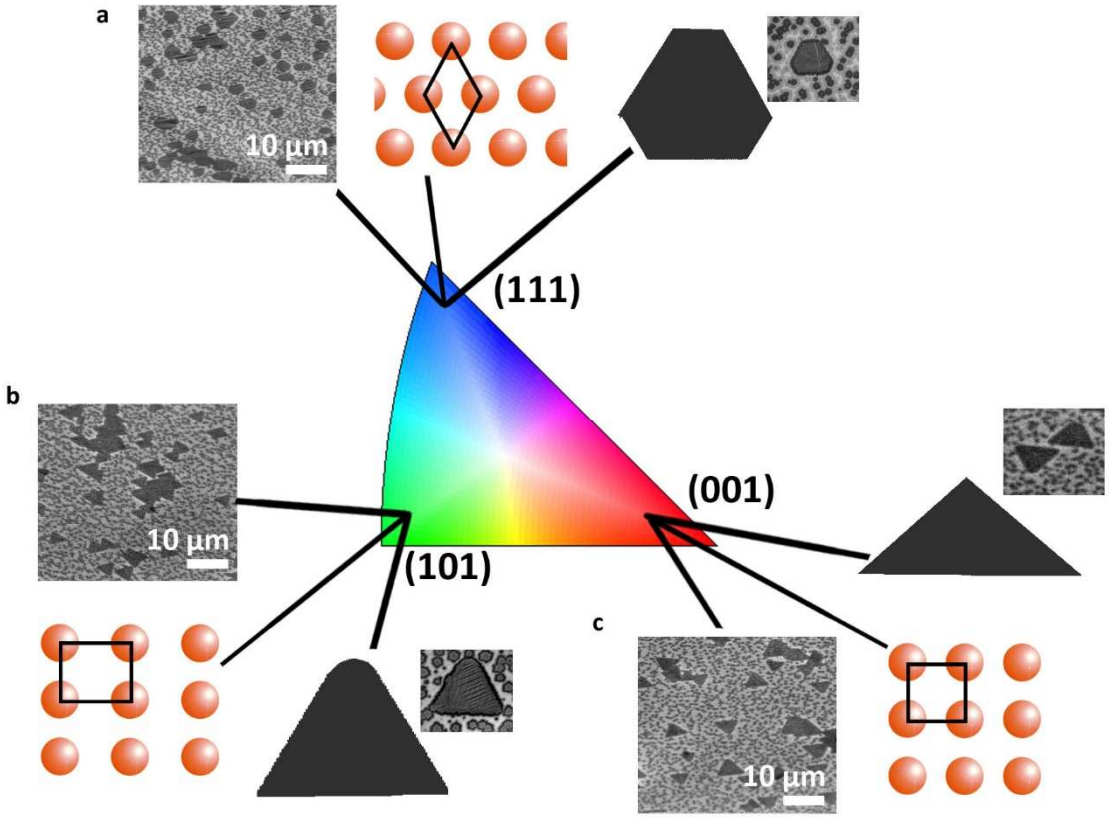

Figure 54. hBN domain morphology dependency on the crystallographic orientation of Cu. a)-c) Overview SEM micrographs are shown for grains close to (111), (101) and (001) respectively, showing the nucleation density and size of hBN domains. Additionally, diagrams of the lattice of the Cu grains and typical hBN domain shapes are shown. The colour coding for the inverse pole figures is for lattice planes in the normal direction to the sample.

hBN synthesis conclusions

Precursor chemistry has significant influence on the CVD synthesis of hBN. Ammonia borane is a complicated precursor to control, but is widely available, stable and safer than the alternatives. By understanding the chemistry of the precursor and its evolution with time I was able to develop methods needed to controllably deliver volatile decomposition species to the substrate. Custom temperature profiles and other methods were developed to synthesise good quality hBN films. Synthesis experiments were performed on Ni and Cu substrates. Ni was found to form significantly more hBN material on the surface compared to Cu, but the thickness of the deposits and their morphology drastically changed from one grain orientation to another. The growth rate on Cu was slower, but the thickness of hBN deposits was very uniform across the whole

sample. Similar to graphene, this can be explained by the lower catalytic ability of Cu compared to Ni for decomposing the hBN precursor. A bimodal domain size distribution was found on Ni and Cu, similar to previous reports[264], and most likely formed due to multiple volatile species entering the CVD system from ammonia borane decomposition or from amorphous BN deposition during the cooling stage of the CVD process. While, less crystalline deposits did not seem to affect the growth of triangular hBN domains or stopped them from merging, the mechanism should be further investigated in future work.

6.2. Gas-phase precursors for catalyst-free WS_2 synthesis*

Monolayer WS_2 is a recently discovered 2D material that possesses "extraordinary" PL at room temperature[73] and is a promising candidate for a variety of applications as discussed in section 1.2.3. Only a small number of methods for synthesising WS_2 or other TMDCs have been shown in the literature prompting the necessity to find novel precursors and chemistries that are easier to control in order to tailor TMDC materials. One commonly used CVD approach in the literature is the sulfurisation of WO_3 at high temperatures[73]. However, developing suitable controls for this process remains challenging due to the low volatility of WO_3. For example, Rong *et al* (2014)[267] explored ways of tailoring the synthesis by varying the starting time for heating the S precursor, while WO_3 was simultaneously gradually heated. With this method, however, it was not known when the reaction started, at what temperature and for how long. The concentrations of precursor vapours continuously varied with time and also spatially, leading to inhomogeneous deposits. To overcome the above problems precursor vapours need to be controllably introduced at a constant level and stopped rapidly to make the synthesis time a meaningful parameter. For this reason, precursors that produce appreciable vapour pressure at lower temperatures need to be studied to improve the continuity and quality of WS_2 films.

Preliminary experiments

Initial synthesis experiments were performed with WCl_6 and S precursors, following previous work in the group in nanoflowers synthesis[268] and a report by Okada *et al* (2014)[124]. The latter study found methods to synthesise triangular monolayer WS_2 domains with lateral dimensions of approximately 2 μm on exfoliated hBN crystals. Larger area (> 20 μm) monolayer WS_2 domains, however, have not been realised with this or other volatile W precursors. In preliminary experiments, WS_2 domains were only occasionally synthesised and the experiments where monolayer WS_2 was formed were not reproducible (monolayer signatures were

* A patent related to this work was filed on 24/03/2016. Application number GB1605121.1.

measured with Raman spectroscopy and PL). Only where large quantities of WCl_6 and S were evaporated produced consistent deposits. These deposits, however, were small (< 1 µm) triangular particles or nanoflowers. One possibility was that the CVD system did not have sufficient precursor controls to achieve reproducibility, but after multiple changes and upgrades to the CVD system the matter remained. I therefore changed the focus of my investigation from improving the apparatus to studying the precursor chemistry as will be discussed in the remainder of this chapter.

Volatile precursor analysis for WS_2 synthesis

A number of widely-available volatile tungsten precursors exist, most importantly tungsten hexachloride (WCl_6), tungsten dioxide dichloride (WO_2Cl_2) and tungsten oxychloride ($WOCl_4$). The vapour pressures of these compounds versus temperature are shown in Figure 55a. As discussed previously, WCl_6 has been shown to produce WS_2 deposits[124], however, during my preliminary experiments it was found that the precursor was moisture and air sensitive and slowly oxidised. The colour of WCl_6 changed from dark grey to a combination of red and yellow (Figure 55b-e). The former is the colour of $WOCl_4$ and the latter is the colour of WO_2Cl_2. While WO_2Cl_2 does not pose a problem because it is the least volatile[269], the formation of the much more volatile $WOCl_4$ presents a significant problem in delivering a consistent W molar flux. For

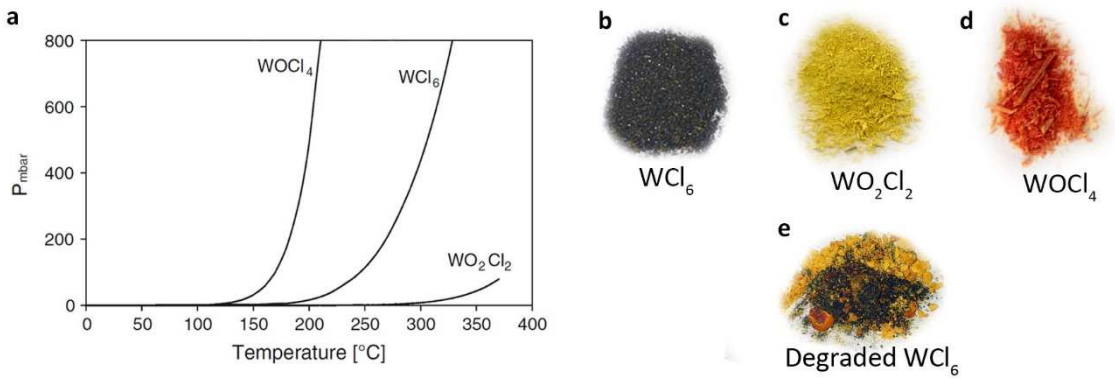

Figure 55. Volatile W precursors. a) Partial pressure of $WOCl_4$, WCl_6 and WO_2Cl_2. Adapted from ref. 269. b-d) Colours of pristine WCl_6, WO_2Cl_2 and $WOCl_4$ precursors respectively. e) Air degraded WCl_6 precursor, showing an orange mixture of $WOCl_4$ (red) and WO_2Cl_2 (yellow) particles.

example, if 5 % of WCl_6 were to be converted to $WOCl_4$, then during synthesis when heated to 200 °C, there would be a spike in the tungsten precursor flux double the required amount. Furthermore, WCl_6 only produces appreciable vapour pressure at higher temperature compared to $WOCl_4$ which requires a three-stage furnace apparatus and does not deliver acceptable control of the evaporation. For these reasons I chose to investigate the $WOCl_4$ precursor (Sigma-Aldrich, 98 %) heated with a custom-built electrical jacket (appendix 9-D) that ensured a very accurate temperature control (± 3 °C). While it is also known that $WOCl_4$ decomposes to WO_2Cl_2 when in contact with moisture, the latter does not pose a significant problem due to lower volatility. The most relevant precursor degradation and decomposition reactions are presented below.

$$WCl_6 + H_2O \rightarrow WOCl_4 + 2\ HCl \quad (43)$$

$$WCl_6 + 0.5\ O_2 \rightarrow WOCl_4 + Cl_2 \quad (44)$$

$$WOCl_4 + H_2O \rightarrow WO_2Cl_2 + 2\ HCl \quad (45)$$

Tailoring precursor thermodynamics

Experiments with $WOCl_4$ and S precursors also resulted in irreproducibility specifically for thin WS_2 deposits, even for experiments at low pressure that typically allow better precursor controls. It was therefore necessary to understand the chemistry of reactions inside the CVD system for these precursors, as it was the most probably explanation for the unsuccessful results. The naively expected reaction that allows WS_2 synthesis from the chloride and sulfur precursors would require S to displace O and Cl atoms from the $WOCl_4$ molecules and is generalised as follows (S_8 is selected because it dominates sulfur vapour at ~ 300 °C[118]):

$$WOCl_4 + 0.6\ S_8 \rightleftharpoons WS_2 + 0.5\ SO_2 + 2\ SCl_2 \quad (46)$$

However, this reaction is not thermodynamically favourable and therefore does not proceed efficiently. I utilised the Fact compound databases[123] through the Fact-Web[123] suite of

interactive programs to calculate the most thermodynamically favourable products of various precursor combinations at 800 °C. Equation 46 can be corrected with the following thermodynamically favourable equation (note, such equations can be considered a probability distribution of products based on the thermodynamics to form each individual product and are a better representation of real systems):

$$WOCl_4 + 0.6\ S_8 \rightleftharpoons \mathbf{0.1}\ WS_2 + 0.5\ WO_2Cl_2 + 0.4\ WCl_4 + 1.5\ S_2 + 0.4\ SCl_2 + 0.2\ S_2Cl + ... \quad (47)$$

Most notably, very small quantity of WS_2 is formed in this reaction (similar for WCl_6 and S), which explains the irreproducibility and points to significant influences of contamination in between experiments. It is possible to try to shift the equilibrium of this reaction towards product formation, such that the very low efficiency reaction still results in measurable WS_2 quantity. For example (note, S_2 sulfur allotrope forms at 800 °C),

$$WOCl_4 + 2.5\ S_8 \rightleftharpoons \mathbf{0.4}\ WS_2 + 8\ S_2 + 0.7\ SCl_2 + 0.6\ S_2Cl + 0.5\ WO_2Cl_2 + 0.4\ S_3 + \ldots \quad (48)$$

In this case, however, 86 % of sulfur simply passes through the system and deposits on the CVD system components, making the tactic unpractical. So far, this approach (with WCl_6 and S) resulted either in bulk 3D deposits[268] (nanoflowers) or small WS_2 domains[124] according to previous studies. The reason behind unfavourable thermodynamics can be understood by considering the stability of the products: S will rapidly remove O group from $WOCl_4$, but its affinity for Cl is very low, leading to the formation of WO_2Cl_2 which simply passes through the system.

I identified a strategy to alter the thermodynamics to nearly 100 % efficiency for WS_2 production by introducing a third reactant that easily strips chlorine atoms from $WOCl_4$. Hydrogen was chosen because of formation of very stable HCl when reacted with chlorine. Conveniently, it also forms stable H_2O when reacted with oxygen, meaning that the oxygen group will be removed from $WOCl_4$ easily. With addition of H_2 equation 47 can be replaced with:

$$WOCl_4 + 0.6\ S_8 + 3\ H_2 \rightleftarrows \mathbf{0.998}\ WS_2 + 4\ HCl + 0.7\ H_2O + S_2 + 0.3\ H_2S + 0.2\ SO_2 + \ldots \quad (49)$$

Using only small quantities of S and H_2 leads to almost full conversion of $WOCl_4$ to WS_2. Experimental observations supported this calculations because the fused silica tube was completely covered with a dark deposit when a small amount of H_2 was added, whereas without H_2 there was no visible deposit. This reaction is equivalent to using $WOCl_4$ and H_2S precursors, which has been employed in previous studies[270, 271] (with WCl_6 and H_2S), but only resulted in nanoparticles, nanotube and nanosheets, likely because there was no chemical mechanism that could discriminate between defective and crystalline deposits. Indeed, as will be shown later in this section, the deposition of WS_2 increased dramatically, however, irregularly-shaped, defective nanocrystalline deposits or nanoflowers were produced.

I hypothesised another alteration to the precursor chemistry based on the fact that in graphene and hBN syntheses there is a mechanism to distinguish between stable crystalline and less stable, defective deposits using an etching gas. For WS_2 synthesis this etching agent could be O_2 or its derivatives (SO_2, H_2O etc.) because the reaction between WO_3 and S (equation 6) produces highly crystalline deposits[73]. I therefore investigated the addition of small and rigorously controller quantity of oxygen with the aim to achieve the following reaction (note, S_8 and O_2 molar coefficients in the thermodynamic calculation were chosen close to the experimentally determined parameters, presented later in the section):

$$WS_{2(crystalline)} + (x)\ WS_{2(defective)} + 0.4\ S_8 + 0.25\ O_2 \rightleftarrows WS_{2(crystalline)} + 10^{-18}\ WO_{3(gas)} + \quad (50)$$
$$+ S_2\ (gas) + 0.2\ SO_2\ (gas) + \ldots$$

With four independent precursors and three CVD variables (substrate temperature, total flow rate and time) the parameter space becomes extraordinarily large, nevertheless, useful trends and materials have been obtained as described in the remainder of this chapter.

Synthesis parameter trends

To narrow the parameters space, set values were chosen for the substrate temperature (800 °C), synthesis time (20 minutes) and the total flow rate (200 sccm). The values were selected because of considerations of thermodynamics, human error and the boundary layers respectively. The synthesis procedure consisted of heating S precursor (in excess, 500 mg) to 270 °C in Ar flow (200 sccm) for 20 minutes to set up an equilibrium evaporation regime while simultaneously annealing the sapphire substrate in S vapour at 800 °C. Immediately after, a pre-heated electrical jacket (135 °C) was moved over the fused silica vial containing $WOCl_4$ precursor and the gas composition was changed to a mixture of pure Ar, Ar with 2.5 % H_2 and Ar with 0.01 % O_2 for 20 minutes, while keeping the total flow rate at 200 sccm throughout. Table 9 presents the parameters used in exemplar experiments.

Addition of only H_2 (as in equation 49) resulted in highly efficient precursor conversion, but irregular-sized, polycrystalline flakes with variable number of layers were formed (experiment A_w, Figure 56a). Raman spectroscopy (section 3.4.1) showed a low ratio of A_{1g} and E^1_{2g} peaks of around 0.23, characteristic for thin deposits[65], however PL measurements (normalised to the sapphire peak at 694 nm) did not result in a high intensity (Figure 57a) suggesting low quality deposits. Such nanocrystalline domains are similar to those produced with the gas-phase synthesis using WCl_6 reported elsewhere[264]. To improve the quality, the effects of adding H_2 and O_2 together were systematically investigated (following equation 50). Small addition of O_2 to

Experi-ment	Ar flow rate (sccm)	Ar/H_2 (2.5%) flow rate (sccm)	Ar/O_2 (0.1%) flow rate (sccm)	S mass evaporation rate (mg min^{-1})	Approximate* molar ratio $WOCl_4$:S:H_2:O_2	Time (mins)
A_W	195	5	0	1	1 : 2.1 : 0.4 : 0.00	20
B_W	180	5	15	2	1 : 4.2 : 0.4 : 0.04	20
C_W	175	10	15	2.4	1 : 5.0 : 0.7 : 0.04	20
D_W	165	20	15	2.2	1 : 4.6 : 1.5 : 0.04	20
E_W	140	20	40	1.9	1 : 4.0 : 1.5 : 0.12	20
F_W	100	20	80	2.5	1 : 5.2 : 1.5 : 0.24	20

Table 9. Synthesis parameters of exemplar WS_2 experiments. Hydrogen trend experiments are highlighted in red and oxygen trend experiments are highlighted in green. (*) The molar flux of W was approximated as 1.5E-5 moles min^{-1} from approximate weight loss and vapour pressure considerations.

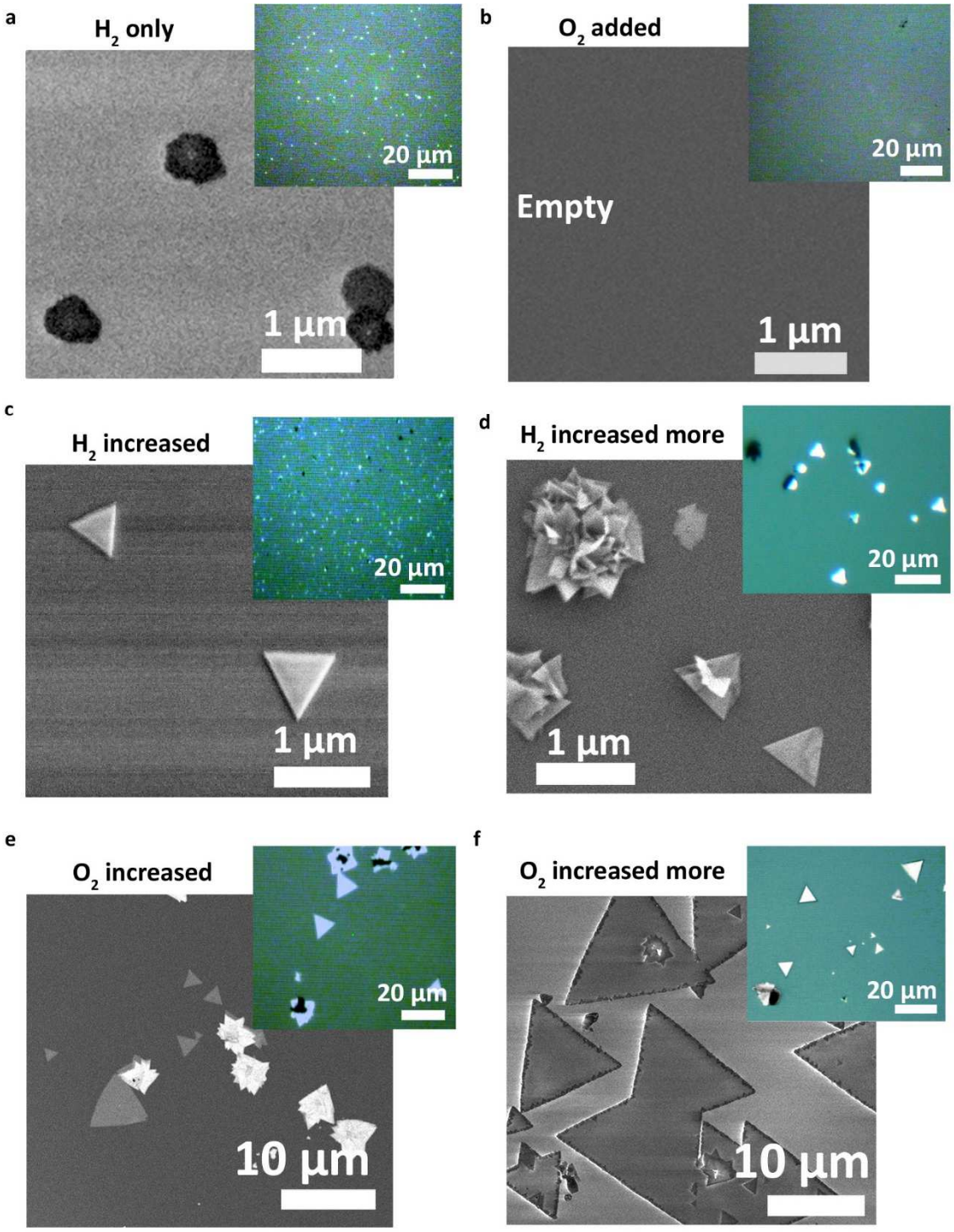

Figure 56. SEM micrographs of WS_2 material synthesised with varying the H_2 and O_2 mole fractions, corresponding to experiments in table 9. Insets are optical images of the samples. a) H_2-only synthesis resulted in very small, circular, polycrystalline WS_2 domains forming. b) A small amount of O_2 is added with the same H_2 flow, resulting in no deposition due to etching by the oxide species. c-d) H_2 is doubled and doubled again resulting in small thick triangular deposits and bulk triangular deposits mixed with nanoflowers respectively. Triangular shape indicates improved crystallinity due to defect etching by the oxide species. e-f) H_2 level is kept constant, while O_2 level is doubled and double again. As a result small thin triangles intermixed with thick triangles and large thin triangles appeared respectively. The latter had completely monolayer triangular domains with lateral dimension of 20 µm (or 40 µm domains for monolayers with patches of multilayers).

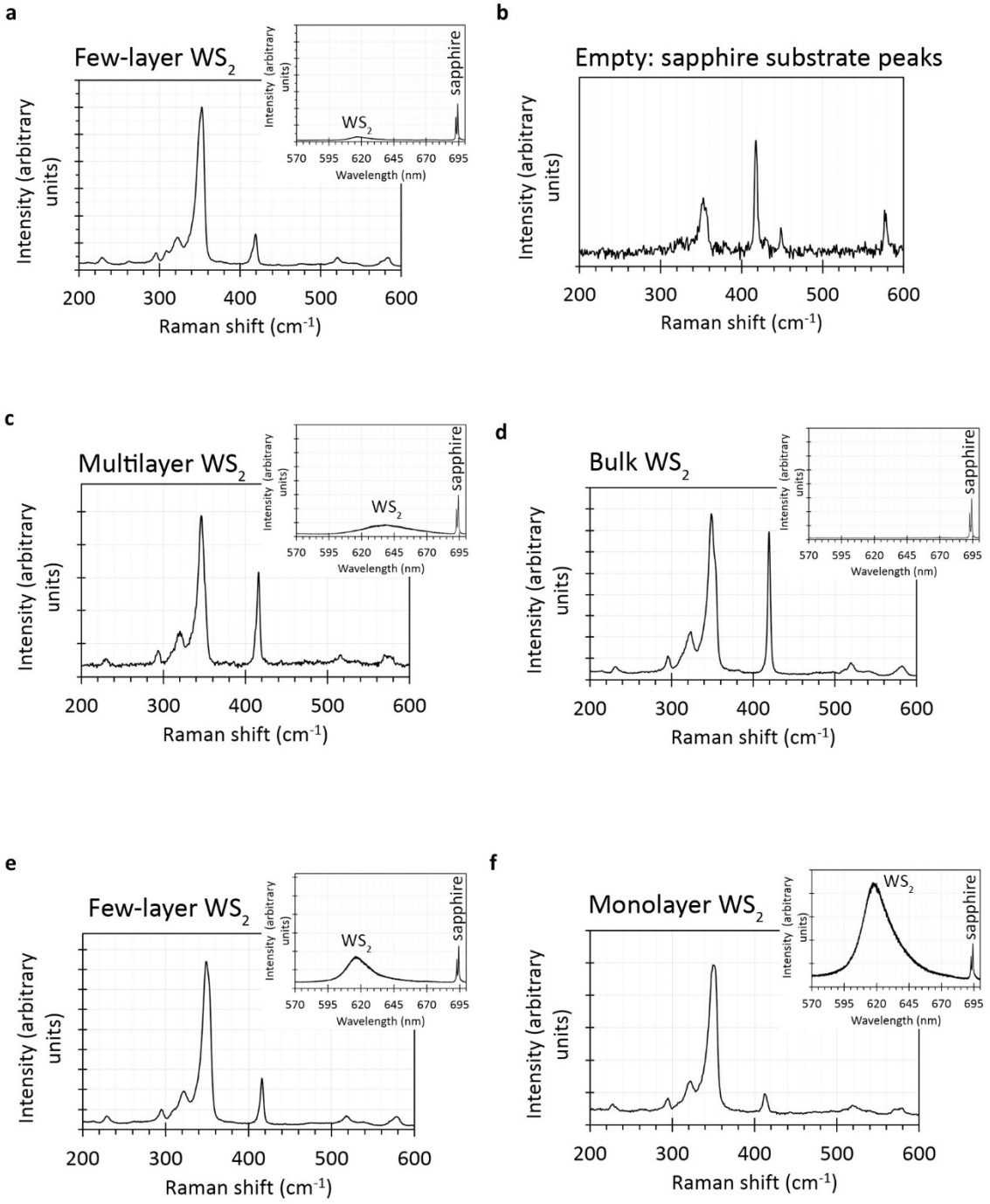

Figure 57. Raman and PL spectra (insets) corresponding to experiments in Table 9 are shown to estimate the thickness of WS_2 domains. a) Polycrystalline domains showed a weak PL peak, although the thickness of the domains was low (likely few layers). Possibly this is due to the small size and defects in the deposits. b) When O_2 was added, the synthesis did not produce any deposits, as expected due to the proposed etching mechanism. c-d) Increasing the amount of H_2 produced more and thicker deposits. The highest amount of H_2 resulted in bulk WS_2 and nanoflowers. e-f) Increasing the amount of O_2 produced thinner and larger deposits. The highest amount of O_2 resulted in monolayer WS_2 with good PL at around 618 nm.

experiment A_w (Table 9) resulted in no deposition of WS_2 (experiment B_w, Figure 56b, Figure 57c), as explained by the etching mechanism in equation 50. However, on subsequent increases in H_2 flow rate in experiments C_w, D_w, highly crystalline, triangular deposits of WS_2 appeared (Figure 56c,d). The domains were very small (~1 μm) and thick, with occasional WS_2 nanoflower deposits (Figure 56d). Raman spectra and the low intensity PL measurements (Figure 57c,d) confirmed multilayer and bulk WS_2 deposits respectively. Therefore, further O_2 addition was warranted to try to make the deposits thinner. As expected, thinner, but also larger triangular WS_2 domains started to appear intermixed with thicker domains when O_2 was doubled (experiment E_w, Figure 56e, Figure 57e). Finally, when O_2 flow was doubled again, many monolayer WS_2 triangles appeared with lateral dimensions of 20 μm or monolayers with small multilayers of 40 μm in size (experiment F_w, Figure 56f), confirmed by the characteristic Raman spectrum (Figure 57f). Most importantly, a very high PL intensity at 618 nm with a narrow spectral bandwidth of 25 nm was observed (Figure 57f, inset) from these monolayer deposits which show promise for the highly sought optoelectronic applications.

WS_2 synthesis conclusions

In this study I identified a suitable gas-phase $WOCl_4$ precursor for WS_2 synthesis that produces appreciable vapour pressure at low temperatures. Many challenges in the CVD apparatus and the synthesis procedure have also been identified and addressed. By proposing a novel precursor chemistry I was able to improve the synthesis efficiency significantly and to bias the reaction towards more crystalline deposits, which also suggests a possible etching mechanism for the gas-phase reactions that are not well understood in the literature[263,264] and so far led to poor quality materials. Triangular monolayer domains with lateral dimensions of 20 μm and good PL have been achieved, which is about an order of magnitude higher than what has been reported with the volatile chloride precursors[124].

6.3. Heterostructures

6.3.1. Graphene and hexagonal boron nitride lateral heterostructures

It has been shown in the literature that transferring graphene onto hBN can lead to significant improvement in the charge carrier mobility[59]. However, this process causes contamination and damage, as discussed in section 3.1. For this reason attempts have been made to grow graphene directly on hBN or vice versa[272], however, Raman spectroscopy showed that the reactant atmosphere for hBN etched graphene, making it more defective and introduced doping[272]. Nevertheless, instead of stacked growth, a number of studies investigated engineered in-plane hBN-graphene heterostructures where lithography was used to make defined trenches in hBN that were "filled" with graphene[273], thus forming circuits and atomically-thin devices. This approach is possible because hBN and graphene have a very small lattice mismatch of 2 %[52] and have been shown to seamlessly connect their unit cells[274]. A number of applications have been proposed such as flexible, light circuits, 2D vibrating resonators in nanoelectromechanical systems and optical devices[273]. So far, only low pressure synthesis methods have been utilised to produce the structures, posing a question whether same etching processes occur at atmospheric pressure and whether the methods can be adapted to the safer and more convenient APCVD configuration. To answer these questions I investigated the synthesis methods at atmospheric pressure to produce lateral heterostructure patchworks with the new controls discussed in sections 4.3 and 6.1.

Experimental

Sequential synthesis of graphene followed by hBN was investigated on Cu; CH_4 (8.1 sccm) and H_2 (500 sccm) gases were introduced for 60 minutes, followed by heating ammonia borane according to the optimised temperature profile (section 6.1.3) for 30 minutes. A very sharp interface (Figure 58a) was observed between graphene and the surrounding hBN domains,

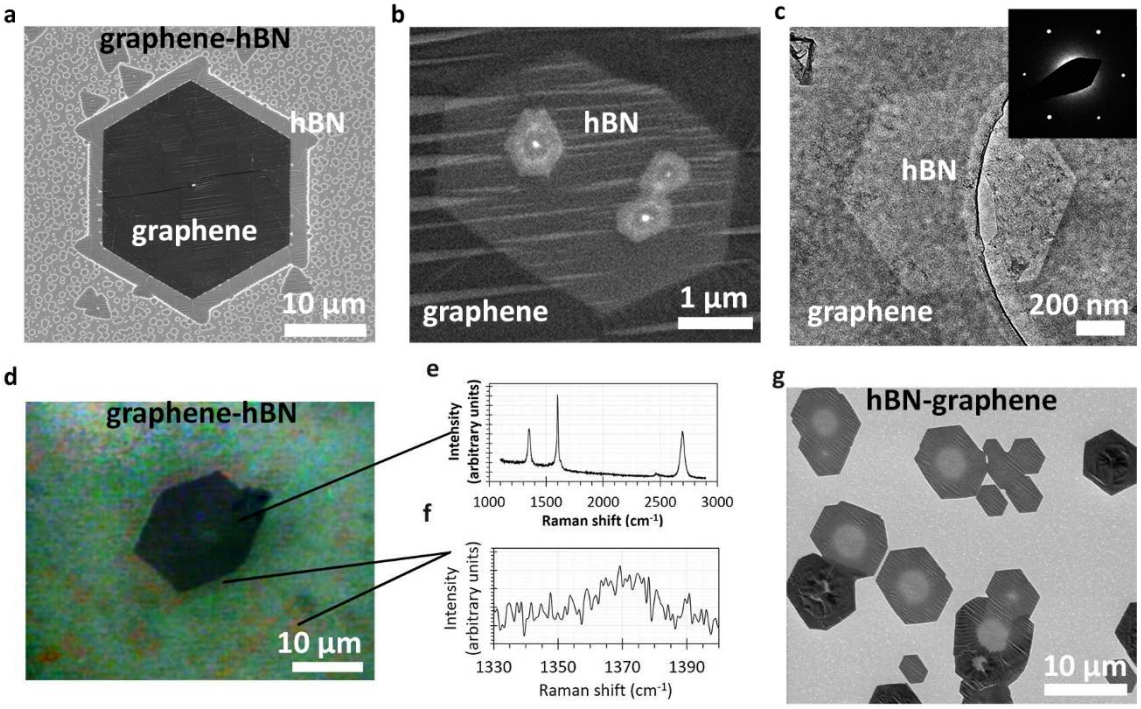

Figure 58. Lateral graphene and hBN heterostructures. a) A SEM micrograph of sequential graphene and hBN growth showing sharp interface between the materials. b) A hole in graphene that is filled with hBN. c) A TEM image of a hexagonal hole in graphene filled with hBN. Inset: SAED of the region. d-f) An optical image of the transferred graphene-hBN structure with corresponding Raman spectra of graphene and hBN. g) A SEM micrograph of the reverse synthesis experiment where graphene was grown after hBN, with methane and B-,N- precursors introduced simultaneously. The Raman signal was similar to the graphene-hBN method and showed defective or doped graphene.

indicating good crystallinity. However, large areas (few microns) of pristine graphene were displaced by hBN as shown in Figure 58b. TEM analysis showed that these hBN patches seamlessly continued graphene lattice producing a single diffraction pattern (Figure 58c). Raman spectra showed that graphene was defective (Figure 58d,e), suggesting that in addition to the observed displacement of graphene by hBN, there was unobservable, possible atomic level substitutional doping by BN. Pristine hBN regions showed a typical Raman peak at 1367 cm^{-1} (Figure 58d,f). This observation is similar to that previously reported for low-pressure methods, where graphene lattice had been displaced by BN, resulting in numerous atomic defects or doping, suggesting that the APCVD method does not give an improvement in graphene quality over LPCVD. However, it is cheaper and more convenient.

A reversed procedure was also investigated, where hBN growth was followed by graphene

growth. However, no hBN deposits remained after this procedure, most likely because hBN was completely etched by H_2. Therefore, a modification was made to simultaneously introduce hBN and graphene precursor during the graphene growth synthesis stage. This allowed to preserve hBN flakes, which were surrounded by graphene as shown in Figure 58g, however, Raman spectrum of graphene again showed a large defect peak, similar to the previous procedure.

In conclusion, hBN-graphene structures have been synthesised with a simpler and safer procedure at atmospheric pressure, but exhibited direct similarities to those produced at low pressure. These materials are expected to be applicable to the already demonstrated flexible and transparent electric devices[273].

I also envision the utilisation of these materials in future work as a benchmark test for STEM detectors. Currently, 2D materials, such as graphene and hBN, require low electron beam energies (< 80 kV) to prevent damage during their characterisation, but also have low z–number resulting in a very low signal-to-noise ratio in STEM mode and push current STEM detectors to their limits. For example, a fluorinated monolayer graphene-hBN patchwork could be the ultimate test material requiring to distinguish between four low-z elements B, C, N, F, and also allowing to study 3D reconstruction techniques due to the sp^3 nature of F bonds[275].

6.3.2. hBN films as dielectric medium for CVD-based light emitting diodes

Utilisation of transition metal dichalcogenides for optoelectronic applications has been investigated in a number of recent studies[73-76, 276, 277]. For example, mechanically cleaved MoS_2 was used as an active medium for electroluminescence in a proof of concept LED device[276]. With a wide range of classes of 2D materials it has become very beneficial to fabricate heterostructure devices that comprise of only 2D materials as building blocks for cheaper, more efficient and tunable LEDs; as demonstrated by Withers *et al* (2015)[75]. In particular, large-area, cost-effective

and tailorable CVD materials would be most suitable for future commercial applications.

Thin hBN films (1-5 layers) synthesised using methods described in section 6.1 were utilised by Dr Freddie Withers as a component of a proof of concept device for electroluminescence measurements in conjunction with other CVD-grown 2D materials: MoS_2 and graphene. The diagram of the device is shown in Figure 59a, which consisted of transferred and lithographically defined 2D materials and contacts. Measurements on the device with dimensions of 25 µm x 115 µm detected weak electroluminescence, but only at very high bias voltages, an order of magnitude larger than mechanically exfoliated devices[75]. The higher bias voltage is most likely due to leakage of the current through pin holes in the CVD hBN films at domain boundaries or through conductive impurities.

This exemplar application shows that thicker hBN materials with larger domains, and therefore fewer domain boundaries need to be synthesised to improve the dielectric performance of the films. Methods described in section 6.1 achieved hBN domains sizes of 5 µm comprising the films; while the developed insight into precursor chemistry will be useful to improve this value in future work.

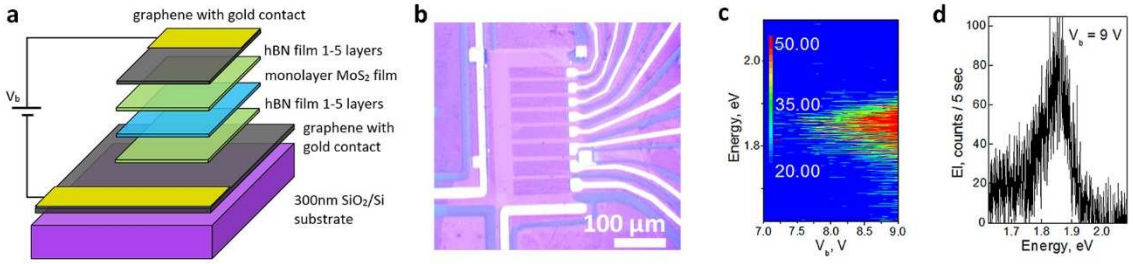

Figure 59. An LED device with main components produced by CVD. a) A schematic diagram of the device. b-d) An optical micrograph of the fabricated device and the corresponding electroluminescence measurements performed at 6K: photon energy vs. bias voltage and photon count vs. photon energy respectively. Data and images courtesy of Dr Freddie Withers.

6.4. Summary

Non-graphene 2D materials are promising candidates for a wide range of applications, either on their own or in heterostructure combinations. My investigation into the CVD synthesis of hBN and WS_2 showed that a number of important control methods have been overlooked by previous studies. Most importantly, *in situ* measurements of ammonia borane showed that simply heating the precursor leads to stochastic and irreproducible decomposition with varying temporal profiles of volatile B, N species. Time-dependent heating and other procedural modifications allowed to achieve good control of the precursor mole fraction and reproducible hBN synthesis. Additionally, Ni and Cu substrates were investigated for hBN synthesis, with the latter exhibiting lower roughness and better uniformity of hBN films.

For WS_2 synthesis, a number of volatile, chlorine-based precursors were reviewed and a novel $WOCl_4$ precursor was studied. It was found that the commonly reported reaction of chlorine-based precursors with sulfur was not thermodynamically favourable and therefore very inefficient. I devised a strategy to improve the efficiency to nearly 100 % by introducing a small amount of H_2 that led to favourable thermodynamics. However, increased WS_2 deposition did not sufficiently improve the quality of WS_2 deposits: the domains were very small, irregularly-shaped and not monolayer. Based on understanding of graphene and hBN synthesis mechanisms I proposed another modification to the reaction chemistry that biased the growth towards more crystalline and thinner deposits, simply by adding oxygen. The experiments showed a good match with the proposed chemistry alternations resulting in the largest reported to date monolayer single-crystal WS_2 deposits from volatile chloride precursors.

The materials were assessed for lateral heterostructure applications and in a prototype LED device.

Chapter 7. Porous nanomaterial structures and composites*

Graphene discovery triggered considerable research into electronic applications[43] based on properties of 2D materials, however, synthesis of high-surface area 3D structures from graphene in 2010[278] also stimulated research in improved composites, battery electrodes, supercapacitors, gas sensors, conductive inks and desalination membranes[43]. These far-reaching applications require large quantities of high quality porous graphene as their basis.

A variety of methods have been reported for producing porous carbon materials as outlined in a review by Jiang & Fan (2014)[279], but most importantly, the synthesis methods directly influence the quality of the resulting materials and therefore their suitability for applications need to be assessed on individual basis. Top-down synthesis methods[279] typically consist of dispersing or milling bulk graphite (or graphite oxide), followed by treatment to assemble the individual pieces into a connected structure, such as hydrothermal reduction, freeze drying or graphitisation under high temperature and pressure[279]. These high volume production techniques consistently produce low quality graphene with small crystal domains, varying number of layers and high number of defects as shown by Raman spectroscopy[280]. On the other hand, the bottom-up CVD-based approach, "template assisted synthesis" has been shown to produce high quality, defect-free graphene with a controllable number of layers[281], but comes at a higher cost. Graphene synthesis methods are the same as those used for metal foils (chapters 2, 4, 5), while the choice of the porous metal template becomes a very important consideration.

Porous "metal foam" templates are commercially-available[282] and are typically produced by melting a metal with salts at high pressure and temperature, where the salts are later washed from the structure[282] as shown in Figure 60a,b. These methods introduce high processing cost considering that the metal may be etched and discarded in order to produce graphene foam. Additionally, metal foams produced in this way typically exhibit very large pore sizes of 500 μm

* A patent related to this work was filed on 01/08/2014. Application number GB1413701.2.

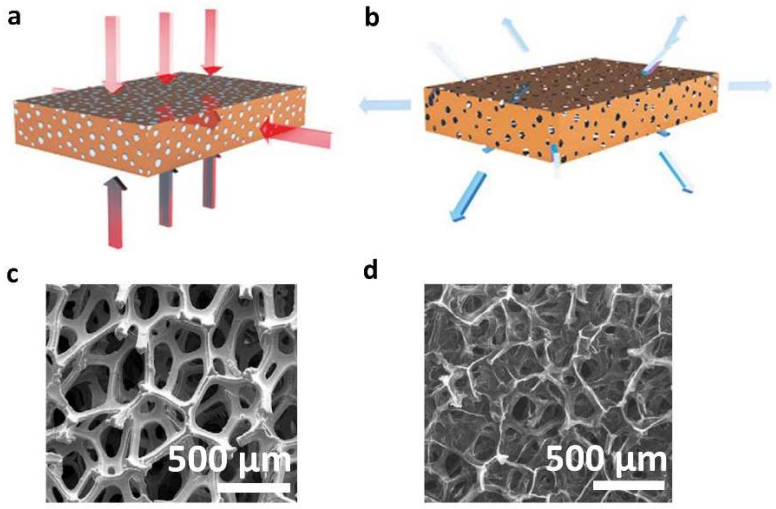

Figure 60. Commercial production methods of metal foams. a-b) A metal and salt powder mix is processed under high pressure and temperature, followed by removal of the salt from the structure. Images from Goodfellow USA[282]. c-d) Commercial Ni foam and corresponding graphene foam (collapsed) with an open-cell structure and very large pores of hundreds of micrometres. Images from ref. 281.

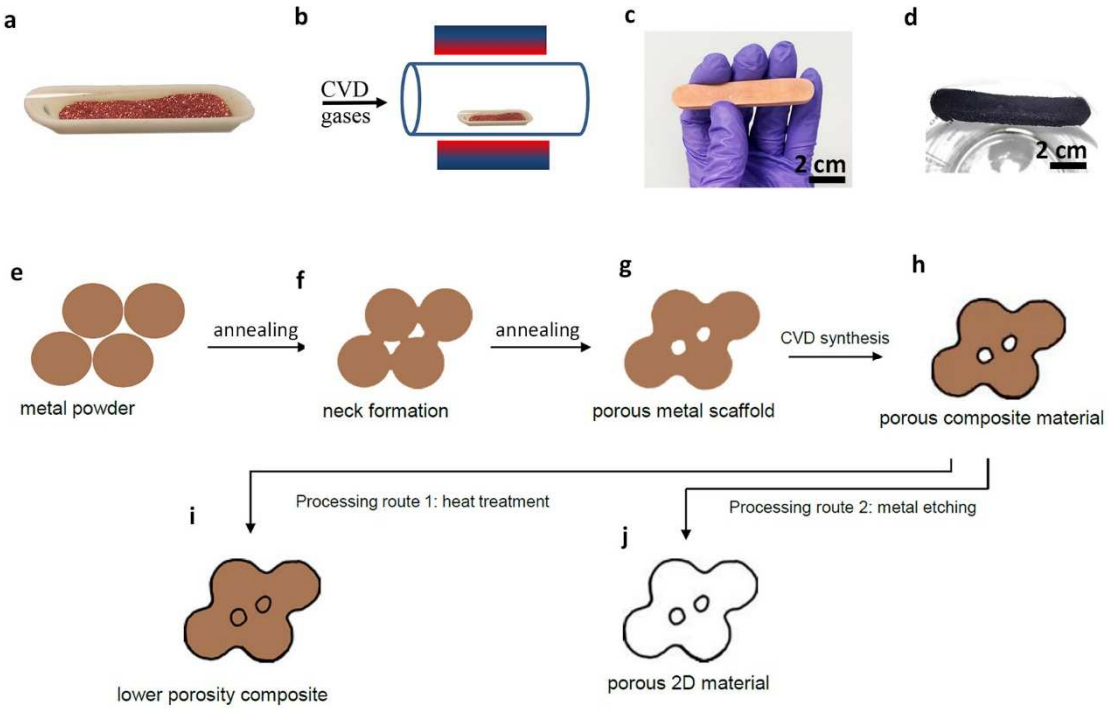

Figure 61. An overview of the possible processing steps for production of metal-graphene composites and graphene foams from powder. a-b) Metal powder is loaded in an alumina boat and put through a standard CVD process consisting of the annealing and synthesis stages. c) An optical image of Cu-graphene composite after synthesis. d) An optical image of graphene foam after Cu metal has been etched. e-h) The mechanism behind the synthesis of a metal-graphene composite consisting of partial fusion of metal powder, followed by coating of the resulting structure with a graphene film. i-j) Further processing routes that could be applied. For example if hot isostatic pressing (HIP) is used the porosity can be lowered for direct structural applications or the metal scaffold can be etched to obtain graphene foam.

with an open cell geometry (Figure 60c,d) and have considerably lower surface area compared to other commonly utilised carbon materials (such as activated carbon). Extensive empty regions between graphene filaments leads to collapse of the structure. To remedy the situation, thick graphite-like deposits have been utilised or alternatively, supporting polymers[281]. However, such carbon foams lose the beneficial properties of monolayer or few-layer graphene. A large reduction in the cost of the substrate is necessary to improve the feasibility for use in commercial applications.

In this chapter I discuss a highly up-scalable method for *in situ* formation of the porous metal template from low-cost powders during the annealing stage (Figure 61a), followed by CVD synthesis to produce a metal-graphene composite (Figure 61b,c) which can be further processed to obtain less porous composites (not discussed, Figure 61i) or graphene foams (Figure 61d,j). The method relies on the property of metallic powders (< 100 μm) to fuse together ("diffusion bonding") at temperatures below their melting point forming a porous scaffold (Figure 61e-g). The structure also possesses novel geometry compared to commercially-available metal foams. Metal-graphene composites have been shown to exhibit improved oxidation and chemical resistance[283], better electrical[284] and thermal[285] conductivity and enhanced mechanical properties[286]. Graphene foams, for comparison, are light, conductive materials that possess high surface area and are suitable for energy storage applications, filtering, sensors and production of novel conductive composites[279]. An exemplar application where the developed graphene foams are utilised as an electrode in a Li-O_2 battery is discussed in section 7.2.2. Methods and understanding developed in this work can be extended to hBN and other 2D materials, which has shown promise in catalysis, catalyst delivery and biomedical applications[287].

7.1. Porous structures from copper powder

7.1.1. Copper-graphene composite synthesis

Commercially-available Cu powders were sonicated in deionised water, acetone and acetic acid (10 minutes each) to remove commonly encountered impurities and organic residues, followed by rinsing in deionised water and drying. A variety of sizes of Cu powders were investigated (Figure 62a-e) with sizes 0.8 ± 0.9 µm, 2.8 ± 1.2 µm, 7.5 ± 3 µm, 14 ± 6 µm and 250 ± 70 µm (values measured by Taylor Uekert to compare to manufacturer supplied specifications). The smallest and the largest powders did not produce useful results because the former fused into a solid Cu block too quickly (Figure 62f), while the latter did not fuse sufficiently and resulted in low porosity. The choice of the powder size can be used to tailor the porosity of the materials. Highest possible porosity is usually desirable; for this reason the powder with particle size of 2.8 ± 1.2 µm was selected for further investigation. Notably, pore sizes on the order of 10 µm were

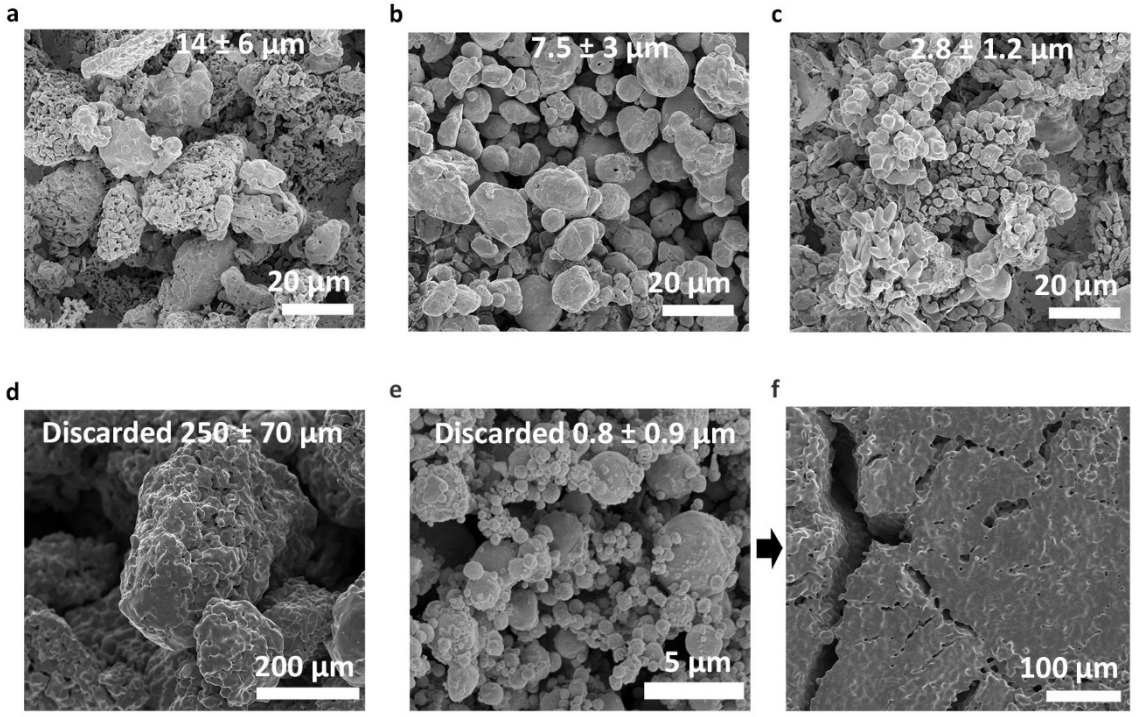

Figure 62. Commercially-available Cu powder characterisation. a-e) SEM micrographs of Cu powders. Images and measurements recorded by Taylor Uekert. f) A SEM micrograph of excessively fused Cu powder due to the small particle size (0.8 ± 0.9 µm).

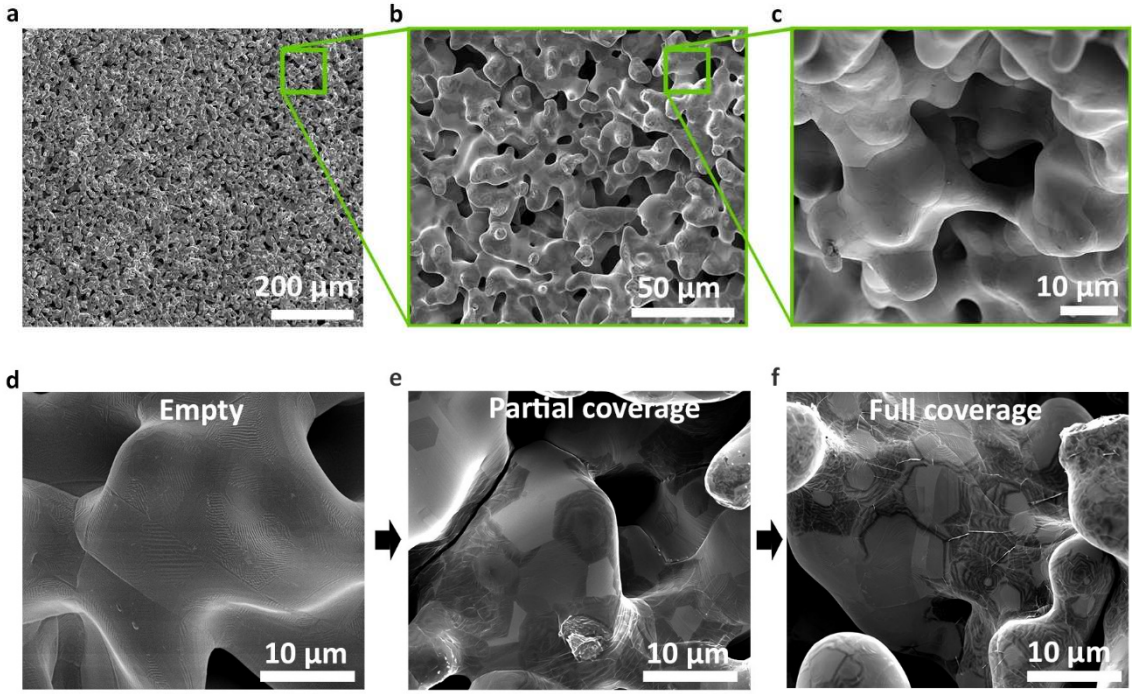

Figure 63. Cu-graphene composite synthesis. a-c) Low, medium and high magnification of the porous scaffold produced from Cu powder after annealing. d-f) Graphene coverage depending on the synthesis parameters: empty, partial coverage and full coverage.

achieved, which is more than an order of magnitude smaller than the typical pore size of commercial metal foams (Figure 60c) and also possessed a new pore-ligament geometry (Figure 63b) rather than the open-cell geometry (Figure 60c).

After the formation of the porous metal template (Figure 63a-c) graphene growth followed the same trends and mechanisms discussed in previous chapters (4, 5). Specifically, higher temperature increased the growth rate, the ratio of H_2 to CH_4 influenced the growth rate and the number of layers, while longer time allowed more deposits to form. For example, a H_2:CH_4 ratio of 50 did not produce graphene, while the value of 40 resulted in partial coverage and lastly few-layer graphene film formed at ratios of 25 as summarised in Figure 63d-f. Few-layer graphene coverage was uniform with depth throughout the metal foam.

The optimised synthesis procedure consisted of loading 15 g of Cu powder into an alumina boat (Sigma-Aldrich), followed by annealing at 1040 °C in H_2 at 200 sccm flow rate for 20 minutes. Immediately after, the gas composition was changed to 10 CH_4 and 250 H_2 to initiate graphene

synthesis and held at these conditions for 50 minutes. The sample was then slowly cooled by shifting the furnace. Slow cooling was necessary to prevent sudden Cu contraction and cracks in the Cu-graphene composite.

7.1.2. Few-layer graphene foam synthesis from copper-graphene composite

The Cu-graphene composite can be further processed to etch the metal and produce graphene foam[281]. Methods were developed specifically for the Cu-graphene composite by testing three etchant solutions:

- ammonium persulfate (0.5M $(NH_4)_2S_2O_8$ in deionised water, Sigma-Aldrich, 98 %)
- 10 % HCl and 10 % H_2O_2 in deionised H_2O
- commercial Cu etchant, 1M $FeCl_3$

$FeCl_3$ solution did not seem to be efficient nor easily washed after etching[197]. The other two solutions worked similarly, and were efficient and clean. Additionally, Raman measurements of graphene directly on the Cu scaffold and after etching did not show an increase in the D peak, confirming that the etchants did not introduce defects or doping. A Cu-graphene block of 15 g was left in the etching solution for 2 days at 60 °C to completely remove the Cu scaffold. Resulting graphene foam ascended to the surface because of low density and bubbles trapped in the structure (due to H_2O_2 decomposition) and indicated that the metal had been fully etched. Figure 64a-c shows the etching steps for a block of Cu-graphene composite. It was found that increasing all the dimensions of the block required significantly longer time to fully etch the metal because the etchant had to penetrate deeper which was limited by diffusion. Such process was very slow and therefore posed a limit for up-scalability. Nevertheless, most applications do not require block-like geometry of the material, but rather an extended sheet of porous material. The thinner dimension allowed quick etching and therefore the approach was suitable for up-scaled production.

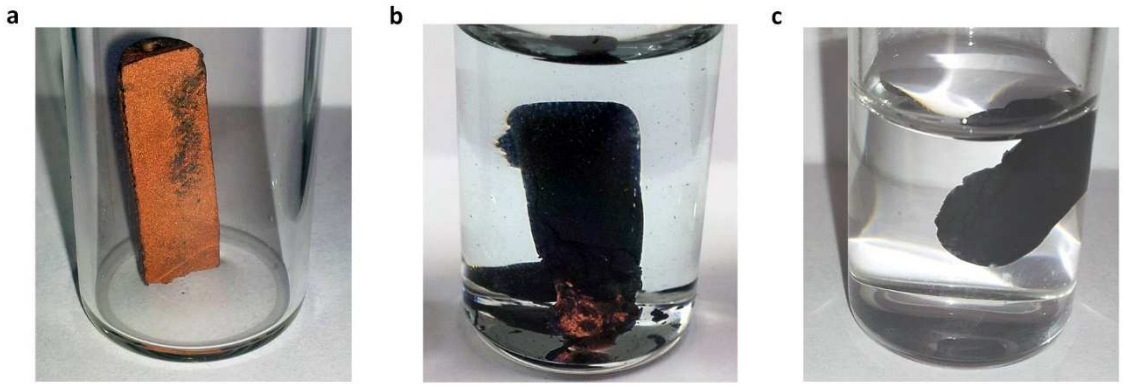

Figure 64. Graphene foam synthesis steps. a) An optical image of the Cu-graphene composite. b) Partial etching of Cu-graphene composite showing remnants of the Cu scaffold inside the black porous structure. c) Once the metal is completely etched, graphene foam floats in water due to the very low density.

The microstructure of graphene foams grown on Cu is shown in Figure 65a, where graphene folds cause effective porosity. The structure is partially collapsed because it was imaged after drying graphene in air. The edge of graphene domains on one such sample varied from bilayer to around 5 atomic layers (Figure 65e), suggesting that "few-layer" graphene (< 10 layers). Although not monolayer, this is still a very thin and flexible material, explaining why the structure could not support itself without collapsing when dried. A number of different ways to dry the material were investigates: drying from a lower surface tension medium (ethanol), in vacuum, at elevated temperatures (120 °C) and supercritical drying that reduced surface tension to zero. These methods did not solve the problem because of the nature of such a thin material. Instead of changing the thickness of the material I chose to develop drying-free processing methods targeted towards specific application integration. For example, batteries typically contain a solvent in the electrolyte making it possible to sequentially swap the liquid medium in graphene foam and use it in a battery without drying. This method will be discussed in more detail in section 7.3. Raman spectroscopy confirmed few-layer graphene coverage with low defect density: the D-peak was acceptably low and the ratio of 2D to G peaks was 0.3 (Figure 65f). Due to the low mass of graphene foam it was difficult to measure this value accurately after full processing, since adsorbed water and small salt impurities resulted in a significant addition to the mass. In order to get an accurate measurement, immediately after the Cu scaffold was

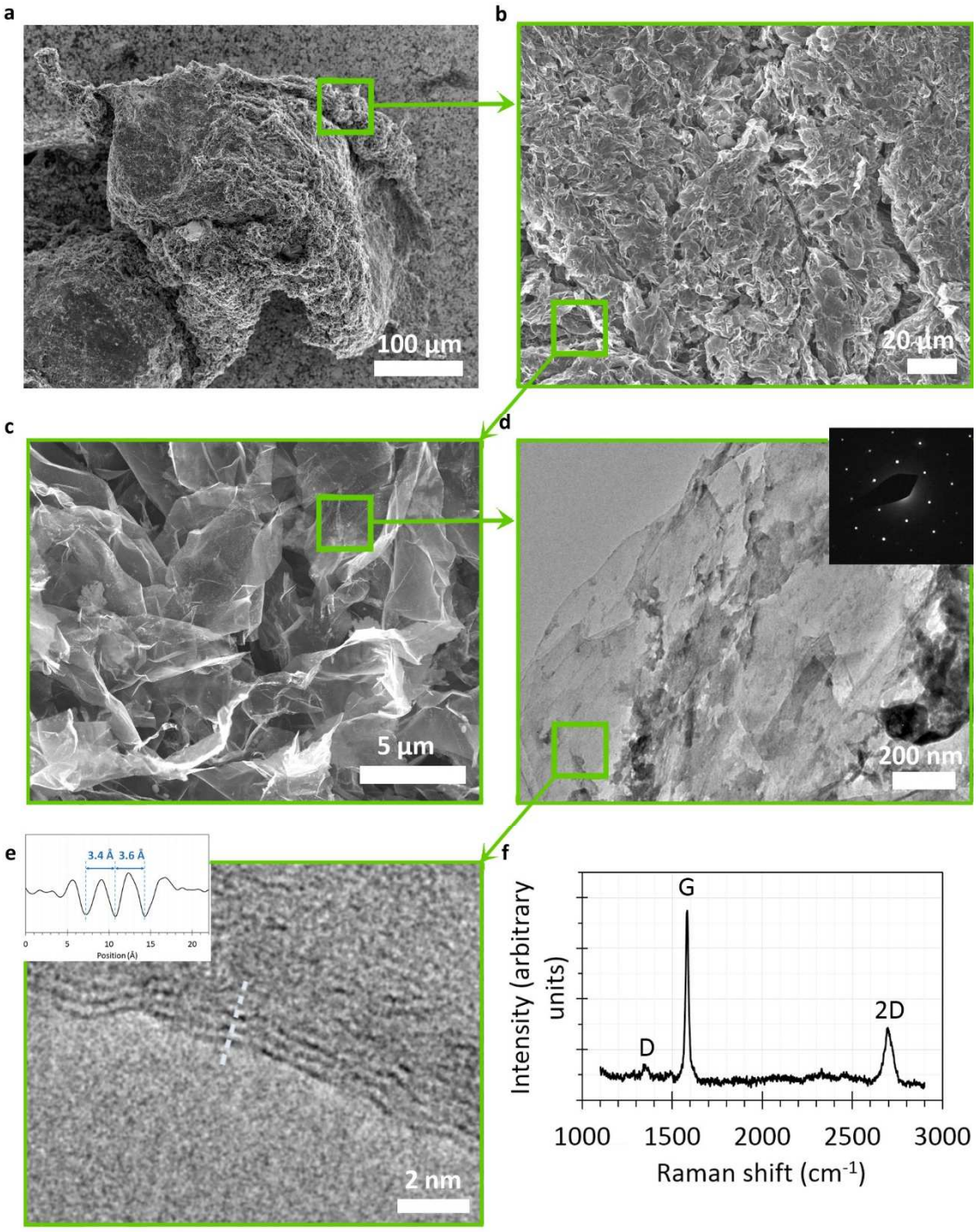

Figure 65. Characterisation of graphene foam produced after etching the metal in Cu-graphene composite. a-c) SEM micrographs of the foam a low, medium and high magnification showing the porous structure. d) A TEM micrograph of graphene foam showing high transparency under the electron beam. Inset: SAED of one sheet from the porous structure. e) An HRTEM micrograph of the edge of graphene foam indicating approximately 2-5 atomic layer thickness. Inset: an intensity profile with distance across the edge showing three graphene layers (dark) with expected separation of approximately 3.5 Å. f) Raman spectra of the foam after the metal has been etched.

formed during annealing, the system was cooled by quenching and the sample was removed from the CVD system and weighted. The sample was then returned back into the system and annealed for a short time, followed by graphene synthesis. The difference in mass was around 2 ± 0.5 mg, while the total mass of the composite was 14400 mg, leading to 0.014 % graphene loading by mass. When in solution, this sample had dimensions of approximately 6 mm x 7 mm x 50 mm, leading to a density of approximately 1 kg m^{-3}. This value is less dense than the density of air (please note, the value does not include the mass of air filling the foam) and is 5 times denser than the lightest reported graphene/carbon nanotube hybrid aerogel[288] prepared via solution processing followed by freeze drying.

There are currently many variations of porous carbons: robust porous graphite structures (POCOfoam[289]) that can be used for structural applications, “aerographite” (ref. 290) comprising rolled tubular graphene ligaments and can be used for ultra-light composites. Also, “vertical graphene”(ref. 291) that has anisotropically aligned pores; solution-synthesised graphene foam[292] that is very cheap to produce but suffers from poor conductivity; aggregated bubble-like graphene network[293] with closed pores and, recently, CVD-synthesised graphene foams. Each of these materials is produced in a very different way and possess different properties. It will take time to determine which one may be suitable for which applications, and, in particular, when their price vs. performance characteristics are assessed.

7.2. Porous structures from nickel powder

7.2.1. Nickel-graphene composite synthesis

Ni powder was utilised to produce Ni-graphene composites and Ni foams using methods discussed in section 7.1. Due to higher catalytic ability and higher carbon solubility in Ni the synthesised graphene was much thicker than that on Cu. Another significant difference was that Ni had a higher melting point than Cu, requiring either smaller powder size or higher synthesis temperatures to produce the scaffold. Since smaller particle size would produce higher porosity that is desirable for a variety of applications. For this reason, Ni powder with size distribution of 1.6 ± 0.5 µm was utilised (measured by Taylor Uekert, Figure 66a). The structure fused into a very finely separated porous scaffold with interesting microstructure (Figure 66b-d).

The optimised synthesis and processing procedures were similar to those on Cu. The powder was washed in deionised water, sonicated in acetone and acetic acid for 10 minutes each, followed by a second rinse in deionised water and drying overnight. An alumina boat was loaded with around 5 g of Ni powder and placed inside the CVD system. Although Ni and Cu have approximately the same density, the mass of Ni powder in the filled alumina boat was four times lower due to the smaller particle size of Ni powder and therefore higher porosity. The annealing stage consisted of heating the powder to 1050 °C for 20 minutes under 200 sccm flow rate of H_2. The synthesis stage utilised H_2 and CH_4 flows of 250 sccm and 2.5 sccm respectively for 60 minutes. The H_2:CH_4 ratio of 100 achieved thick graphene coverage on Ni, whereas on Cu this ratio did not result in graphene deposition. Tall wrinkles could be observed in graphene coverage on Ni, indicating very thick deposits (Figure 66d).

As a consideration for up-scaling, an investigation into synthesis of the composite under inert atmosphere was conducted with John Hotson using methods discussed in section 4.3. The synthesis gases were replaced with mixtures of Ar/H_2 (2.5 %) and Ar/CH_4 (0.025 %). While on Cu it was not possible to achieve full coverage with any combination of gases, on Ni it was achieved,

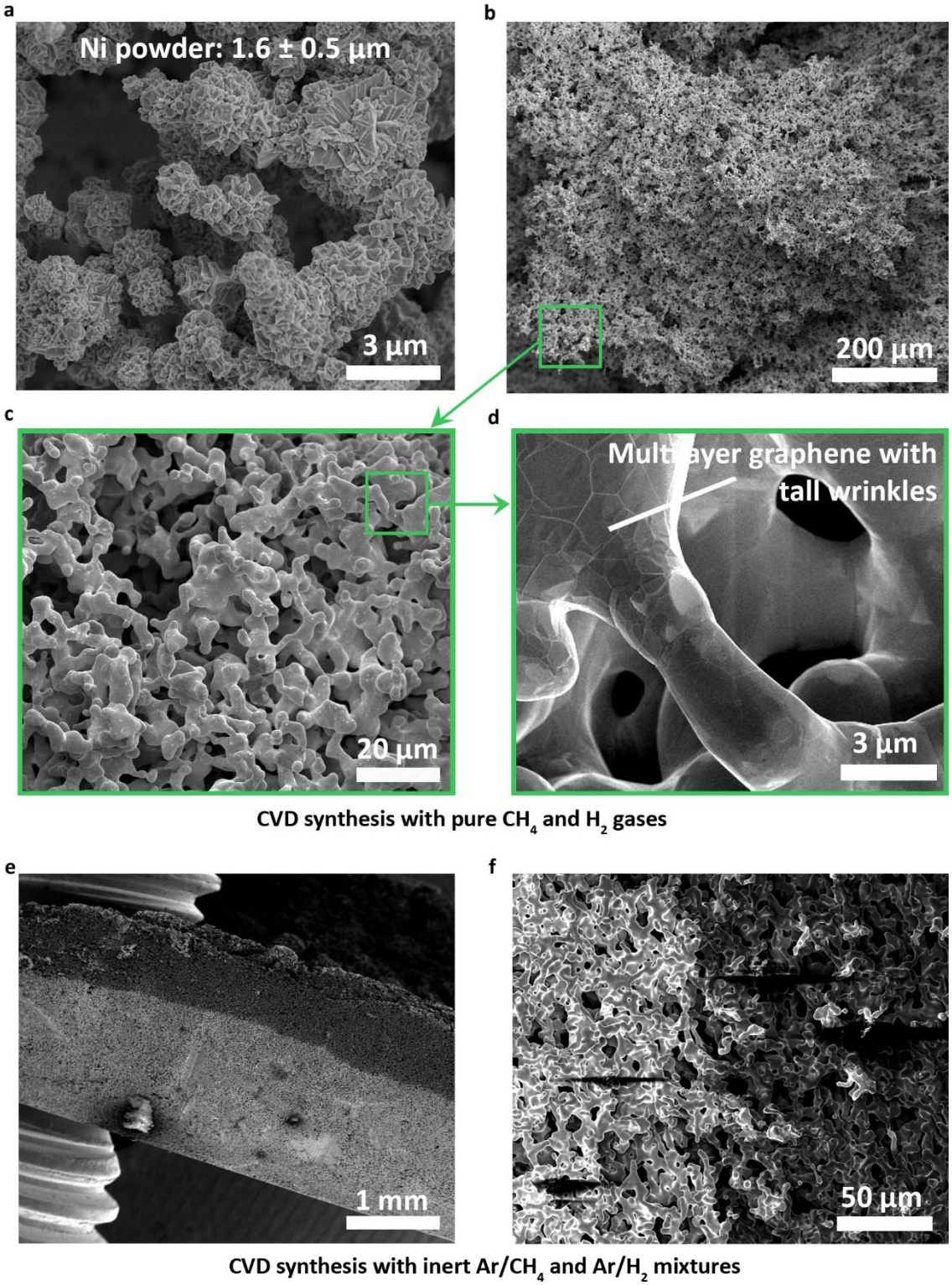

Figure 66. Ni-graphene composite synthesis. a) A SEM micrograph of the source Ni powder. Image taken by Taylor Uekert. b-d) SEM micrographs of Ni-graphene composite at low, medium and high magnifications. Showing the microstructure and porosity. Thick graphene coverage can be inferred from very high wrinkles observable in (d). e-f) SEM images of samples from a different graphene synthesis investigation with inert gas mixtures. Incomplete graphene coverage of the Ni-graphene is observed due to the low CH_4 and H_2 partial pressures that exhausted with the depth of penetration into the metal scaffold. A sharp interface between multilayer graphene film and empty Ni regions can be seen, however, few mm penetration depth can be achieved, which is sufficient for a variety of applications (such as battery electrodes).

but only for a limited depth inside the Ni scaffold. Figure 66e,f shows two SEM micrographs of the metal scaffold at low and high magnification. The depth of penetration of graphene coverage was approximately 1 mm and there was a sharp interface between empty and fully covered regions. It is expected that because of low partial pressure of CH_4 gas it was exhausted by the time it reached into deeper regions of Ni scaffold. The synthesis procedure consisted of annealing the Ni powder at 1050 °C with 500 sccm Ar/H_2 flow rate (2.5 %) for 20 minutes, followed by the synthesis with 100 sccm Ar/CH_4 (0.025 %) and 25 sccm Ar/H_2 (2.5 %) flow rates respectively for 60 minutes. Graphene coverage depth of 1 mm is sufficient for many applications and crucially, such sample geometry will facilitate faster etching of the Ni-graphene composites to produce graphene foam.

7.2.2. Multilayer graphene foam synthesis from nickel-graphene composite

Similar to the methods discussed in section 7.1.2, processing methods were developed for the production of thick multilayer graphene foam from Ni-graphene composites. Due to thicker graphene deposits, the composition of the etchant solution was changed. To completely etch 5 g of the Ni-graphene composite, a 15 % HCl, 15 % HNO_3 and 5 % H_2O_2 solution in deionised water was used. The sample was left in the solution for 2 days at 60 °C until the solution turned bright green and the foams ascended to the surface. The foams were then transferred to a beaker with 500 mL of deionised H_2O heated to 60 °C for one day to allow diffusion of salts from the foam. The process was then repeated with fresh 500 mL of deionised water. The resulting graphene foams are shown in Figure 67a-d. TEM micrographs showed good transparency under the electron beam and multilayer SAED. This material had a rigid hollow structure that followed the shape of the Ni scaffold. It was possible to dry the material with about 30 % loss in volume due to the thicker graphene walls that could support the structure. The drying procedure consisted of replacing water medium with ethanol (due to lower surface tension in air), followed by drying in an oven at 80 °C. As a result, free-standing graphene foams were obtained as shown

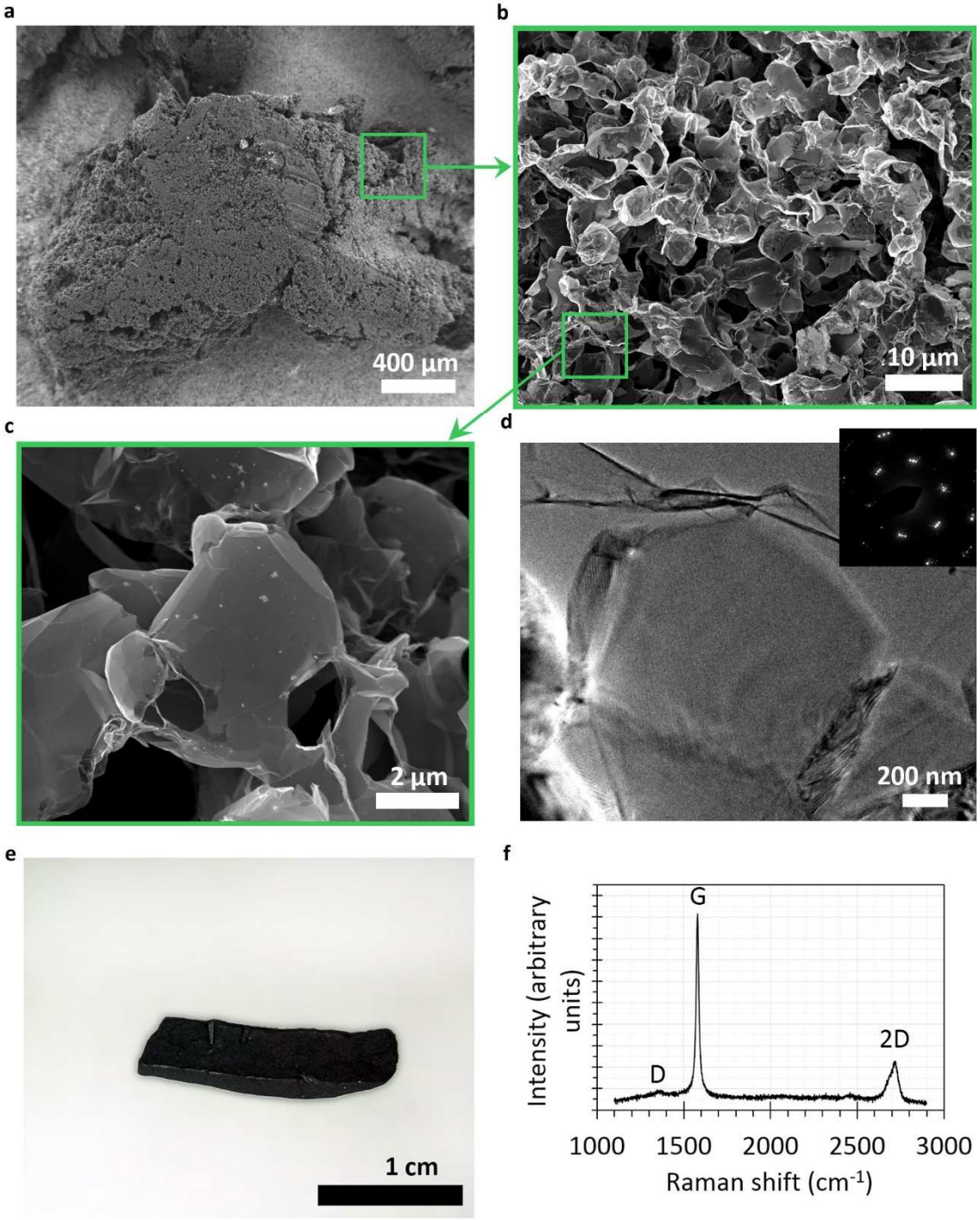

Figure 67. Synthesised thick multilayer graphene foam from Ni-graphene composite. a-c) SEM micrographs of the foam showing the microstructure and porosity. Thicker walls allow to preserve the structure of the metal template resulting in a hollow, rigid cells. d) A TEM micrograph of a region of graphene foam from Ni-graphene composite. Inset: SAED of the region showing rotated and inclined crystallites of multilayer graphene. e-f) An optical image of free-standing thicker graphene foam from the Ni-graphene composite and the corresponding Raman spectrum, indicating multilayer graphene.

in Figure 67e. Raman spectra of dried graphene showed low D-peak and the 2D to G peaks ratio of 0.2, confirming low-defect multilayer graphene (Figure 67f). In order to measure graphene loading in the composite the foam was dried in vacuum and weighted. Approximately 1.1 g of Ni-graphene composite resulted in 7.5 mg of rigid graphene foam, corresponding to 0.7 % carbon loading by weight. The density was estimated to be around 50 kg m^{-3} or about an order of magnitude higher than the thinner graphene from the Cu-graphene composite. This material is expected to be more suited towards applications where a rigid, porous and light conductive material is needed.

7.3. Graphene foam as the porous cathode in the Li-O_2 battery

Porous carbon electrodes or carbon additives, such as milled graphite, activated carbon, carbon nanotubes, templated carbons and others have been used extensively in Li-based batteries and other types of energy storage devices[294] due to their high surface area, low weight and good conductivity. Recently, a variety of graphene-based electrodes and composites have been explored in a number of prototype energy storage devices[295], typically showing considerable improvements, especially in the charge storage capacity per mass (specific capacity) and in the charge/discharge rates. For example, graphene nanosheets[295] used as an anode can increase the specific capacity of Li-ion batteries from 372 mAh g^{-1} to 540 mAh g^{-1} when compared to other commercial carbons. Graphene materials are particularly suited to improve the gravimetric energy density of Li-based batteries due to their low density. One of the main future applications for such battery systems is as an energy source of electric vehicles. However, consumer demand is expected to peak only when the mileage is appreciably close to that of petrol[296]. The Li-air battery is one of the most promising technologies that can potentially achieve this goal.

The Li-air battery has the highest theoretical gravimetric energy density of any other type of battery[296]. For example, it is nine times higher than the theoretical capacity of the Li-ion battery (Figure 68a) and could realise 500 miles travel distances per charge[296]. Foremost, a working

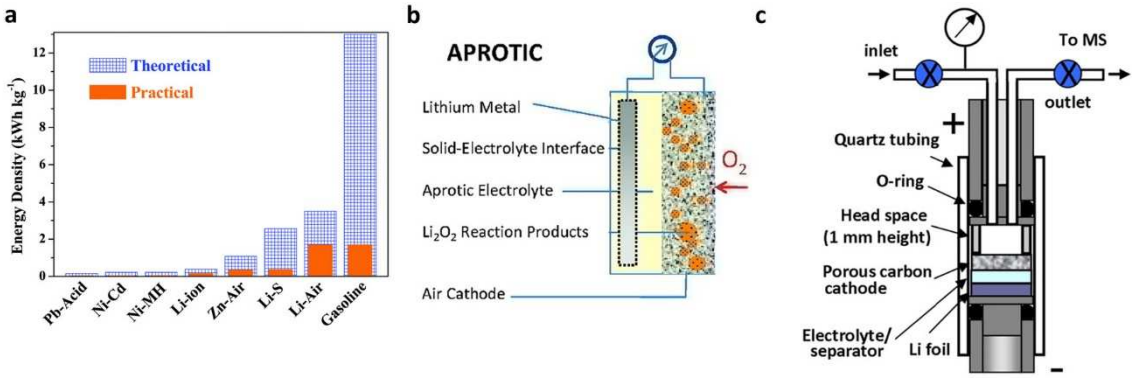

Figure 68. The Li-air battery concepts. a) A comparison of the theoretical and practical energy densities of different types of batteries. Image from ref. 296. b) A schematic diagram of an aprotic Li-O_2 battery showing that it is an open system with a porous cathode material. Image from ref. 297. c) A Swagelok-type Li-O_2 cell diagram with main components labelled. Image from ref. 298.

configuration needs to be found for an aprotic Li-oxygen battery. A diagram of the battery is shown in Figure 68b. The principle of operation is based on forming a solid lithium peroxide (Li_2O_2) on the cathode during discharge and its dissolution during charging, as in the following equations[297]:

$$2 \cdot Li^+ + O_2 \leftrightarrow Li_2O_2 \text{ (cathode)} \quad (51)$$

$$Li \leftrightarrow Li^+ + e^- \text{ (anode)} \quad (52)$$

The forward reaction occurs during discharge and the reverse reaction occurs on charge.

There are significant challenges in engineering every component of the battery, most importantly because of the following processes[297]:

- Degradation of cathode material due to reactions with Li superoxides.
- "Cathode clogging": growth of excessively large insoluble Li_2O_2 deposits.
- Degradation of the solvent due to decomposition during charge.
- Insufficient power generation due to the low speed of reaction.
- Dendrite growth on the anode.
- Delivery of oxygen into the system and degradation due to impurities.

Many different potential solutions are being researched targeted towards solving the above problems. Graphene-based foams have potential to improve this and other types of batteries because they consist of an interconnected, conductive structure that has low weight, high surface area and enhanced chemical resistance.

Graphene foams prepared using methods described in sections 7.1.2 and 7.2.2 were measured in a prototype Li-O_2 battery by Dr Lee Johnson and Dr Shanmu Dong. To prepare electrodes of suitable dimensions I machined the Cu-graphene composites into 4 mm x 4 mm x 0.5 mm blocks and etched them in ammonium persulfate, followed by washing of the resulting graphene foams in mQ water. The solution was then displaced with the battery solvent, dimethyl sulfoxide

(DMSO) or tetraethylene glycol dimethylether (TEGDME) and left for 7 days to allow the diffusion of water molecules from the foam. The samples were further dried with activated molecular sieves and the moisture content was measured with the Karl Fischer titration, achieving < 20 ppm impurity level. The thicker graphene foams from the Ni-graphene composite were processed differently: the metal was etched, followed by washing the foam in mQ water. Water was then displaced with ethanol and dried at 80 °C to obtain free-standing porous samples, followed by drying in vacuum and handing in a glovebox under N_2 atmosphere.

The foams were mounted on a stainless steel grid and loaded into a Swagelok-type cell (Figure 68c), which had components according to the work by Lee *et al* (2014)[299]: a $LiFePO_4$ anode as the source of Li^+, graphene foam as the porous carbon cathode and an electrolyte, 0.5 M $LiClO_4$ in DMSO or TEGDME. The discharge curves were recorded at a constant current of I = 30 μA and the corresponding specific capacities were extracted as follows:

$$Q_C = {I \times \Delta t}/{(\text{carbon mass})} \text{ (in mAh g}^{-1}\text{)} \quad (53)$$

The measurement with thinner graphene – DMSO configuration (0.021 mg of graphene foam was used) exhibited an extraordinary high specific capacity of around 85 000 mAh g_C^{-1} on the first cycle, which dropped to around 30 000 mAh g_C^{-1} on the second cycle and significantly lower in follow-on cycles (Figure 69a,b). Poor cycling is common for porous carbons and is attributed to the "cathode clogging" by Li_2O_2 and consequent electrode degradation[297] when an overpotential is used in attempt to dissolve the solid peroxide deposits. For comparison, porous gold electrodes showed a much better cycling performance[300], retaining 95 % of the first cycle capacity after 100 cycles, but admittedly will not result in commercial technology due to high cost and low specific capacity.

An alternative battery chemistry was also investigated, where the thinner graphene foam (0.021 mg) synthesised from the Cu-graphene composite was measured in the electrolyte consisting of 0.5 M $LiClO_4$ in TEGDME. The cycling performance noticeably improved

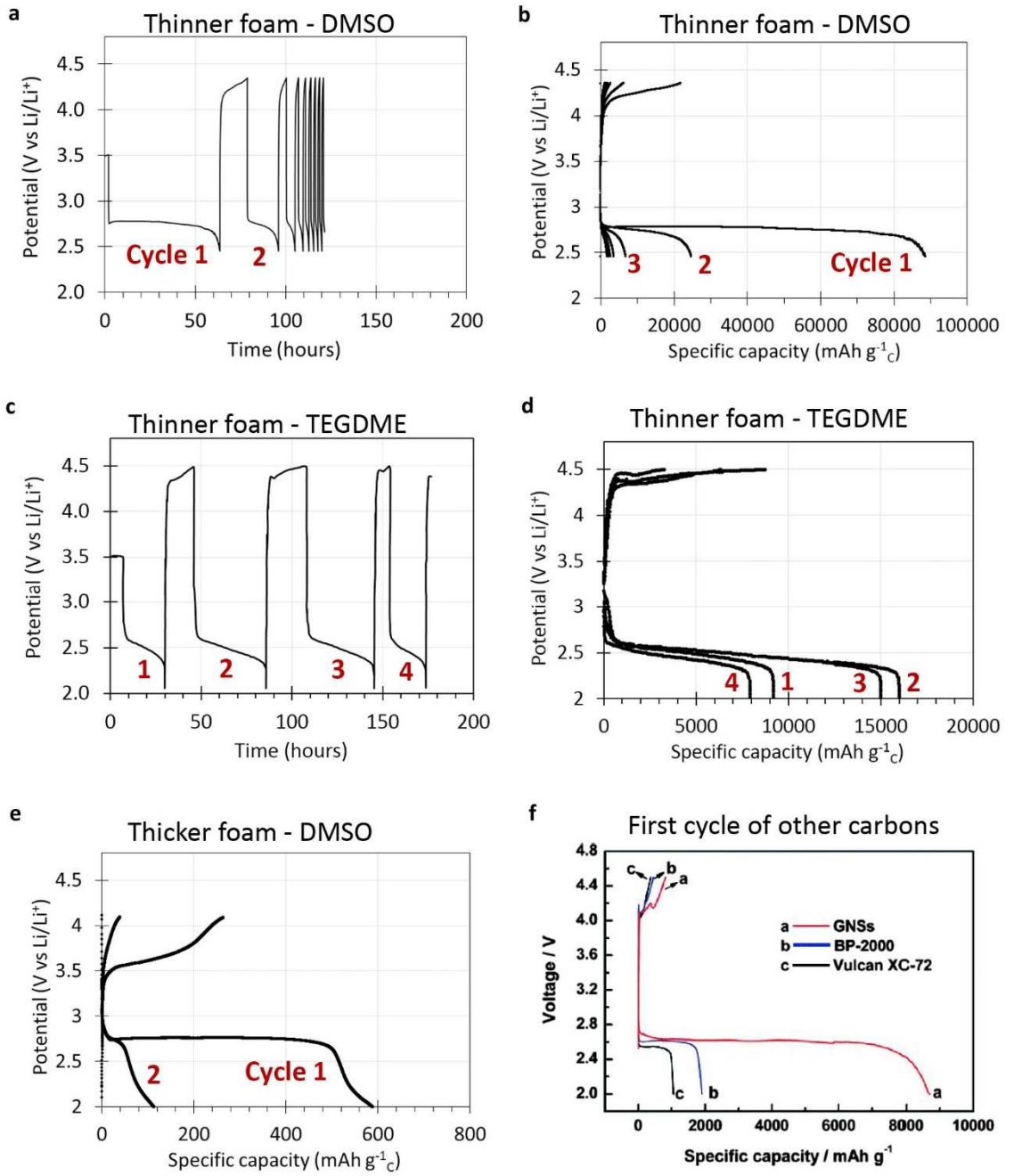

Figure 69. Measurements of graphene foams in a Li-O_2 battery configuration. a-b) Thinner graphene foam performance in DMSO, showing an extraordinary high specific capacity of the first cycle of around 85 000 mAh g_C^{-1}, but poor cyclability, with the second cycle capacity dropping approximately to about a third of the first cycle. c-d) Thinner graphene foam performance in TEGDME, showing better cyclability than in DMSO, but lower specific capacity. e) A specific capacity measurement of the thicker graphene foams in DMSO; showing a slightly better coulombic efficiency (the ratio of the charge to discharge capacities), but poor cycling. (a-e) Data recorded by Dr Lee Johnson and Dr Shanmu Dong. f) First cycle specific capacity measurements of exemplar commercial porous carbon electrodes: graphene nanosheets (GNSs), BP-2000 and Vulcan XC-72, achieving around 8000, 2000 and 1000 mAh g_C^{-1} respectively, at a current density of 75 mA g_C^{-1}. Image credit Ma *et al* (2015)[296].

(Figure 69c,d), however, the specific capacity was lower than in DMSO, but still higher than many other porous carbon materials[296] (Figure 69f). For comparison, graphene nanosheets[296] achieved specific capacity of about 8 000 mAh g_C^{-1}. The observed difference between the solvents had been reported previously[299] and is explained by the higher carbon-surface growth of Li_2O_2 in TEGDME compared to solution growth of Li_2O_2 in DMSO.

When thicker graphene foams (2.2 mg) synthesised from the Ni-graphene composite were measured in the same configuration, neither the cyclability nor the capacity (600 mAh g_C^{-1}) improved (Figure 69e). Only the coulombic efficiency of the battery, or the ratio of the charge to discharge capacities improved slightly. If cathode degradation was the main reason for poor cyclability, it would be reasonable to expect an appreciable improvement with thicker graphene foams. Therefore, it is more likely that the battery chemistry needed further optimisation to work with carbon electrodes and that graphene cathodes were not the limiting factor.

Many other ways to improve the performance have been identified in the literature[296], such as utilising catalytic particles on the cathode, carbon defects passivation or tweaking the battery chemistry and are expected to be applicable to graphene foams presented here. Very recently, a Li-O_2 battery with a novel LiOH chemistry and a reduced GO electrode was demonstrated by Liu *et al* (2015)[301] that achieved zero capacity loss after 100 cycles at 8000 mAh g_C^{-1} or 15 cycles at 20000 mAh g_C^{-1}; showing promise for the utilisation of porous graphene foams in future Li-O_2 batteries.

These tests show that while graphene foams exhibited limited cyclability similar to other unmodified carbon cathodes[296], the very high specific capacity shows promise for future utilisation of this material in advanced battery configurations. Tailoring the porosity, thickness and crystallinity of graphene foams in conjunction with other reported electrode modifications[296] can be useful tools to improve the performance of the Li-air batteries towards utilisation as stable and rechargeable energy storage in electric vehicles.

7.4. Summary

A cheap and up-scalable method for the production of porous metal-graphene composites and graphene foams from metal powders has been developed, that also resulted in novel 3D geometry. Graphene foams grown on Cu scaffolds were thin conductive films of very low density. To prevent collapse of the structure methods were developed to process the material in solution towards final device fabrication.

Ni-graphene composites resulted in thick, multilayer graphene deposits that were rigid and supported the structure after etching the metal scaffold. These materials could be dried to obtain free-standing graphene foams.

The developed porous carbons were tested in a proof of concept Li-O_2 battery configuration as cathodes. Such batteries are a promising technology for energy storage in electric vehicles. While the cyclability of the battery was similar to those with other non-modified carbon materials, the specific capacity achieved from thinner graphene foams reached an extraordinary high value of around 85 000 mAh g_C^{-1}, one of the highest reported to date. Modified graphene foams or composites could prove as suitable electrodes in this or other energy storage devices.

Chapter 8. Conclusions and future work

Nanomaterials will undoubtedly play a major role in future technology with the next "nano generation" of devices already appearing in laboratories. Only 11 years have passed since the discovery of the first pioneering 2D material, and already graphene-enhanced light bulb, tennis racket and conductive inks have been commercialised[27]. Other families of 2D material that possess different, yet complimentary properties will soon be utilised in applications either individually or in synergistic assemblies.

Many lab-scale applications have been initially demonstrated using the "sticky tape" method, invented by graphene discoverers Andre Geim and Konstantin Novoselov. In order to proceed towards real-life applications, the next step forward has to be the development of scalable synthesis methods for high quality 2D materials. CVD is recognised as the most promising large area synthesis technique that can deliver high quality, tailorable materials at acceptable cost.

My investigation into the CVD synthesis of 2D materials focused on a broad variety of unsolved issues. For example, on the instrumentation side, custom, automated and up-scaled CVD systems with rigorous controls have been assembled and used to study the synthesis of 2D materials. Understanding the CVD variables and mapping the parameter space allowed to find methods to reproducibly synthesise graphene, hBN and WS_2 on different substrates. In particular, catalytic substrate effects on Pt and Pd were investigated that led to the development of a novel silicidation procedure for graphene synthesis that achieved super-fast growth rates of monolayer single crystal graphene domains. The cause for the improvement was elucidated with a number of chemical characterisation techniques: the liquid silicide layer screened Pt grains and locally smoothed the surface. Furthermore, most transition metals form silicides and there are also other binary, ternary and higher eutectic compound that can be used in future work to make the procedure cheaper and more tailorable. The possibility to separate the

chemical phases of the substrate could lead to transfer-free synthesis of 2D materials, which is one of the biggest challenges facing CVD.

In situ measurements of the hBN precursor decomposition led to improved understanding of the complicated precursor chemistry and it particular its behaviour with time, which was inadequate for reproducible hBN synthesis at atmospheric pressure. New temporal control methods of the precursor vapour were subsequently developed that improved the quality and reproducibility of hBN syntheses. These methods can be further optimised in future work to achieve larger hBN domain sizes and better dielectric properties of hBN films.

Identifying a novel gas-phase precursor, $WOCl_4$, for the production of WS_2 and tailoring the thermodynamics of the CVD reaction allowed to gain insight into the reaction mechanisms and significantly improve the quality of the material. The crystallinity, size and optoelectronic properties of the synthesised WS_2 improved significantly compared to other volatile precursors reported in the literature. This method can easily be extended in future work to other TMDCs, for example selenides and tellurides, and also to tailored intermetallic alloys such as $Mo_xW_{1-x}S_2$.

Methods for the production of porous metal-graphene composites and graphene foams have also been developed that show potential for numerous far-reaching applications. The powder-based CVD approach allows a significant reduction in consumable costs compared to commercial metal foams. Additionally, new, improved morphology is expected to be beneficial for applications where light and conductive materials are needed. In future work this procedure can also be adapted to hBN to produce porous structures that have better biocompatibility and lower cell toxicity compared to carbon materials[302].

A number of proof of concept applications of the developed CVD materials have been investigated in interdisciplinary collaborations: single crystal graphene in QHE for metrology applications, hexagonal boron nitride as a dielectric material for LED devices and graphene

foams as the cathode in a Li-O_2 battery. Other far-reaching applications have been proposed in this thesis.

Some of the key parts of this thesis resulted in patent filings and attracted additional funding. Further development is planned to continue of the equipment, synthesis methods and applications for 2D materials in the Nanomaterials by Design group at Oxford University together with the research and industrial partners.

Chapter 9. Appendices

A. Automation devices and control software

Device description

The CVD systems had a number of peripheral devices connected to a computer:

- Gas controllers:
    - MKS 647C gas flow controller connected via RS-232 interface to regulate the flow of pure CH_4, H_2 and Ar gases.
    - Brooks 0254 gas flow controller connected via RS-232 interface to regulate the flow of gas mixtures from a separate gas line: Ar/2.5 % H_2, Ar/0.025 % CH_4, pure Ar and Ar/0.1 % O_2.
- Furnace movement control:
    - Stepper Bee + stepper drive board connected via USB 2.0.
    - A 12V stepper motor (0.52 Nm torque) to move the TSH12/38/500 Elite furnace.
    - A 12V stepper motor (0.52 Nm torque) to move the larger CTF12/65/550 Carbolite furnace.
    - A 12V DC power supply.
    - Two 5V “button” sensors (Maplin electronics) for the position calibration.
- Thermocouple temperature measurement with a TC-08 Pico Technology data logger connected via USB. K-type mineral thermocouples were used as the sensors.

- Electrical heater control:
    - Three PID controllers were used on different CVD systems (Omega Engineering CN743) connected via RS-485 interface that were relaying mains power to the electrical heaters.
    - Two electrical heaters (appendix 9-D) and one heating tape were used as the heat sources.

Automation software description

The graphical user interface of the automation software consisted of three regions: **the command list for equipment control**, a text-based **main recipe window**, **the recipe execution log** and buttons. Due to the large size of the source code, it is not possible to include it in the documentation, therefore, the user interface and the functionality will be discussed instead.

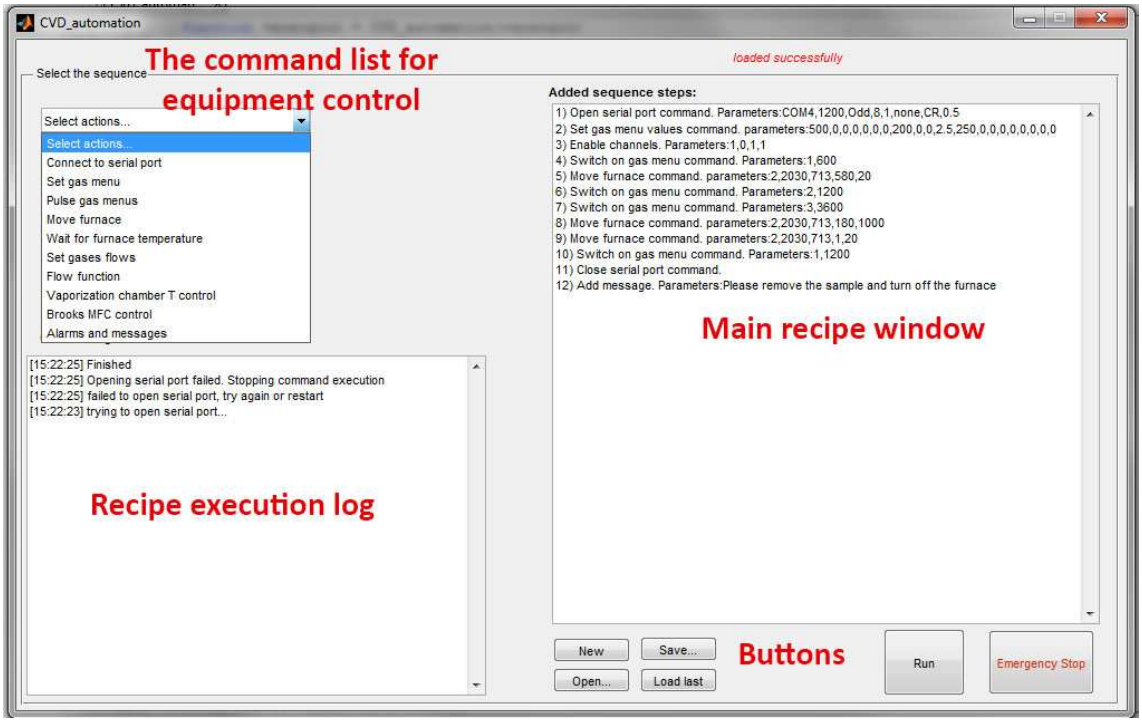

The command list for equipment control allowed the user to build a recipe without any knowledge of Matlab or how the hardware operated and consisted of 10 options:

1) **A command to connect to the serial port of the 647C gas flow controller**. This command allowed to connect to different MKS gas mixture controllers and run multiple experiments simultaneously by changing the id of the command port, for example, COM1, COM2, COM6 etc. Other default settings were used, such as timeout, parity etc.

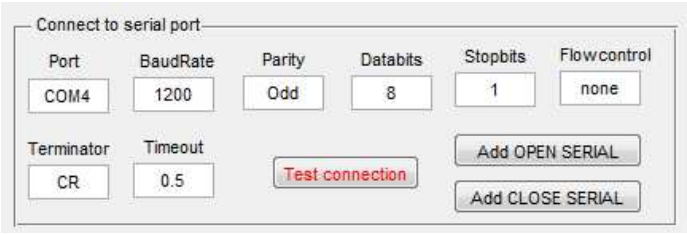

2) **A command to set the gas menus of the 647C gas flow controller**. The gas mixture controller allowed to pre-define 5 gas mixtures (labelled m1, m2… m5) consisting of up to 4 gases (columns or "channels"). In the used gas panel configuration, column 1 corresponded to pure Ar gas, column 2 corresponded to NH_3 gas, column 3 corresponded to CH_4 and column 4 corresponded to H_2 gas. Additionally, each gas channel had to be enabled before any flow was permitted.

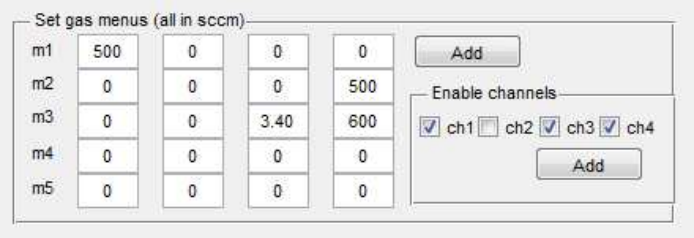

3) **A command to set a specific gas menu for a defined amount of time**. The options allowed to either set a gas menu and pause recipe execution for a defined number of seconds or switch on a specific gas menu and immediately continue program execution.

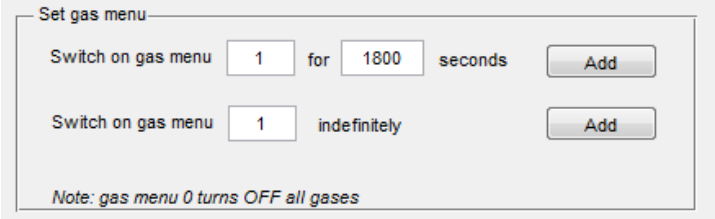

4) **A command to sequentially alternate between gas menus or "pulse gas menus".** This functionality was programmed for future work and allowed to set two repeatedly switching gas menus with pre-defined intervals for a set synthesis period.

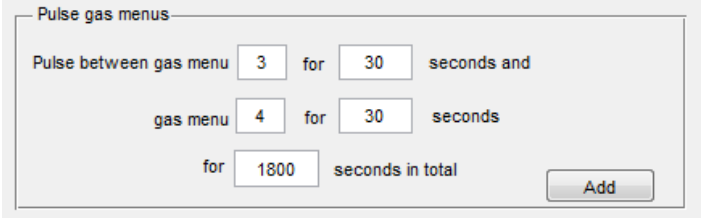

5) **A command to vary the flow following a custom function.** This option allowed to continuously vary the flow on a single gas channel according to any function permitted in Matlab. The function was evaluated every defined time interval within the total time of execution.

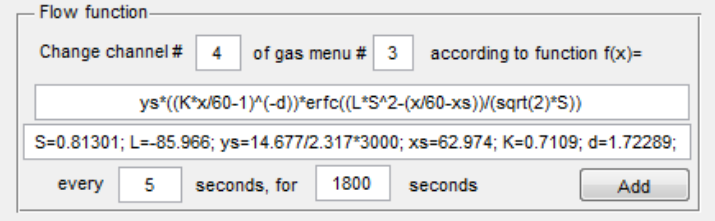

6) **A command to measure the temperature of the furnace.** The voltage of an external thermocouple inserted into the furnace was monitored and converted to a temperature reading in °C. It was possible to pause recipe execution until desired temperature was reached, either from below (heating up) or from above (cooling down).

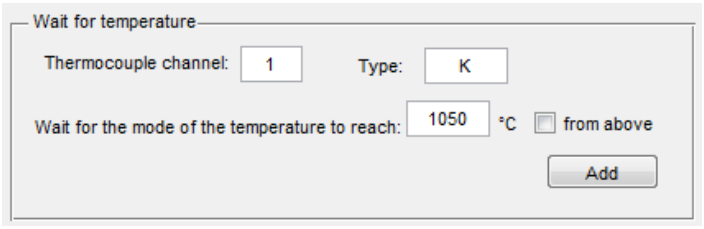

7) **A command to program the furnace movement.** Two CVD systems had stepper motors (Motor ID 1 and Motor ID 2) connected via metal chains to the furnaces on rails. Each system had two “home” sensors that switched their state when the furnace touched each end of the platform. These devices allowed to calibrate the distance moved by the furnace per step of the motor and therefore the furnace position. Precision of around 2 mm was achieved. Additionally, the cooling or heating rates and other advanced heating regimes could be programmed.

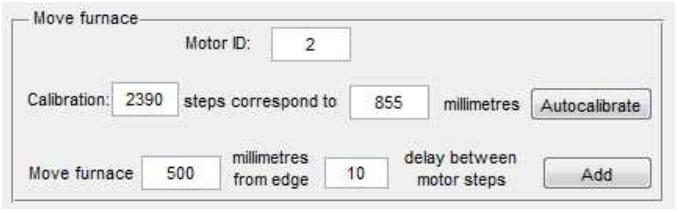

8) **A command to control the temperature of the precursor vaporisation chamber for the solid or liquid precursor evaporation.** The PID controller connected to the electrical heater for hBN synthesis was controlled via the specified com port (RS-485), such that custom temporal temperature profiles could be loaded from a csv file containing two columns: time in seconds, temperature in °C.

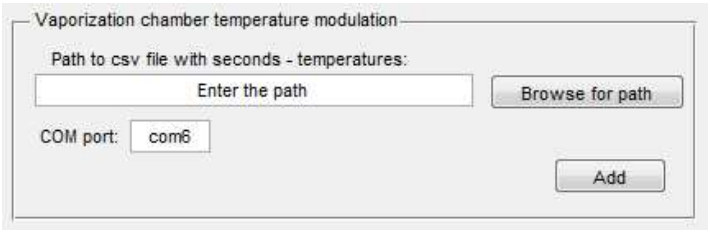

9) **A command to control the gas flows of the inert gas system.** A separate dilute gas mixture line, consisting of Ar, Ar/CH_4 and Ar/H_2 utilised Brooks 0254 gas flow controller. The flows of gases and specific time for the mixture could be set in the recipe.

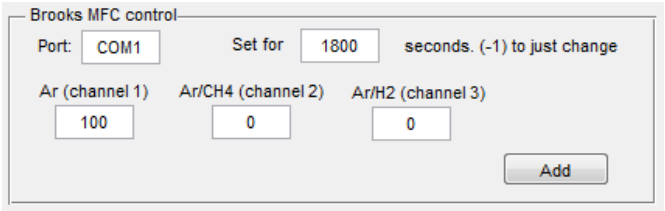

10) **Alarms and messages**. Sound notification or a pop-up message could also be added in the recipe.

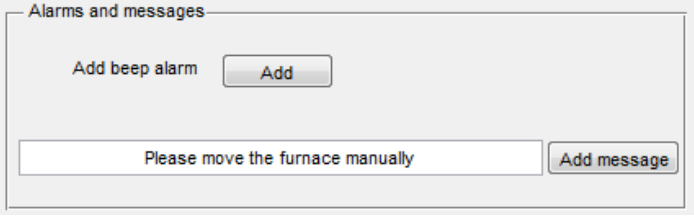

The main recipe window allowed the user to view steps of the recipe and recognise text-based parameters. This window also permitted editing of the recipe if only small modifications of the parameters were necessary. The recipe could also be saved as a text file and loaded from a text file. Once the recipe had been completed and the sample was loaded into the system, clicking the “Run” button initiated command execution. In case of a problem, clicking the “Emergency Stop” button allowed to terminate the recipe execution.

The recipe execution log output which command was being executed and its status in real time with a timestamp. If a problem occurred the command log typically showed suggestions of possible causes and ways to fix them.

B. Pt-Si phase diagram

The Pt-Si binary system phase diagram showing a number of eutectic points that can form depending on the stoichiometry of Pt and Si. Diagram calculated by Xu *et al* (2008)[228].

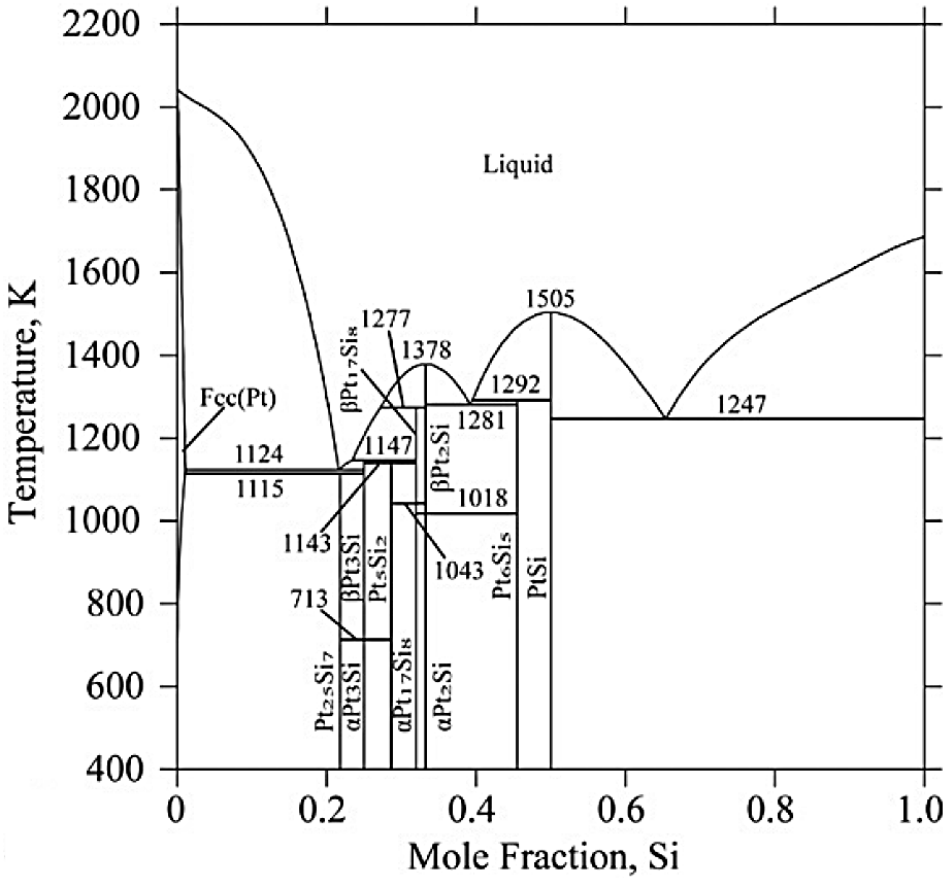

C. Hexagonality analysis algorithm

The **pseudo code** for the algorithm was as follows:

- An image was loaded into computer memory using the *uigetfile* and *imread* functions.

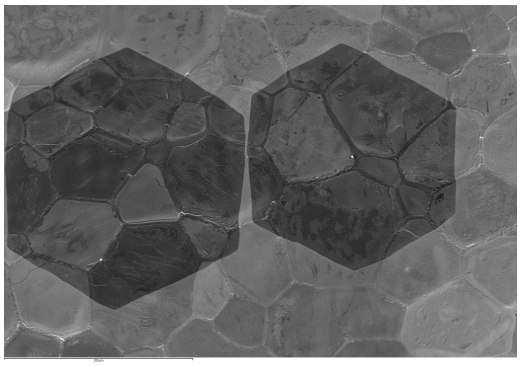

- The image was blurred with the *imfilter* function to reduce noise.

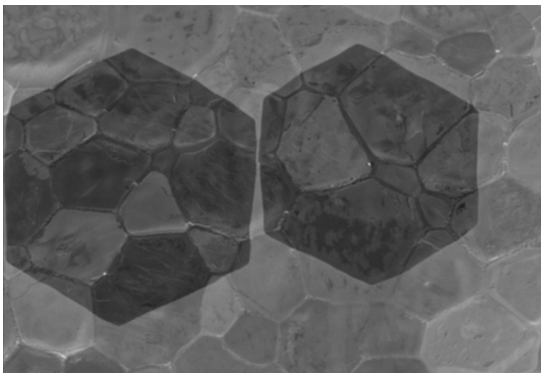

- A threshold was manually found and the image was converted to black and white using the function *im2bw.*

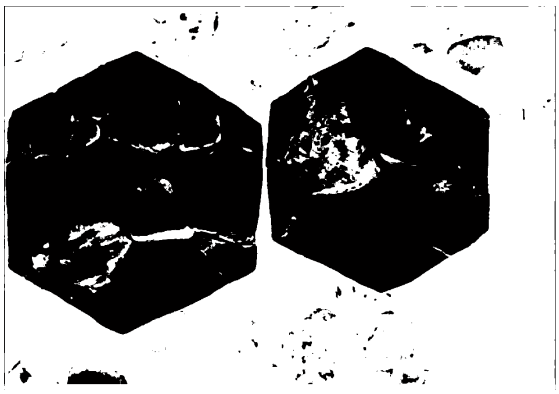

- The binary image was split into connected regions ignoring the inner holes using the function *bwboundaries.*

- Each region was then analysed separately and its properties ('FilledArea', 'Centroid', 'Eccentricity', 'Perimeter', 'FilledImage') were saved into a matrix using the function *regionprops*.
- The user was then asked to assess whether the identified region was a graphene domain.

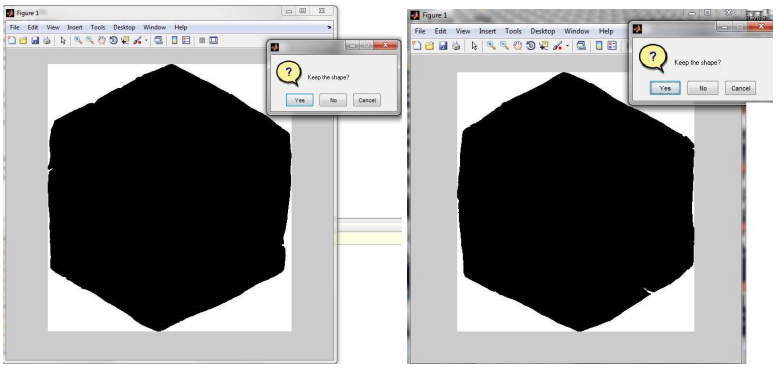

- All accepted regions were saved and the mean and standard deviation of the hexagonality value (equation 30) were calculated.

The **source code** is as follows:

```
clear all;
[filename, pathname] = uigetfile('*.tif;');

img = imread(strcat(pathname, filename));

imshow(img);

H=fspecial('average', [9 9]);
img = imfilter(img, H);

img_bw = im2bw(img, 0.357);
% medfilt2(img_bw);

imshow(img_bw, []);
img_bw = bwareaopen(1-img_bw, 400);
[B,L] = bwboundaries(img_bw,'noholes');
stats = regionprops(L,'FilledArea','Centroid', 'Eccentricity',
'Perimeter', 'FilledImage');

countt =1;
for kl=1:length(B)
    boundary = B{kl};
    imshow(1-stats(kl).FilledImage,[]);
    pause(0.01);
```

```
    button = questdlg('Keep the shape?');
    close figure 1;
    if strcmp(button, 'Yes')
        mtrx (countt) = (stats(kl).Perimeter)^2/stats(kl).FilledArea;
        countt=countt+1;
    end;
    if strcmp(button, 'Cancel')
        break;
    end;


 end;
csvwrite(strcat(pathname, filename(1:end-4), '.csv'),
transpose(mtrx));
mtrx_processed =100-100*abs((mtrx - sqrt(192)))/sqrt(192);
[mean(mtrx_processed) std(mtrx_processed)]
```

Some images, where the background did not permit to find a suitable threshold value were measured manually.

D. Electrical jacket

Kanthal wire (an alloy of Fe, Cr, Al with resistivity of 27 Ω m and diameter of 0.25 mm) was wound around a 1" fused silica container with equal spacing between the coils of around 2mm. High temperature woven silica sheet (Silicaflex blanket), covered with heat resistant adhesive was used to insulate the wire from inside and outside with a number of layers. The sheet was also a good electrical insulator. A K-type thermocouple was inserted at the bottom of the electrical jacket and connected to the CN743 PID controller.

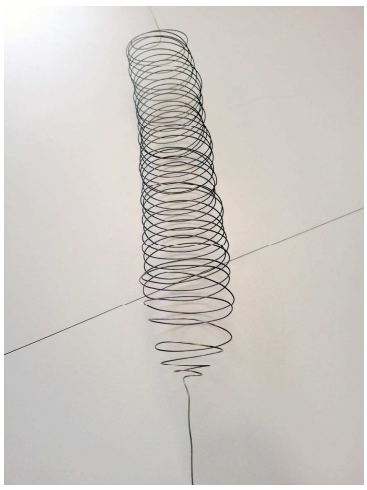

The total resistance of the coil was 365 Ω. Two power supplies were used: a 100 W DC power supply for the finer temperature control with accuracy of ± 0.5 °C and the mains power for the slightly lower accuracy temperature control of ± 3 °C. To estimate the power dissipated when the mains source was used, the root mean square current in the coil was calculated by dividing the root mean square voltage (V_{rms} = 230 V) by the resistance of the coil. The value of the current was I_{rms} = 0.6 A, therefore the total power dissipation was expected to be around 145 W. The coils with either power source achieved target temperatures within seconds after the set point change. The temperature range utilised in the experiments was typically between 60 – 200 °C, however, the thermal insulation was stable at higher temperatures, up to 980 °C, allowing the possibility to expand the usability of the device to a wide variety of applications.

Chapter 10. Bibliography

1. Soule, D.E. & Mcclure, J.W. Band Structure and Transport Properties of Single-Crystal Graphite. *J Phys Chem Solids* **8**, 29-35 (1959).
2. Robertson, J. Electronic-Structure and Core Exciton of Hexagonal Boron-Nitride. *Phys Rev B* **29**, 2131-2137 (1984).
3. Wilson, J.A. & Yoffe, A.D. The transition metal dichalcogenides discussion and interpretation of the observed optical, electrical and structural properties. *Advances in Physics* **18**, 193-335 (1969).
4. Peierls, R. Quelques propriétés typiques des corps solides. *Annales de l'institut Henri Poincaré* **5**, 177-222 (1935).
5. Landau, L.D. Zur Theorie der phasenumwandlungen II. *Phys. Z. Sowjetunion* **11**, 26-35 (1937).
6. Meyer, J.C. et al. The structure of suspended graphene sheets. *Nature* **446**, 60-63 (2007).
7. Novoselov, K.S. et al. Electric field effect in atomically thin carbon films. *Science* **306**, 666-669 (2004).
8. Novoselov, K.S. et al. Two-dimensional atomic crystals. *P Natl Acad Sci USA* **102**, 10451-10453 (2005).
9. Nagashima, A. et al. 2-Dimensional Plasmons in Monolayer Graphite. *Solid State Commun* **83**, 581-585 (1992).
10. Land, T.A., Michely, T., Behm, R.J., Hemminger, J.C. & Comsa, G. STM Investigation of Single Layer Graphite Structures Produced on Pt(111) by Hydrocarbon Decomposition. *Surface Science* **264**, 261-270 (1992).
11. Nagashima, A. et al. Electronic States of Monolayer Graphite Formed on TiC(111) Surface. *Surface Science* **291**, 93-98 (1993).
12. Nagashima, A. et al. Electronic-Structure of Monolayer Graphite on Some Transition-Metal Carbide Surfaces. *Surface Science* **287**, 609-613 (1993).
13. Nagashima, A., Tejima, N. & Oshima, C. Electronic States of the Pristine and Alkali-Metal-Intercalated Monolayer Graphite/Ni(111) Systems. *Phys Rev B* **50**, 17487-17495 (1994).
14. Gamo, Y., Nagashima, A., Wakabayashi, M., Terai, M. & Oshima, C. Atomic structure of monolayer graphite formed on Ni(111). *Surface Science* **374**, 61-64 (1997).
15. Nagashima, A., Tejima, N., Gamou, Y., Kawai, T. & Oshima, C. Electronic-Structure of Monolayer Hexagonal Boron-Nitride Physisorbed on Metal-Surfaces. *Phys Rev Lett* **75**, 3918-3921 (1995).
16. Nagashima, A., Tejima, N., Gamou, Y., Kawai, T. & Oshima, C. Electronic Dispersion-Relations of Monolayer Hexagonal Boron-Nitride Formed on the Ni(111) Surface. *Phys Rev B* **51**, 4606-4613 (1995).
17. Nagashima, A., Tejima, N., Gamou, Y., Kawai, T. & Oshima, C. Electronic states of monolayer hexagonal boron nitride formed on the metal surfaces. *Surface Science* **357**, 307-311 (1996).
18. Nagashima, A. et al. Electron spectroscopic studies of monolayer hexagonal boron nitride physisorbed on metal surfaces. *Int J Mod Phys B* **10**, 3517-3537 (1996).
19. Gamou, Y., Terai, M., Nagashima, A. & Oshima, C. Atomic structural analysis of a monolayer epitaxial film of hexagonal boron nitride Ni(111) studied by LEED intensity analysis. *Sci Rep Res Tohoku A* **44**, 211-214 (1997).
20. Rokuta, E. et al. Phonon dispersion of an epitaxial monolayer film of hexagonal boron nitride on Ni(111). *Phys Rev Lett* **79**, 4609-4612 (1997).

21. Sandoval, S.J., Yang, D., Frindt, R.F. & Irwin, J.C. Raman-Study and Lattice-Dynamics of Single Molecular Layers of MoS_2. *Phys Rev B* **44**, 3955-3962 (1991).
22. Nagashima, A., Gamou, Y., Terai, M., Wakabayashi, M. & Oshima, C. Electronic states of the heteroepitaxial double-layer system: Graphite/monolayer hexagonal boron nitride/Ni(111). *Phys Rev B* **54**, 13491-13494 (1996).
23. Geim, A.K. & Novoselov, K.S. The rise of graphene. *Nature Materials* **6**, 183-191 (2007).
24. Kroto, H.W., Heath, J.R., Obrien, S.C., Curl, R.F. & Smalley, R.E. C-60 - Buckminsterfullerene. *Nature* **318**, 162-163 (1985).
25. Iijima, S. Helical Microtubules of Graphitic Carbon. *Nature* **354**, 56-58 (1991).
26. Gibney, E. *Andre Geim: Graphene's buzz has spread*. 2015. http://www.nature.com/news/andre-geim-graphene-s-buzz-has-spread-1.17861 (accessed 09/07/2015).
27. Stoye, E. *Graphene beyond the hype*. 2015. http://www.rsc.org/chemistryworld/2015/06/graphene-beyond-hype (accessed 07/09/2015).
28. Ehrenfreund, P. & Foing, B.H. Fullerenes and Cosmic Carbon. *Science* **329**, 1159-1160 (2010).
29. Novoselov, K.S. Nobel Lecture: Graphene: Materials in the Flatland*. *Rev Mod Phys* **83**, 837-849 (2011).
30. Gass, M.H. et al. Free-standing graphene at atomic resolution. *Nat Nanotechnol* **3**, 676-681 (2008).
31. Wintterlin, J. & Bocquet, M.L. Graphene on metal surfaces. *Surface Science* **603**, 1841-1852 (2009).
32. Tsukamoto, T. & Ogino, T. Morphology of Graphene on Step-Controlled Sapphire Surfaces. *Appl Phys Express* **2** (2009).
33. Wallace, P.R. The Band Theory of Graphite. *Physical Review* **71**, 622-634 (1947).
34. Reich, S., Maultzsch, J., Thomsen, C. & Ordejon, P. Tight-binding description of graphene. *Phys Rev B* **66** (2002).
35. Jeon, C. et al. Opening and reversible control of a wide energy gap in uniform monolayer graphene. *Sci Rep-Uk* **3** (2013).
36. Novoselov, K.S. et al. Two-dimensional gas of massless Dirac fermions in graphene. *Nature* **438**, 197-200 (2005).
37. Semenoff, G.W. Condensed-Matter Simulation of a Three-Dimensional Anomaly. *Phys Rev Lett* **53**, 2449-2452 (1984).
38. Castro Neto, A.H., Guinea, F., Peres, N.M.R., Novoselov, K.S. & Geim, A.K. The electronic properties of graphene. *Rev Mod Phys* **81**, 109-162 (2009).
39. Partoens, B. & Peeters, F.M. From graphene to graphite: Electronic structure around the K point. *Phys Rev B* **74** (2006).
40. Pumera, M. Electrochemistry of Graphene: New Horizons for Sensing and Energy Storage. *Chem Rec* **9**, 211-223 (2009).
41. Morozov, S.V. et al. Giant intrinsic carrier mobilities in graphene and its bilayer. *Phys Rev Lett* **100** (2008).
42. Nair, R.R. et al. Fine structure constant defines visual transparency of graphene. *Science* **320**, 1308-1308 (2008).
43. Novoselov, K.S. et al. A roadmap for graphene. *Nature* **490**, 192-200 (2012).
44. Lee, C., Wei, X.D., Kysar, J.W. & Hone, J. Measurement of the elastic properties and intrinsic strength of monolayer graphene. *Science* **321**, 385-388 (2008).
45. Balandin, A.A. et al. Superior Thermal Conductivity of Single-Layer Graphene. *Nano Letters* **8**, 902-907 (2008).
46. Bunch, J.S. et al. Impermeable atomic membranes from graphene sheets. *Nano Letters* **8**, 2458-2462 (2008).

47. Schedin, F. et al. Detection of individual gas molecules adsorbed on graphene. *Nature Materials* **6**, 652-655 (2007).
48. Liu, Y.B. et al. A graphene-based electrochemical filter for water purification. *J Mater Chem A* **2**, 16554-16562 (2014).
49. Surwade, S.P. et al. Water desalination using nanoporous single-layer graphene. *Nat Nanotechnol* **10**, 459-464 (2015).
50. Schwierz, F. Graphene transistors. *Nat Nanotechnol* **5**, 487-496 (2010).
51. Liu, Z. et al. Ultrathin high-temperature oxidation-resistant coatings of hexagonal boron nitride. *Nat Commun* **4** (2013).
52. Giovannetti, G., Khomyakov, P.A., Brocks, G., Kelly, P.J. & van den Brink, J. Substrate-induced band gap in graphene on hexagonal boron nitride: Ab initio density functional calculations. *Phys Rev B* **76** (2007).
53. Taylor, R. & Coulson, C.A. Studies in Graphite and Related Compounds .3. Electronic Band Structure in Boron Nitride. *P Phys Soc Lond A* **65**, 834-838 (1952).
54. Usachov, D. et al. Quasifreestanding single-layer hexagonal boron nitride as a substrate for graphene synthesis. *Phys Rev B* **82** (2010).
55. Ma, H., Lin, S.H., Carpenter, R.W., Rice, P. & Sankey, O.F. Abinitio Calculation of Band-Structure, X-Ray-Emission, Quantum Yield, and Electron-Energy-Loss Spectra of Hexagonal Boron-Nitride. *J Appl Phys* **73**, 7422-7426 (1993).
56. Watanabe, K., Taniguchi, T. & Kanda, H. Direct-bandgap properties and evidence for ultraviolet lasing of hexagonal boron nitride single crystal. *Nature Materials* **3**, 404-409 (2004).
57. Geim, A.K. & Grigorieva, I.V. Van der Waals heterostructures. *Nature* **499**, 419-425 (2013).
58. Tang, S. et al. Precisely aligned graphene grown on hexagonal boron nitride by catalyst free chemical vapor deposition. *Sci. Rep.* **3** (2013).
59. Hao, Y.F. et al. The Role of Surface Oxygen in the Growth of Large Single-Crystal Graphene on Copper. *Science* **342**, 720-723 (2013).
60. Song, L. et al. Large Scale Growth and Characterization of Atomic Hexagonal Boron Nitride Layers. *Nano Letters* **10**, 3209-3215 (2010).
61. Remes, Z., Nesladek, M., Haenen, K., Watanabe, K. & Taniguchi, T. The optical absorption and photoconductivity spectra of hexagonal boron nitride single crystals. *physica status solidi (a)* **202**, 2229-2233 (2005).
62. Chen, S.S. et al. Oxidation Resistance of Graphene-Coated Cu and Cu/Ni Alloy. *ACS Nano* **5**, 1321-1327 (2011).
63. Lindsay, L. & Broido, D.A. Enhanced thermal conductivity and isotope effect in single-layer hexagonal boron nitride. *Phys Rev B* **84** (2011).
64. Yun, W.S., Han, S.W., Hong, S.C., Kim, I.G. & Lee, J.D. Thickness and strain effects on electronic structures of transition metal dichalcogenides: 2H-MX_2 semiconductors (M = Mo, W; X = S, Se, Te). *Phys Rev B* **85** (2012).
65. Zeng, H.L. et al. Optical signature of symmetry variations and spin-valley coupling in atomically thin tungsten dichalcogenides. *Sci Rep-Uk* **3** (2013).
66. Iqbal, M.W. et al. High-mobility and air-stable single-layer WS_2 field-effect transistors sandwiched between chemical vapor deposition-grown hexagonal BN films. *Sci Rep-Uk* **5** (2015).
67. Liang, L.B. & Meunier, V. First-principles Raman spectra of MoS_2, WS_2 and their heterostructures. *Nanoscale* **6**, 5394-5401 (2014).
68. Liu, Z. et al. Identification of active atomic defects in a monolayered tungsten disulphide nanoribbon. *Nat Commun* **2** (2011).
69. Cao, T. et al. Valley-selective circular dichroism of monolayer molybdenum disulphide. *Nat Commun* **3** (2012).

70. Liu, L.T., Kumar, S.B., Ouyang, Y. & Guo, J. Performance Limits of Monolayer Transition Metal Dichalcogenide Transistors. *Ieee T Electron Dev* **58**, 3042-3047 (2011).
71. Koppens, F.H.L. et al. Photodetectors based on graphene, other two-dimensional materials and hybrid systems. *Nat Nanotechnol* **9**, 780-793 (2014).
72. Bernardi, M., Palummo, M. & Grossman, J.C. Extraordinary Sunlight Absorption and One Nanometer Thick Photovoltaics Using Two-Dimensional Monolayer Materials. *Nano Letters* **13**, 3664-3670 (2013).
73. Gutierrez, H.R. et al. Extraordinary Room-Temperature Photoluminescence in Triangular WS_2 Monolayers. *Nano Letters* **13**, 3447-3454 (2013).
74. Chen, Y.F. et al. Tunable Band Gap Photoluminescence from Atomically Thin Transition-Metal Dichalcogenide Alloys. *ACS Nano* **7**, 4610-4616 (2013).
75. Withers, F. et al. Light-emitting diodes by band-structure engineering in van der Waals heterostructures. *Nat Mater* **14**, 301-306 (2015).
76. Ye, Y. et al. in ArXiv e-prints, Vol. 1503 6141 (2015).
77. Hernandez, Y. et al. High-yield production of graphene by liquid-phase exfoliation of graphite. *Nat Nanotechnol* **3**, 563-568 (2008).
78. Lee, J.H. et al. One-Step Exfoliation Synthesis of Easily Soluble Graphite and Transparent Conducting Graphene Sheets. *Adv Mater* **21**, 4383 (2009).
79. Qian, W. et al. Solvothermal-Assisted Exfoliation Process to Produce Graphene with High Yield and High Quality. *Nano Res* **2**, 706-712 (2009).
80. Pu, N.W., Wang, C.A., Sung, Y., Liu, Y.M. & Ger, M.D. Production of few-layer graphene by supercritical CO_2 exfoliation of graphite. *Mater Lett* **63**, 1987-1989 (2009).
81. Van Noorden, R. Production: Beyond sticky tape. *Nature* **483**, S32-S33 (2012).
82. Chen, W.F. & Yan, L.F. Preparation of graphene by a low-temperature thermal reduction at atmosphere pressure. *Nanoscale* **2**, 559-563 (2010).
83. Zhang, L. et al. Size-controlled synthesis of graphene oxide sheets on a large scale using chemical exfoliation. *Carbon* **47**, 3365-3368 (2009).
84. Dideykin, A. et al. Monolayer graphene from graphite oxide. *Diam Relat Mater* **20**, 105-108 (2011).
85. Zhang, L. et al. Controlled synthesis of few-layered graphene sheets on a large scale using chemical exfoliation. *Carbon* **48**, 2367-2371 (2010).
86. Kang, N. & Khondaker, S.I. The impact of carbon sp^2 fraction of reduced graphene oxide on the performance of reduced graphene oxide contacted organic transistors. *Appl Phys Lett* **105**, 223301 (2014).
87. Rozada, R., Paredes, J.I., Villar-Rodil, S., Martinez-Alonso, A. & Tascon, J.M.D. Towards full repair of defects in reduced graphene oxide films by two-step graphitization. *Nano Res* **6**, 216-233 (2013).
88. El-Kady, M.F., Strong, V., Dubin, S. & Kaner, R.B. Laser Scribing of High-Performance and Flexible Graphene-Based Electrochemical Capacitors. *Science* **335**, 1326-1330 (2012).
89. Joshi, R.K. et al. Precise and Ultrafast Molecular Sieving Through Graphene Oxide Membranes. *Science* **343**, 752-754 (2014).
90. Valles, C., Nunez, J.D., Benito, A.M. & Maser, W.K. Flexible conductive graphene paper obtained by direct and gentle annealing of graphene oxide paper. *Carbon* **50**, 835-844 (2012).
91. Nicolosi, V., Chhowalla, M., Kanatzidis, M.G., Strano, M.S. & Coleman, J.N. Liquid Exfoliation of Layered Materials. *Science* **340**, 1420 (2013).
92. Li, L.H., Guo, Y.Z., Zhang, X.Y. & Song, Y.L. Inkjet-printed highly conductive transparent patterns with water based Ag-doped graphene. *J Mater Chem A* **2**, 19095-19101 (2014).

93. Zhu, C. et al. Highly compressible 3D periodic graphene aerogel microlattices. *Nat Commun* **6** (2015).
94. Mi, X. et al. Preparation of graphene oxide aerogel and its adsorption for Cu^{2+} ions. *Carbon* **50**, 4856-4864 (2012).
95. Nair, R.R., Wu, H.A., Jayaram, P.N., Grigorieva, I.V. & Geim, A.K. Unimpeded Permeation of Water Through Helium-Leak–Tight Graphene-Based Membranes. *Science* **335**, 442-444 (2012).
96. Robert D. Ohrenschall, Charles Milton. (1931). The Occurrence of Moissanite (Silicon Carbide) in Sediments. Journal of Sedimentary Research. 1 (1,2), 96-99.
97. Nassau, K. Synthetic moissanite: A new man-made jewel. *Curr Sci India* **79**, 1572-1577 (2000).
98. Sutter, P. Epitaxial graphene: How silicon leaves the scene. *Nat Mater* **8**, 171-172 (2009).
99. Hu, Y.K. et al. Structured epitaxial graphene: growth and properties. *J Phys D Appl Phys* **45** (2012).
100. Yu, Q.K. et al. Graphene segregated on Ni surfaces and transferred to insulators. *Appl Phys Lett* **93** (2008).
101. Sutter, P.W., Flege, J.-I. & Sutter, E.A. Epitaxial graphene on ruthenium. *Nat Mater* **7**, 406-411 (2008).
102. Liu, X. et al. Segregation Growth of Graphene on Cu-Ni Alloy for Precise Layer Control. *J Phys Chem C* **115**, 11976-11982 (2011).
103. Li, X.S. et al. Large-Area Graphene Single Crystals Grown by Low-Pressure Chemical Vapor Deposition of Methane on Copper. *Journal of the American Chemical Society* **133**, 2816-2819 (2011).
104. Malesevic, A. et al. Synthesis of few-layer graphene via microwave plasma-enhanced chemical vapour deposition. *Nanotechnology* **19** (2008).
105. Terasawa, T. & Saiki, K. Growth of graphene on Cu by plasma enhanced chemical vapor deposition. *Carbon* **50**, 869-874 (2012).
106. Yamada, T., Kim, J., Ishihara, M. & Hasegawa, M. Low-temperature graphene synthesis using microwave plasma CVD. *J Phys D Appl Phys* **46** (2013).
107. Riikonen, J. et al. Photo-thermal chemical vapor deposition of graphene on copper. *Carbon* **62**, 43-50 (2013).
108. Moorfield. *NanoCVD-8G for Graphene Synthesis*. 2015. http://www.nanocvd.co.uk/products_nanoCVD_8G.html (accessed 25/06/2015).
109. Piner, R. et al. Graphene Synthesis via Magnetic Inductive Heating of Copper Substrates. *ACS Nano* (2013).
110. Dong, X.C. et al. Growth of large-sized graphene thin-films by liquid precursor-based chemical vapor deposition under atmospheric pressure. *Carbon* **49**, 3672-3678 (2011).
111. Srivastava, A. et al. Novel Liquid Precursor-Based Facile Synthesis of Large-Area Continuous, Single, and Few-Layer Graphene Films. *Chem Mater* **22**, 3457-3461 (2010).
112. Gao, H. et al. Synthesis of S-doped graphene by liquid precursor. *Nanotechnology* **23** (2012).
113. Wu, T. et al. Triggering the Continuous Growth of Graphene Toward Millimeter-Sized Grains. *Adv Funct Mater* **23**, 198-203 (2013).
114. Guo, N. et al. Controllable growth of triangular hexagonal boron nitride domains on copper foils by an improved low-pressure chemical vapor deposition method. *Nanotechnology* **23** (2012).
115. Tay, R.Y. et al. A systematic study of the atmospheric pressure growth of large-area hexagonal crystalline boron nitride film. *Journal of Materials Chemistry C* **2**, 1650-1657 (2014).

116. Tay, R.Y. et al. Growth of Large Single-Crystalline Two-Dimensional Boron Nitride Hexagons on Electropolished Copper. *Nano Letters* **14**, 839-846 (2014).
117. Dobkin, D.M. Principles of Chemical Vapor Deposition. (Springer Science+Business Media Dordrecht 2003).
118. Rau, H., Kutty, T.R.N. & Decarval.Jr Thermodynamics of Sulfur Vapor. *J Chem Thermodyn* **5**, 833-844 (1973).
119. NIST Chemistry WebBook, NIST Standard Reference Database Number 69. (National Institute of Standards and Technology, 2005).
120. Ohare, P.A.G., Hubbard, W.N., Johnson, G.K. & Flotow, H.E. Calorimetric Measurements of the Low-Temperature Heat-Capacity, Standard Molar Enthalpy of Formation at 298.15 K, and High-Temperature Molar Enthalpy Increments Relative to 298.15 K of Tungsten Disulfide (WS_2), and the Thermodynamic Properties to 1500 K. *J Chem Thermodyn* **16**, 45-59 (1984).
121. Xu, Z.-Q. et al. Synthesis and Transfer of Large-Area Monolayer WS_2 Crystals: Moving Toward the Recyclable Use of Sapphire Substrates. *ACS Nano* (2015).
122. Li, X.-L., Ge, J.-P. & Li, Y.-D. Atmospheric Pressure Chemical Vapor Deposition: An Alternative Route to Large-Scale MoS_2 and WS_2 Inorganic Fullerene-like Nanostructures and Nanoflowers. *Chemistry – A European Journal* **10**, 6163-6171 (2004).
123. Bale, C.W. & Bélisle, E. *Fact-Web suite of interactive programs*. 2010. http://www.crct.polymtl.ca/equiweb.php (accessed 29/09/2015).
124. Okada, M. et al. Direct Chemical Vapor Deposition Growth of WS_2 Atomic Layers on Hexagonal Boron Nitride. *ACS Nano* **8**, 8273-8277 (2014).
125. Vlassiouk, I. et al. Role of Hydrogen in Chemical Vapor Deposition Growth of Large Single-Crystal Graphene. *ACS Nano* **5**, 6069-6076 (2011).
126. Losurdo, M., Giangregorio, M.M., Capezzuto, P. & Bruno, G. Graphene CVD growth on copper and nickel: role of hydrogen in kinetics and structure. *Phys Chem Chem Phys* **13**, 20836-20843 (2011).
127. Zhang, W., Wu, P., Li, Z. & Yang, J. First-Principles Thermodynamics of Graphene Growth on Cu Surfaces. *The Journal of Physical Chemistry C* **115**, 17782-17787 (2011).
128. Kim, H., Saiz, E., Chhowalla, M. & Mattevi, C. Modeling of the self-limited growth in catalytic chemical vapor deposition of graphene. *New J Phys* **15** (2013).
129. Choi, J.-H. et al. Drastic reduction in the growth temperature of graphene on copper via enhanced London dispersion force. *Sci. Rep.* **3** (2013).
130. Sun, J. et al. Growth mechanism of graphene on platinum: Surface catalysis and carbon segregation. *Appl Phys Lett* **104** (2014).
131. Chen, K. & Kamran, S. Bonding Characteristics of TiC and TiN. *Modeling and Numerical Simulation of Material Science* **3** (2013).
132. Luo, Y.-R. Handbook of Bond dissociation energies in organic compounds. (CRC Press, Boca Raton, University of Science and Technology of China; 2003).
133. Long, L.H. & Norrish, R.G.W. The Thermochemistry of Carbon - Valence States, Heats of Sublimation and Energies of Linkage. *Proc R Soc Lon Ser-A* **187**, 337-357 (1946).
134. Reina, A. et al. Large Area, Few-Layer Graphene Films on Arbitrary Substrates by Chemical Vapor Deposition. *Nano Letters* **9**, 30-35 (2009).
135. Yang, R.T., Goethel, P.J., Schwartz, J.M. & Lund, C.R.F. Solubility and diffusivity of carbon in metals. *Journal of Catalysis* **122**, 206-210 (1990).
136. Ping, J.L. & Fuhrer, M.S. Carbon impurities on graphene synthesized by chemical vapor deposition on platinum. *J Appl Phys* **116** (2014).
137. Babenko, V. et al. Rapid epitaxy-free graphene synthesis on silicidated polycrystalline platinum. *Nat Commun* **6**, 7536 (2015).

138. Gross, H., Campbell, C.T. & King, D.A. Metal–carbon bond energies for adsorbed hydrocarbons from calorimetric data. *Surface Science* **572**, 179-190 (2004).
139. McLellan, R.B. The solubility of carbon in solid gold, copper, and silver. *Scripta Metallurgica* **3**, 389-391 (1969).
140. Böhme, M. & Frenking, G. The Cu-C bond dissociation energy of $CuCH_3$. A dramatic failure of the QCISD(T) method. *Chem Phys Lett* **224**, 195-199 (1994).
141. Zhou, H. et al. Chemical vapour deposition growth of large single crystals of monolayer and bilayer graphene. *Nat Commun* **4**, 2096 (2013).
142. Vlassiouk, I. et al. Graphene Nucleation Density on Copper: Fundamental Role of Background Pressure. *The Journal of Physical Chemistry C* **117**, 18919–18926 (2013).
143. Carlsson, J.-O. & Martin, P.M. in Handbook of Deposition Technologies for Films and Coatings (Third Edition). (ed. P.M. Martin) 314-363 (William Andrew Publishing, Boston; 2010).
144. Gao, L.B. et al. Repeated growth and bubbling transfer of graphene with millimetre-size single-crystal grains using platinum. *Nat Commun* **3**, 699 (2012).
145. Li, X. et al. Transfer of Large-Area Graphene Films for High-Performance Transparent Conductive Electrodes. *Nano Letters* **9**, 4359-4363 (2009).
146. Kim, K.S. et al. Large-scale pattern growth of graphene films for stretchable transparent electrodes. *Nature* **457**, 706-710 (2009).
147. Suk, J.W. et al. Transfer of CVD-Grown Monolayer Graphene onto Arbitrary Substrates. *ACS Nano* **5**, 6916-6924 (2011).
148. Fan, Y., He, K., Tan, H.J., Speller, S. & Warner, J.H. Crack-Free Growth and Transfer of Continuous Monolayer Graphene Grown on Melted Copper. *Chem Mater* **26**, 4984-4991 (2014).
149. Hallam, T., Berner, N.C., Yim, C. & Duesberg, G.S. Strain, Bubbles, Dirt, and Folds: A Study of Graphene Polymer-Assisted Transfer. *Adv Mater Interfaces* **1** (2014).
150. Ko, P.J. et al. Simple method to transfer graphene from metallic catalytic substrates to flexible surfaces without chemical etching. *Irago Conference 2012* **433** (2013).
151. Lock, E.H. et al. High-Quality Uniform Dry Transfer of Graphene to Polymers. *Nano Letters* **12**, 102-107 (2012).
152. Wood, J.D. et al. Annealing free, clean graphene transfer using alternative polymer scaffolds. *Nanotechnology* **26** (2015).
153. Song, J. et al. A general method for transferring graphene onto soft surfaces. *Nat Nanotechnol* **8**, 356-362 (2013).
154. Bae, S. et al. Roll-to-roll production of 30-inch graphene films for transparent electrodes. *Nat Nanotechnol* **5**, 574-578 (2010).
155. Her, M., Beams, R. & Novotny, L. Graphene transfer with reduced residue. *Phys Lett A* **377**, 1455-1458 (2013).
156. Suk, J.W. et al. Enhancement of the Electrical Properties of Graphene Grown by Chemical Vapor Deposition via Controlling the Effects of Polymer Residue. *Nano Letters* (2013).
157. Garcia, M.T., Gracia, I., Duque, G., de Lucas, A. & Rodriguez, J.F. Study of the solubility and stability of polystyrene wastes in a dissolution recycling process. *Waste Manage* **29**, 1814-1818 (2009).
158. Lee, S. et al. Graphene transfer in vacuum yielding a high quality graphene. *Carbon* **93**, 286-294 (2015).
159. Cheng, Z.G. et al. Toward Intrinsic Graphene Surfaces: A Systematic Study on Thermal Annealing and Wet-Chemical Treatment of SiO_2-Supported Graphene Devices. *Nano Letters* **11**, 767-771 (2011).
160. Pirkle, A. et al. The effect of chemical residues on the physical and electrical properties of chemical vapor deposited graphene transferred to SiO_2. *Appl Phys Lett* **99** (2011).

161. Lin, Y.C. et al. Graphene Annealing: How Clean Can It Be? *Nano Letters* **12**, 414-419 (2012).
162. Jeong, H.J. et al. Improved transfer of chemical-vapor-deposited graphene through modification of intermolecular interactions and solubility of poly(methylmethacrylate) layers. *Carbon* **66**, 612-618 (2014).
163. Croft, W.J. Under the microscope : a brief history of microscopy. (World Scientific, Hackensack, NJ; 2006).
164. Cox, G. Biological confocal microscopy. *Mater Today* **5**, 34-41 (2002).
165. ZEISS. *MERLIN is an instrument dedicated to the high-end analytical FE-SEM market*. 2015. http://www.zeiss.com/microscopy/en_de/products/scanning-electron-microscopes/merlin-materials.html (accessed 25/06/2015).
166. Mescher, A. Junqueira's basic histology : text and atlas, Edn. 13th. (McGraw-Hill Medical, New York ; London; 2013).
167. Zhou, W., Apkarian, R., Wang, Z. & Joy, D. in Scanning Microscopy for Nanotechnology. (eds. W. Zhou & Z. Wang) 1-40 (Springer New York, 2007).
168. Xie, J. & Spallas, J.P. Different contrast mechanisms in SEM imaging of graphene. *Technical Report, Agilent Technologies* (2012).
169. Yoon, D., Son, Y.W. & Cheong, H. Negative Thermal Expansion Coefficient of Graphene Measured by Raman Spectroscopy. *Nano Letters* **11**, 3227-3231 (2011).
170. Zhu, W.J. et al. Structure and Electronic Transport in Graphene Wrinkles. *Nano Letters* **12**, 3431-3436 (2012).
171. Griffin, B.J., Joy, D.C. & Michael, J.R. Characteristics of secondary electron images from in-lens and conventional Everhart-Thornley detectors - evidence for the energy-based differentiation of high resolution SE1 and delocalized SE2 signals. *Microscopy and Microanalysis* **15**, 46-47 (2009).
172. JEOL. *JEOL Solutions for Innovation*. 2015. http://www.jeolusa.com/ (accessed 06/07/2015).
173. O'Connor, D.J., Sexton, B.A. & Smart, R.S.C. Surface analysis methods in materials science Edn. 2. (Springer, Berlin ; London; 2003).
174. Naumkin, A.V., Kraut-Vass, A., Gaarenstroom, S.W. & Powell, C.J. NIST X-ray Photoelectron Spectroscopy Database. (National Institute of Standards and Technology (NIST), 2012).
175. Gan, L. & Luo, Z.T. Turning off Hydrogen To Realize Seeded Growth of Subcentimeter Single-Crystal Graphene Grains on Copper. *ACS Nano* **7**, 9480-9488 (2013).
176. Glish, G.L. & Vachet, R.W. The basics of mass spectrometry in the twenty-first century. *Nat Rev Drug Discov* **2**, 140-150 (2003).
177. Jorio, A., Saito, R., Dresselhaus, G. & Dresselhaus, M.S. in Raman Spectroscopy in Graphene Related Systems (Wiley-VCH Verlag GmbH & Co. KGaA, 2011).
178. Thomsen, C. & Reich, S. Double Resonant Raman Scattering in Graphite. *Phys Rev Lett* **85**, 5214-5217 (2000).
179. Ferrari, A.C. & Basko, D.M. Raman spectroscopy as a versatile tool for studying the properties of graphene. *Nat Nanotechnol* **8**, 235-246 (2013).
180. Lee, S. et al. Flexible organic solar cells composed of P3HT:PCBM using chemically doped graphene electrodes. *Nanotechnology* **23** (2012).
181. Dresselhaus, M.S., Jorio, A., Hofmann, M., Dresselhaus, G. & Saito, R. Perspectives on Carbon Nanotubes and Graphene Raman Spectroscopy. *Nano Letters* **10**, 751-758 (2010).
182. Wu, W. et al. Control of thickness uniformity and grain size in graphene films for transparent conductive electrodes. *Nanotechnology* **23** (2012).
183. Kumar, C.S.S.R. in Raman Spectroscopy for Nanomaterials Characterization. (ed. C.S.R. Kumar) (Springer Berlin Heidelberg, 2012).

184. Jorio, A. Raman Spectroscopy in Graphene-Based Systems: Prototypes for Nanoscience and Nanometrology. *ISRN Nanotechnology* **2012**, 16 (2012).
185. Hoffman, D.M., Doll, G.L. & Eklund, P.C. Optical-Properties of Pyrolytic Boron-Nitride in the Energy-Range 0.05-10 Ev. *Phys Rev B* **30**, 6051-6056 (1984).
186. Berkdemir, A. et al. Identification of individual and few layers of WS_2 using Raman Spectroscopy. *Sci Rep-Uk* **3** (2013).
187. Malard, L.M., Pimenta, M.A., Dresselhaus, G. & Dresselhaus, M.S. Raman spectroscopy in graphene. *Phys Rep* **473**, 51-87 (2009).
188. Pecharsky, V.K. & Zavalij, P.Y. in Fundamentals of Powder Diffraction and Structural Characterization of Materials (Springer US, 2009).
189. Meyer, J.C. et al. On the roughness of single- and bi-layer graphene membranes. *Solid State Commun* **143**, 101-109 (2007).
190. Munoz, R. & Gomez-Aleixandre, C. Review of CVD Synthesis of Graphene. *Chem Vapor Depos* **19**, 297-322 (2013).
191. An, X.H., Liu, F.Z., Jung, Y.J. & Kar, S. Large-Area Synthesis of Graphene on Palladium and Their Raman Spectroscopy. *J Phys Chem C* **116**, 16412-16420 (2012).
192. Ma, D.L. et al. High-Quality Monolayer Graphene Synthesis on Pd Foils via the Suppression of Multilayer Growth at Grain Boundaries. *Small* **10**, 4003-4011 (2014).
193. Geng, D.C. et al. Uniform hexagonal graphene flakes and films grown on liquid copper surface. *P Natl Acad Sci USA* **109**, 7992-7996 (2012).
194. Yan, Z. et al. Toward the Synthesis of Wafer-Scale Single-Crystal Graphene on Copper Foils. *ACS Nano* **6**, 9110-9117 (2012).
195. Mohsin, A. et al. Synthesis of Millimeter-Size Hexagon-Shaped Graphene Single Crystals on Resolidified Copper. *ACS Nano* (2013).
196. Peng, Z.W. et al. Toward the Synthesis of Wafer-Scale Single-Crystal Graphene on Copper Foils (vol 6, pg 9110, 2012). *ACS Nano* **7**, 875-875 (2013).
197. Vlassiouk, I. et al. Large scale atmospheric pressure chemical vapor deposition of graphene. *Carbon* **54**, 58-67 (2013).
198. Suyitno, Thoharudin & Suhendra, B. Mechanism of the Char Reduction Reaction in a Staged Gasification: Sensitivity of Water Gas Shift Reaction. *International Journal of Engineering & Technology* **11**, 86-93 (2002).
199. Reckinger, N., Felten, A., Santos, C.N., Hackens, B. & Colomer, J.-F. The influence of residual oxidizing impurities on the synthesis of graphene by atmospheric pressure chemical vapor deposition. *Carbon* **63**, 84-91 (2013).
200. De Laeter, J.R. et al. Atomic weights of the elements: Review 2000 - (IUPAC technical report). *Pure Appl Chem* **75**, 683-800 (2003).
201. Choubak, S. et al. Graphene CVD: Interplay Between Growth and Etching on Morphology and Stacking by Hydrogen and Oxidizing Impurities. *J Phys Chem C* **118**, 21532-21540 (2014).
202. Zhang, B. et al. Low-Temperature Chemical Vapor Deposition Growth of Graphene from Toluene on Electropolished Copper Foils. *ACS Nano* **6**, 2471-2476 (2012).
203. Costa, S.D. et al. Resonant Raman spectroscopy of graphene grown on copper substrates. *Solid State Commun* **152**, 1317-1320 (2012).
204. Britton, J. et al. A Graphene Surface Force Balance. *Langmuir* **30**, 11485-11492 (2014).
205. Yu, Q. et al. Control and characterization of individual grains and grain boundaries in graphene grown by chemical vapour deposition. *Nat Mater* **10**, 443-449 (2011).
206. Wood, J.D., Schmucker, S.W., Lyons, A.S., Pop, E. & Lyding, J.W. Effects of Polycrystalline Cu Substrate on Graphene Growth by Chemical Vapor Deposition. *Nano Letters* **11**, 4547-4554 (2011).
207. Zhao, L. et al. Influence of copper crystal surface on the CVD growth of large area monolayer graphene. *Solid State Commun* **151**, 509-513 (2011).

208. Ogawa, Y. et al. Domain Structure and Boundary in Single-Layer Graphene Grown on Cu(111) and Cu(100) Films. *The Journal of Physical Chemistry Letters* **3**, 219-226 (2011).
209. Murdock, A.T. et al. Controlling the Orientation, Edge Geometry, and Thickness of Chemical Vapor Deposition Graphene. *ACS Nano* **7**, 1351-1359 (2013).
210. Tapasztó, L. et al. Mapping the electronic properties of individual graphene grain boundaries. *Appl Phys Lett* **100**, 053114 (2012).
211. Weatherup, R.S. et al. In Situ Characterization of Alloy Catalysts for Low-Temperature Graphene Growth. *Nano Letters* **11**, 4154-4160 (2011).
212. Dai, B.Y. et al. Rational design of a binary metal alloy for chemical vapour deposition growth of uniform single-layer graphene. *Nat Commun* **2** (2011).
213. Shin, H.A.S. et al. Highly uniform growth of monolayer graphene by chemical vapor deposition on Cu-Ag alloy catalysts. *Phys Chem Chem Phys* **16**, 3087-3094 (2014).
214. Yan, K., Fu, L., Peng, H.L. & Liu, Z.F. Designed CVD Growth of Graphene via Process Engineering. *Accounts of Chemical Research* **46**, 2263-2274 (2013).
215. Sun, J.Y. et al. Direct Growth of High-Quality Graphene on High-kappa Dielectric $SrTiO_3$ Substrates. *Journal of the American Chemical Society* **136**, 6574-6577 (2014).
216. Ott, D. & Raub, C.J. Affinity of the platinum metals for refractory oxides. *Platinum Metals Review* **20**, 79-85 (1976).
217. Guselnikov, L.E. & Nametkin, N.S. 1,1-Dimethyl-1-Silaethylene - Heat of Formation, Ionization-Potential and the Energy of the Silicon-Carbon Pi-Bond. *J Organomet Chem* **169**, 155-164 (1979).
218. Kua, J., Faglioni, F. & Goddard, W.A. Thermochemistry for hydrocarbon intermediates chemisorbed on metal surfaces: $CH_{n-m}(CH3)_{(m)}$ with n=1, 2, 3 and m <= n on Pt, Ir, Os, Pd, Ph, and Ru. *Journal of the American Chemical Society* **122**, 2309-2321 (2000).
219. Lee, J., Zhou, W., Pennycook, S.J., Idrobo, J.C. & Pantelides, S.T. Direct visualization of reversible dynamics in a Si-6 cluster embedded in a graphene pore. *Nat Commun* **4** (2013).
220. Wang, Z.G. et al. Synthesis, characterization and electrical properties of silicon-doped graphene films. *Journal of Materials Chemistry C* **3**, 6301-6306 (2015).
221. Lamber, R. & Jaeger, N.I. On the reaction of Pt with SiO_2 substrates: Observation of the Pt_3Si phase with the Cu_3Au superstructure. *J Appl Phys* **70**, 457-461 (1991).
222. Wang, D. et al. Silicide formation on a Pt/SiO_2 model catalyst studied by TEM, EELS, and EDXS. *Journal of Catalysis* **219**, 434-441 (2003).
223. Penner, S. et al. Platinum nanocrystals supported by silica, alumina and ceria: metal–support interaction due to high-temperature reduction in hydrogen. *Surface Science* **532–535**, 276-280 (2003).
224. Tsui, B.-Y. & Chen, M.-C. Dielectric degradation of $Pt/SiO_2/Si$ structures during thermal annealing. *Solid-State Electronics* **36**, 583-593 (1993).
225. Grunthaner, P.J., Grunthaner, F.J. & Madhukar, A. Chemical Bonding and Charge Redistribution - Valence Band and Core Level Correlations for the Ni/Si, Pd/Si, and Pt/Si Systems. *J Vac Sci Technol* **20**, 680-683 (1982).
226. Nguyen, T.P. & Lefrant, S. XPS Study of SiO Thin-Films and SiO Metal Interfaces. *J Phys-Condens Mat* **1**, 5197-5204 (1989).
227. Chou, T.C. Anomalous Solid-State Reaction between SiC and Pt. *J Mater Res* **5**, 601-608 (1990).
228. Xu, L.L., Wang, J., Liu, H.S. & Jin, Z.P. Thermodynamic assessment of the Pt–Si binary system. *Calphad* **32**, 101-105 (2008).
229. Tzalenchuk, A. et al. Towards a quantum resistance standard based on epitaxial graphene. *Nat Nanotechnol* **5**, 186-189 (2010).
230. Alexander-Webber, J.A. et al. Phase Space for the Breakdown of the Quantum Hall Effect in Epitaxial Graphene. *Phys Rev Lett* **111**, 096601 (2013).

231. Baker, A.M.R., Alexander-Webber, J.A., Altebaeumer, T. & Nicholas, R.J. Energy relaxation for hot Dirac fermions in graphene and breakdown of the quantum Hall effect. *Phys Rev B* **85**, 115403 (2012).
232. Lartsev, A. et al. Tuning carrier density across Dirac point in epitaxial graphene on SiC by corona discharge. *Appl Phys Lett* **105**, 063106 (2014).
233. Moser, J., Verdaguer, A., Jimenez, D., Barreiro, A. & Bachtold, A. The environment of graphene probed by electrostatic force microscopy. *Appl Phys Lett* **92**, 123507 (2008).
234. Lafkioti, M. et al. Graphene on a Hydrophobic Substrate: Doping Reduction and Hysteresis Suppression under Ambient Conditions. *Nano Letters* **10**, 1149-1153 (2010).
235. Mattevi, C., Kim, H. & Chhowalla, M. A review of chemical vapour deposition of graphene on copper. *Journal of Materials Chemistry* **21**, 3324-3334 (2011).
236. Bointon, T.H., Barnes, M.D., Russo, S. & Craciun, M.F. High Quality Monolayer Graphene Synthesized by Resistive Heating Cold Wall Chemical Vapor Deposition. *Adv Mater* **27**, 4200-4206 (2015).
237. Tien, D.H. et al. Study of Graphene-based 2D-Heterostructure Device Fabricated by All-Dry Transfer Process. *Acs Appl Mater Inter* **8**, 3072-3078 (2016).
238. Gannett, W. et al. Boron nitride substrates for high mobility chemical vapor deposited graphene. *Appl Phys Lett* **98**, 242105 (2011).
239. Okamoto, H. Pd-Si (Palladium-Silicon). *J Phase Equilib* **14**, 536-538 (1993).
240. Chen, L.J. Metal silicides: An integral part of microelectronics. *Jom-Us* **57**, 24-30 (2005).
241. Lizzit, S. et al. Transfer-Free Electrical Insulation of Epitaxial Graphene from its Metal Substrate. *Nano Letters* **12**, 4503-4507 (2012).
242. Ismach, A. et al. Toward the Controlled Synthesis of Hexagonal Boron Nitride Films. *ACS Nano* **6**, 6378-6385 (2012).
243. Auwarter, W., Suter, H.U., Sachdev, H. & Greber, T. Synthesis of one monolayer of hexagonal boron nitride on Ni(111) from B-trichloroborazine $(ClBNH)_{(3)}$. *Chem Mater* **16**, 343-345 (2004).
244. Chatterjee, S. et al. Chemical Vapor Deposition of Boron Nitride Nanosheets on Metallic Substrates via Decaborane/Ammonia Reactions. *Chem Mater* **23**, 4414-4416 (2011).
245. Shi, Y.M. et al. Synthesis of Few-Layer Hexagonal Boron Nitride Thin Film by Chemical Vapor Deposition. *Nano Letters* **10**, 4134-4139 (2010).
246. Morscher, M., Corso, M., Greber, T. & Osterwalder, J. Formation of single layer h-BN on Pd(111). *Surface Science* **600**, 3280-3284 (2006).
247. Corso, M., Greber, T. & Osterwalder, J. h-BN on Pd(110): a tunable system for self-assembled nanostructures? *Surface Science* **577**, L78-L84 (2005).
248. Preobrajenski, A.B. et al. Influence of chemical interaction at the lattice-mismatched h-BN/Rh(111) and h-BN/Pt(111) interfaces on the overlayer morphology. *Phys Rev B* **75** (2007).
249. Sutter, P., Lahiri, J., Albrecht, P. & Sutter, E. Chemical Vapor Deposition and Etching of High-Quality Monolayer Hexagonal Boron Nitride Films. *ACS Nano* **5**, 7303-7309 (2011).
250. Joshi, S. et al. Boron Nitride on Cu(111): An Electronically Corrugated Monolayer. *Nano Letters* **12**, 5821-5828 (2012).
251. Gibb, A.L. et al. Atomic Resolution Imaging of Grain Boundary Defects in Monolayer Chemical Vapor Deposition-Grown Hexagonal Boron Nitride. *Journal of the American Chemical Society* **135**, 6758-6761 (2013).
252. Kim, K.K. et al. Synthesis and Characterization of Hexagonal Boron Nitride Film as a Dielectric Layer for Graphene Devices. *ACS Nano* **6**, 8583-8590 (2012).
253. Lee, Y.H. et al. Growth selectivity of hexagonal-boron nitride layers on Ni with various crystal orientations. *Rsc Adv* **2**, 111-115 (2012).

254. Gao, Y. et al. Repeated and Controlled Growth of Monolayer, Bilayer and Few-Layer Hexagonal Boron Nitride on Pt Foils. *ACS Nano* **7**, 5199-5206 (2013).
255. Lee, K.H. et al. Large-Scale Synthesis of High-Quality Hexagonal Boron Nitride Nanosheets for Large-Area Graphene Electronics. *Nano Letters* **12**, 714-718 (2012).
256. Wang, L.F. et al. Monolayer Hexagonal Boron Nitride Films with Large Domain Size and Clean Interface for Enhancing the Mobility of Graphene-Based Field-Effect Transistors. *Adv Mater* **26**, 1559-1564 (2014).
257. Hu, M.G., Geanangel, R.A. & Wendlandt, W.W. The thermal decomposition of ammonia borane. *Thermochim Acta* **23**, 249-255 (1978).
258. Bowden, M., Autrey, T., Brown, I. & Ryan, M. The thermal decomposition of ammonia borane: A potential hydrogen storage material. *Current Applied Physics* **8**, 498-500 (2008).
259. Baitalow, F., Baumann, J., Wolf, G., Jaenicke-Rossler, K. & Leitner, G. Thermal decomposition of B-N-H compounds investigated by using combined thermoanalytical methods. *Thermochim Acta* **391**, 159-168 (2002).
260. Wolf, G., Baumann, J., Baitalow, F. & Hoffmann, F.P. Calorimetric process monitoring of thermal decomposition of B–N–H compounds. *Thermochim Acta* **343**, 19-25 (2000).
261. Shore, S.G. & Parry, R.W. Chemical Evidence for the Structure of the "Diammoniate of Diborane." II. The Preparation of Ammonia-Borane. *Journal of the American Chemical Society* **80**, 8-12 (1958).
262. Chen, X., Bao, X., Billet, B., Shore, S.G. & Zhao, J.-C. Large-Scale and Facile Preparation of Pure Ammonia Borane through Displacement Reactions. *Chemistry – A European Journal* **18**, 11994-11999 (2012).
263. Fang, Z.Z. et al. Facile solid-phase synthesis of the diammoniate of diborane and its thermal decomposition behavior. *Phys Chem Chem Phys* **13**, 7508-7513 (2011).
264. Lu, G.Y. et al. Synthesis of large single-crystal hexagonal boron nitride grains on Cu-Ni alloy. *Nat Commun* **6** (2015).
265. Hielscher, R. *Homepage of the MTEX toolbox*. 2014. http://mtex-toolbox.github.io/ (accessed 13/01/2014).
266. Wood, G.E. et al. van der Waals epitaxy of monolayer hexagonal boron nitride on copper foil: growth, crystallography and electronic band structure. *2d Mater* **2** (2015).
267. Rong, Y.M. et al. Controlling sulphur precursor addition for large single crystal domains of WS_2. *Nanoscale* **6**, 12096-12103 (2014).
268. Prabakaran, A. et al. WS_2 2D nanosheets in 3D nanoflowers. *Chem Commun* **50**, 12360-12362 (2014).
269. Schädel, M. & Shaughnessy, D. The Chemistry of Superheavy Elements. (Springer, 2014).
270. Margolin, A. et al. Fullerene-like WS_2 nanoparticles and nanotubes by the vapor-phase synthesis of WCl_n and H_2S. *Nanotechnology* **19**, 095601 (2008).
271. Park, J. et al. Layer-modulated synthesis of uniform tungsten disulfide nanosheet using gas-phase precursors. *Nanoscale* **7**, 1308-1313 (2015).
272. Kim, S.M. et al. Synthesis of Patched or Stacked Graphene and hBN Flakes: A Route to Hybrid Structure Discovery. *Nano Letters* **13**, 933-941 (2013).
273. Liu, Z. et al. In-plane heterostructures of graphene and hexagonal boron nitride with controlled domain sizes. *Nat Nanotechnol* **8**, 119-124 (2013).
274. Lu, J., Gomes, L.C., Nunes, R.W., Neto, A.H.C. & Loh, K.P. Lattice Relaxation at the Interface of Two-Dimensional Crystals: Graphene and Hexagonal Boron-Nitride. *Nano Letters* **14**, 5133-5139 (2014).
275. Kashtiban, R.J. et al. Atomically resolved imaging of highly ordered alternating fluorinated graphene (vol 5, pg 4902, 2014). *Nat Commun* **5** (2014).

276. Sundaram, R.S. et al. Electroluminescence in Single Layer MoS_2. *Nano Letters* **13**, 1416-1421 (2013).
277. Ye, Y. et al. in CLEO: 2014 STh4B.4 (Optical Society of America, San Jose, California; 2014).
278. Xu, Y.X., Sheng, K.X., Li, C. & Shi, G.Q. Self-Assembled Graphene Hydrogel via a One-Step Hydrothermal Process. *ACS Nano* **4**, 4324-4330 (2010).
279. Jiang, L.L. & Fan, Z.J. Design of advanced porous graphene materials: from graphene nanomesh to 3D architectures. *Nanoscale* **6**, 1922-1945 (2014).
280. Niu, Z.Q., Chen, J., Hng, H.H., Ma, J. & Chen, X.D. A Leavening Strategy to Prepare Reduced Graphene Oxide Foams. *Adv Mater* **24**, 4144-4150 (2012).
281. Chen, Z.P. et al. Three-dimensional flexible and conductive interconnected graphene networks grown by chemical vapour deposition. *Nature Materials* **10**, 424-428 (2011).
282. www.goodfellow.com. *LCS Copper foam*. 2015. http://www.goodfellowusa.com/larger-quantities/metals/lcs-copper-foam/ (accessed 06/10/2015).
283. Prasai, D., Tuberquia, J.C., Harl, R.R., Jennings, G.K. & Bolotin, K.I. Graphene: Corrosion-Inhibiting Coating. *ACS Nano* **6**, 1102-1108 (2012).
284. Li, W., Li, D., Fu, Q. & Pan, C. Conductive enhancement of copper/graphene composites based on high-quality graphene. *Rsc Adv* **5**, 80428-80433 (2015).
285. Goli, P. et al. Thermal Properties of Graphene-Copper-Graphene Heterogeneous Films. *Nano Letters* **14**, 1497-1503 (2014).
286. Kim, Y. et al. Strengthening effect of single-atomic-layer graphene in metal-graphene nanolayered composites. *Nat Commun* **4** (2013).
287. Shuai, C. et al. Akermanite scaffolds reinforced with boron nitride nanosheets in bone tissue engineering. *J Mater Sci-Mater M* **26** (2015).
288. Sun, H.Y., Xu, Z. & Gao, C. Multifunctional, Ultra-Flyweight, Synergistically Assembled Carbon Aerogels. *Adv Mater* **25**, 2554-2560 (2013).
289. Poco Graphite, I. *Poco Graphite*. 2015. http://poco.com (accessed 20/11/2015).
290. Mecklenburg, M. et al. Aerographite: Ultra Lightweight, Flexible Nanowall, Carbon Microtube Material with Outstanding Mechanical Performance. *Adv Mater* **24**, 3486-3490 (2012).
291. Zhu, M.Y., Outlaw, R.A., Bagge-Hansen, M., Chen, H.J. & Manos, D.M. Enhanced field emission of vertically oriented carbon nanosheets synthesized by C_2H_2/H_2 plasma enhanced CVD. *Carbon* **49**, 2526-2531 (2011).
292. Ahn, H.S. et al. Self-assembled foam-like graphene networks formed through nucleate boiling. *Sci Rep-Uk* **3** (2013).
293. Wang, X.B. et al. Three-dimensional strutted graphene grown by substrate-free sugar blowing for high-power-density supercapacitors. *Nat Commun* **4** (2013).
294. Candelaria, S.L. et al. Nanostructured carbon for energy storage and conversion. *Nano Energy* **1**, 195-220 (2012).
295. Zhu, J.X., Yang, D., Yin, Z.Y., Yan, Q.Y. & Zhang, H. Graphene and Graphene-Based Materials for Energy Storage Applications. *Small* **10**, 3480-3498 (2014).
296. Ma, Z. et al. A review of cathode materials and structures for rechargeable lithium-air batteries. *Energ Environ Sci* **8**, 2144-2198 (2015).
297. Girishkumar, G., McCloskey, B., Luntz, A.C., Swanson, S. & Wilcke, W. Lithium - Air Battery: Promise and Challenges. *J Phys Chem Lett* **1**, 2193-2203 (2010).
298. Luntz, A.C. & McCloskey, B.D. Nonaqueous Li-Air Batteries: A Status Report. *Chemical Reviews* **114**, 11721-11750 (2014).
299. Johnson, L. et al. The role of LiO_2 solubility in O_2 reduction in aprotic solvents and its consequences for Li–O_2 batteries. *Nat Chem* **6**, 1091-1099 (2014).

300. Peng, Z., Freunberger, S.A., Chen, Y. & Bruce, P.G. A Reversible and Higher-Rate Li-O_2 Battery. *Science* **337**, 563-566 (2012).
301. Liu, T. et al. Cycling Li-O_2 batteries via LiOH formation and decomposition. *Science* **350**, 530-533 (2015).
302. Weng, Q.H. et al. Highly Water-Soluble, Porous, and Biocompatible Boron Nitrides for Anticancer Drug Delivery. *ACS Nano* **8**, 6123-6130 (2014).